Universidade de São Paulo
Instituto de Astronomia, Geofísica e Ciências Atmosféricas
Departamento de Geofísica

Caio Morelli Vicentini

The contribution of chaotic dynamics on the genesis of Chapecó silicic rocks from Paraná-Etendeka Magmatic Province: an experimental approach

São Paulo
2023

Caio Morelli Vicentini

The contribution of chaotic dynamics on the genesis of Chapecó silicic rocks from Paraná-Etendeka Magmatic Province: an experimental approach

Versão Corrigida. O original encontra-se disponível na Unidade.

Thesis presented to the Geophysics Department of Instituto de Astronomia, Geofísica e Ciências Atmosféricas of the University of São Paulo as a partial requirement for the Ph.D title.
Concentration Area: Geophysics

Advisor: Prof. Dra. Leila Soares Marques
Co-advisor: Prof. Dr. Donald Bruce Dingwell

São Paulo

2023

À minha família...

AGRADECIMENTOS/AKNOWLEDGEMENTS

As pessoas que fazem parte desta longa jornada são muitas. Em primeiro lugar agradeço a Deus por ter chegado até aqui. Agradeço imensamente à minha amada esposa pelo apoio, esforço, companheirismo, carinho e a paciência. Sem você, Maria Julia, tudo seria pesado demais. Agradeço ao Ícaro, que participou tanto quanto nós deste processo, e que junto com Luiz e Clara alegram muito a nossa vida. Agradeço muitíssimo aos meus pais e ao Pedro, de quem nunca faltaram apoio e encorajamento. Vocês me ensinaram a valorizar o estudo e a dedicação no aprendizado. Muito obrigado, família!

Eu agradeço muito à Prof. Dra. Leila Marques, que sempre me orientou, apoiou e buscou aperfeiçoar em mim o olhar crítico-científico através de muitas discussões. Igualmente, agradeço à Prof. Dra. Cristina de Campos, que esteve conosco desde a concepção do projeto, e que me acolheu como um filho durante o estágio em Munique. Muito obrigado!

Também agradeço àqueles que contribuíram em cada etapa deste projeto: ao Prof. Dr. Antonio Nardy pelas discussões e viagem de campo; Carol, Júlio, Zanon e Limeira, que me ajudaram na coleta de amostras; agradeço a todos os professores do IAG, mas em especial, aos professores Carlos Mendonça e Victor Sacek, que contribuíram com aulas, opiniões e discussões; todo os funcionários do IAG, em especial à Sonia; e ao Prof. Dr. Valdecir Janasi, que viabilizou o meu período de estágio na LMU.

Agradeço às agências de fomento CAPES e CNPq pelas bolsas de estudo (CAPES: processos 88882.332947/2019-01, 88887.363370/2019-00 e 88887.650486/2021-00), diárias de campo e análises (CNPq processo: 303139/2017-0).

I would like to thank Professor Dr. Don Dingwell for the supervision during my time at LMU, and for extending it during COVID pandemic. Thank you for all support!
I am very grateful for the LMU staff that patiently helped me. In especial, I thank Dr. Werner Ingrisch who performed all experiments with me. I also thank Kai Hess, Melanie Kaliwoda, Dirk Müller, Corrado Cimarelli and Ulrich Küppers, who helped me with all equipment and analysis. Finally, I thank Hilger Lohringer for helping with

sample preparation, and Rosa, Rike and Margot for helping with the bureaucracy. I am very grateful for everything!

ABSTRACT

Vicentini, C.M. (2023). The contribution of chaotic dynamics on the genesis of Chapecó silicic rocks from Paraná-Etendeka Magmatic Province: an experimental approach. (Doctoral thesis). Instituto de Astronomia, Geofísica e Ciências Atmosféricas, Universidade de São Paulo, São Paulo.

Mixing dynamics is thought to decisively influence volcanism on Earth. Magma mixing is pointed to occur under chaotic dynamics in nature based on several field observations of fractal patterns (i.e., scale invariant) emerging on geological sites. Using a chaotic mixing approach, this work is the first attempt to experimentally study the mutual contamination between mafic and felsic phases using natural samples from the Paraná-Etendeka Magmatic Province (PEMP) as end-members. Our final aim is to unravel the origin of the high-Ti Chapecó dacites from PEMP, distinguishing between Chapecó-Guarapuava (CGD) and Chapecó-Ourinhos dacites (COD). A campaign of four chaotic mixing experiments was performed using an apparatus that operates at high temperatures (i.e., T_{exp} > 1,000 °C) under 1 atm pressure to mix silicate melts with stark contrasting rheologies (i.e., viscosities) by means of controlled chaotic dynamics. Experiments 1, 2 and 3 consist in the mixing of 80% of an identical basaltic glass (high-Ti Pitanga type from PEMP) with 20% of rhyolitic glasses that vary according to the experiment (rocks from the Paraná Basin basement) at a constant temperature T_{exp} = 1,350 °C. Experiment 4 is the mixing of 80% of a dacitic glass (high-Ti CGD from PEMP) with 20% of a rhyolitic glass (the identical used in Exp2) at T_{exp} = 1,500 °C. After experiments, morphological aspects of the experimental products include stretched and folded filaments of alternating phases, confirming that chaotic dynamics was achieved. In the experiments 1, 2 and 3, orbicular structures containing dendritic crystals and remnant portions of glass in the basaltic area were described for the first time. The observed dendritic areas of the basaltic regions point towards an early crystallization process during the initial quenching, and that the crystallization process occurs heterogeneously. In Exp4, sections develop fractal structures that are expected theoretically (i.e., Poincaré sections). The fractal dimension D_{box} = 1.60(3) calculated for a representative section is similar to literature data. Chemical transects along contact zones between the interconnected end-members confirm chemical exchanges (or contamination) between the melts, which occur by diffusion. The highest contamination degrees in the mafic phases are observed for SiO_2, K_2O, Cs, Rb, U, Th and Pb (trace elements were not determined in Exp4). As a consequence, these elements depict strong non-linear curves when plotted against other elements. Regarding trace analyses, the group of elements V, Sc, Sr, Cs, Rb, U and Th (G1) show normal diffusion profiles, whilst the elements Ga, Nb, Zr, Y, Ba, REE, Ta, Hf and Pb (G2) show uphill diffusion.

It causes anomalous concentrations along chemical transects and a more marked non-linear behaviour in inter-elemental plots associated to G2. For all experiments, the elemental mobility along the contact areas was quantified calculating the normalized variance (σ^2_n), which consistently indicates the connection between viscosity and mobility for major/minor (all experiments) and for G1 elements (experiments 1, 2 and 3). Moreover, it was identified that the most mobile elements present low (< 1.0) or high field strength Z/r^2 (> 4.0). In the case of G2 elements, the most expressive values of (σ^2_n) are associated to the smallest initial gradients (e.g., Ga, Nb and REEs). Considering data from G1 and G2, it is proposed that differences up to 30% in the initial gradient enhance considerably the probability of uphill diffusion. In respect to the Exp4, expected (σ^2_n) patterns emerge in comparison with the values computed using available data from Chapecó dacites. It supports the generation of COD from the interaction of pre-existing CGD melts with crustal material. In respect to the linear mixing model LM, initial calculations are in disagreement with our experimental results regarding the best contaminant candidate on the formation of the Chapecó dacites. Taking into account the same degree of evolution derived from Ti contents, different pairs of trace elements lead to distinct contamination degrees *f*. The intervals of *f* are: i) 0.2 to 0.5 to generate CGD from Exp2 results; and ii) 0.3 to 0.7 to generate COD from Exp1 results. The best fits (i.e., similar *f*) are found for elements of G1 and Ti (such as Rb, Sr, U and Th) although REE and Pb are in good agreement as well. Data from Exp4 well reproduce the COD chemical behaviour of major compounds that usually act as network formers in melts (Fe, Al, Ti and Si). The experimental data produced in this thesis suggest that magma mixing might develop a central role on Chapecó dacites genesis by means of a chaotic dynamics. Reproduced features, such as morphological, chemical and frequency patterns, are similar to the PEMP dacitic rare outcrops, particularly for elements that present expressive initial gradients in the mixing system. It points towards short interaction times, low convective forces, and a predominance of density driven separation of contrasting melts (*i.e.*, simulated conditions) as possible mechanisms involved in the genesis of these rocks. Further studies on trace elements (e.g., Exp4) and isotopic systems in the hybrid experimental glasses are necessary and may shed more light on the genesis of such relevant silicic magmatism.

Keywords: Magma Mixing, Chaotic Dynamics at High-Temperature, Paraná-Etendeka Magmatic Province, Chapecó-type Silicic Rocks, Mafic-Felsic Mutual Contamination, Experimental Petrology at High-Temperature.

RESUMO

Vicentini, C.M. (2023). A contribuição da dinâmica caótica à gênese das rochas do tipo Chapecó da Província Magmática Paraná-Etendeka: um estudo experimental. (Tese de doutorado). Instituto de Astronomia, Geofísica e Ciências Atmosféricas, Universidade de São Paulo, São Paulo.

O vulcanismo terrestre é influenciado de modo relevante pela dinâmica de misturas. Na natureza, a mistura de magmas ocorre possivelmente sob princípios dinâmicos caóticos, pensamento baseado na observação de padrões fractais (i.e., independentes de escala) em diversos trabalhos de campo. Deste modo, este trabalho é a primeira tentativa de se estudar experimentalmente a contaminação mútua entre fases máficas e félsicas usando amostras naturais da Província Magmática Paraná-Etendeka (PEMP) como membros da mistura, levando-se em consideração uma dinâmica caótica governando este processo. O objetivo é avançar no conhecimento sobre a origem dos dacitos do tipo Chapecó da PEMP, distinguindo entre os dacitos Chapecó-Guarapuava (DCG) e os Chapecó-Ourinhos (DCO). Portanto, uma campanha de quatro experimentos de mistura caótica foi realizada usando um aparato experimental que opera em altas temperaturas (i.e., T_{exp} > 1000 °C) sob pressão de 1 atm para misturar *melts* silicáticos com reologias contrastantes (i.e, viscosidade). Os experimentos 1, 2 e 3 consistem na mistura de 80% de um vidro basáltico idêntico (o tipo alto-Ti Pitanga da PEMP) com 20% de vidros riolíticos que variam de acordo com o experimento (rochas do embasamento da Bacia do Paraná) a uma temperatura constante T_{exp} = 1350 °C. Já o experimento 4 consiste na mistura de 80% de um vidro dacítico (o tipo alto-Ti DCG da PEMP) com 20% de um vidro riolítico (o mesmo utilizado no Exp2) a uma temperatura T_{exp} = 1500 °C. Após os experimentos, os aspectos morfológicos dos produtos experimentais incluíram filamentos estirados e dobrados de fases alternadas, confirmando que a dinâmica caótica foi reproduzida. Nos experimentos 1, 2 e 3, foram descritas pela primeira vez estruturas orbiculares contendo cristais dendríticos e porções remanescentes de vidro na zona basáltica. As áreas dendríticas observadas nas regiões basálticas apontam para um processo de cristalização precoce durante o início do resfriamento, e que o processo de cristalização ocorre de forma heterogênea. No Exp4, as secções desenvolvem estruturas fractais que são previstas teoricamente (i.e., secções de Poincaré). A dimensão fractal D_{box} = 1,60(3) calculada para uma secção representativa se assemelha à dados encontrados na literatura. Os perfis químicos ao longo de zonas de contato entre as fases confirmam que houve trocas química (ou contaminação) entre os membros, as quais ocorrem por difusão. Os graus de contaminação mais elevados nas fases máficas são observados para SiO_2, K_2O, Cs, Rb, U, Th e Pb (os elementos traço não foram determinados no Exp4). Consequentemente, estes elementos

apresentam curvas não lineares bem demarcadas quando comparados com outros elementos. Relativamente às análises de traços, o grupo de elementos V, Sc, Sr, Cs, Rb, U e Th (G1) apresenta perfis de difusão normais, enquanto que os elementos Ga, Nb, Zr, Y, Ba, REE, Ta, Hf e Pb (G2) apresentam uma difusão tipo *uphill* (i.e., contrária ao gradiente químico). Em todos os experimentos, a mobilidade elementar ao longo das interfaces foi quantificada calculando a variância normalizada (σ^2_n), que indica consistentemente a ligação entre a viscosidade e a mobilidade dos elementos maiores/menores (em todos os experimentos) e para os elementos de G1 (experimentos 1, 2 e 3). Além disso, foi identificado que os elementos com maior mobilidade apresentam baixo (< 1,0) ou alto *field strenght* Z/r^2 (> 4,0). No caso dos elementos de G2, os valores mais expressivos de (σ^2_n) estão associados aos menores gradientes químicos iniciais (e.g., Ga, Nb e REEs). Considerando-se os dados de G1 e G2, propõe-se que diferenças de até 30% no gradiente inicial aumentam consideravelmente a probabilidade de ocorrência do fenômeno de difusão *uphill*. Em relação ao Exp4, padrões esperados de (σ^2_n) emergem em comparação com os valores calculados usando os dados disponíveis de análises químicas nos dacitos do tipo Chapecó. Na comparação com o modelo de mistura linear LM, os cálculos iniciais estão em desacordo com os resultados dos experimentos de mistura caótica no que diz respeito ao melhor candidato a contaminante para a formação do Chapecó. Considerando-se o mesmo grau de evolução derivado dos teores de Ti, diferentes pares de elementos traço resultam em graus de contaminação *f* distintos. Os intervalos de *f* encontrados são: i) 0,2 a 0,5 para gerar DCG a partir dos resultados do Exp2; e ii) 0,3 a 0,7 para gerar DCO a partir dos resultados do Exp1. Os melhores ajustes (i.e., *f* semelhante) são encontrados para pares de elementos de G1 e Ti (como Rb, Sr, U e Th), embora ETRs e Pb também se ajustem bem ao modelo LM. Os dados do Exp4 reproduzem bem o comportamento químico dos principais componentes dos DCO, que geralmente atuam como formadores de rede cristalina (Fe, Al, Ti e Si). Os dados experimentais produzidos nesta tese sugerem que a mistura de magmas, via dinâmica caótica, pode ter desenvolvido um papel central na gênese dos dacitos do tipo Chapecó. As características reproduzidas, tais como padrões morfológicos, químicos e de frequência, são semelhantes aos afloramentos dacíticos raros da PEMP, particularmente no caso de elementos que apresentam gradientes iniciais expressivos no sistema. Estes fatores apontam para curtos tempos de interação, forças convectivas reduzidas e uma predominância da separação dos *melts* contrastantes devido ao contraste de densidade (i.e., condições simuladas) como possíveis mecanismos envolvidos na génese destas rochas. São necessários mais estudos sobre o comportamento dos elementos traço (e.g., Exp4) e dos sistemas isotópicos nos vidros experimentais híbridos, os quais poderão elucidar ainda mais a gênese deste relevante magmatismo silicático.

Palavras-chave: Mistura de Magmas, Dinâmica Caótica a Altas Temperaturas, Província Magmática Paraná-Etendeka, Rochas Silicáticas do tipo Chapecó, Contaminação Mútua em Sistemas Máfico-Félsico, Petrologia Experimental em Altas Temperaturas.

CONTENTS

CHAPTER 1 – INTRODUCTION

The Paraná-Etendeka Magmatic Province (PEMP – Figure 1.1) is the second largest continental magmatic province in the world, whose emplacement is associated with the continental breakup of the Western Gondwana and South Atlantic Ocean opening (Piccirillo & Melfi, 1988; Marsh et al., 2001). The volcanic material exceeds 700,000 km^3 of volume (Piccirillo & Melfi, 1988) and outcrops over an area that 900,000 km^2 (Frank et al., 2009) mainly in the Brazilian S-SW region, and establishes the Serra Geral Formation of the Paraná Basin. In the African side, the sequences develop in relatively smaller areas along the coast of Namibia (Milner et al., 1992; Marsh et al., 2001), and, to a lesser extent, in Angola (Alberti et al., 1992; Marsh & Swart, 2016).

Tholeiitic magmatism is predominant in the PEMP, with basic rocks (SiO_2 < 52 wt.%) representing 90% of occurrences (Piccirillo & Melfi, 1988). In addition, PEMP presents two particular silicic rocks: a) rhyolites with aphyric texture (denoted Palmas type at the Brazilian side), and b) dacites with porphyritic texture (denoted Chapecó type at the Brazilian side). Palmas and Chapecó cover an area of 64,000 km² (Nardy et al., 2002, 2008). These rocks are associated with basaltic flows and outcrop most commonly on the top of basaltic units, indicating a relation with the final stages of volcanism (Piccirillo & Melfi, 1988). Palmas and Chapecó are limited mostly to the southern and central regions of the province, with the exception of a small number of flows occurring in the northern region (Ourinhos/SP) including some dykes that occur on São Sebastião Island and the adjacent coastal area of São Paulo state (Bellieni et al, 1990; Garda, 1995; Garda et al., 1996; Vicentini, 2015).

The geochemistry of PEMP silicic rocks also indicates that they evolved from basaltic unit rocks. A clear distinction emerges especially regarding TiO_2 contents, classifying the province volcanism as bi-modal and dividing it as follows (Bellieni et al., 1984; Mantovani et al., 1985a; Piccirillo & Melfi, 1988; Marques et al., 1989; Peate, 1997): a) Southern region – low-Ti basalts (LTi: TiO_2 < 2%), with associated Palmas rhyolites; and b) Northern region – high-Ti basalts (HTi: $TiO_2 \geq 2\%$), with associated Chapecó dacites.

Figure 1.1: Paraná-Etendeka Magmatic Province map with the localization of silicic rocks according to Nardy et al. (2008), from Machado et al. (2015) and references therein.

The genesis and evolution of such expressive magmatism have been under severe debate. The first models discussed the generation of silicic rocks occurring by lower crust partial melting (e.g. Cordani et al., 1980) in contrast with an evolution by fractional crystallization (Mantovani et al., 1985a). It was also proposed that re-melting of LTi and HTi basaltic material trapped in crust-mantle interface (underplating) might generate Palmas and Chapecó respectively (Piccirillo et al., 1988; Marques, 1988). In addition, varying degrees of crustal contamination during ascent of magmas and/or residence time are claimed to explain the trace and isotopic signatures. Considering

such signatures, most recent models reinforced the hypothesis of Chapecó dacites being generated by partial melting of underplated HTi basaltic material (Garland et al., 1995), and an evolution of LTi basaltic magmas by fractional crystallization with crustal assimilation to generate Palmas rhyolites (Garland et al., 1995; Polo et al., 2018).

Such models can explain general features of silicic rocks, not taking into account the variability observed on field though (e.g., Chapecó subtypes Guarapuava, Tamarana and Ourinhos – Nardy et al., 2008). Recent investigations point especially towards the presence of xenocrystals or anticrystals in Chapecó dacites (Luchetti et al., 2018), which may be an indicative that the magmas at distinct evolution stages got into contact at some point. This context depicts a scenario of interconnected magma chambers leading to heterogeneities and possibly to the development of different contamination rates.

A near-ubiquitous mechanism involved on petrogenetic processes is the mixing of silicate melts (Morgavi et al., 2022). Evidence for magma mixing can be found on scales from hand specimens to batholiths and volcanic sequences. Moreover, mixing is able to generate a large compositional variability in rock suites as well as to trigger volcanic eruptions (Anderson, 1982; Bateman, 1995; Leonard et al., 2002; Perugini et al., 2010).

The concept of magma mixing has been applied on Earth Sciences since the popularization of linear mixing equation (Langmuir et al., 1978), which is especially employed on isotopic systematics. However, a common problem found in literature of magma mixing is the terminology. In petrology, the term “mingling“ is preferred to refer to a first order physical dispersion of a magma body through another magma (*i.e.*, enclave in a host magma) without any chemical exchange (by diffusion, etc). Whether chemical exchange does occur it is referred to as “mixing”. The central point on this discussion is the resolution that an observer has to confirm chemical exchanges and/or to quantify them.

Several experimental studies have considered diffusion as the main mechanism to produce the chemical exchanges in melt-melt and melt-crystal systems (e.g., Watson, 1982, 1985; Lesher & Walker, 1986; Zhang et al., 1989, 2010; Lesher 1990). It is known that diffusion depends on composition (e.g., Zhang et al., 2010), which in turn determines the melt viscosity. Systems with stark contrasting rheologies (or viscosities) are often considered immiscible since intermingling fails and causes little interaction between phases. Consequently the mixing is commonly reduced to a local problem and

is discussed in terms of diffusion rates. It is usual referring "contamination" as the process in which a mafic body locally incorporates felsic material and "selective contamination" if some elements are captured by mafic phases rather than others (Watson, 1982; Lesher, 1990; Waight & Lesher, 2010).

The relative novelty on magma mixing study was the inclusion of dynamical approach that can exponentially enhance chemical diffusion. This approach is based on several field observations of fractal patterns (i.e., scale invariant) emerging on geological sites (e.g. De Rosa et al., 2002; Poli and Perugini, 2002; Perugini et al., 2003b, 2006). Thus, chaotic dynamics has been proposed to control such mixing processes (Perugini & Poli, 2000, Perugini et al., 2003a,b) in contrast to the usual geochemical assumption of linear mixing model (Langmuir et al., 1978). Numerical simulations considering both processes, namely advection, by means of stretching and folding, and diffusion, resulted in good agreement with geochemical data (e.g. Perugini et al. 2003a,b, 2006, 2008, 2010). Although such models are a simplification, they have reproduced similar patterns in face to those found in nature.

More comprehensive works were possible after the development of an experimental apparatus that reproduces the chaotic dynamics, mimicking the mixing between two silicate melts at high temperatures (> 1,200 °C) with strong viscosity contrasts (> 10^3) (De Campos et al., 2011). The chaotic mixing device applies a specific motion protocol to reproduce the stretching and folding mechanism that develops fractal structures during magma mixing. It leads to an exponential increase of intermingled filaments between the end-members (such as in nature), which enhances the contact surface and, hence, chemical exchanges by diffusion. The first experiments were performed with synthetic samples, analogue to volcanic rocks, and have demonstrated that the mixing of silicate melts can be considered as a chaotic process (De Campos et al., 2011; Perugini et al., 2012). Further experiments using natural samples revealed more complex scenarios in natural systems, although new insights and applications emerged as well (Morgavi et al., 2013; Perugini et al., 2015; this work).

1.1 OBJECTIVES

The aim of this thesis is to experimentally study the genesis of HTi Chapecó dacites (Figure 1.1) evaluating the role that chaotic mixing may have played on this process. The employed methodology was to perform a campaign of four new chaotic mixing experiments using the apparatus developed by De Campos et al. (2011). The experimental setups were as follows:

i) Three experiments performed starting from a natural basaltic melt composition while solely varying the chemical composition of the contaminant. In this way the influence of: a) chaotic dynamics prevailing over a fixed period of time, and b) changes in the contaminant melt chemistry were systematically investigated. All three contaminants, named LMC-027, LMC-020 and LMC-018, were respectively collected on Paraná Basin basement based located on HP-254, HP-21 and HP-223 sites (Prazeres Filho, 2005; Prazeres Filho et al., 2003). The choice was made considering the reported isotopic signatures. The KS-700 basaltic sample is considered representative of HTi Pitanga type from northern PEMP and was selected based on previous exhausting analysis (Rocha-Junior et al., 2013). The experiments are referred as:

- Exp1 – the mixing between 80% of KS-700 basaltic starting glass (HTi Pitanga type from PEMP) and 20% of LMC-027 rhyolitic glass (a sienogranite from Capão Bonito Stock, Campo Belo/SP);
- Exp2 – the mixing between 80% of KS-700 basaltic starting glass (HTi Pitanga type from PEMP) and 20% of LMC-020 rhyolitic glass (a monzogranite from Conhaporanga Batholith, Paraí do Sul/PR);
- Exp3 – the mixing between 80% of KS-700 basaltic starting glass (HTi Pitanga type from PEMP) and 20% of LMC-018 rhyolitic glass (a monzogranite from Sguário Granite, Castro/PR).

ii) one final experiment performed starting from the CPG-012 Chapecó-Guarapuava dacite (CGD) and the LMC-020 monzogranite from Cunhaporanga batholith. The tested hypothesis is that Chapecó-Ourinhos dacites (COD), the most evolved unit of Chapecó dacites, could be formed from CGD during ascent and/or replenishment events. Both groups are compositionally similar, although COD is more

enriched in SiO_2, incompatible elements such as Ba, U, Th and Zr, and radiogenic isotopes. COD characteristics are considered typical of a crustal contamination process. The experiment is referred as:

- Exp4 – the mixing between 80% of Chapecó-Guarapuava starting glass (high-Ti dacite from PEMP) and 20% of LMC-020 rhyolitic glass (a monzogranite from Conhaporanga Batholith, Paraí do Sul/PR).

1.2 THE CHAPECÓ DACITES: HIGH-TI SILICIC ROCKS FROM PEMP

The Chapecó silicic flows are distributed in plateaus along the Central and Northern regions of the Paraná Basin. It is noteworthy that the occurrence of Chapecó rocks represents a small fraction (approx. 0.5%) of the total volume of Fm. Serra Geral silicic volcanics (approx. 2.5%) (Nardy, 1996; Nardy et al., 2002, 2008). Bodies are tabular and extended laterally for some dozens of kilometers. Chapecó is divided into two main groups called Guarapuava (occurring on northern of Rio Grande do Sul, Santa Catarina and southern of Paraná States) and Ourinhos (occurring southwestern of São Paulo State). A third group named Tamarana is placed on between Guarapuava and Ourinhos, however it is less expressive and composed only by two plateaus in Paraná State. The Ourinhos subtype is distributed along the Paranapanema River and contacts directly the sandstones of the Fm. Botucatu Formation. Guarapuava subtype is located between the alignments of Uruguay and Iguazú Rivers, with the highest plateaus occurring in Pinhão, Três Pinheiros and Xanxerê regions (Nardy et al., 2008).

Chapecó dacites are porphyritic with up to 24% phenocrysts of plagioclase (ca. 2 cm long) inside an aphanitic matrix composed mainly by augite, pigeonite, magnetite and apatite (Bellieni et al., 1986; Garland et al., 1995; Nardy et al., 2008; Janasi et al., 2011; Luchetti et al., 2014, 2018).

In respect to the geochemistry, Chapecó is enriched in K_2O, P_2O_5, Ba, Nb, Zr, Y, and REE (La, Ce, Nd, Yb, Lu), and depleted in Rb, Th, and U, relatively to the low-Ti Palmas rhyolites from PEMP. The Chapecó-Guarapuava dacites (CGD) exhibit lower contents of SiO_2, total alkalis ($Na_2O + K_2O$), and the incompatible trace elements Rb, Ba, Th, U, and Pb. relative to Chapecó-Ourinhos dacites (COD), and higher amounts of TiO_2, Fe_2O_{3t}, MgO, P_2O_5, as well as Sr, Zr and Y (Bellieni et al., 1986; Piccirillo *et al.*, 1987; Garland *et al.*, 1995; Janasi et al., 2007; Nardy et al., 2008; Freitas, 2009).

Regarding the isotopic ratios, the Chapecó dacites are generically characterised by slightly higher initial ($^{87}Sr/^{86}Sr)_i$ ratios initial Sr than the Hi-Ti basalts (corrected to 134 Ma – Janasi et al., 2011; Gomes & Vasconcelos, 2021): $^{87}Sr/^{86}Sr_i$ between 0.70488 and 0.70806 (mean = 0.70674 ± 0.00116; N = 21); $^{143}Nd/^{144}Nd_i$ between 0.51174 and 0.51228 (mean = 0.51216 ± 0.00015; N = 10). CODs are considered contaminated with crustal material (Sr_i approx. 0.7085) in comparison to CGD (Sr_i approx. 0.7060) (Mantovani et al., 1985b; Piccirillo et al., 1987; Peate et al., 1992; Garland et al., 1995; Freitas, 2009; Angelini, 2018).

Thermobarometric analyses indicated that the mean temperature of crystallization ranges from 900 °C to 1100 °C, they formed under pressures of up to. 4.0 kbar and H_2O content varying between 0.6% and 1.2% (Garland et al., 1995; Luchetti et al., 2018). Data point towards small and shallower magmatic chambers feeding the flow units, also with lower volatile contents. Crystal size distribution (CSD) in Chapecó reveals different thermal regimes generating crystallization inside magma chamber (pre-eruptive) and during the magma ascent (syn-eruptive) (Luchetti et al., 2018). Although these authors do not recognized mingling or mixing structures on analyzed outcrops and thin sections, this hypothesis was claimed as a potential explanation to the CSD curve obtained since data was considered insufficient to an exhausting investigation.

1.3 THESIS OUTLINE

The thesis consists of five chapters and an appendix as follows:

- Chapter 1: The Introduction presents the investigated problem and the initial considerations. The aim of this thesis and the approach adopted to solve the problem are defined as well.
- Chapter 2: The research article published in Chemical Geology journal is presented, entitled *"Contamination of basalt through silicic melts: The first chaotic dynamics experiments with Paraná-Etendeka starting materials"*. It explores three experimental simulations of the impact of high-Ti basaltic melt from Paraná-Etendeka Magmatic Province (PEMP) on a pre-existing continental crust. The aim is to unravel the role of chaotic mixing on the origin of the Chapecó dacites from PEMP.

- Chapter 3: It presents the trace element analysis for the three experiments of Chapter 2. It will be submitted for latter publication in a high impact journal that focuses on experimental works (e.g., *Geochimica et Cosmochimica Acta*).
- Chapter 4: The research article submitted to Geoscience Frontiers journal is presented, entitled *"Chaotic Mixing Experiments: Unravelling Contamination Processes on Dacitic Melts"*. Data from electron probe microanalysis performed in one experiment unravel dacitic-rhyolitic melt interaction at high temperatures. The aim is to study the role of chaotic mixing on the origin of the Chapecó-Ourinhos dacites from Chapecó-Guarapuava dacitic melts interacting with crustal rocks from the PEMP basement.
- Chapter 5: The *"Final Considerations"* section summarizes what has been achieved from the chaotic mixing experiments performed in this thesis. In addition, it proposes future research lines to achieve a more comprehensive overview on generation of such relevant magmatic rocks.
- Appendix: Tables with the chemical analyses are presented (links to repository files). It includes: i) new data obtained by X-ray fluorescence (XRF) and laser ablation inductively coupled plasma mass spectrometry (LA-ICP-MS) for bulk rock analysis performed on the collected samples, prior the chaotic mixing experiments; ii) data obtained by electron probe microanalysis (EPMA) and LA-ICP-MS on the representative transects in the experimental glasses, produced after the chaotic mixing experiments.

CHAPTER 2 – CONTAMINANTION OF BASALT THROUGH SILICIC MELTS: THE FIRST CHAOTIC DYNAMIC EXPERIMENTS WITH PARANÁ-ETENDEKA STARTING MATERIALS (PUBLISHED IN CHEMICAL GEOLOGY)

Caio M. Vicentini[1,2], Cristina P. de Campos[1], Werner Ertel-Ingrisch[1], Leila S. Marques[2], Donald B. Dingwell[1], Diego Perugini[3]

[1] *Department of Earth and Environmental Sciences, Ludwig Maximilians University, Theresienstrasse 41/III, 80333 Munich, Germany*

[2] *Instituto de Astronomia, Geofísica e Ciências Atmosféricas – Universidade de São Paulo, Rua do Matão, 1226, Cidade Universitária, 05508-090, São Paulo, Brazil*

[3] *Department of Physics and Geology, University of Perugia, Via Alessandro Pascoli, s.n.c, 06123, Perugia, Italy*

DOI: https://doi.org/10.1016/j.chemgeo.2022.121200

ABSTRACT

This work is the first attempt to simulate experimentally the impact of underplating high-Ti basaltic melt from Paraná-Etendeka Magmatic Province (PEMP) on a pre-existing continental crust. Our final aim is to unravel the origin of high volumes of high-Ti Chapecó dacitic melts. A campaign of three new chaotic mixing experiments was performed starting from a natural basaltic melt composition (*i.e.*, high-Ti Pitanga-type) while solely varying the chemical composition of rhyolitic end-member (*i.e.*, the contaminant). The choice of end-members was based on the major oxide composition and isotopic signatures. After experiments, chemical analyses were performed by electron microprobe microscopy along contact zones between the interconnected end-members on the experimental charges produced. The results confirm and quantify elemental homogenization in the melt, which occurs by diffusion. The degree of homogenization varies according to the element, and the differential mobility in the mixing system culminates in non-linear correlation in inter-elemental plots. The mobility of major/minor elements along contact areas was quantified calculating the

normalized variance, which consistently indicates the connection between viscosity and mobility. Orbicular structures containing dendritic crystals and remnant portions of glass in the basaltic area were described in detailed for the first time. The observed dendritic areas of the basaltic regions point towards an early crystallization process during the initial quench phase of the experiment, and that the crystallization process does not happen homogeneously. Chaotic mixing experiments confirmed that mixing between melts with vastly different viscosities is physically possible. Chaotic dynamics governs this process initially producing vortex structures, and stretched and folded filaments within regions that appear to correspond to remnants of the unmixed end-members. The created filaments become systematically thinner as continuously stretched and folded process develops. It exponentially increases the contact surfaces and, therefore, the mixing efficiency. In respect to the formation of the PEMP high-Ti Chapecó dacites, our results lead us to infer that basalts commonly melt crustal rocks, partially or totally, on their way to the surface. Initial calculations using the linear mixing model are in disagreement with our experimental results regarding the best contaminant candidate, which reflects the very complex simulated scenario. Nevertheless, the reproduced features such as the variability of basaltic compositions and chemical similarities with PEMP intermediary rare outcrops point towards short interaction times, low convective forces, and a predominance of density driven separation of contrasting melts (*i.e.*, simulated conditions) as possible mechanisms involved in the genesis of Chapecó dacites.

Keywords: Magma Mixing, Chaotic Dynamics at High-Temperature, Underplating, Paraná-Etendeka Magmatic Province, Chapecó-type Silicic Rocks.

2.1 INTRODUCTION

Mixing of silicate melts is a near-ubiquitous phenomenon in igneous petrogenesis (Morgavi *et al.*, 2022). Evidence for magma mixing can be found on scales from hand specimens to batholiths and volcanic sequences. It can generate a large compositional variability in rock suites as well as to trigger volcanic eruptions (Anderson, 1982; Russell, 1990; Bateman, 1995; Abe, 1997; Leonard *et al.*, 2002; Perugini *et al.*, 2010; Borisova *et al.*, 2012, 2014; Tomiya *et al.*, 2013). Magma mixing

may be controlled by temperature, oxygen fugacity, pressure, and volatile contents (*e.g.*, Borisova *et al.*, 2014) that influence the melt viscosity (*e.g.*, Avramov, 2000; Giordano *et al.*, 2008), which is the parameter controlled on magma mixing experimental studies (*e.g.*, De Campos *et al.*, 2011). Based on several examples of field observations (Flinders & Clemens, 1996; De Rosa *et al.*, 2002; Perugini *et al.*, 2003b) chaotic dynamics has been proposed to control such mixing processes (Perugini & Poli, 2000; Perugini *et al.*, 2003a,b) in stark contrast to the common geochemical assumption of linear mixing model (Langmuir *et al.*, 1978).

A new experimental approach and the application of numerical tools allowed, respectively, to mimic and model chaotic dynamics since the beginning of the 1990s (*e.g.,* Swanson & Ottino, 1990; Liu *et al.*, 1994; Galaktionov *et al.*, 2002). However, the first apparatus capable of performing experimental routines designed to generate chaotic dynamics at high temperatures (*i.e.*, 1,300 °C) comparable to natural phenomena was constructed a decade ago (De Campos *et al.*, 2011). The first studies using this device were conducted on well-characterized model silicate samples, and contributed significantly to the knowledge of petrological and volcanological processes (De Campos *et al.*, 2011; Perugini *et al.*, 2012). Subsequently, experiments using natural basaltic and rhyolitic samples (Morgavi *et al.*, 2013a,b; Perugini *et al.*, 2015) followed in order to explore mixing in more realistic compositions to natural observations at varying interaction times, further improving our picture of elemental mobility in truly natural silicate melts through time.

Here, with the aim to understand the role of chaotic mixing processes in crustal contamination, a campaign of three new experiments were performed starting from a natural basaltic melt composition while solely varying the chemical composition of one end-member (*i.e.*, the contaminant). In this way the influence of: a) chaotic dynamics prevailing over a fixed period of time, and b) changes in the contaminant melt chemistry was systematically experimentally investigated. Furthermore, this scenario was developed against the backdrop of the Chapecó high-Ti dacites originating from the Paraná-Etendeka Magmatic Province (PEMP), whose petrogenesis has been proposed by several authors to involve remelted high-Ti reservoirs trapped at the crust/mantle boundary (underplating, *e.g.*, Piccirillo *et al.*, 1987; Piccirillo & Melfi, 1988; Garland *et al.*, 1995). Thus our experimental setup is designed to mimic a process in which a hotter basaltic magma encounters pre-existing continental crust during ascent, leading to the

ingestion of felsic blocks and the establishment of chaotic mixing as a petrogenetic process.

2.2 CHAOTIC MIXING EXPERIMENT

2.2.1 STARTING MATERIALS, GEOLOGICAL SETTINGS AND PERTINENT QUESTIONS

The Paraná-Etendeka Magmatic Province (PEMP – Figure 2.1) is the second largest continental area created by continental flood basaltic volcanism in the world. It is located mainly in the S-SW region of Brazil, associated with the continental breakup of the Western Gondwana and opening of the South Atlantic ocean. In this region, predominant tholeiitic magmatism (90% of the extrusive volcanism) is followed by silicic volcanism and intrusive sills and dyke swarms (Piccirillo & Melfi, 1988). Geochemically, the PEMP rocks are divided into two groups, according to their TiO_2-content: i) high-Ti ($TiO_2 \geq 2\%$) basalts and associated felsic rocks named “Chapecó”; and ii) low-Ti ($TiO_2 < 2\%$) basalts and associated felsic rocks named “Palmas”. In general, the high-Ti group is dominant in the northern PEMP while low-Ti occurs mainly in the southern PEMP (Bellieni *et al.*, 1984; Mantovani *et al.*, 1985; Piccirillo & Melfi, 1988; Marques *et al.*, 1989; Peate, 1997; Garland *et al.*, 1995; Nardy *et al.*, 2008). High-Ti silicic outcrops are less abundant than other rock types in PEMP and several studies have highlighted the absence of intermediate high-Ti lithologies (*i.e.*, gap of SiO_2: 55-63%), leading authors to invoke mechanisms such as partial melting of high-Ti basaltic sources, associated with underplating to explain their genesis (Piccirillo *et al.*, 1987; Piccirillo & Melfi, 1988; Garland *et al.*, 1995).

The Chapecó is porphyritic and enriched in K_2O and P_2O_5, trace elements (Ba, Nb, Zr, Y), and REE (La, Ce, Nd, Yb, Lu) contents, whereas it is depleted in Rb, Th, and U in comparison with Palmas. The low-Ti Palmas is aphyric and more radiogenic than high-Ti Chapecó (*i.e.*, Sr and Pb isotopic ratios). Chapecó dacites can be subdivided into two main groups named Chapecó-Guarapuava (CGD) and Chapecó-Ourinhos dacites (COD). The former is characterized by relatively lower contents of SiO_2, total alkalis ($Na_2O + K_2O$), incompatible trace elements such as Rb, Ba, Th, U, Pb, and initial $(^{87}Sr/^{86}Sr)_i$ ratios (approx. 0.7060), whereas the latter presents lower

amounts of TiO_2, Fe_2O_{3t}, MgO, P_2O_5, and trace elements such as Sr, Zr and Y in comparison to CGD. Due to their higher Sr_i isotopic ratios (approx. 0.7085) COD is, in comparison with CGD, widely considered to be contaminated with crustal material (Piccirillo *et al.*, 1987; Garland *et al.*, 1995). The silicic rocks occur in the field closely associated to and most commonly above lithostratigraphic units formed by basaltic lava flows (Piccirillo & Melfi, 1988; Peate *et al.*, 1992; Nardy *et al.*, 2008), consistent with them being related to the final stages of evolution of magmatic events.

Figure 2.1: Map of Paraná-Etendeka Magmatic Province (PEMP) showing the end-members location. Stars represent the end-members: black – contaminants (granites) and grey – high-Ti Pitanga basalt. Based on Nardy *et al.* (2008), Machado *et al.* (2018) and references therein.

Table 2.1: bulk rock chemical analysis performed on end-members and representative samples of Chapecó-Guarapuava (CGD) and Chapecó-Ourinhos dacites (COD). Techniques: X-ray fluorescence *XRF* (major and minor oxides); inductively coupled plasma mass spectrometry *ICP-MS*, neutron activation analysis *INAA*, isotope dilution *ID* (trace elements); and thermal ionization mass spectrometry *TIMS* (initial $(^{87}Sr/^{86}Sr)_i$ ratios). Isotopic data were calculated considering the magmatism age of 134 Ma (Janasi *et al.*, 2011; Gomes & Vasconcelos, 2021). Averages of Chapecó dacites were obtained compiling data from Piccirillo *et al.* (1987), Peate *et al.* (1992), Garland *et al.* (1995), Janasi *et al.* (2007), Nardy *et al.* (2008) and data from the present study (CGD and COD samples CPG-012 and CRC-015, respectively). End-members: rhyolites LMC-027, LMC-020 and LMC-018 were collected based on HP-027, HP-021 and HP-223 locations (Prazeres-Filho *et al.*, 2003 and references therein); basalt KS-700 data are reported in Rocha-Júnior *et al.* (2013).

	CPG-012	**CGD (N=64)**	**CRC-015**	**COD (N=69)**	**LMC-027**	**LMC-020**	**LMC-018**	**KS-700**
[1] **SiO_2**	65.13	65.35	66.66	66.98	76.05	70.94	73.75	50.31
[1] **TiO_2**	1.45	1.46	1.24	1.20	0.18	0.45	0.28	3.54
[1] **Al_2O_3**	12.9	13.1	12.8	13.1	12.2	14.8	13.8	13.2
[1] **Fe_2O_{3t}**	7.42	7.38	7.19	6.69	1.71	2.60	2.03	14.8
[1] **MnO**	0.15	0.14	0.14	0.13	0.02	0.05	0.04	0.20
[1] **MgO**	1.38	1.37	0.96	1.04	0.10	0.83	0.28	4.94
[1] **CaO**	3.16	3.02	2.50	2.51	0.78	2.04	1.13	9.27
[1] **Na_2O**	3.51	3.48	3.72	3.43	3.37	3.39	3.23	2.37
[1] **K_2O**	4.43	4.23	4.56	4.58	5.54	5.14	5.42	0.95
[1] **P_2O_5**	0.48	0.47	0.35	0.34	0.04	0.20	0.07	0.41
Rb	[2] 97.8	[2] 97.3	[2] 122	[2] 127	[3] 321	[3] 212	[3] 379	[4] 22.9
Sr	[2] 347	[2] 369	[2] 335	[2] 304	[3] 33	[3] 405	[3] 90	[1] 474
		[*] N>10		[*] N>13				
[5] **$^{87}Sr/^{86}Sr_{134}$**	0.70615 (2)	0.70581 (20)	0.70835 (2)	0.70802 (16)	0.86998 (8)	0.72054 (60)	0.78799 (4)	0.70542 (10)

[1] Determined by X-Ray Fluorescence (XRF)
[2] Determined by Inductively Coupled Plasma Mass Spectroscopy (ICP-MS)
[3] Determined by Isotope Dilution (ID)
[4] Determined by Instrumental Neutron Activation Analysis (INAA)
[5] Determined by Thermal Ionization Mass Spectroscopy (TIMS)
[*] $^{87}Sr/^{86}Sr$ averages are reported in literature, thus N is unknown in some cases

Against this backdrop, three different chaotic mixing experiments were performed using as end-members the basalt from Pitanga high-Ti group (KS-700; from Rocha-Júnior *et al.*, 2013) and three distinct contaminants from the Paraná Basin basement. Initially, isotopic data reported in Prazeres Filho *et al.* (2003) and references therein were recalculated to the age of Chapecó emplacement (134 Ma; Janasi *et al.*, 2011; Gomes & Vasconcelos, 2021). Mixing lines between these contaminant candidates and the high-Ti basalt were established to initially test the viability of the process pondering: a) chemical variability; and b) corresponding isotopic signatures. Thus, the composition and location of three possible contaminants were selected. Figure 2.1 shows the location of collected samples, which were named as: i) LMC-027: Capão Bonito Stock – Campo Belo/SP; ii) LMC-020: Cunhaporanga Batholit – Paraí do Sul/PR); and iii) LMC-018: Sguário Granite – Castro/PR. Table 2.1 shows the chemical bulk rock composition determined by XRF, trace element analysis (Rb and Sr) determined by ICP-MS, ID and INAA, and additional isotopic analyses determined by TIMS used in calculations (Prazeres-Filho *et al.*, 2003 and references therein; Rocha-Júnior *et al.*, 2013; this work).

2.2.2 SAMPLE PREPARATION AND EXPERIMENTAL SETUP

The homogenization of the end-members and the measurement of their in-situ viscosities at high temperatures were performed according to Dingwell (1986). It consists basically on: i) crushing approx. 200 g of sample; ii) melting approx. 80 g of the prepared rock powders at 1,400 °C and 1,600 °C (basaltic and rhyolitic material, respectively) at 1 atm in a $MoSi_2$-heated Nabertherm box furnace in air; iii) followed by stirring of the synthesized melt in a DELTEC high temperature melting furnace equipped with a rheometer that was connected via stainless steel segments to a spindle made of $Pt_{80}Rh_{20}$. Depending on viscosity, melts were stirred in air at speeds of 5-20 rpm for 6h (KS-700) and 72h (LMC-027, LMC-020, and LMC-018).

At the end of stirring the viscosity was simultaneously measured by means of the concentric cylinder method at high temperatures between 1,200 °C and 1,600 °C (Dingwell, 1986). At the experimental conditions (*i.e.*, 1,350 °C, at atmospheric pressure), homogenized starting materials have the physical properties presented in Table 2.2. The viscosity measurements present precision of 3.0% (±2σ) and calculated

densities (Lange & Charmichael, 1987) present precision better than 2.0% (±2σ). This entire process resulted in final glasses essentially free of bubbles and volatiles.

Table 2.2: Average compositions of end-members, with respective standard deviation (std = 1σ) calculated for N chemical analysis, and its physical properties at T_{exp} = 1,350 °C. Standard deviations of calculated density and measured viscosity are, respectively, 1.0% and 1.5% (1s). Samples LMC-027, LMC-020 and LMC-018 were collected based on previous works (Prazeres Filho *et al.*, 2003 – details in the text). Units: composition [wt.%], density [g/cm³], viscosity [Pa.s] (log units).

	LMC027	**std (N=14)**	**LMC020**	**std (N=20)**	**LMC018**	**std (N=15)**	**KS700**	**std (N=30)**
SiO_2	76.55	0.26	70.64	0.24	72.96	0.39	50.31	0.29
TiO_2	0.14	0.04	0.44	0.07	0.26	0.04	3.60	0.12
Al_2O_3	12.48	0.15	14.90	0.14	14.77	0.26	12.88	0.14
Fe_2O_{3t}	1.87	0.13	2.75	0.14	1.79	0.12	14.80	0.21
MnO	0.02	0.03	0.05	0.04	0.05	0.04	0.21	0.06
MgO	0.12	0.02	0.84	0.04	0.27	0.03	5.00	0.12
CaO	0.65	0.05	2.14	0.09	1.32	0.10	9.33	0.18
Na_2O	2.70	0.13	2.96	0.11	3.11	0.13	2.48	0.10
K_2O	5.43	0.10	5.08	0.12	5.43	0.17	0.92	0.05
P_2O_5	0.03	0.03	0.19	0.04	0.03	0.03	0.46	0.05
r_{1350}	2.29	0.02	2.32	0.02	2.30	0.02	2.47	0.02
log η_{1350}	5.09	0.08	4.66	0.07	4.24	0.06	0.94	0.01
log	**Exp1**		**Exp2**		**Exp3**		**M13**	
η_{rhy}/η_{bas}	4.14		3.29		3.71		3.89	

Experimental charges (KS-700 and contaminant) were prepared according to Morgavi *et al.* (2013b) inside a cylindrical Pt_{80}-Rh_{20} crucible already used for concentric cylinder (viscosity) measurements, by drilling out cylinders at the location of the future spindle and contaminant position (Figure 2.2). These removed cylinders (= cores drilled out) resulted in a ratio of the starting basaltic composition (KS-700) to contaminant (LMC-027; LMC-020; LMC-018) of: i) 80% of KS-700 basaltic starting glass (contained in the $Pt_{80}Rh_{20}$ crucible), and ii) 20% of rhyolitic glass (cores consisting of the contaminant compositions: LMC-027; or LMC-020; or LMC-018, respectively). Prior to start of any experiment, the experimental charge was positioned into a vertical GERO muffle tube furnace equipped with gas mixing device. A spindle of 8.6 mm diameter made of $Pt_{80}Rh_{20}$ was inserted into a pre-machined void (cylindrical

void) in the starting KS-700 basaltic glass and connected to a rotary drive outside of the GERO muffle tube furnace (upper motor – Figure 2.2.a).

The mixing experiments were performed using the in house-built chaotic mixing device (De Campos *et al.*, 2011) at the Dept. of Earth and Environmental Sciences (DEES/Ludwig Maximilian University Munich) as illustrated in Figure 2.2. This device is originally based on the Journal Bearing System (JBS: Swanson & Ottino, 1990), which generates chaotic flow patterns by means of: i) a precise geometry, and ii) a preset protocol of motion. The chaotic mixing device of the DEES/LMU is identical in dimensions to the Journal Bearing System (JBS) of Swanson & Ottino (1990). The scientific theory behind these experiments is based on the one-dimensional advection-diffusion equation (see Appendix A for details):

$$\frac{\partial n_C}{\partial t} + V_{\hat{x}}.\nabla n_C = D\nabla^2 n_C \qquad \text{(Eq. 2.I)}$$

where $\partial n_C/\partial t$ is the variation of the particle density n_c [particles*m^{-3}] in time t [s]; $V_{\hat{x}}$ is the vectorial velocity field (*i.e.*, $\hat{\imath}$ direction) [m*s^{-1}] that such a particle is submitted; D is the diffusivity [m²*s^{-1}], which means the capability of the particle to move in a medium through time; and ∇ is the divergence operator.

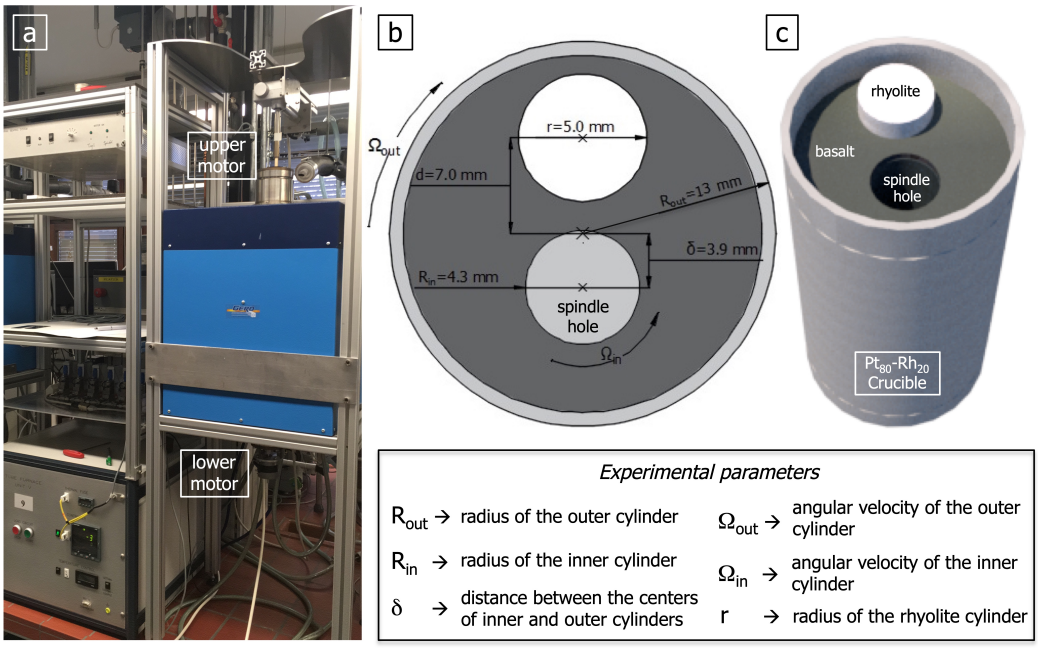

Figure 2.2: schematic cross section of the chaotic mixing device and experimental setup: a) experimental apparatus composed by furnace, upper and lower motor; b) 2D-sketch with details about dimensions; and

c) 3D schematic of the crucible and the location of the starting materials (basaltic and rhyolitic glasses) and the spindle. Details about the experimental setup can be found in De Campos *et al.* (2011).

The rhyolitic inset and the surrounding basalt are juxtaposed across a planar horizontal contact inside the crucible. Static diffusion equation would be valid in case that the contact surface does not change during the experimental run. This would be the case if we would section the cylinder vertically downwards in horizontal slices (*e.g.*, every 4 mm) and all sections would show the same morphological aspects, which means a single diffuse circular area. However, the geometry of the experiment and the surfaces created in consequence does not remain static during the experiments. The motion protocol of the outer cylinder and the inner spindle will result in a mingling of the two end-member bodies into each other in horizontal direction, and additionally, the density contrast between the end-members will lead to a vertical movement and, in consequence, deformation and alteration of the two phase ratios in y-axis. Both processes will result in a stretching and folding of systematically smaller filaments with time and the appearance of new contact areas in different sections of the entire cylindrical melt body. Note that the velocity field in Eq. (2.I) is well known where the motion protocol becomes reproducible. Thus, these experiments contain the fundamental factors controlling elemental mobility during chaotic mixing. Nonetheless, its influence on the initial mingling efficiency (*i.e.*, stretching and folding) and, when a critical thickness of the filaments is obtained so that the final diffusion-driven chemical mixing becomes the governing process in the homogenization of the entire sample, is a function of other parameters such as viscosity, density, wetting conditions, strain distribution, absolute and relative diffusivities of species, charge transfer of diffusive species, and absolute surface charging of intermediate or final end-member compositions relative to each other, and not at least, final crystallization during cooling of kinetically or thermodynamically stable phases (crystals), etc. All these parameters and processes have to be taken into account to better understand and improve our knowledge and theories about elemental mobility during chaotic mixing events, which has immense implications in petrological systems and the models developed.

Geometry and motion protocol have been adapted for high temperature applications, as well applicable and functional for high viscosity liquids (De Campos *et al.*, 2011). The motion protocol applied to produce the chaotic mixing patterns in all

experiments performed was: (i) two complete clockwise rotations of the crucible (720° rotation of outer cylinder) over 35 min; (ii) six anti-clockwise rotations of the spindle (2160° rotation of inner cylinder) over 18 min; (iii) two clockwise rotations of crucible (720° rotation of outer cylinder) over 35 min; (iv) six anti-clockwise rotations of the spindle (2160° rotation of inner cylinder) over 18 min. This accumulates in 106 min of non-simultaneous and independent movements, which guarantees and results in reproducible chaotic flow patterns. This choice was based on previous experimental conditions from Morgavi *et al.* (2013a,b), who studied the variation of mixing efficiency in time (*i.e.*, by varying the number of protocol repetitions) using natural materials. Mixing efficiency was not a parameter in this study and was kept constant within all performed experiments.

After the mixing protocol was achieved, each run was quenched to ambient temperature by switching off the furnace power supply and the experimental charge (crucible with hybrid melt assembly and spindle) cooled down to room temperature, at an initial cooling rate of approximately 80 °C/min.

2.2.3 ANALYTICAL METHODS

The major oxide concentrations of the glassy samples obtined were measured using a Cameca SX100 electron microprobe (DEES/LMU) using wavelength dispersive spectrometers. Instrumental and analytical conditions were: accelerating voltage of 15 kV, a probe current of 5 nA, and a standard beam size of 10 μm. To minimize potential loss of alkali elements (especially Na and K) during ongoing analysis duration, these elements were the first to be measured. These settings were applied for all analyses performed. Reproducibility was determined using the standard deviation of starting materials analysis. The analysed elements exhibit a reproducibility better than 5.3%, except for P (= 10%) and Mn (= 20%) whose concentrations were closer to the detection limits. For these reasons, Mn was neglected and P data are treated as a reconnaissance study. Accuracy was considered lower than 3.4% relative for all elements based on the analysis of ML3B-G, StHs6/80-G, and ATHO-G standard glasses (MPI-DING; Jochum *et al.*, 2000). The following standards, X-ray lines, and crystals were used: *synthetic wollastonite*, **Ca** Ka, PET; *periclase*, **Mg** Kα, TAP; Fe_2O_3 *synthetic,* **Fe** Ka, LLIF; *orthoclase*, **Al** Ka, TAP, and **K** Ka, PET; *albite*, **Na** Ka, TAP, and **Si** Ka, TAP; *apatite*,

P Ka, LPET; *ilmenite*, **Ti** Ka, PET; and *bustamite*, **Mn** Ka, LLIF. Matrix correction has been performed according to the PAP procedure (Pouchou and Pichoir, 1984). Table 2.2 shows the initial composition of basaltic and rhyolitic starting glasses used in all chaotic mixing experiments, and relevant physical properties at T_{exp} = 1,350 °C.

2.3 RESULTS

2.3.1 MORPHOLOGY AND EMERGING STRUCTURES

As consequence of the chaotic dynamics, all experiments produced vortex structures, and stretched and folded filaments within regions that appear to correspond to remnants of the unmixed end-members (Figure 2.3). Such features are indicators that chaotic dynamics were achieved during the experiments (Ottino 1989; Perugini *et al.*, 2003b, 2012; De Campos *et al.*, 2011; Morgavi *et al.*, 2013a,b). Using a stereomicroscope (natural light) three distinguishable regions are identified (Fig. 2.3.a, g): i) dark grey areas corresponding to the original rhyolitic glass; ii) light grey areas, corresponding to the original basaltic glass; and iii) a dark intermediary zone in between pristine, unaltered or unmixed regions, respectively. The composition of the remnant regions and zones between them are discussed bellow. In some sections portions i), ii), and iii) are visible with bare eye, and in the most basal sections only ii) and iii) are found (Fig 3.h). The absence of i) is expected since the lower density forcing the rhyolitic melt phase to accumulate at the top. Exp2 exhibits larger amounts of area iii) in comparison to experiments 1 and 3, which indicates higher mixing efficiency.

Contact surfaces and structures were analysed using SEM techniques (Fig. 2.3.b-d). The deformation of the initial rhyolitic body is more evident in experiments 1 and 3 showing clear evidence for longer (more efficient stretching) and barely perturbed contact lines compared to Exp2. On the other hand, Exp2 shows less linear contact lines (*i.e.*, sinusoidal lines) especially near the spindle (Fig. 2.3.b-d). Exp3 shows a higher number of filaments in comparison to Exp1, such as the number of blobs (*i.e.*, elongated structures but not separated of the main body – Fig. 2.3.d) and blocks (*i.e.*, small pieces of one glass entirely surrounded by the other glass – Fig. 2.3.d). In Exp2 (Fig. 2.3.c) the few filaments of the rhyolitic glass are thin and concentrated near the spindle. In

stereomicroscope images some of these structures seem diffuse (Fig. 2.3.e-f), resulting in shadow zones that are more abundant in Exp2.

The development of described morphological features is based on the initial viscosity ratio (η_{rhy}/η_{bas}) between the end-members. Table 2.2 indicates that $(\eta_{rhy}/\eta_{bas})_{Exp2}$ is smaller than $(\eta_{rhy}/\eta_{bas})_{Exp3}$ and $(\eta_{rhy}/\eta_{bas})_{Exp1}$ respectively. Therefore, more melt interaction is expected in the case of Exp2, which is observed. Interaction means that the deformation of the initial bodies due to the motion protocol will produce interconnections (stretched and folded filaments), which increases the area where diffusion occurs. Eventually, material from the thinnest filaments will diffuse more effectively, at some moment becoming blurred areas and finally undetectable.

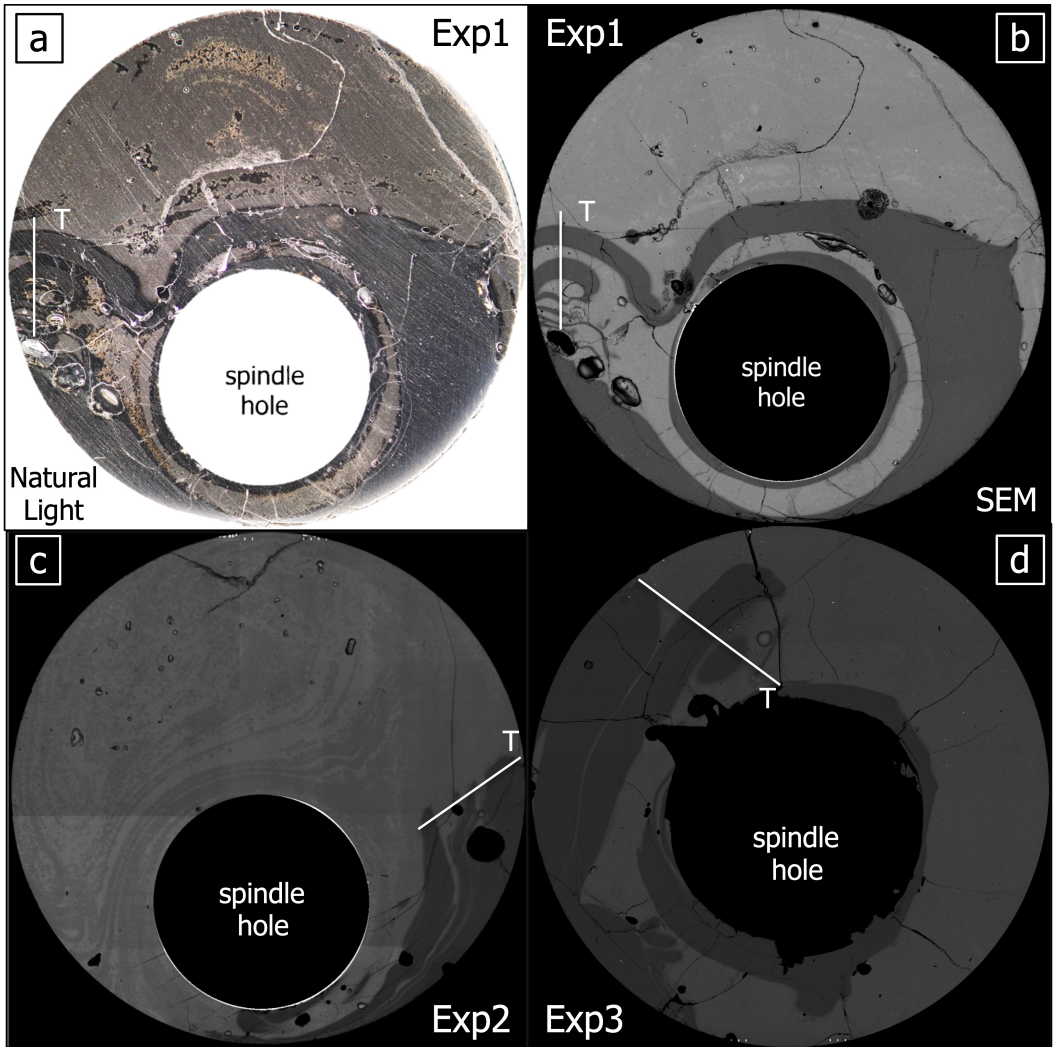

Figure 2.3: representative sections (diameter = 23 mm) of experiments 1, 2 and 3: a) section Exp1_7top obtained through 8 Carl Zeiss Discovery V8.0 microscope under natural light to illustrate the main visible characteristics of the hybrid glasses (details in the text); b-d) BSE-images produced by scanning electron microscopy (SEM) over the analysed sections. White lines represent EPMA transects T.

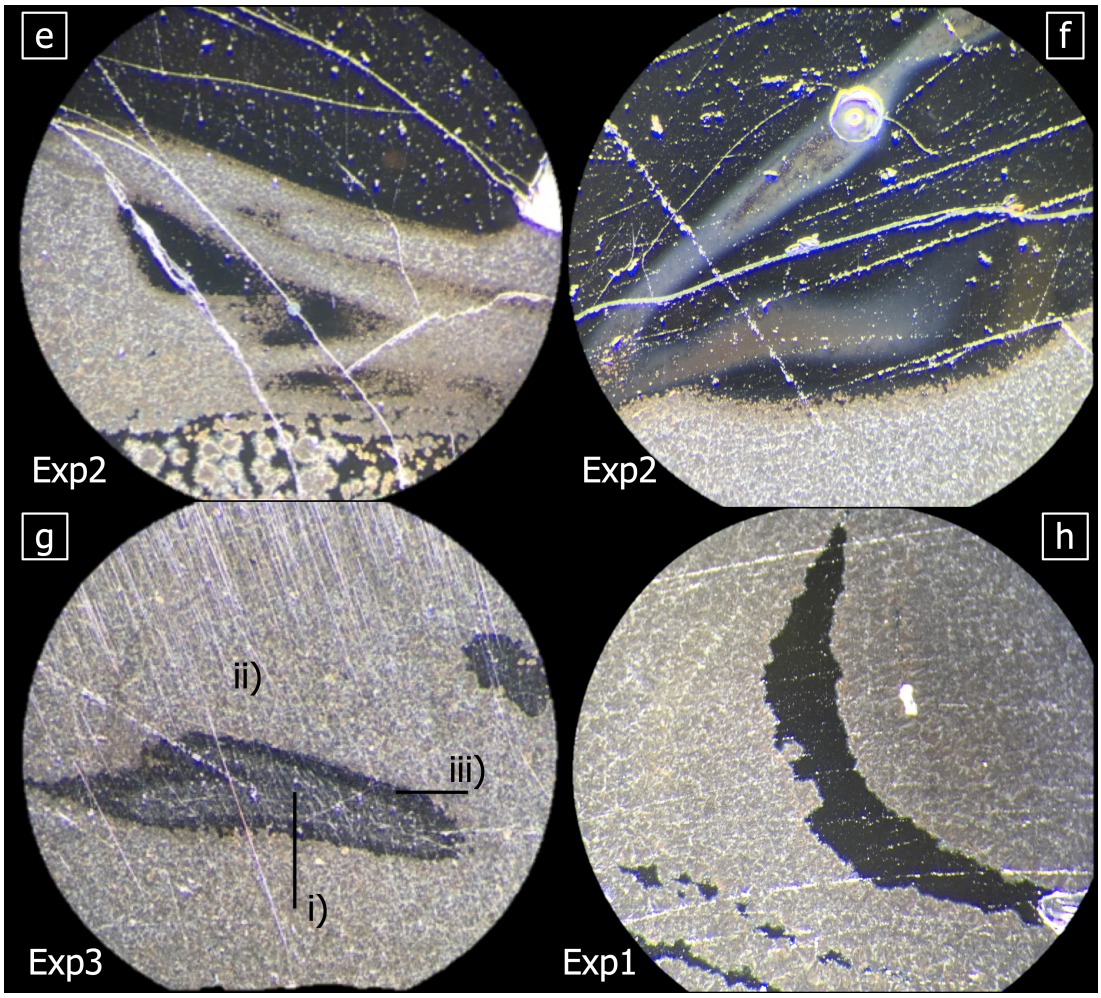

Figure 2.3 (cont.): details on resulting structures of chaotic dynamics, obtained through 8x zoom from Carl Zeiss Discovery V8.0 microscope (object field = 2.9 mm): e) transitional zones (more frequent in Exp2) and orbicular structures; f) stretched and folded filaments of basaltic material inside the rhyolitic glass; g) rhyolitic block, illustrating the three distinguishable regions i), ii) and iii) (details in the text); h) dark elongated filaments.

In all experiments performed, some dark elongated filaments can be observed inside the basaltic areas (Fig 3.h). However, these filaments are not related to transitional zones. Such filaments are observed from bottom to top sections and highlight the existence of orbicular structures, which also mark the boundary between basaltic grey and darker intermediary areas. The orbicular structures are characterized by circular shapes and internal greyish colour, similar to the basaltic glass. In sections located near the top of the crucible their colour become systematically more yellowish in some parts (Fig. 2.3.e). In summary, microscopic investigations show clear evidence that the orbicules are associated with the presence of spherical clusters of acicular crystals. These structures are believed to be the early crystallization products of iron

oxides and silicates during the cooling process. Crystal free areas would be remnant portions of basaltic glass where no crystallization took place. Although these regions are abundant in most basal sections, they are visible in some areas of the section Exp1_7top under natural light (Fig. 2.3.a). This is in contrast with the BSE-image of Exp1 (Fig. 2.3.b) that shows a more homogeneous basaltic portion. It indicates the presence of two basaltic phases coexisting with similar composition (*i.e.*, close densities revealed in BSE-images), however distinct in terms of optical properties. Details on chemical composition of the crystals and its effects on microprobe analysis will be discussed later.

2.3.2 GEOCHEMICAL FEATURES

Figure 2.4 shows EPMA analyses of the transects indicated in Figure 2.3.b-d as white lines. Each transect is assumed to be representative to evaluate the elemental mobility for the corresponding experiment. Dark and light grey bars in Figure 2.4 represent the interval of, respectively, rhyolitic and basaltic compositional averages of EPMA determinations on starting end-members plus or minus one standard deviation (= $\pm 1\sigma$) (Table 2.2). The error bars drown for single points in Figure 2.4 represent 1σ as well. General results can be summarized as follows: the analysed transects present two compositional plateaus in respect to the major oxides (*e.g.*, SiO_2 and TiO_2): (i) one close (but significantly different) to the original basaltic composition; and (ii) the second corresponding to the rhyolitic glass. In respect to the analysed K_2O and CaO-concentrations measured over the indicated transects, the K_2O concentrations in regions which plot closer to the original rhyolitic starting composition, are systematically (by approx. 0.5%) lower than the original rhyolitic values. This is not the same in the performed CaO results, which reach the original concentrations determined in the starting rhyolitic compositions. Measurements on the initial materials, however, were performed before and after each transect indicating no significant variation. Therefore, this effect is not related to an analytical drift or loss of alkalis, although this could potentially occur during microprobe analysis (*e.g.* due to local heating).

Between the plateaus, “S” shaped curves can be observed. Typical diffusive patterns are symmetric “S” shaped curves, although asymmetric slopes may also be more frequent here. The asymmetry is observed close to the rhyolitic region, where “S”

curves are abruptly turned in plateaus. In contrast, on basaltic regions the curves smoothly change the inflexion as closer the points are to the intermediary zones.

It can be observed that SiO_2, TiO_2, MgO and K_2O show few perturbations in comparison with Al_2O_3, Fe_2O_3, CaO (particularly close basaltic portions), Na_2O and P_2O_5. Results point towards Fe and Ca being the major constituents observed in orbicular regions, which are dominant in the basaltic zones. The patterns occur reproducibly, similarly and independently in all experiment performed. Results for Na_2O and Al_2O_3 indicate that uphill diffusion (*i.e.,* opposite to the concentration gradient) might play an important role, once this effect is prominent in cases where differences in initial compositions are relatively small (Table 2.2). However, this becomes increasingly difficult to identify if absolute concentrations approach the detection limits of the analytical technique (EPMA). Similar can be said about the P_2O_5 determinations, once concentrations approach trace element levels (especially in rhyolitic glasses).

2.4 DISCUSSION

2.4.1 ORBICULAR STRUCTURES

Hybrid glasses from quenched products of experiments presented orbicular structures detectable even in macroscopic scale in some cases. However, optical microscopy reveals crystallization processes occurring inside these structures, as shown in Figure 2.3.e. The crystals present dendritic shape (named dendritic structures DS) and high brightness under reflected light. The length of their major axis is about dozens of microns (in average 50 μm), with the longest filaments reaching more than 150 μm though. As mentioned earlier, the glass colour changes due to the presence (light grey) or the absence (dark) of the DS (Fig. 2.3.f). Additionally, nanocrystals (or nanolites; order of $500*10^{-9}$ m) were detected in some regions of basaltic starting material (*i.e.*, before the experiment).

Figure 2.4 (colour): Representative transects as indicated as white lines in Figure 2.3.b-d of Exp1 (KS-700 and LMC-027 – yellow), Exp2 (KS-700 and LMC-020 – green) and Exp3 (KS-700 and LMC-018 – blue). Transects: units in weight percent (wt.%); light grey shadow: original content on basaltic glass (±1σ); dark grey shadow: original content on rhyolitic glass (±1σ). Interval between points: Exp1 – dx = 14 μm; Exp2 – dx = 22 μm; Exp3 – dx = 16 μm.

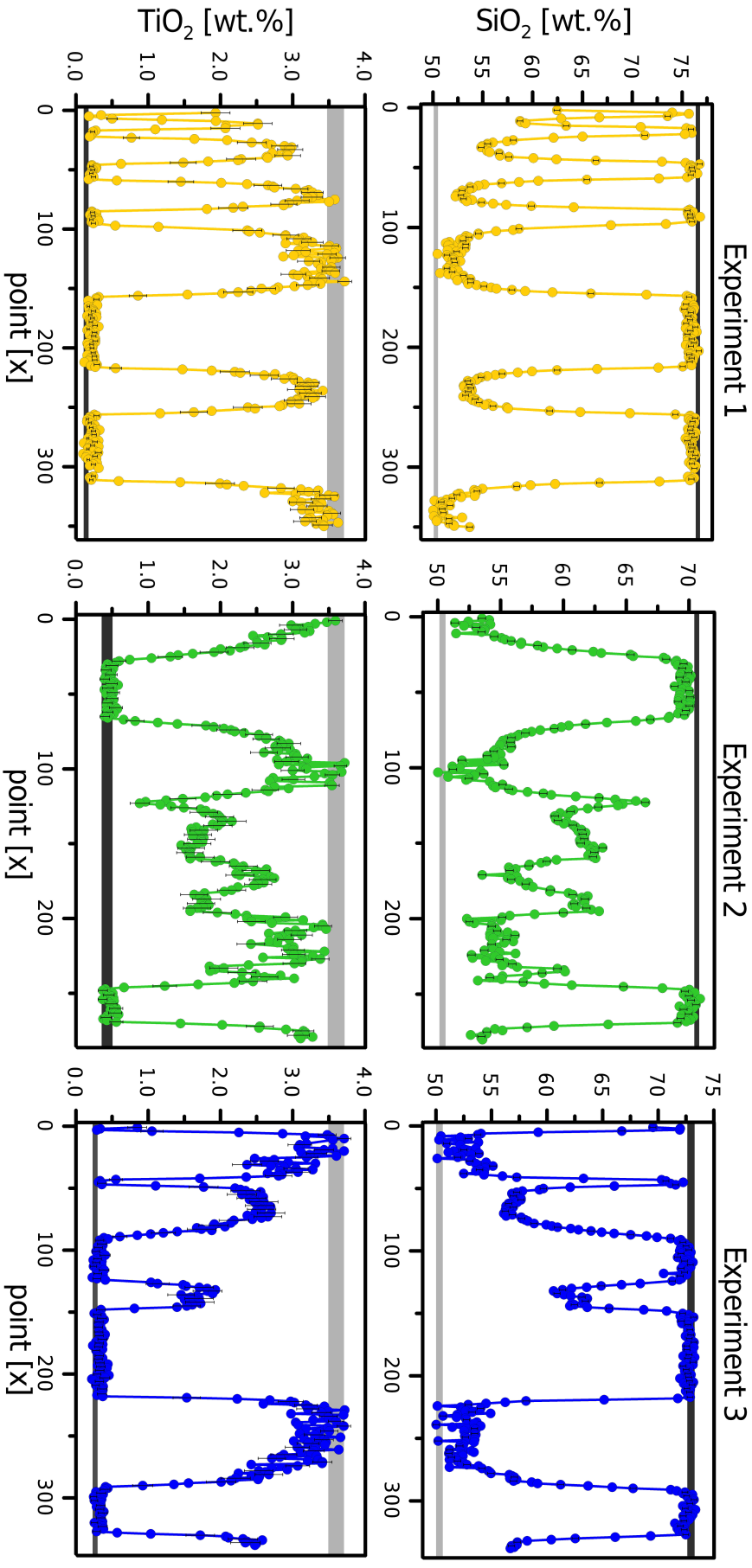
SiO2 [wt.%]
TiO2 [wt.%]
point [x]
Experiment 1
Experiment 2
Experiment 3

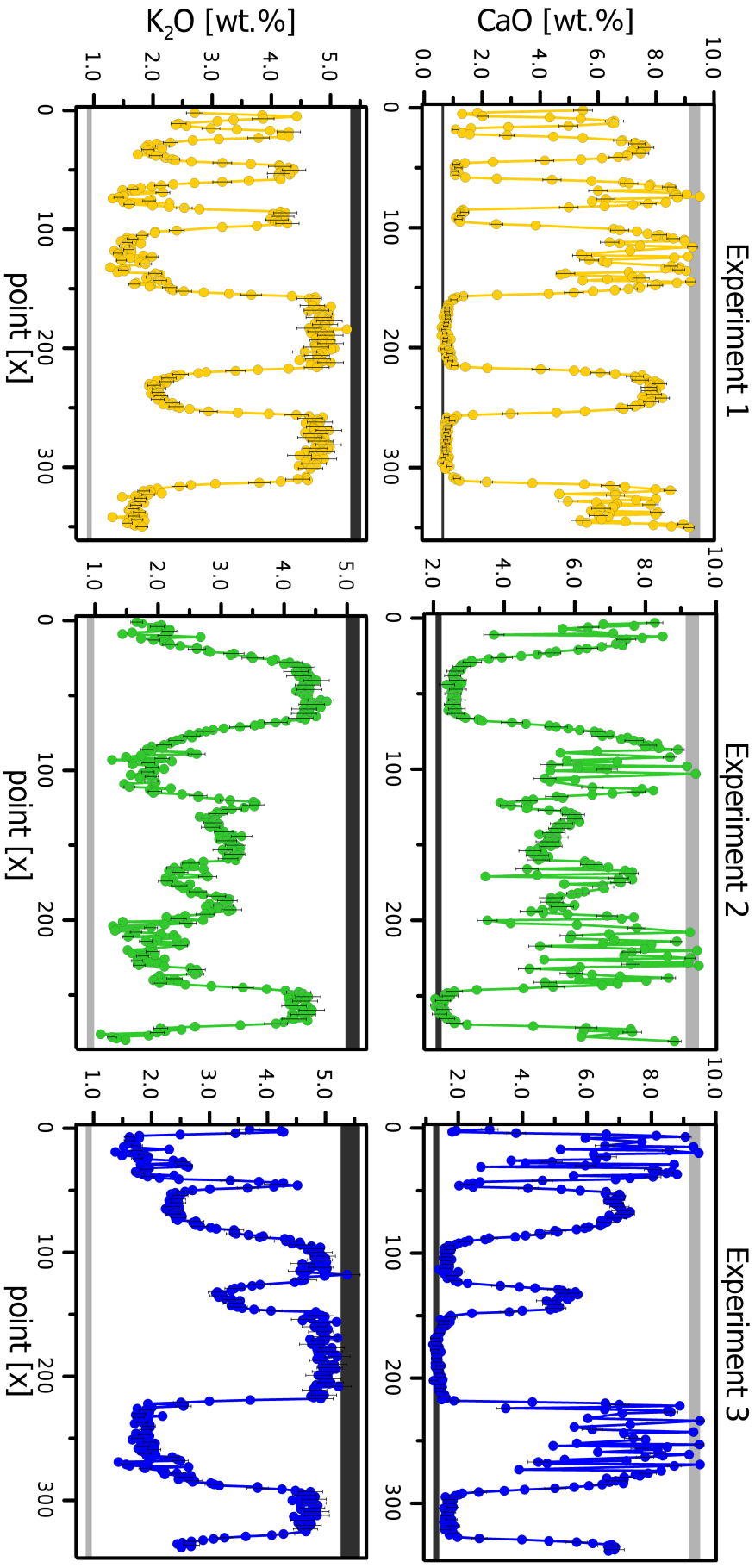
CaO [wt.%]
K2O [wt.%]
Experiment 1
Experiment 2
Experiment 3
point [x]
0.0
2.0
4.0
6.0
8.0
10.0
1.0
2.0
3.0
4.0
5.0
0
100
200
300

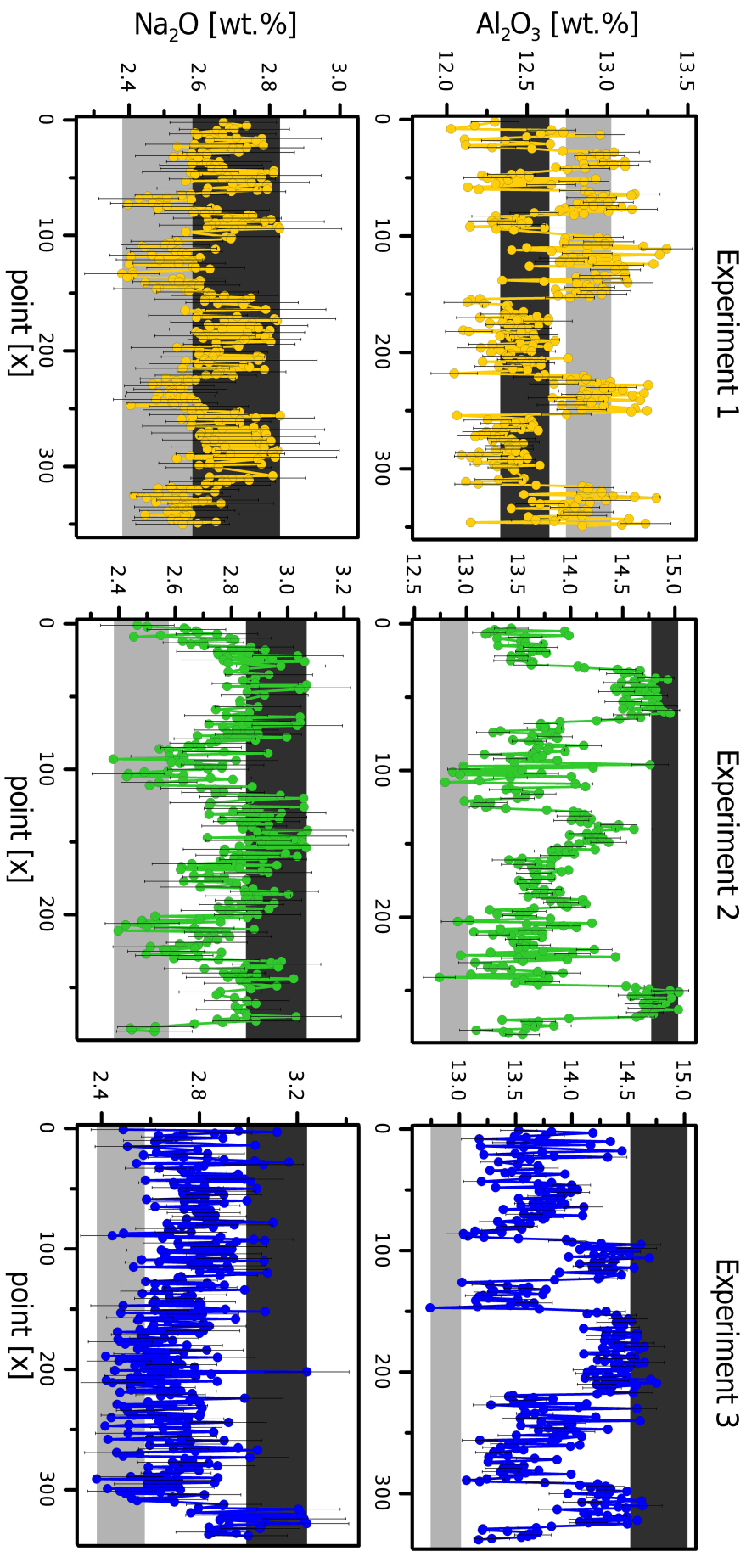
Experiment 1
Experiment 2
Experiment 3
Al2O3 [wt.%]
Na2O [wt.%]
point [x]

Analysis of phases on such small structures is challenging endeavour and was neglected in previous works using natural samples (*e.g.*, Morgavi *et al.*, 2013a). Therefore, DS were investigated by different analytical techniques in order to obtain more information regarding their potential composition and to minimize ambiguities. Appendix B describes this investigation and discusses the results. At least two main phases are crystallizing, which are visible in SEM mapping. The most abundant phase seems to consist mainly of hematite (Fe_2O_3). Since glasses were homogenized in air, they are relatively oxidized due to practically all Fe^{2+} will be transformed into Fe^{3+}. The second phase claimed is Ca-pyroxene, once maps of K (enriched in plagioclase) show no preferential distribution of this element while Mg (enriched in pyroxene) occurs associated to Ca. Magnetite is probably present though, supported by XRD, Raman spectroscopy, and magnetic observations (*e.g.*, movement of fragments with the approximation of magnetic objects). Likewise, the presence of plagioclase cannot be discarded, since XRD data indicates it. Crystallization is inferred to occur during the early stages of cooling, since during the experiments both end-members are superliquidus, condition that are unfavourable for crystallization. In addition, considering an entire section of run product this phenomenon occurs preferentially locally (*i.e.*, stretched and folded filaments inside the basaltic portion), which is plausible if the material is still fluid. The presence of crystals enhances the viscosity of a melt (*e.g.*, Cáceres *et al.*, 2020) and viscosity influences the stress distribution (*e.g.*, Caricchi *et al.*, 2007). Since the quench occurs from outside towards the interior of the crucible, the temperature field produces a stress field from the first solidifying front near the wall in direction to the persistently hotter interior of the sample. In this way, a stress field pointing from outside to the interior of the sample is generated and can enhance crystallization in the same direction (*e.g.*, Lee *et al.*, 2003).

2.4.2 COMPARING ELEMENTAL MOBILITY IN DIFFERENT MELTS

Several factors can influence the mobility of chemical elements during mixing in a multi-component magmatic system such as their compositional and rheological dependence, their melt structure, presence or absence of crystals beside others. In fluid dynamics, the concentration variance (σ^2) is commonly used as a measure to evaluate the degree of homogenization and, hence, to quantify the elemental mobility during

fluid mixing (*e.g.*, Rothstein *et al.*, 1999; Liu & Haller, 2004; Rossi *et al.*, 2017). The variance of concentration for a given chemical element (C_i) can be calculated as:

$$\sigma_{C_i}^2 = {\sum_{k=1}^{N}(C_{i\,k} - \mu_i)^2}/{N} \qquad \text{(Eq. 2.II)}$$

where N is the number of samples, C_i is the concentration of element *i* and μ is the mean composition of element *i*. Variance defined by Eq. (2.II) depends on absolute values of chemical element concentrations. For comparative purposes, the variance values need to be normalized given the wide range of concentrations for the different elements (*i.e.*, from a few to tens of percent). Therefore, the initial variance of each element (*i.e.*, before the mixing starts) can be used as normalizing parameter. Thus, the normalized concentration variance (σ^2_n), or here named normalized variance, is defined as:

$$\sigma_n^2 = {\left(\sigma_{C_i}^2\right)_t}\Big/{\left(\sigma_{C_i}^2\right)_{t=0}} \qquad \text{(Eq. 2.III)}$$

where $\left(\sigma_{C_i}^2\right)_t$ and $\left(\sigma_{C_i}^2\right)_{t=0}$ are the concentration variance of a given chemical element C_i at time *t* (*i.e.*, 106 minutes for our experiments) and time *t* = 0 respectively. The initial variance $\left(\sigma_{C_i}^2\right)_{t=0}$ was calculated using the end-member compositions reported in Table 2.2. This measure quantifies the degree of homogeneity of a chemical element in the mixing system. Ideally, as the system progressively achieves homogeneity it is expected that (σ^2_n) decreases, varying between unity at *t* = 0 (*i.e.*, the time at which the system is most heterogeneous) and zero at *t* = ∞ (*i.e.*, the time at which the system is completely homogeneous).

The calculated normalized variances are given in Table 2.3 and Figure 2.5.a shows the variation of (σ^2_n) for each run according to the elemental field strength. It is defined as the nominal charge Z of the element divided by the distance between metal cation and oxygen at room temperature R^2 = d(M-O) at 298 K (after Brown Jr. *et al.*, 1995). In addition, the comparison with data from similar experiments (Morgavi *et al.*, 2013b; referred as M13) is included. The results indicate good consistency: for all elements of Exp2 (with the exception of Na and Al) the normalized variances show the lowest values, which means higher mixing efficiency. For Exp1 all elements show higher values of (σ^2_n), meaning less efficiency. Exp3 and M13 follow the same trend.

Table 2.3: Normalized variance (σ^2_n) for experiments 1, 2 and 3. The normalization was calculated using Eq. (2.III). (σ^2_n) of Al in Exp1 is out of the expected range 0.0 – 1.0 (details in the text). M13: Morgavi *et al.* (2013); R: ionic radius (after Shannon, 1976); Z: nominal charge; r^2: correlation coefficient.

(σ^2_n)	**Exp1**	**Exp2**	**Exp3**	**M13**	**R**	**Z**
SiO_2	0.63	0.34	0.54	0.46	0.40	4
TiO_2	0.58	0.35	0.50	0.44	0.75	4
Al_2O_3	-	0.21	0.15	0.40	0.53	3
Fe_2O_{3t}	0.49	0.23	0.41	0.30	0.92	2
MnO	0.55	0.34	0.47	-	0.86	3
MgO	0.50	0.29	0.40	0.43	1.20	2
CaO	0.21	0.20	0.16	0.35	1.13	2
Na_2O	0.33	0.19	0.29	0.07	1.51	1
K_2O	0.34	0.15	0.27	0.22	0.31	1
P_2O_5	0.63	0.34	0.54	-	0.40	5
Network Modifiers (MgO, CaO, Na_2O, K_2O)						
Angular Coef.	0.75(6)	0.39(3)	0.62(5)	0.72		
Linear Coef.	0.17	0.14	0.14	0.05		
r^2	0.77	0.99	0.73	0.72		
Network Formers (SiO_2, TiO_2, Al_2O_3, Fe_2O_{3t})						
Angular Coef.	0.22(2)	0.18(2)	0.20(2)	0.21		
Linear Coef.	0.30	0.08	0.24	0.15		
r^2	0.99	0.80	0.99	0.75		
Mod./Form.	3.45	2.16	3.15	3.37		
log η_{bas}/η_{rhy}	4.14	3.29	3.71	3.89		

Furthermore, each experiment demonstrates similar (σ^2_n) paths with increasing field strength of the cation involved: a) (σ^2_n) decreases from K to Na (also noted in M13), however increases towards Mg; b) (σ^2_n) decreases from Mg over Fe to Al (opposite to M13), followed by an increase towards Ti and Si; and finally c) (σ^2_n) decreases from Si to P. Notice the differences in melt structural functionality of these groups: group a) is formed by elements like K, Na, Ca and Mg (named KNCM), which are typical network modifiers in silicate melts; while group b) consists of elements like Fe, Al, Ti and Si (named FATS), which are typical network forming elements. Thus,

Figure 2.5.a depicts independent slopes for groups that play different roles in the melt structure. For estimating the effect of field strength on KNCM and FATS during chaotic mixing process linear regressions were applied for each of them. Results reported in Table 2.3 indicate that the field strength influences KNCM 2 to 3.5 times more than FATS during the process (*i.e.*, higher angular coefficients). In addition, experiments present a positive correlation between KNCM angular coefficients and initial viscosity ratios (M13 included). On the other hand, FATS show equivalent angular coefficients independently of the experiment. The decoupling mobility observed for different elemental groups (network formers and modifiers) might be one reasonable factor, causing and explaining the observed inconsistencies in linear mixing models. Some authors have pointed out that the decoupling effect might be the source of misinterpretation in very complex geological setups (*e.g.*, Rosing *et al.*, 1989; Lesher, 1990; Blichert-Toft *et al.*, 1992; Waight & Lesher, 2010).

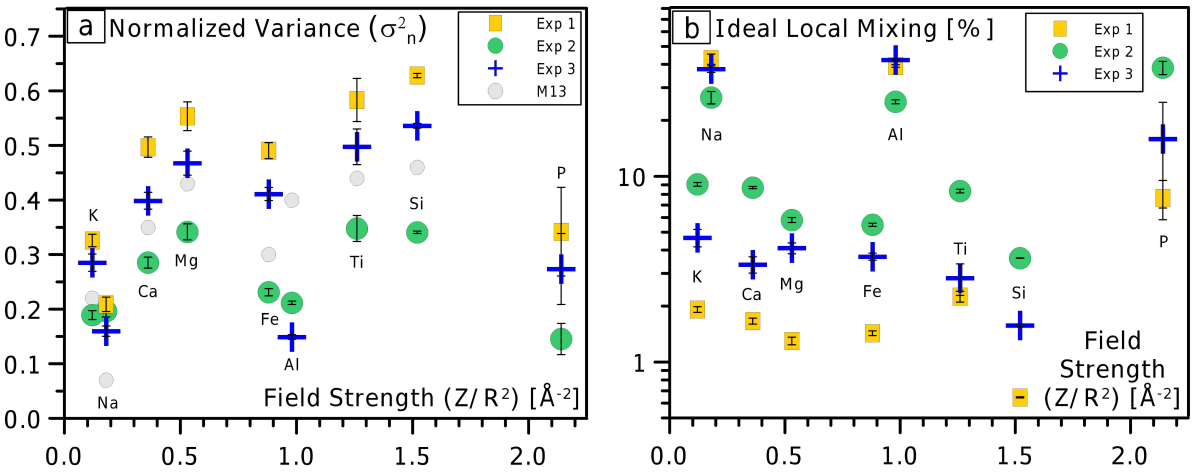

Figure 2.5: a) Variation of the normalized variance (σ^2_n) of major oxides as a function of the field strength (nominal charge Z of the element divided by the ionic radius squared R^2 – after Brown Jr. *et al.*, 1995) for experiments 1, 2 and 3 (this work) and M13 – (Morgavi *et al.*, 2013b); b) Variation of the elemental mixing degree ([number of points that reached the local equilibrium]*100/[total number of points]) as a function of the field strength (Z/R^2). Local mixing is considered the expected concentration in the case of $f = 0.5$ (contamination fraction) in a linear mixing model (details in the text).

The results for Fe need to be evaluated more carefully since it can occur in different oxidation state as Fe^{2+} and/or Fe^{3+} in melts, which additionally bear different melt structural roles. Since the experiments were all performed under atmospheric pressure in air, the experimental conditions are highly oxidized, and the elements

present inside the melt will be shifted towards the highest oxidation state possible during the mixing process and its duration. Thus Fe_{tot} should be assumed to be very close to Fe^{3+}, which means to state the Fe concentration in form of Fe_2O_{3tot}. Moreover, using FeO_{tot} and Fe_2O_{3tot} contents to compute $(\sigma^2_n)_{Fe2+}$ and $(\sigma^2_n)_{Fe3+}$, respectively, results only in a small discrepancy of less than 1%, irrelevant in this context. Assuming the presence of Fe to be totally in the state of Fe^{2+}, changes the corresponding field strength dramatically (Brown Jr. *et al.*, 1995), placing Fe between Ca and Mg, at 0.44-0.51 $Å^{-2}$. Additionally, the assumed coordination number enhances the differences. This is ultimately leading to a negative anomaly in this region (Figure 2.5.a). Hence, $(\sigma^2_n)_{Fe}$ is in better conformity with FATS, while supporting this argument. In this respect it is necessary to point out that (σ^2_n) data for M13 were originally reported assuming Fe as FeO_{tot}, hence, plotting $(\sigma^2_n)_{Fe}$ using the corresponding value for Fe^{2+} field strength. In Figure 2.5, M13 values were plotted using Fe^{3+} field strength, assuming this value as more realistic for Fe.

The abrupt decrease in (σ^2_n) shown in Figure 2.5.a is indicative that P is not acting as a network former as usually assumed for silicate melts (Mysen *et al.*, 1982). In contrast, calculated $(\sigma^2_n)_P$ is comparable with $(\sigma^2_n)_K$ and $(\sigma^2_n)_{Na}$ in our experiments (see Supplementary Material S1 for details on these computations). This observation is suggestive that P behaves similar to other trace elements in experimental charges. It is coherent with results of this study since it occurs in trace element levels in the vast majority of analysed points, and, in consequence, considering the standard deviation. Although trace elements are not scope of this work, by comparison with M13 data it is possible to infer that $(\sigma^2_n)_U$ should be very similar to $(\sigma^2_n)_K$. The proximity of P and U cations in terms of ionic radius and valence leads to very similar fields strength of 2.14 $Å^{-2}$ and 1.89 $Å^{-2}$ respectively (Brown Jr. *et al.*, 1995), allowing to speculate that $(\sigma^2_n)_P$ and $(\sigma^2_n)_U$ also might be close.

In the case of Na and Al some differences emerged from this study. The three experiments resulted in very similar (σ^2_n) which is in good agreement with the initial low gradients. If the initial Na and Al contents in the basaltic and rhyolitic melts at the beginning of the experiments become very similar, the average distance of each point to the hypothetical equilibrium composition are small and close to $(\sigma^2_{Ci})_{t=0}$. It leads to the impression these elements homogenize faster and present the lowest (σ^2_n) values. In Figure 2.5.a, $(\sigma^2_n)_{Al}$ for Exp1 (yellow square) is outside of the shown range. This is

mainly due to the fact that the Al data spread over a larger range than the confidence level of initial compositions (Figure 2.4), which means $(\sigma^2_{Al})_{t=106} > (\sigma^2_{Al})_{t=0}$ and, consequently, $(\sigma^2_n)_{Al} > 1$ (Eq. 2.III). Furthermore, the possibility that low concentration gradients may be responsible for an uphill diffusion process (Emmanuel *et al.*, 2004), cannot be excluded, however, it is very difficult to be detected due to the EPMA resolution.

In general, amongst the performed experiments it can be stated that elements tend to systematically achieve their homogenization faster from Exp2 over Exp3 to Exp1. The explanation for this lies in the fact that the initial viscosity ratio in Exp2 was 3.29 (log units), and hence was the smallest in comparison to Exp3 and Exp1, whose ratios are 3.71 and 4.14, respectively. Therefore, this points towards a correlation between the mixing efficiency and the initial viscosity ratio of the end-members. Based on the similarity of M13 and Exp3 in respect to their initial (η_{rhy}/η_{bas}) ratios, similar values of (σ^2_n) were expected, which is observed for Ca, Mg, Ti and Si. However, it occurs neither for K and Fe, whose M13 values are closer to Exp2 than Exp3, nor Na and Al that substantially differ from our results. Besides, based on its higher initial (η_{rhy}/η_{bas}) of 3.89, M13 data should result in points systematically above the curve of Exp3 in Figure 2.5.a. The discrepancies are thought to occur partially due to the spatial distribution of filaments crossed by transects (*e.g.*, the filament thickness), and in part due to the influence of other physical parameters still not quantified such as the chemical potential. Viscosity depends on chemical composition, however the use of different end-members could hypothetically culminate in close (η_{rhy}/η_{bas}) and, hence, in similar elemental behavior. Nevertheless, the chemical potential is the driving force for chemical mixing (*e.g.*, Emmanual et al., 2004) that varies according to starting compositions as well and might be playing the important role on experiments globally. Locally, the spatial distribution of mixing patterns (*e.g.*, filament thickness) is positively correlated to concentration variances (Morgavi *et al*., 2013a), and in turn affecting the local properties again as well. Therefore, even selecting transects in regions with similar filament distribution/thickness, which is related to the final configuration at the end of experiments, the non-linear nature of the interaction between rhyolitic and basaltic melt during experiments enhances their complexity. More chaotic mixing experiments performed at the same conditions also varying the compositional arrangement (*i.e.*, basaltic, andesitic, dacitic and rhyolitic starting materials) might help to describe more

precisely these effects in different mixing systems.

2.4.3 A TERMINOLOGICAL ATTEMPT: MIXING *VS.* MINGLING

In petrology, the term “mingling“ refers to a first order physical dispersion of a magma body through another magma (*i.e.*, enclave in a host magma) without any chemical exchange by diffusion, etc. If chemical exchange does occur it is referred to as “mixing”. Following the same definitions, the visual criterion (Fig. 2.3.a) can result in multiple potential misinterpretations. The processes of initial physical mingling of new phases (without chemical exchange) and mixing (including chemical equilibration by diffusion) to its thermodynamic equilibrium state needs to be discussed here in more depth: the substantial difference in viscosity between the end-members (up to 4 orders of magnitude) does not really facilitate chemical exchange, thus it is not trivial to identify a wide contact and interaction zone. Nevertheless, the interaction does emerge locally along the contact area between the end-members. The BSE-images of representative sections (Fig. 2.3.b-d) indicate blurred areas between the filaments in all experiments, which increase as the (η_{rhy}/η_{bas}) ratio decreases. The patterns produced by the chaotic dynamics are better developed and, therefore, better observable. Stretched and folded filaments increase the contact area between the end-members, which finally result in an exponential increase of diffusion efficiency when filament thicknesses become sufficiently small. As an effect, the number of points whose compositions lye on between those of the starting materials (*i.e.*, grey bars in Figure 2.4) systematically increases as well. Additionally, the number of measured points that achieved the local equilibrium in mixture increases with decreasing viscosity contrast. This is depicted on Figure 2.5.b, which represents results of calculating the final composition of a hybrid material by varying the fraction of mixing f between the end-members using the classical linear mixture equation (Langmuir *et al.*, 1978):

$$C_H = C_R^i * f + C_B^i * (1 - f) \qquad \text{(Eq. 2.IV)}$$

where C_B^i and C_R^i are respectively the initial concentrations of an element i in the, basaltic and rhyolitic glasses and C_H is the hybrid glass final concentration. In the case of Figure 2.5.b, the selected fraction of f = 0.5 means that 50% of the contaminant

(rhyolitic end-member) is mixed in. The results are in agreement with elemental mobility calculations, which predict that the more mobile an element is, the faster it will achieve the local equilibrium. As an example, data for K in Exp2 show about 9% of the total points inside the expected interval, while data for Si in Exp1 show less than 1%. It should be noted that K has the smallest value for (σ^2_n) in Exp2, while the value for (σ^2_n) for Si in contrast to Si in Exp1 is the highest.

Although the initial rhyolite/basalt ratio is 20/80 for all experiments performed, the histograms of Figure 2.6 show the systematically increase of points that fits within the interval $0.5 < f < 0.6$. In this diagram a value of $f = 0.0$ represents the original basaltic composition, and a value of $f = 1.0$ corresponds to the original rhyolitic composition. The mentioned interval reflects the elemental diffusion occurring in small distances, essentially along the contact zones (approx. 300 mm thick, independent of experiment) achieving a local homogeneity in an initial moment. Then, diffusion starts from the equilibrated to unequilibrated areas. The local homogeneity is sensitive to experimental time (*e.g.*, Morgavi *et al.*, 2013a,b) and approaches the thermodynamic equilibrium at $t = \infty$. During this process, the viscosity changes continuously on a local scale due to local changes in chemical composition, and can play a significant role defining the direction diffusion will occur next. Notice that this process is three-dimensional, although observed only two-dimensionally here.

The histograms highlight the contamination effect occurring faster in the basaltic phase as well. The expressive number of data points inside the range between $0.9 < f < 1.0$, and $0.1 < f < 0.4$ is remarkable. This implies that the rhyolitic melt experiences less physical and chemical exchange during the experiment, losing only up to 10% of its original composition, while the basaltic melt is extraordinary altered during the chaotic mixing process (up to 40%, with the peak at approx. 20%). Furthermore, the histogram for K in Exp2 presents a unique behaviour between 20-55%, with a similar distribution of the data points over this interval. As K achieves its homogenization, no more extreme data points at $f = 0.0$ and $f = 1.0$ are observed, and the tendency is towards more points gathering around the equilibrium point. This observation confirms the higher mobility and, in consequence, faster equilibration of this element (*i.e.*, smaller (σ^2_n)).

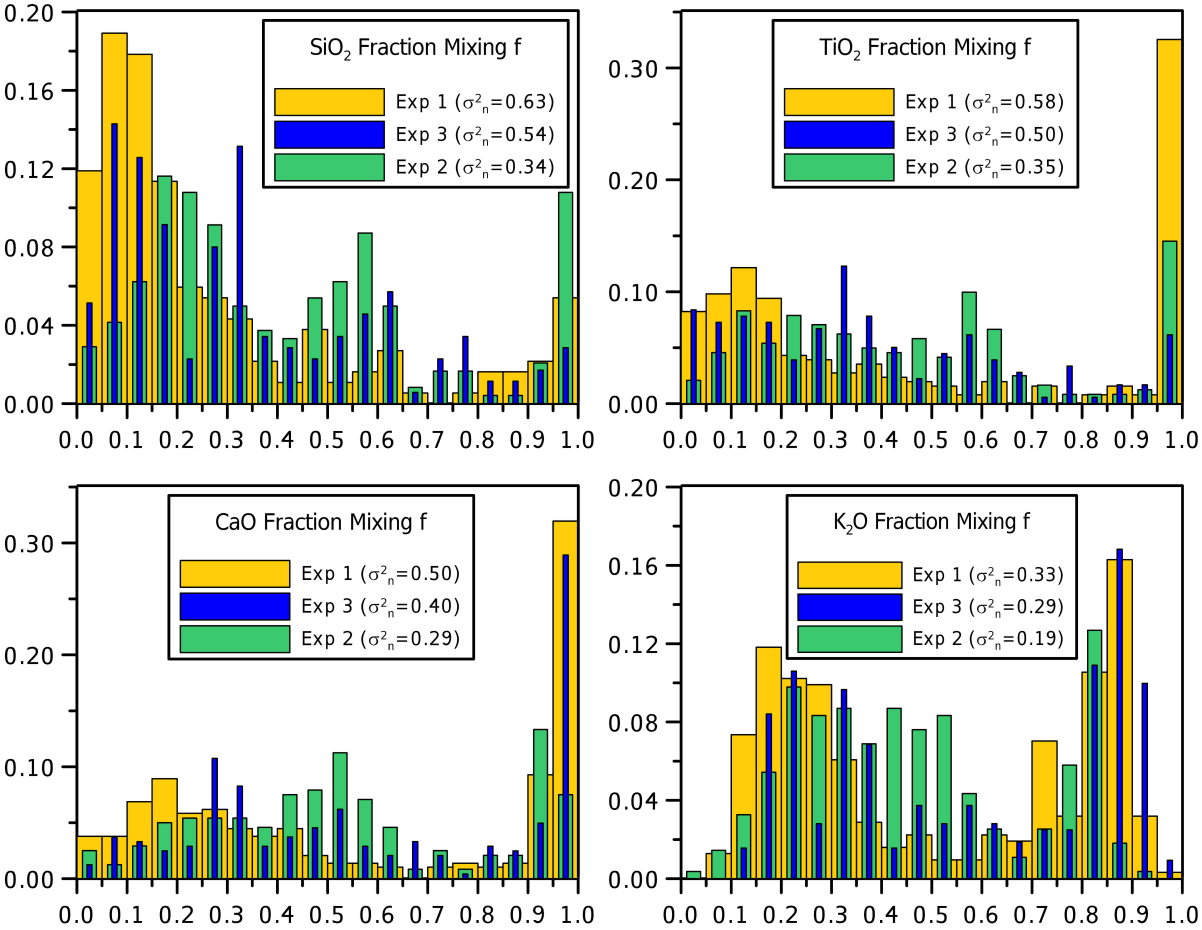

Figure 2.6: Frequency of points with different degrees of contamination *f*. Data is divided in groups (bins) of 0.05, varying from *f* = 0.0 (no contamination, only basaltic material) to *f* = 1.0 (no basalt, only rhyolitic material). The histograms show the percentage of analysed points that fit in each group for representative elements for each experiment.

4.4 GEOCHEMISTRY OF PEMP HIGH-TI ROCKS *VS.* EXPERIMENTAL RESULTS

In order to compare the transect data of the experimental charges of this study with natural rocks from the field, a correction regarding the chemical compositions found in a specific transect is required. Naturally, starting from a ratio of originally 80% basaltic composition versus 20% rhyolitic composition in the performed experiments, the chance of transects crossing basaltic areas is higher than crossing rhyolitic regions. Therefore, the BSE-images shown in Figure 2.2.b-d were analysed using an image analysis software (ImageJ; Rasband, 2016) to identify the portions covered by the assumed rhyolitic composition (darker areas – grey scale histogram) and the assumed basaltic composition (lighter areas). Peaks from those areas in the histogram were

identified and the extreme pixels (black and white) were discarded. All pixels that did not fit in the intervals described were assumed as portions of intermediary composition, which means they represent analyses of areas where mixing occurred. Table 2.4 presents the results for each analysed section. Comparing the sections from experiments 1 and 3 with similar areas of rhyolite and basalt, it is possible to notice the increase of intermediary regions in Exp3. This fact is in agreement with the decrease of (h_{rhy}/h_{bas}) previously appointed. Concerning Exp2, the comparison with Exp1 and Exp3 is not directly possible since the rhyolitic and basaltic areas in the section Exp2_6top are substantially different from those observed in the sections Exp1_7top and Exp3_11top.

The experimental datasets 1, 2 and 3 were sectioned according to SiO_2 content in order to determine the number of points corresponding to basic, intermediate and acid (or silicic) compositions, respectively, for each dataset. The IUGS sub-commission of igneous rocks (Le Bas *et al.*, 1986) defined basic rocks as those with $SiO_2 < 52\%$, and intermediate rocks as those with SiO_2 contents between 52% and 63%, and acid rocks as those with $SiO_2 > 63\%$. This is illustrated in Figure 2.7 (x-axis). In this work, however, the range of basic compositions (corresponding to lighter colours in Figure 2.7) includes SiO_2 contents up to 55%, while compositions with SiO_2 contents between 55% and 63% were considered as intermediate (darker colours in Fig. 2.7). This adaptation was based on PEMP high-Ti gap in SiO_2 data between 55% and 63% (*e.g.*, Piccirillo & Melfi, 1988), which is the object of the comparison. Silicic composition follows IUGS convention (*i.e.*, $SiO_2 > 63\%$). Thus, we corrected the frequency of points with basic, intermediate, and silicic compositions, respectively, in each transect according to the area that each of them represent in the entire section (Table 2.4).

Table 2.4: Calculated area for each section from experiments 1, 2 and 3 using ImageJ free software. The areas represent the percentage pixels that attend the criteria (discussion in the text). “Silicic” represents rhyolites and dacites; “intermediate” represents andesites; and “basic” represents basalts.

Area [%]	Exp1_7top	Exp2_6top	Exp3_11top
Silicic	29	7	32
Intermediate	14	10	18
Basic	57	83	50

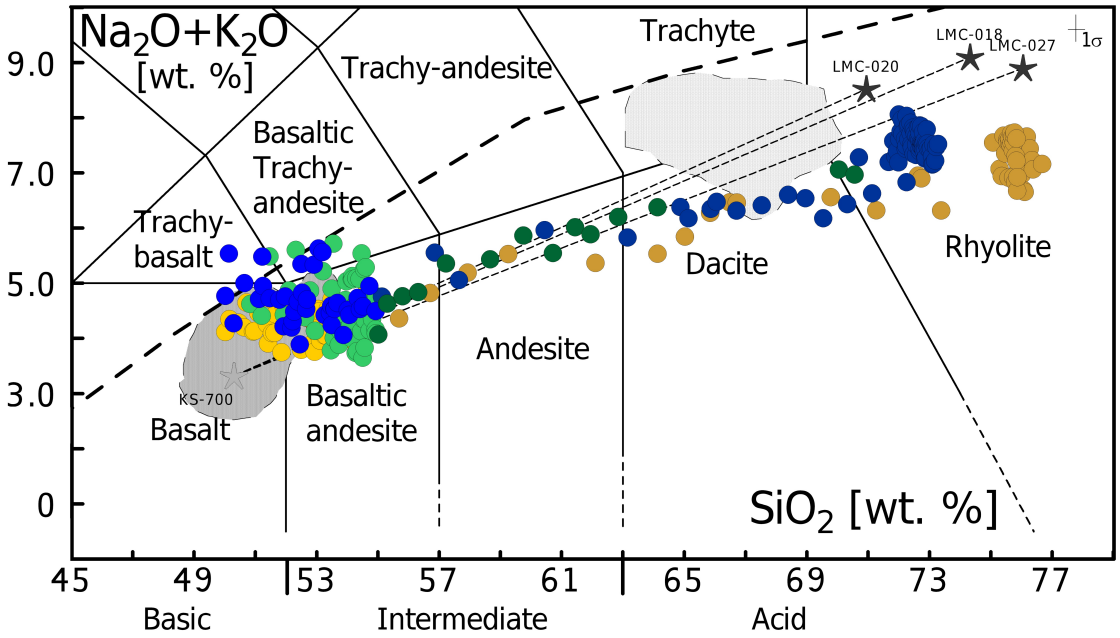

Figure 2.7 (colour): Lithological classification of analysed points according Le Bas *et al.* (1986). Legend: circles = analysed points from experiments 1 (yellow), 2 (green) and 3 (blue); darker colours = intermediate and silicic compositions (SiO_2 > 55%; details in text); stars = end-members (grey = basalt; black = contaminants); fields = representative rocks of high-Ti PEMP (Garland *et al.*, 1995; Nardy *et al.*, 2008; Rocha-Júnior *et al.*, 2013); 1σ = 1 standard deviation; thick dashed line = division between alkaline and sub-alkaline groups (Irvine & Baragar, 1971); thin dashed line = linear mixing line corresponding to Eq. (2.IV).

Figures 7 (TAS) and 8 (elemental variation) illustrate experimental results reported here after corrections mentioned above, and compile the main data on PEMP high-Ti rocks. In the TAS diagram the basaltic points spread over a large area, more enriched in alkalis than the original basaltic glass. Experimental data of this study are in agreement with main data on PEMP, which includes the two northern high-Ti basaltic flow units (Pitanga- and Paranapanema-type). The experiments produced a small number of alkaline compositions that lies on trachy-basaltic and basaltic trachy-andesite fields, plotting above the alkaline line (Irvine & Baragar, 1971), which is not observed in the northern PEMP. In the intermediary part, the number of data points are comparatively smaller, which corresponds with to the relative lower natural abundance of high-Ti andesitic flows (virtually absent in Paraná). The silicic high-Ti Chapecó rocks comprehend dacites and trachytes. Nevertheless, the present chaotic mixing experiments reproduce an alkali-poor trend compared with Chapecó, which could reflect some alkali loss during the experiments (*i.e.*, melts submitted to 1,350 °C).

Finally, data points in the rhyolitic field represent the original glasses from each experiment that could not preserve the total alkali contents, opposite to what is observed in the basaltic data. This opposing observation supports the idea that alkali elements are moving faster and reach final equilibrium due to faster diffusivities than other elements, since its loss would be detected in basaltic surveys as well. Notice that the relatively absence of data from Exp2 (green) on rhyolitic field is a consequence of the small area that this phase represents in the analysed section (= 7% – Table 2.4).

The elemental variation diagrams shown in Figure 2.8 confirm that the obtained experimental basaltic compositions plot inside the PEMP high-Ti basaltic field (Fig. 2.8). It is worth being mentioned that some points considered as basaltic in the TAS diagram are out of the PEMP basaltic field, and some intermediate points (darker colours) falls inside the basaltic field, especially in respect to CaO and P_2O_5 in Exp2 and Exp3. This demonstrates the very complex elemental behaviour possible during chaotic mixing processes. In addition, elements with contrasting (σ^2_n) show higher non-linear trends (*i.e.*, P_2O_5 *vs.* MgO), particularly evident in the end-members portions. It should be noted that the main trend is coherent with PEMP data. Exceptionally, P_2O_5 is considerably more enriched in PEMP rocks than in the experimental charges of the present study, showing the most remarkable behaviour. Finally, as obvious from Fig. 2.8, the compounds TiO_2, CaO, and P_2O_5 show an increased number of data points close to the end-member initial concentrations (symbolized in Figure 2.8 by the black stars), which represent regions where starting glass compositions are still preserved. For K, the concentrations systematically differ from the initial values as mentioned before. In general, rhyolitic regions show a significant loss in K while basaltic regions show a significant gain in K, reflecting the higher mobility (smallest (σ^2_n)) of this element, resulting in a faster homogenization and equilibration.

In respect to Chapecó dacites, CaO and K_2O precisely represent the natural occurrences in all experiments. This is in complete contrast to the observed for TiO_2 and P_2O_5, which are apparently underestimated. Nonetheless, analytical effects might explain this observation since their measured concentrations are very close to the detection limits (*i.e.*, rhyolitic region) of the EPMA method. In this respect the performed analyses for P_2O_5 – especially due to their extremely low concentrations in the contaminants LMC-027 (Exp1) and LMC-018 (Exp3) were not considered for deeper discussion in this study. Considering the standard deviation, P_2O_5 data are in

better agreement with the COD group, which is comparatively less enriched in TiO_2 and P_2O_5 than the CGD. Finally, we point that Exp2 was most successful in reproducing compositions occurring in natural COD samples.

2.4.5 COMPARING MODELS: LINEAR MIXING *VS.* CHAOTIC MIXING

The origin of high-Ti Chapecó dacites is hotly contested. The geochemistry cannot be fully explained by models such as fractional crystallization and mantle partial melting, due to a compositional gap existent in SiO_2 (55-63%) and, analogously, in MgO (2.0-3.5%). The virtual absence of intermediate lithologies and singular trace and isotopic signatures (*e.g.*, Piccirillo & Melfi, 1988; Garland *et al.*, 1995) point towards more complex processes acting during their genesis, which are yet not fully understood.

The development of accurate of non-linear mixing models is a difficult task. In a first approximation, one solution would be to compare the linear models with available experimental data. Thus, the expected compositions were calculated initially for different interaction scenarios (*i.e.*, f varying from 0 to 1) using Eq. (2.IV) (linear mixing; Langmuir *et al.*, 1978). Although major oxides and isotopic systems behave differently, some correlations are expected (*i.e.*, similar f). Taking this into account, the chemical analysis of the end-members KS-700 (high-Ti Pitanga basalt), LMC-027 (sienogranitic contaminant of Exp1), LMC-020 (monzogranitic contaminant of Exp2), and LMC-018 (monzogranitic contaminant of Exp3) were used in the linear mixing model (Langmuir *et al.*, 1978), and the results were compared with the average compositions of Chapecó (Guarapuava and Ourinhos) and representative samples (Table 2.1). The discussion follows the sequence of the granitic contaminants (*i.e.*, the rhyolitic end-member) in each chaotic mixing experiment.

Figure 2.8 (colour): Variation diagrams of representative elements. Units in weight percent (wt.%). Legend: circles = analysed points from experiments 1 (yellow), 2 (green) and 3 (blue); darker colours = intermediate and silicic compositions (SiO_2 > 55% on TAS diagram – Figure 2.7; details in text); stars = end-members (grey = basalt; black = contaminants); fields = natural high-Ti PEMP representative rocks (Garland *et al.*, 1995; Nardy *et al.*, 2008; Rocha-Júnior *et al.*, 2013); 1σ = 1 standard deviation; thin dashed line = linear mixing line corresponding to Eq. (2.IV).

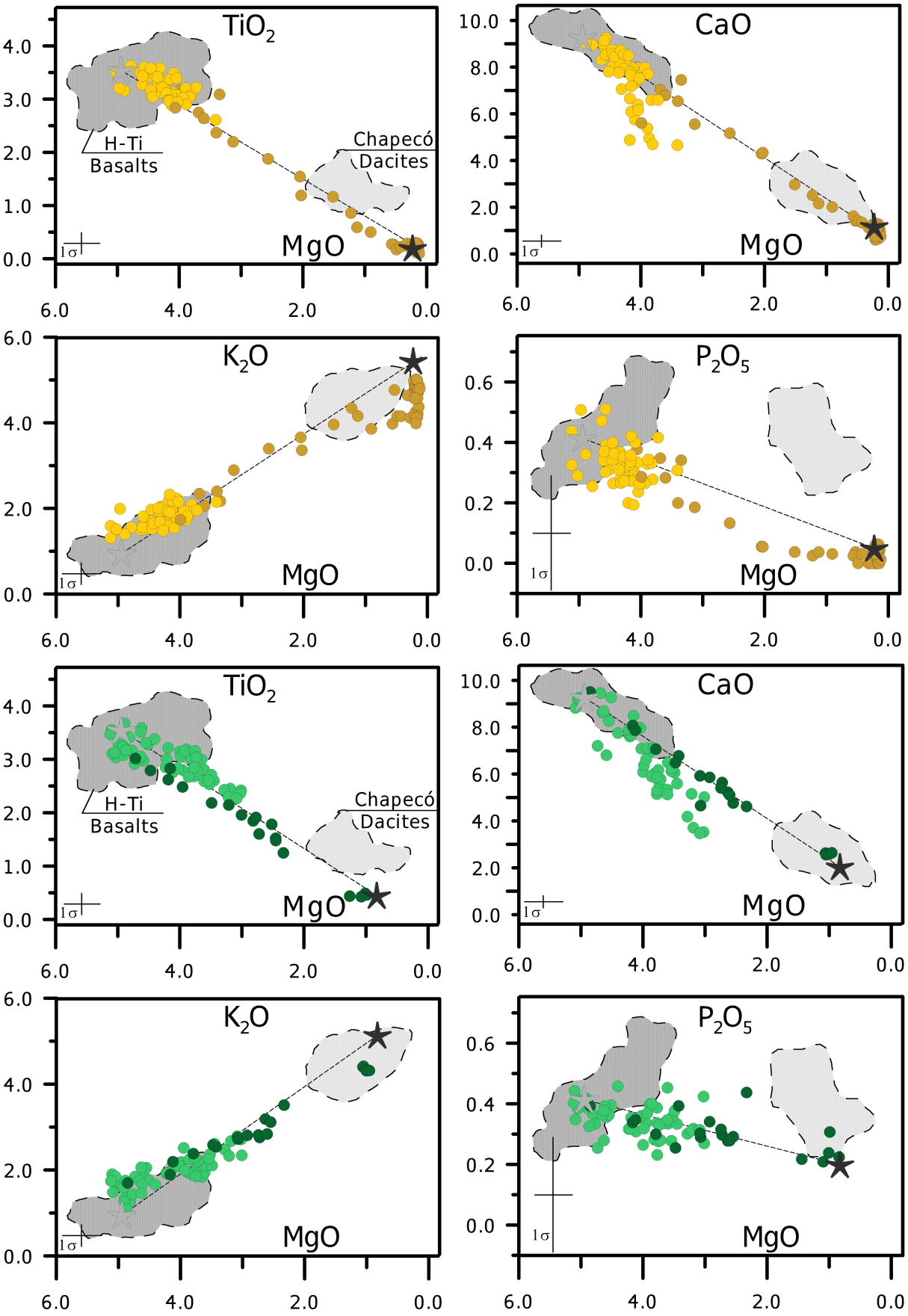
TiO2
H-Ti
Basalts
Chapecó
Dacites
MgO
1σ
CaO
K2O
P2O5

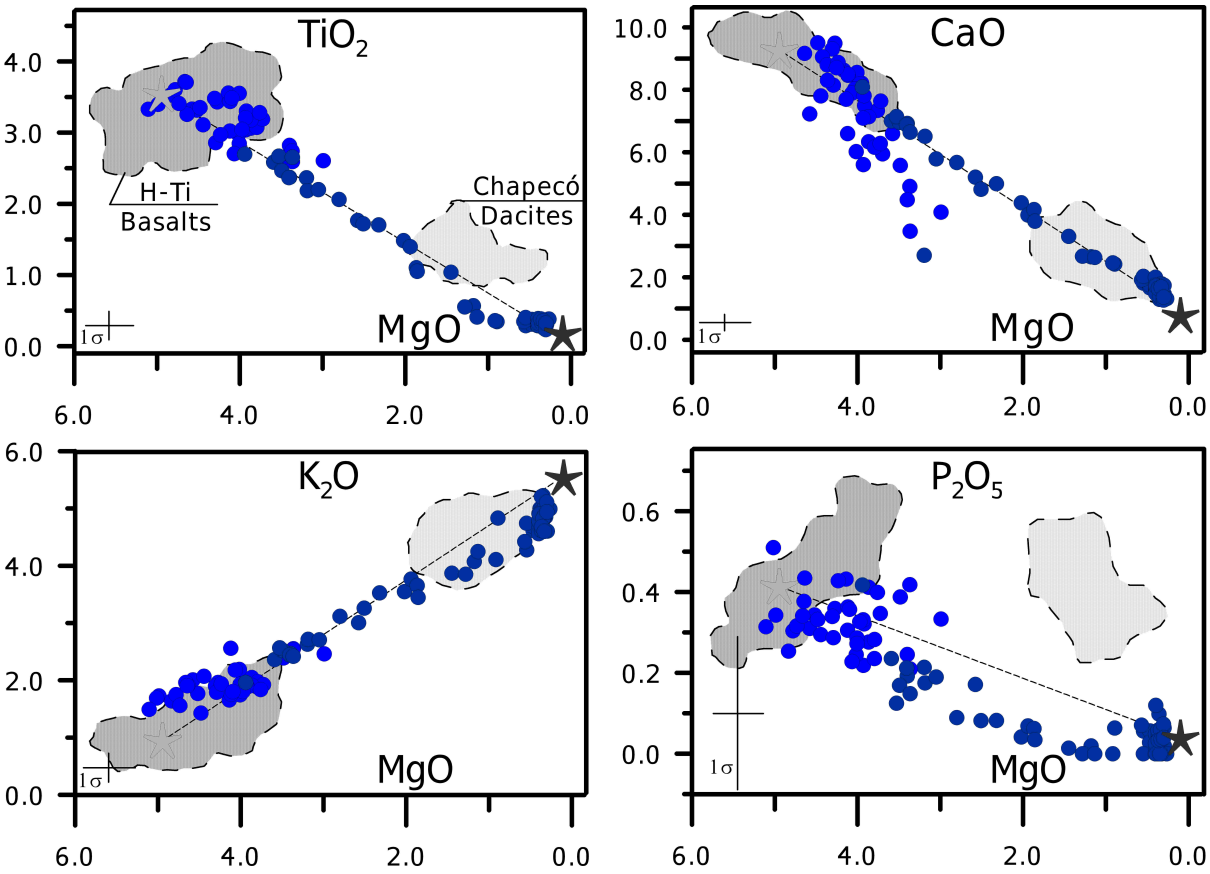

2.4.5.1 LMC-027 (EXP1)

According to theoretical considerations, the mixing of 50-60% of LMC-027 into a Pitanga-type basalt could generate major oxide compositions similar to those observed for Chapecó-Guarapuava dacites (CGD), especially regarding network formers (*e.g.*, SiO_2, TiO_2 and Al_2O_3). However, to reproduce the lower Sr_i isotopic signatures, the contaminant fraction *f* must lie between 4-6%. For this, the trace elements Rb and Sr, directly involved in $(^{87}Sr/^{86}Sr)_i$ isotope system, require contaminant fraction ranging between 20% and 30%. In the case of Chapecó-Ourinhos dacites (COD), a slightly higher contaminant fraction *f* between 60-70% of LMC-027 is required to match the major oxide compositions, while Rb and Sr concentrations would be matched if *f* would lie between 40% < *f* < 50%, while the $(^{87}Sr/^{86}Sr)_i$ isotopic ratio would require 20% < *f* < 30% to match the natural observations.

In summary, a linear mixing process between the end-member starting compositions cannot reproduce the elemental and isotopic compositions observed for natural CGD and COD rocks: the required contamination fractions *f* for CGD compositions are off by approx. 40% between major oxide compositions and the

($^{87}Sr/^{86}Sr)_i$. In the case of COD rock compositions, the contamination fraction *f* is off by approx. 30% from ($^{87}Sr/^{86}Sr)_i$, and approx. 10% from Rb and Sr.

2.4.5.2 LMC-018 (EXP3)

Using LMC-018 as rhyolitic contaminant composition requires approx. 60% of LMC-018 being mixed into KS-700 basalt to reproduce oxide compositions similar to those observed for CGD. As observed in linear mixing calculations for LMC-027, network formers exhibit better fits than classic network modifiers (*e.g.*, MgO, Na_2O and K_2O). The same accounts as observed with LMC-027 for the Sr_i isotopic signatures, which require contaminant fraction *f* between 4% and 6%. However, again to duplicate the Rb and Sr concentrations in natural CGD compositions, a contaminant fraction *f* of 20-30% is required. In the case of COD compositions, a contaminant fraction of $f \approx$ 70% is necessary to match the major oxide components, while the Sr concentrations could already been matched mixing approx. 60% of LMC-018 with KS-700 basalt. However, the Rb content would require $f \approx 25\%$ while the ($^{87}Sr/^{86}Sr)_i$ would only require $f \approx 15\%$.

Again the conclusion has to be drawn that linear mixing models for LMC-018 mixed into a basaltic starting composition of KS-700 cannot reproduce the elemental or isotopic distributions and concentrations observed in natural rocks of CGD and COD compositions. Major/minor oxide contents are off by up to 55% from the ($^{87}Sr/^{86}Sr)_i$ requirements. Although Rb and Sr seem to agree better for CGD compositions (coherent with Sr_i isotopic ratio), major oxide compositions are in better agreement in respect to the required contamination fractions for Sr in the COD compositions.

2.4.5.3 LMC-020 (EXP2)

In case of LMC-020 as contaminant, CGD major oxide compositions could be reproduced by mixing approx. 60-70% of LMC-020 into the starting basaltic composition KS-700. Network formers (SiO_2, TiO_2, Al_2O_3, Fe_2O_3) are better reproduced than modifiers, and Na_2O and P_2O_5 are in good agreement as well. For a correct ($^{87}Sr/^{86}Sr)_i$ ratio, however, a contaminant fraction of $f \approx 4\%$ is already sufficient to mirror natural observations with experimental data. In the case of trace elements, only

Rb can be modelled with an $f \approx 40\%$ due to its starting concentrations. In case of COD compositions, the amount of LMC-020 between $60\% < f < 70\%$ mixed into KS-700 would be sufficient to reproduce major/minor oxide compositions. Correct Rb concentrations would be reproduced with f ranging from 50% to 60% for Rb, while the $(^{87}Sr/^{86}Sr)_I$ could already be established with a contamination fraction of $10\% < f < 20\%$.

As found in cases of LMC-027 and LMC-018, there are big discrepancies in LMC-020 results between naturally observed CGD and COD compositions with recalculated experimental data using a linear mixing model: in case of CGD compositions, the determined contaminant fractions f required for matching either major element oxide concentrations or the $(^{87}Sr/^{86}Sr)_i$ ratios, are off by approx. 55%. To generate rocks similar to COD compositions, the contamination fraction f vary by approx. 40% between major/minor oxides and the required Sr_i isotopic signature. Furthermore, Rb concentrations can be reproduced in good agreement with COD mineralogy (10% difference from initial Sr_i isotopic ratio).

2.4.5.4 PETROGENETIC CONSIDERATIONS FROM PRESENT RESULTS

In an attempt to correlate or reproduce observed rock mineralogy with experimental data from mixing experiments with Pitanga basalt and a rhyolitic body, and recalculation of the results using a linear mixing model between these two end-members, the following conclusions have to be faced: i) a linear mixing model is not able to reproduce the elemental features of the observed rock types (COD, CGD); potentially some non-linear mechanisms have to be taken into account; ii) amongst all initial contaminant compositions, LMC-027 results in the best reproduction of the compositions observed in COD and CGD natural rocks; iii) the compliance is better for COD than for CGD rock types; iv) differences in the analytical tools used at different laboratories during the analysis of natural rocks can additionally influence the obtained results (*e.g.*, *ICP-MS* and *INAA*) and their reliability and comparability. All experimental glasses of the present study were analysed with the same technique and identical analytical conditions at the same laboratory (electron probe microanalysis *EPMA*), which guarantees internal compatibility of the experimental data set.

The performed calculations based on a linear mixing model generically point to contamination fractions *f* ranging between 50% and 60% to be able to reproduce the major/minor oxides, while already up to 10% would be sufficient to end up with the matching Sr_i isotopic ratio. This result is partially in agreement with the major/minor oxide histograms of Figure 2.6 showing peaks in the regions 10% < *f* < 20%, and 50% < *f* < 60% as well. It indicates higher probabilities of finding values of *f* similar to these where the interaction takes place (*i.e.*, filaments, stretched and folded arms) since data were taken precisely over such regions. Although the discrepancies between the contamination fractions for major/minor and Sr_i are relevant, natural and experimental investigations revealed this type of decoupled behaviour (*i.e.*, bulk mixing; Rosing *et al.*, 1989; Lesher, 1990; Blichert-Toft *et al.*, 1992; Waight & Lesher, 2010). The most commonly used linear models do not consider this behaviour. In this respect, our results are in agreement with the observation that dramatic differences in elemental diffusivities can mislead interpretations. It may have implications on isotopic systems (e.g., Rosing *et al.*, 1989), which are measured on trace elements that also present different mobilities (*e.g.*, Perugini *et al.*, 2006; Morgavi *et al.*, 2013b).

In the PEMP context, several authors pointed the correspondence between Paraná-Chapecó dacites and Etendeka quartz-latite groups in African portion (Alberti *et al.*, 1992; Marsh *et al.*, 2001; Ewart *et al.*, 2004; Marsh & Swart, 2018). They consider the initial PEMP high-Ti silicic magmatism more extensive describing more rocks with intermediate compositions, however a relevant part has been lost. These works also argue that the mixing between high-Ti basalts and felsic rocks might be involved in the origin of Etendeka quartz-latites, although apparent inconsistences emerged especially in respect to isotopic signatures (*e.g.*, Sr and Pb). Authors suggest these isotopic inconsistencies demand more comprehensive studies (Marsh & Swart, 2018). Furthermore, recent investigations on Chapecó dacites revealed features that are consistent with a mixing process as well (Luchetti *et al.*, 2018). The crystal size distribution (CSD) shows clear evidence for different families of plagioclase growing at different rates at different depths and in mineral disequilibrium (*e.g.*, Luchetti et al., 2018). Another argument is the presence of a large number of crustal rocks in the adjacency of Chapecó dacite outcrops (Prazeres-Filho *et al.*, 2003; Rodrigues *et al.*, 2011) that could have interacted with basaltic material from PEMP. Reported chemical and isotopic variability of batholiths (Cunhaporanga, and Três Córregos) and granitic

rocks were considered amongst other contaminants. In this study, samples were collected with the aim to cover the maximum range of compositions, however it was not a priori guaranteed. The sampling area, the basement of Paraná Basin, where the bi-modal magmatism of Paraná developed between 135-132 Ma (compiled by Gomes & Vasconcelos, 2021), lies within a very complex and heterogeneous geological site, and makes sampling not easy. Some domains that compose this framework are cratonic blocks (*e.g.*, São Francisco, Congo, and Angola), large orogenic belts surrounding them (*e.g.*, Araçuai-Ribeira, West Congo and Dom Feliciano), smaller continental blocks and magmatic arcs (Almeida *et al.*, 2013). All this information together defines a very complex scenario in which mixing might have played a significant role through chaotic dynamics.

2.5 FINAL REMARKS

The major result of the performed chaotic mixing experiments confirmed that mixing between melts with vastly different viscosities is physically possible. Mixing should be evaluated in terms of efficiency, which is well represented by the normalized variance (σ^2_n). The use of this parameter is an important tool to quantify the elemental mobility during chaotic mixing processes.

Concerning the morphological aspects, emerging features such as stretched and folded filaments and vortex structures, are direct products of chaotic dynamics. The interaction between end-members can directly been observed in all experiments, with three distinguishable regions associated to basaltic, rhyolitic and intermediate portions. Orbicular structures containing dendritic crystals and remnant portions of glass were observed and described in the basaltic areas for the first time. The observed DS areas of the basaltic regions indicate two specific characteristic features: i) an early crystallization process during the initial quench phase of the experiment; and ii) the crystallization process does not happen homogeneously.

Chemical analyses by EPMA show transects where the initial rhyolite is preserved more widely than the initial basalt (*i.e.*, plateaus of original concentrations). Rhyolitic preserved areas are by far more often than basaltic areas with preserved initial composition, even though the higher absolute amount of the initial basaltic phase (80%). Perfect “S” shaped diffusive profiles are typical symmetrical, which was not observed

in this study. The observed unsymmetric diffusion profile argues that a basaltic phase becomes faster contaminated than rhyolitic phase during chaotic mixing processes. Histograms of chemical distribution reinforce this effect since we observe more points dispersed close to the original basaltic composition (*i.e.*, f = 0.0) then the rhyolitic region (*i.e.*, f = 1.0). Along contact zones, curves have different slopes with associated inflexion points for each analysed element, meaning the mobility varies accordingly.

The normalized variance (σ^2_n) consistently indicates the connection between viscosity and elemental mobility. Exp1 exhibits the highest contrast in viscosity (η_{rhy}/η_{bas}), therefore the lesser capability of elemental diffusion. It is expressed by higher values of (σ^2_n) in contrast with Exp3 and Exp2 respectively. Consequently, the number of compositional data points that reached the assumed local chemical equilibrium of the ideal mixture is less extensive in comparison with Exp3 and Exp2, respectively. The direct dependence between calculated (σ^2_n) and the elemental field strength, a well-established parameter that influences mobility (*e.g.*, Rossi *et al.*, 2017), allows the parameterization of mixing process. The positive correlation between field strength and mobility of network formers (FATS) differs significantly from network modifiers (KNCM), indicating a decoupled behavior between these groups.

The chaotic mixing experiments confirmed that mingling and mixing of magmas is a highly complex three-dimensional process as illustrated in the advection-diffusion equation (Eq. 2.I). In an initial step, physical penetration of one phase into the other is initiated by shearing the spindle through the contaminant phase and physically mingling both melts into each other. The created filaments are continuously stretched and folded which increases the contact surfaces while the filaments are getting systematically thinner. Finally, this subsequent physical thinning of the created filaments reaches sufficiently small length scales, which finally sets the stage for diffusion to efficiently wiping out all concentration gradients and bringing the original two melts to their local intermediate equilibrium composition. This, is however, a highly non-linear, and over sample size locally inhomogeneous process with locally different mixing efficiencies. The good news is, however, that it is a very reproducible process in itself, as the comparison of our data to previous studies can show (M13: Morgavi *et al.*, 2013b). In respect to viscosity contrasts, M13 would be anticipated to behave very similar to Exp3 of the present study (Figure 2.5.a). For the major elements like Si and Ti, the agreement is good between the present study (Exp3) and M13. Similar dependencies are found as

well for the network modifying elements Ca and Mg, while Na and K show higher values of (σ^2_n). The most expressive differences in (σ^2_n) are detected for Fe and Al, indicating that either the difference in chosen oxidation state (for Fe: 2+ in M13; while 3+ in our study) as well as additional other parameters (like melt structural influences, coordination number, etc.) might have an influence which shows the need for more studies on natural samples clarifying these discrepancies.

In respect to the formation of the PEMP high-Ti Chapecó dacites, our results lead us to infer that basalts commonly melt crustal rocks, partially or totally, on their way to the surface. The potential interaction between these contrasting melts ranges from cracking off parts of the wall rock, partial leaching of wall rock components to complete remelting and mixing, and, therefore, a highly complex process which will result in some peculiar geochemical signatures, with vastly different influences on major, minor and trace element and isotopic behavior, for the bi-modal magmas generated. The complexity of geological setups certainly contributes to this peculiarity, and even may have facilitated the involvement of multiple contaminants and stages of contamination. As stated above, initial calculations using the linear mixing model pointed that the mixing of LMC-027 contaminant (Exp1) and Pitanga basalt resulted in a better match with compositions for Chapecó dacites. Nonetheless, the use of LMC-020 as contaminant in Exp2 resulted in compositions that are in better agreement with Chapecó dacites in respect to analysed major elements. From the present study, COD rock compositions could be generated more easily during mixing processes than GCD rocks. Nevertheless, the reproduced features such as the variability of basaltic compositions and chemical similarities with PEMP intermediary rare outcrops point towards short interaction times, low convective forces, and a predominance of density driven separation of contrasting melts (*i.e.*, simulated conditions) as possible mechanisms involved in the genesis of Chapecó dacites. Further studies on trace elements and isotopic systems in the hybrid experimental glasses are necessary and will help to understand the overview on generation of such expressive magmatic rocks.

ACKNOWLEDGEMENTS

C.M. Vicentini is grateful by the assistance of C. Luchetti, J. Silva, R. Zanon and D. Conego (field trips); M. Kaliwoda (Raman spectroscopy); D. Müller (EPMA and

XRD investigations); C. Cimarelli (SEM imaging); A. Nardy and K. Hess (discussion and laboratory support); H. Lohringer (sample preparation). Vicentini acknowledges PROBAL CAPES/DAAD grant (process 88887.363370/2019-00; responsible: V. Janasi). D. Dingwell acknowledges the support of ERC 2018 ADV grant 834225 (EAVESDROP).

APPENDIX

2.A – THE INTERPLAY BETWEEN DIFFUSION AND ADVECTION DURING CHAOTIC MIXING

Motion is crucial to any natural system. Nonetheless, it is not regularly considered in petrogenetic analysis due to the complexity it adds to the problem. In the last decades though, several works have highlighted the motion as a trigger of magmatic processes (*i.e.*, mixing), in special non-linear dynamics (Flinders & Clemens, 1996; De Rosa *et al.*, 2002; Perugini *et al.*, 2003b). The authors consider magma as a fluid that responds to applied forces, resulting in a certain particle flux. Hence, it is important to include the dynamics of the system. In this sense, the system obeys the continuity equation and the divergent of the particle flux $\nabla.F$ [particles*m^{-3}*s^{-1}] has to be equivalent to the variation of the particle density n_c [particles*m^{-3}] in time t [s]. It can be expressed as follows (based on Achterberg, 2014):

$$\frac{\partial n_C}{\partial t} + \nabla.F = 0 \qquad \text{(Eq. 2.A.1)}$$

Assuming that the concentration C [wt.%] varies in one direction (*i.e.*, î), we have $n_C = n_C(x,t)$ [particles*m^{-3}], therefore the flux of particles [particles*m^{-2}*s^{-1}] due to the diffusion (Fick's first law) can be expressed as:

$$F_{diff}(x,t) = -D.\left(\frac{\partial n_C}{\partial x}\right) \qquad \text{(Eq. 2.A.2)}$$

where D is the diffusivity [m²*s^{-1}] of a such particle, which means the capability of the particle to move in a mean through time. Replacing F_{dff} in Eq. 2.A.2 results in:

$$\frac{\partial n_C}{\partial t} + \nabla.(-D(\frac{\partial n_C}{\partial_x})) = 0 \rightarrow \frac{\partial n_C}{\partial t} = \nabla.D + D.\nabla(\frac{\partial n_C}{\partial_x}) \quad \text{(Eq. 2.A.3)}$$

Considering $\nabla.D = 0$ (*i.e.*, diffusion is uniform) we obtain the one-dimensional diffusion equation (Fick's second law):

$$\frac{\partial n_C}{\partial t} = D\nabla^2 n_C \quad \text{(Eq. 2.A.4)}$$

in which both sides of Eq. 2.A.4 are given in [particles*m^{-3}*s^{-1}]. Now, if the fluid is not static, the advective term is included in the particle flux [particles*m^{-2}*s^{-1}]:

$$F_{adv}(\vec{x}, t) = V(\vec{x}, t) * n_C(\vec{x}, t)$$

where $V(\vec{x}, t)$ is the vectorial velocity field [m*s^{-1}] that such a particle is submitted. If the diffusion is isotropic (*i.e.*, occurs equally in all directions), then Eq. 2.A.2 becomes:

$$F(x,t) = F_{adv}(x,t) + F_{diff}(x,t) = V(x,t)n_C - D.\left(\frac{\partial n_C}{\partial x}\right) \text{ (Eq. 2.A.2.b)}$$

Substituting Eq. 2.A.2.b in Eq. 2.A.1:

$$\frac{\partial n_C}{\partial t} + \nabla.[Vn_C - D.\left(\frac{\partial n_C}{\partial x}\right)] = 0$$

$$\frac{\partial n_C}{\partial t} + [(\nabla.V)n_C + V(\nabla.n_C)] - [(\nabla.D)\left(\frac{\partial n_C}{\partial x}\right) + D(\nabla.\left(\frac{\partial n_C}{\partial x}\right))] = 0 \text{ (Eq. 2.A.3.b)}$$

Considering $\nabla.V = 0$ (*i.e.*, velocity is uniform) and $\nabla.D = 0$ (*i.e.*, diffusion is uniform) finally it is obtained the one-dimensional advection-diffusion equation:

$$\frac{\partial n_C}{\partial t} + V_{\hat{x}}.\nabla n_C = D\nabla^2 n_C \quad \text{(Eq. 2.A.4.b)}$$

whose terms have units of [particles*m^{-3}*s^{-1}] as well.

This concept is applicable to the chaotic mixing experiments proposed here and it can improve considerably the study of elemental mobility during the chaotic mixing.

2.B – ORBICULAR STRUCTURES

The experimental products of Exp1, Exp2 and Exp3 present orbicular structures that reflect crystallization processes. Using X-ray diffraction analysis (XRD) on produced glasses three phases were identified (Figure 2.B.1.a): i) pyroxene; ii) magnetite; iii) plagioclase. In respect to the starting materials, the nanolites appear to be below XRD detection limits. Raman spectroscopy (Figure 2.B.1.b) shows an expressive peak at 670-690 cm^{-1} indicating Fe and Ti in the composition of such structures (*e.g.*, Di Genova *et al.*, 2017), which is consistent with high brightness observed in optical microscopy. Recent work using Raman spectroscopy has demonstrated the presence of nanocrystals in natural and experimental volcanic systems (Di Genova *et al.*, 2017, 2020; Cáceres *et al.*, 2020, 2022). Using scanning electron microscopy (SEM) to obtain detailed images as depicted in Figure 2.B.2, two phases inside the orbicular structures could be identified: i) the iron-bearing dendritic crystals (named dendritic structures DS), with higher brightness (*i.e.*, more dense), and ii) greyish crystals between the DS and similar in shape, enriched in calcium. Furthermore, some darker portions free of crystals are believed to be remnants from the original basaltic glass composition. Analyses of the pristine starting materials showed that only in the basaltic glass some crystallization on the nanoscale could be detected, which occurred, however, inhomogeneously. In addition, qualitative mapping was performed using SEM on sample areas with excessive crystal populations from all experiments. Elemental maps for Fe, O, Ca, Mg, and Si in Figure 2.B.3 show a significant enrichment in Fe and O in the filaments, while the adjacent area is relatively enriched in Ca, Mg and Si. No significant increase in Ti was detected.

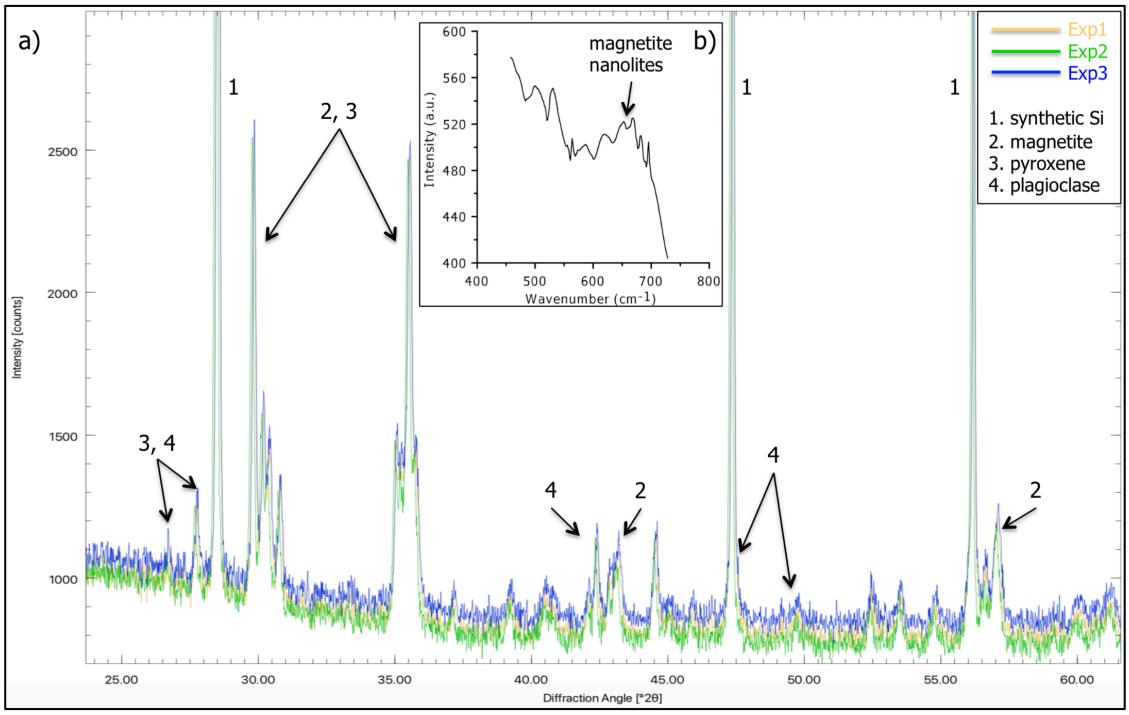

Figure 2.B.1: investigations on orbicular structures with different analytical techniques: a) XRD spectra of Exp1 (yellow), Exp2 (green), and Exp3 (blue); b) Raman spectrum of a representative sample of Exp1.

The presence of DS raises the question how big its influence is during the chemical analysis performed by EPMA. Two independent procedures were adopted to check on this. In a first approach areas with and without DS on an identical sample were measured by EPMA, and the results were directly compared. Figure 2.B.4 shows one transect over a basaltic core of Exp1_5bottom section, analogous to basaltic plateaus illustrated in Figure 2.4. From this figure filaments with and without DS can be clearly identified, and 13 single spot analyses were performed to verify the influence on the SiO_2 data. The individual vertical error bars represent 1σ, and the grey horizontal rectangle represents the average composition of starting basaltic glass plus or minus 1σ (Table 2.B.1). Notice that the spot #1 is outside of the image due to the maximum EPMA aperture could not capture the entire transect. SiO_2 is a good parameter to check on general behaviour of melts, since it is the most abundant oxide and has the strongest influence on melt structure. Analytical conditions were identical as described above (*i.e.*, accelerating voltage of 15 kV; current beam of 5 nA; electron spot size of 10 µm). Independently of the sample, if values obtained for analyses performed over the basaltic glass in crystal-populated areas are statistically equivalent to those obtained in crystal-free areas no significant variation will be observed within a confidence interval.

Moreover, if basaltic cores in a given section preserve the original composition after experiments the average of the 13 single analyses depicted in Figure 2.B.4 should fit within the grey rectangle, since this interval reflects random analyses over the starting end-member. Thus, considering the analytical confidence level of 2σ adequate to distinguish between absolute values, data fits inside the expected interval (grey area) except points 9, 10 and 13. The SiO_2 average of 49.99 ± 0.85 (N = 13) for the transect of Figure 2.B.4 is in agreement with the average presented in Table 2.B.1 for KS-700 end-member as well (= 50.31 ± 0.29). It is expected that regions full of crystals should show a decrease in SiO_2 based on the presence of a more Fe-Ti-bearing phase. However points 10 and 13 are directly within the crystalline area, and present opposite results in respect to the SiO_2 content. Similarly, point 9 and 10 are aimed at both areas (with and without DS), however, presenting the lowest measured, but identical SiO_2 concentrations.

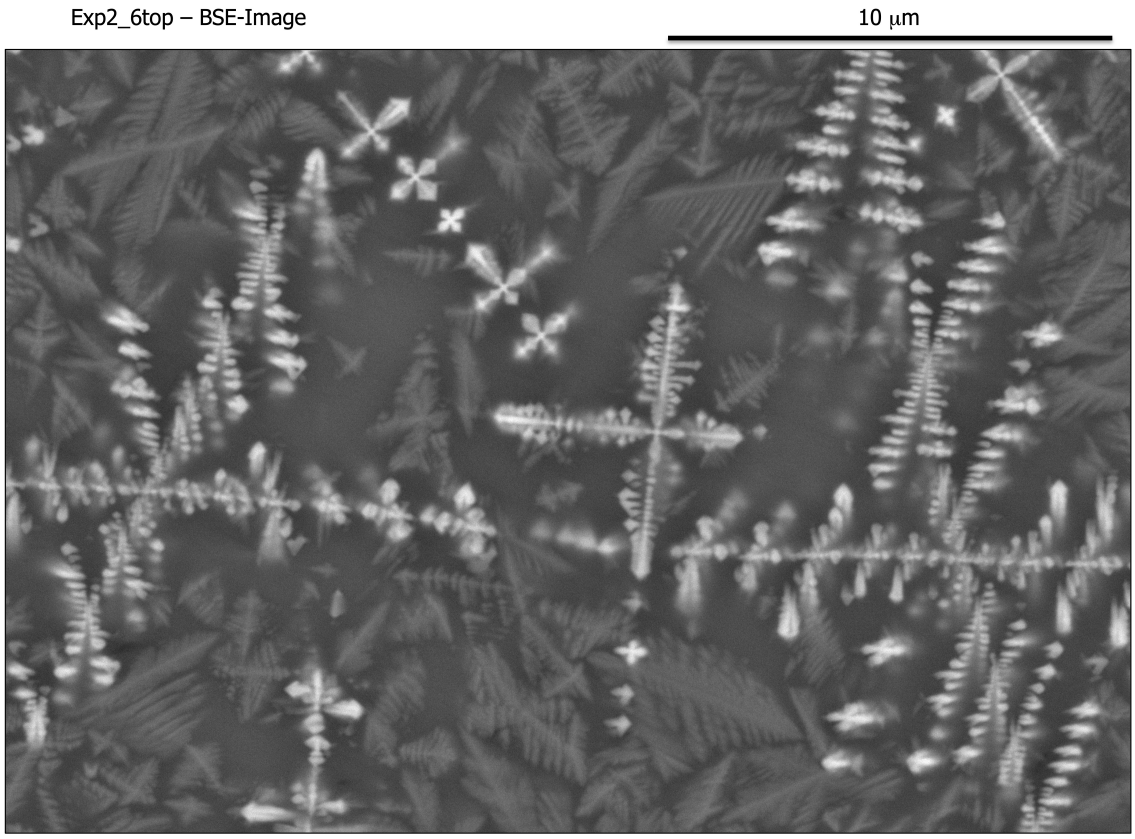

Figure 2.B.2: SEM detailed image on orbicules. The crystallization of two different phases (DS) and a crystal-free region is detected, most likely a residual portion of the original glass.

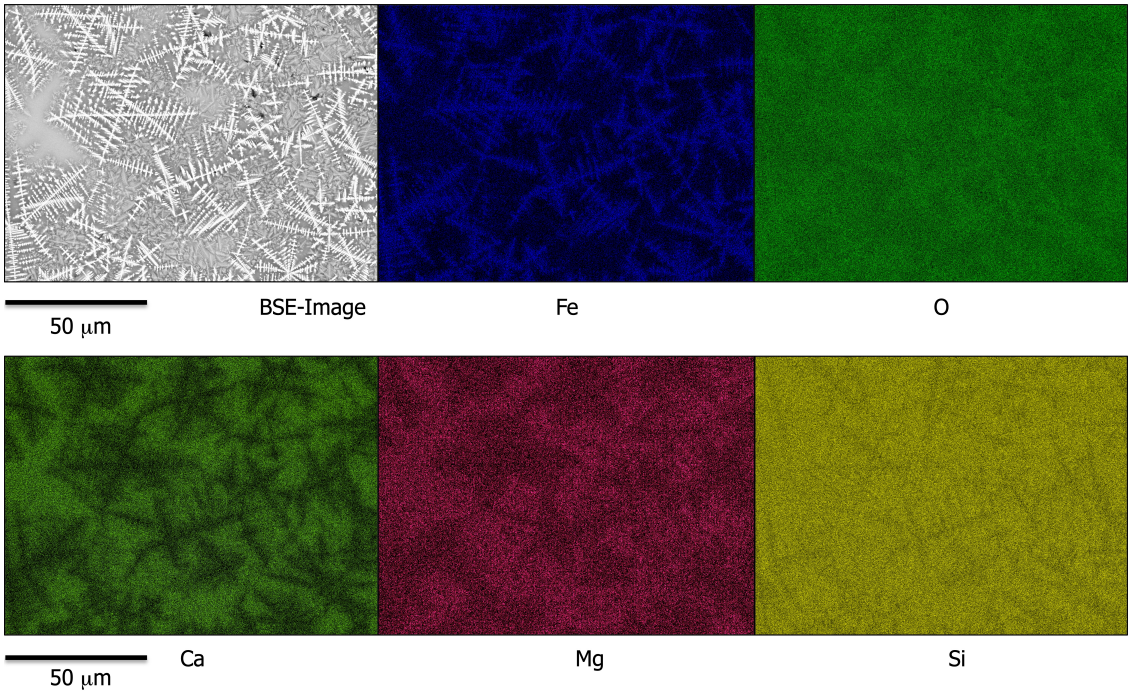

Figure 2.B.3 (colour): maps of representative elements over areas with excessive crystal populations.

The second procedure was to compare an identical sample of KS-700 produced under more reducing conditions with the identical starting material equilibrated with air to avoid oxidation processes and, in consequence, the formation of dendritic structures. To do so, a portion of the identical basaltic glass was processed by stirring it inside a gas mixing muffle tube furnace under reducing fO_2 conditions (*i.e.*, CO_2 = 90% and CO = 10% – $\log fO_2 \approx -10$) for two days, while all other parameters during homogenization (*i.e.*, using a viscometer) were kept constant. This resulted in a crystal-free basaltic glass sample. Table 2.B.1 shows the chemical analysis by EPMA under identical analytical conditions of this sample prepared under reducing atmosphere (KS700_RED1) compared to results obtained in air (KS700_AIR). Notice the applied statistical test *Z-score* that is used to check if two values are equivalent considering their standard deviations s. The calculated Z is proportional to s and it is acceptable if $-3 < Z < 3$. It means the values are compatible up to 3 times the standard deviation, obeying a Gaussian distribution. The absolute concentrations differ less then 2s for the majority of elements, which is an acceptable result. The oxides SiO_2 and Na_2O show higher values, which are still inside the confidence level of the test, though. Alkaline elements such as Na_2O and K_2O are very volatile elements that can be affected by differences in duration of the homogenization process. The average of the fourteen SiO_2 analyses determined is

slightly higher in KS700_AIR and could reflect more analysed points on crystal-free portions (its distribution is not homogeneous), which are relatively enriched in SiO_2 (Figure 2.B.3). Therefore, the comparison demonstrates that compositions of both glasses are statistically equivalent, with the majority of elements inside 2σ interval.

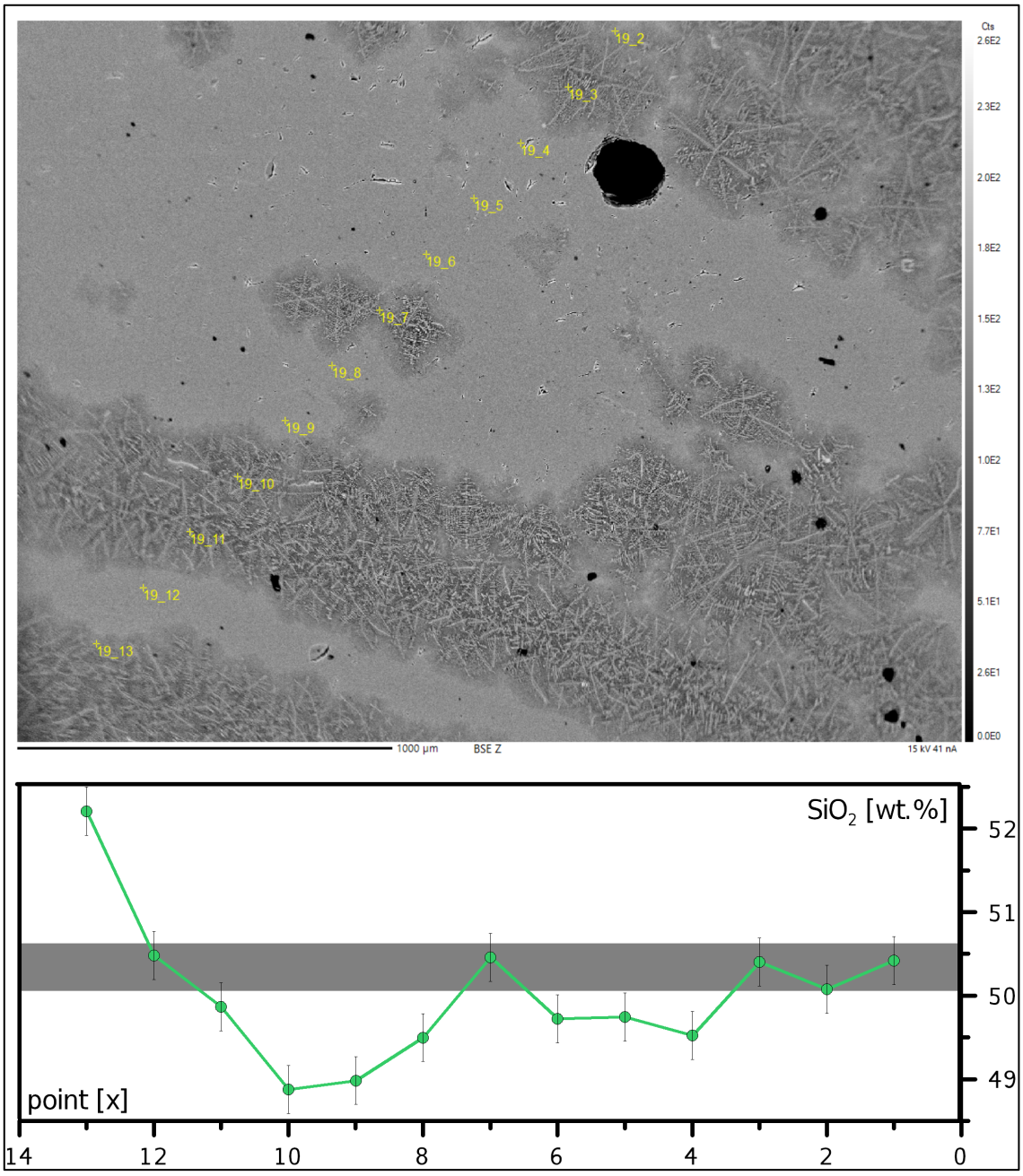

Figure 2.B.4: Transect on section Exp1_5bottom over filaments with and without crystals. Legend: bars = 1σ (standard deviation); grey zone = initial concentration of basaltic end-member (±1σ).

Table 2.B.1: Resume of chemical analysis on basaltic glass prepared in air (KS700_AIR) and in reduced atmosphere (KS700_RED1). Units in wt.%; 1σ = 1 standard deviation; 1σ (%) = 1 standard deviation * 100/oxide concentration; N = number of analysed points; *Z-score*: Z = (concentration1 – concentration2)/square root ($\sigma_1^2 + \sigma_2^2$) → if $-3 < Z < 3$ the values are considered equivalents inside a Z*σ interval (*i.e.*, Gaussian distribution).

	SiO_2	TiO_2	Al_2O_3	Fe_2O_{3t}	MnO	MgO	CaO	Na_2O	K_2O	P_2O_5
KS700_AIR	50.31	3.60	12.88	14.80	0.21	5.00	9.33	2.48	0.92	0.46
σ	0.29	0.12	0.14	0.21	0.06	0.12	0.18	0.10	0.05	0.05
σ (%)	0.57	3.3	1.1	1.4	28	2.3	2.0	4.1	5.8	10
N	30	30	30	30	30	30	30	30	30	30
KS700_RED 1	49.26	3.59	13.09	14.75	0.20	5.21	9.76	2.82	0.92	0.42
σ	0.22	0.09	0.16	0.30	0.05	0.11	0.16	0.09	0.07	0.05
σ (%)	0.45	2.6	1.3	2.0	27	2.0	1.7	3.3	7.2	13
N	14	14	14	14	14	14	14	14	14	14
Z-score	2.9	0.0	-0.9	0.1	0.1	-1.3	-1.8	-2.5	0.1	0.6

Although the presence of crystals can slightly disturb the determined chemistry (*i.e.*, Fe), the two described procedures support the conclusion that the DS do not significantly compromise the analysis, which attend established confidence limits. The strategy of defocusing the current beam to 10 mm and to maintain the current intensity inside the range 5 – 10 nA was sufficient to guarantee the data quality required.

SUPPLEMENTARY MATERIAL

S1 – Normalized variance computation

The supplementary material can be found on the online version.

REFERENCES

Abe, Y. (1997). Thermal and chemical evolution of the terrestrial magma ocean. Physics of The Earth and Planetary Interiors 100, 27–39.

Achterberg (2014). Theory of diffusion and Viscosity, University of Groningen, Neetherlands, pp.427-264, https://www.astro.rug.nl/~weygaert/tim1publication/astrohydro2014/achterberg.ngsa.diffusion_viscosity.pdf , data accessed: 29/04/2022

Alberti, A.; Piccirillo, E.M.; Bellieni, G.; Civetta, L.; Comin-Chiaramonti, P.; Morais, E.A.A. (1992). Mesozoic acid volcanics from southern Angola: petrology, Sr-Nd isotope characteristics and

correlation with the acid stratoid volcanic suites of the Paraná basin (south-eastern Brazil). European Journal of Mineralogy 4, 597–604.

Almeida, J.; Dios, F.; Mohriak, W.U.; Valeriano, C.D.M.; Heilbron, M.; Eirado, L.G.; Tomazzoli, E. (2013). Pre-rift tectonic scenario of the Eo-Cretaceous Gondwana break-up along SE Brazil–SW Africa: insights from tholeiitic mafic dyke swarms. Geological Society, London, Special Publications, 369 (1), 11-40.

Anderson, D.L. (1982). Isotopic evolution of the mantle: the role of magma mixing. Earth and Planetary Science Letters 57 (1), 1–12.

Avramov, I. (2000). Pressure dependence of viscosity of glass forming melts Journal of Non-Crystalline Solids 262, 258–263.

Bateman R. (1995). The interplay between crystallization, replenishment and hybridization in large felsic magma chambers. Earth-Science Reviews 39, 91–106.

Bellieni, B.; Comin-Chiaramonti, P.; Marques, L.S.; Melfi, A.J., Nardy, A.J.R.; Piccirillo, E.M.; Roisenberg, A. (1984). High- and Low-TiO_2 flood basalts from the Paraná plateau (Brazil): petrology and geochemical aspects bearing on their mantle origin. Neues Jahrbuch für Mineralogie-Abhandlungen 150, 273-306.

Blichert-Toft, J.; Lesher, C.E.; Rosing, M.T. (1992). Selectively contaminated magmas of the Tertiary East Greenland macrodike complex. Contributions to Mineralogy and Petrology 110, 154-172.

Borisova, A.Y.; Toutain, J-P; Stefansson, A.; Gouy, S.; de Parseval, Ph. (2012). Processes controlling the 2010 Eyjafjallajökull explosive eruption. Journal of Geophysical Research: Solid Earth, 117, B05202, doi:10.1029/2012JB009213.

Borisova, A.Y.; Toutain, J-P; Dubessy, J.; Pallister, J.; Zwick, A.; Salvi, S. (2014) H2O–CO2–S fluid triggering the 1991 Mount Pinatubo climactic eruption (Philippines). Bulletin of Volcanology 76, 800, doi:10.1007/s00445-014-0800-3.

Brown Jr., G.E; Farges, F.; Calas, G. (1995). X-ray scattering and x-ray spectroscopy studies of silicate melts. In: "Structure, Dynamics, and Properties of Silicate Melts", Jonathan F. Stebbins, Paul F. McMillan and Donald B. Dingwell, editors, 1995, Vol. 32:i-xvi + 616 pg. ISBN: 0-939950-39-1; ISBN: 13 978-0-939950-39-3.

Cáceres, F.; Wadsworth, F.B.; Scheu, B.; Colombier, M.; Madonna, C.; Cimarelli, C.; Hess, K.-U.; Kaliwoda, M.; Ruthensteiner, B.; Dingwell, D.B. (2020). Can nanolites enhance eruption explosivity? Geology 48, 997–1001. https://doi.org/10.1130/G47317.1

Cáceres, F.; Scheu, B.; Colombier, M.; Hess, K.-U.; Feisel, Y.; Ruthensteiner, B.; Dingwell, D.B. (2022). The roles of microlites and phenocrysts during degassing of silicic magma. Earth and Planetary Science Letters 577 (*in press*). DOI: https://doi.org/10.1016/j.epsl.2021.117264

Caricchi, L.; Burlini, L.; Ulmer, P.; Gerya T.; Vassalli, M.; Papale P. (2007). Non-Newtonian rheology of crystal-bearing magmas and implications for magma ascent dynamics. Earth and Planetary Science Letters 264, 402–419.

De Campos, C. P.; Perugini, D.; Ertel-Ingrisch, W.; Dingwell, D. B. & Poli, G. (2011). Enhancement of magma mixing efficiency by chaotic dynamics: an experimental study. Contributions to Mineralogy and Petrology 161, 863–881.

De Rosa, R.; Donato, P.; Ventura, G. (2002). Fractal analysis of mingled/mixed magmas: an example from the Upper Pollara eruption (Salina Island, southern TyrrhenianSea, Italy). Lithos 65, 299–311.

Di Genova, D.; Kolzenburg, S.; Wiesmaier, S.; Dallanave, E.; Neuville, D.R.; Hess, K.-U.; Dingwell, D.B. (2017). A compositional tipping point governing the mobilization and eruption style of rhyolitic magma. Nature 552, 235–238, https://doi.org/10.1038/nature24488.

Di Genova, D.; Brooker, R.A.; Mader, H.M.; Drewitt, J.W.E.; Longo, A.; Deubener, J.; Neuville, D.R.; Fanara, S.; Shebanova, O.; Anzellini, S.; Arzilli, F.; Bamber, E.C.; Hennet, L.; La Spina, G.; Miyajima, N. (2020). In situ observation of nanolite growth in volcanic melt: A driving force for explosive eruptions. Sciences Advances 6 (39).

Dingwell, D. (1986). Viscosity–temperature relationships in the system $Na_2Si_2O_5$–$Na_4Al_2O_5$. Geochimica et Cosmochimica Acta 50, 1261–1265.

Emmanuel, S.; Cortis, A.; Berkowitz, B. (2004). Diffusion in multicomponent systems: a free energy approach. Chemical Physics 302, 21–30.

Ewart, A.; Marsh, J.S.; Milner, S.C.; Duncan, A.R.; Kamber, B.S.; Armstrong, R.A. (2004). Petrology and geochemistry of Early Cretaceous bimodal continental flood volcanism of the NW Etendeka, Namibia. Part 2, characteristics and petrogenesis of the high-Ti latite and high-Ti and low-Ti voluminous quartz latite eruptives. Journal of Petrology 45, 107–138.

Flinders, J. & Clemens, J. (1996). Non-linear dynamics, chaos, complexity and enclaves in granitoid magmas. Earth and Environmental Science Transactions of the Royal Society of Edinburgh 87 (1-2), 217-223. DOI: 10.1017/S0263593300006623

Galaktionov, O.S.; Anderson, P.D.; Peters, G.W.M. (2002). Structure development during chaotic mixing in the journal bearing flow. Physics of Fluids 14, 3009–3017.

Garland F.; Hawkesworth C.J.; Mantovani M.S.M. (1995). Description and petrogenesis of the Paraná rhyolites, Southern Brazil. Journal of Petrology 36 (5), 1193-1227, https://doi.org/10.1093/petrology/36.5.1193

Giordano, D.; Russell, J.K.; Dingwell, D.B. (2008). Viscosity of magmatic liquids: a model. Earth and Planetary Science Letters 271, 123–134. doi:10.1016/j.epsl.2008.03.038

Gomes, A.S. & Vasconcelos, P.M. (2021). Geochronology of the Paraná-Etendeka large igneous province. Earth-Science Reviews 220 (*in press*). https://doi.org/10.1016/j.earscirev.2021.103716

Irvine, T.N. & Baragar, W.R.A. (1971). A guide to the chemical classification of the common volcanic rocks. Canadian Journal of Earth Sciences 8, 523-548.

Janasi, V.A.; Montanheiro, T.J.; Freitas, V.A.; Reis, P.M.; Negri, F.A.; Dantas, F.A. (2007). Geology, petrography and geochemistry of the acid volcanism of the Paraná Magmatic Province in the Piraju-Ourinhos region, SE Brazil. Revista Brasileira de Geociências 37 (4), 745-759.

Janasi, V.A.; Freitas, V.A.; Heaman, L.H. (2011). The onset of flood basalt volcanism, Northern Paraná Basin, Brazil: A precise U–Pb baddeleyite/zircon age for a Chapecó-type dacite. Earth and Planetary Science Letters 302, 147–153.

Jochum, K.P.; Dingwell, D.B.; Rocholl, A.; Stoll, B.; Hofmann, A.W., *et al.* (2000). The preparation and preliminary characterisation of eight geological MPI-DING reference glasses for in situ microanalysis. Geostandard Newsletter 24, 87–133.

Lange, R.A. & Carmichael, I.S.E. (1987). Densities of Na_2O-K_2O-CaO-MgO-FeO-Fe_2O_3-Al_2O_3-TiO_2-SiO_2 liquids: new measurements and derived partial molar properties. Geochimica et Cosmochimica Acta 51, 2931–2946.

Langmuir, C.H.; Vocke, R.D.; Hanson, G.N. (1978). A general mixing equation with applications to Icelandic basalts. Earth and Planetary Science Letters 37 (3), 380–392.

Le Bas, M.J.; Le Maitre, R.W.; Streckeisen, A.; Zannetin, B. (1986). A chemical classification of volcanic rocks based on total alkali-silica diagram. Journal of Petrology 27, 745-750.

Lee, B.-J.; Lee, C.S.; Lee, J.C. (2003). Stress induced crystallization of amorphous materials and mechanical properties of nanocrystalline materials: a molecular dynamics simulation study. Acta Materialia 51, 6233–6240.

Leonard, G.; Cole, J.; Nairn, I.; Self, S. (2002). Basalt triggering of the c. AD 1305 Kaharoa rhyolite eruption, Tarawera Volcanic Complex, New Zealand. Journal of Volcanology and Geothermal Research 115, 461–486.

Lesher, C.E. (1990). Decoupling of chemical and isotopic exchange during magma mixing. Nature 344, 235-237.

Liu, M.; Peskin R.L.; Muzzio F.J.; Leong C.W. (1994). Structure of the stretching field in chaotic cavity flows. American Institute of Chemical Engineers Journal 40, 1273–1286.

Liu, W. & Haller, G. (2004). Strange eigenmodes and decay of variance in the mixing of diffusive tracers. Physica D 188, 1–39.

Luchetti, A.C.F.; Gravley, D.M.; Gualda, G.A.R.; Nardy, A.J.R. (2018a). Textural evidence for high-grade ignimbrites formed by low-explosivity eruptions, Paraná Magmatic Province, southern Brazil. Journal of Volcanology and Geothermal Research 355, 87–97.

Luchetti, A.C.F.; Nardy, A.J.R.; Madeira, J.E.O. (2018b). Silicic High-Grade to Extremely High- Grade Ignimbrites and Associated Deposits from Paraná Magmatic Province, Southern Brazil. Journal of Volcanology and Geothermal Research 355, 270–286.

Machado, F.B.; Rocha-Júnior, E.R.V.; Marques, L.S.; Nardy, A.J.R.; Zezzo, L.V.; Marteleto, N.S. (2018). Geochemistry of the Northern Paraná Continental Flood Basalt (PCFB) Province: implications for regional chemostratigraphy**.** Brazilian Journal of Geology 48 (2), 177-199. DOI: 10.1590/2317-4889201820180098

Mantovani, M.S.M.; Marques, L.S.; Sousa, M.A. de; Atalla, L.T.; Civetta, L.; Inoccenti I, F. (1985). Trace element and strontium isotope constraints on the origin and evolution of the Paraná Continental flood basalts of Santa Catarina State (Southern Brazil). Journal of Petrology 26, 187-209.

Marques, L.S., Piccirilo, E.M., Melfi, A.J., Comin-Chiaramonti, P., and Bellieni, G. (1989). Distribuição de terras raras e outros elementos traços em basaltos da Bacia do Paraná, Geochimica Brasiliensis 3, 33–50.

Marsh, J.S.; Ewart, A.; Milner, S.C.; Duncan, A.R.; Miller, R. McG. (2001). The Etendeka Igneous Province: magma types and their stratigraphic distribution with implications for the evolution of the Paraná-Etendeka flood basalt province. Bulletin of Volcanology 62, 464–486.

Marsh, J.S. & Swart, R. (2018). The Bero Volcanic Complex: Extension of the Paraná-Etendeka Igneous Province into SW Angola. Journal of Volcanology and Geothermal Research 355, 21-31.

Morgavi, D.; Perugini, D.; De Campos, C.; Ertel-Ingrisch, W.; Lavallée, Y.; Morgan, L.; Dingwell, D. (2013a). Interactions between rhyolitic and basaltic melts unraveled by chaotic mixing experiments. Chemical Geology 346, 199–212.

Morgavi, D.; Perugini, D.; De Campos, C.; Ertel-Ingrisch, W.; Dingwell, D. (2013b). Time evolution of chemical exchanges during mixing of rhyolitic and basaltic melts. Contributions to Mineralogy and Petrology 166, 615–638.

Morgavi, D.; Laumonier, M.; Petrelli, M.; Dingwell, D.B. (2022). Magma Mixing in Igneous Systems , EGU General Assembly 2022, Vienna, Austria, 23–27 May 2022, EGU22-6510, https://doi.org/10.5194/egusphere-egu22-6510, 2022.

Mysen, B.O.; Virgo, D.; Seifert, F.A. (1982). The Structure of Silicate Melts: Implications for Chemical and Physical Properties of Natural Magmas. Reviews of Geophysics and Space Physics 20 (3), 353–383.

Nardy, A.J.R.; Machado, F.B.; Oliveira, M.A.F. (2008). As rochas vulcânicas mesozoicas ácidas da Bacia do Paraná: litoestratigrafia e considerações geoquímico-estratigráficas. Revista Brasileira de Geociências 38 (1), 178–195.

Ottino, J.M. (1989). The kinematics of mixing: stretching, chaos and transport. Cambridge University Press, Cambridge.

Peate, D.W.; Hawkesworth, C.J.; Mantovani, M.S.M. (1992). Chemical stratigraphy of the Paraná lavas, South America: classification of magma types and their spatial distribution. Bulletin of Volcanology 55, 119-139.

Peate, D.W. (1997). The Paraná-Etendeka Province. In: J Mahoney & M Coffin (eds), Large Igneous Provinces: Continental, Oceanic, and Planetary Flood Volcanism. AGU Geophysical Monograph 100, 217-245.

Perugini, D. & Poli, G. (2000). Chaotic dynamics and fractals in magmatic interaction processes: a different approach to the interpretation of mafic microgranular enclaves. Earth and Planetary Science Letters 175, 93–103.

Perugini, D.; Busa, T.; Poli, G.; Nazzareni, S. (2003a). The role of chaotic dynamics and flow fields in the development of disequilibrium textures in volcanic rocks. Journal of Petrology 44, 733–756.

Perugini, D.; Poli, G.; Mazzuoli, R. (2003b). Chaotic advection, fractals and diffusion during mixing of magmas: evidence from lava flows. Journal of Volcanology and Geothermal Research 124, 255–279.

Perugini, D.; Petrelli, M.; Poli, G. (2006). Diffusive fractionation of trace elements by chaotic mixing of magmas. Earth and Planetary Science Letters 243, 669–680, doi:10.1016/j.epsl.2006.01.026

Perugini, D.; Petrelli, M.; Poli, G.; De Campos, C.; Dingwell, D.B. (2010). Time-scales of recent phlegrean fields eruptions inferred from the application of a 'diffusive fractionation' model of trace elements. Bulletin of Volcanology 72, 431–447.

Perugini, D.; De Campos, C.P.; Ertel-Ingrisch, W.; Dingwell, D.B. (2012). The space and time complexity of chaotic mixing of silicate melts: implications for igneous petrology. Lithos 155, 326–340.

Perugini, D.; De Campos, C.P.; Petrelli, M. & Dingwell, D. (2015). Concentration variance decay during magma mixing: a volcanic chronometer. Scientific Reports 5, 14225.

Piccirillo, E.M.; Raposo, M.I.B.; Melfi, A.J.; Comin-Chiaramonti, P.; Bellieni, B.; Cordani, U.G.; Kawashita, K. (1987). Bimodal fissural volcanic suites from the Paraná Basin (Brazil): K-Ar age, Sr-isotopes and geochemistry. Geochimica Brasiliensis 1, 53-69.

Piccirillo, E. M. & Melfi, A. J. (1988). The Mesozoic flood volcanism of the Paraná Basin: petrogenetic and geophysical aspects. São Paulo, Brazil. IAG, University of São Paulo (ed.). 600p.

Pouchou, L. & Pichoir, F. (1984). A new model for quantitative X-ray microanalysis: part i: applications to the analysis of homogeneous samples. Recherche Aerospatiale 3, 13–38.

Prazeres-Filho, H.J.; Harara, O.M.; Basei, M.A.S.; Passarelli, C.R.; Siga Jr., O. (2003). Litoquímica, Geocronologia U-Pb e Geologia Isotópica (Sr-Nd-Pb) das Rochas Graníticas dos Batólitos Cunhaporanga e Três Córregos na Porção Sul do Cinturão Ribeira, Estado do Paraná. São Paulo, Geologia USP Série Científica 3, 51-70.

Rasband, W.S. (2016). ImageJ. U. S. National Institutes of Health. http://rsb.info.nih.gov/nih-image, data accessed: 29/04/2022

Rocha-Júnior, E.R.V.; Marques L.S.; Babinski, M.; Nardy, A.J.R.; Figueiredo, A.M.G.; Machado, F.B. (2013). Sr-Nd-Pb isotopic constraints on the nature of the mantle sources involved in the genesis of the high-Ti tholeiites from northern Paraná Continental Flood Basalts (Brazil). Journal of South American Earth Sciences 46, 9-25.

Rodrigues, S.W.O.; Caltabeloti, F.P.; Almeida, V.V.; Brumati, M.; Archanjo, C.J.; Hollanda, M.H.B.M.; Salazar, C.A.; Liu, D. (2011). Petrography, Geochemistry and Geochronology of the Patrimônio Santo Antônio and São Domingos Granites (Cunhaporanga Granitic Suite, Paraná, Southeast Brazil). São Paulo, Geologia USP Série Científica 11 (3), 03-21.

Rosing, M.T.; Lesher, C.E; Bird, D.K. (1989). Chemical modification of east Greenland Tertiary magmas by two-liquid interdiffusion. Geology 17, 626-629.

Rossi, S.; Petrelli, M.; Morgavi, D.; González-García, D.; Fischer, L.A.; Vetere, F.; Perugini, D. (2017). Exponential decay of concentration variance during magma mixing: Robustness of a volcanic chronometer and implications for the homogenization of chemical heterogeneities in magmatic systems. Lithos 286–287, 396–407.

Rothstein, D.; Henry, E.; Gollub, J.P. (1999). Persistent patterns in transient chaotic fluid mixing. Nature 401, 770–772.

Russell, J.K. (1990). Magma mixing processes: insights and constraints from thermodynamic calculations. Reviews in Mineralogy and Geochemistry 24 (1), 153–190.

Shannon, R.D. (1976). Revised effective ionic radii and systematic studies of interatomic distances in halides and chalcogenides. Acta Crystallographica Section A 32, 751–767.

Swanson, P.D. & Ottino, J.M. (1990). A comparative computational and experimental study of chaotic mixing of viscous fluids. Journal of Fluid Mechanics 213, 227–249.

Tomiya, A.; Miyagi, I.; Saito, G.; Gesh, N. (2013). Short time scales of magma-mixing processes prior to the 2011 eruption of Shinmoedake volcano, Kirishima volcanic group, Japan. Bulletin of Volcanology 75, 750, DOI:10.1007/s00445-013-0750-1.

Waight, T.E. & Lesher, C.E. (2010). Pb isotopes during crustal melting and magma mingling — A cautionary tale from the Miki Fjord macrodike, central east Greenland. Lithos, 118, 191–201.

CHAPTER 3 – THE BEHAVIOUR OF TRACE ELEMENTS IN CHAOTIC MIXING EXPERIMENTS

3.1 INTRODUCTION

This chapter presents and discusses the results from using laser ablation-inductively coupled plasma-mass spectroscopy (LA-ICP-MS or simply ICP) on the experimental glasses from chaotic mixing experiments 1, 2 and 3. The analyzed sections were described in detail in section 2 *"Contamination of basalt through silicic melts: The first chaotic dynamics experiments with Paraná-Etendeka starting materials"*. Experimental conditions are T_{exp} = 1,350 °C, at atmospheric pressure. These are believed to mimic the most relevant natural conditions for shallower magmatic systems (i.e., viscosities).

The main objectives are: (1) to investigate the diffusive behaviors of trace elements under chaotic dynamics, correlating the results to major element diffusivity presented by Vicentini et al. (2023); and (2) to assess the influence of different contaminants with varying compositional gradients on the same basaltic melt. The possible implications of this study are discussed for the genesis of Chapecó dacites from PEMP.

3.2 METHODS

Concentration profiles of 34 trace elements (Mg, Al, Ca, Sc, Ti, V, Mn, Ga, Rb, Sr, Y, Zr, Nb, Cs, Ba, La, Ce, Pr, Nd, Sm, Eu, Gd, Tb, Dy, Ho, Er, Tm, Yb, Lu, Hf, Ta, Pb, Th and U) in the glasses were obtained at the Department of Physics and Geology, University of Perugia. The instrumentation consisted in a Teledyne Photon Machine G2 laser ablation device equipped with the two-volume HelEx 2 cell coupled to a Thermo Fischer Scientific iCAP Q quadrupole mass spectrometer (Petrelli et al., 2016a). A circular 20 μm spot size and 25 μm spot spacing was used. Ablation times were 25 s per spot, preceded by a 25 s background measurement and followed by 25 s of washout. Analytical precision is about 12% for concentrations close to 0.1 μg/g and better than

5% above 20 μg/g; accuracy is always better than 10% (Petrelli et al., 2016b). Table 3.1 shows the starting composition of samples used in chaotic mixing experiments.

3.2 RESULTS

The focus of this section is the trace element analysis based on LA-ICP-MS data (referred as ICP). Figure 3.1 shows representative ICP and EPMA data to confirm the coherence between the surveys. Titanium transects indicate the same filaments (represented by vertical bars) were crossed, thus the same patterns are expected. In order to minimize any bias and to avoid artefacts, Ti data is expressively pointed to correlate LA-ICP-MS and EPMA datasets whether the correspondence between them is convenient.

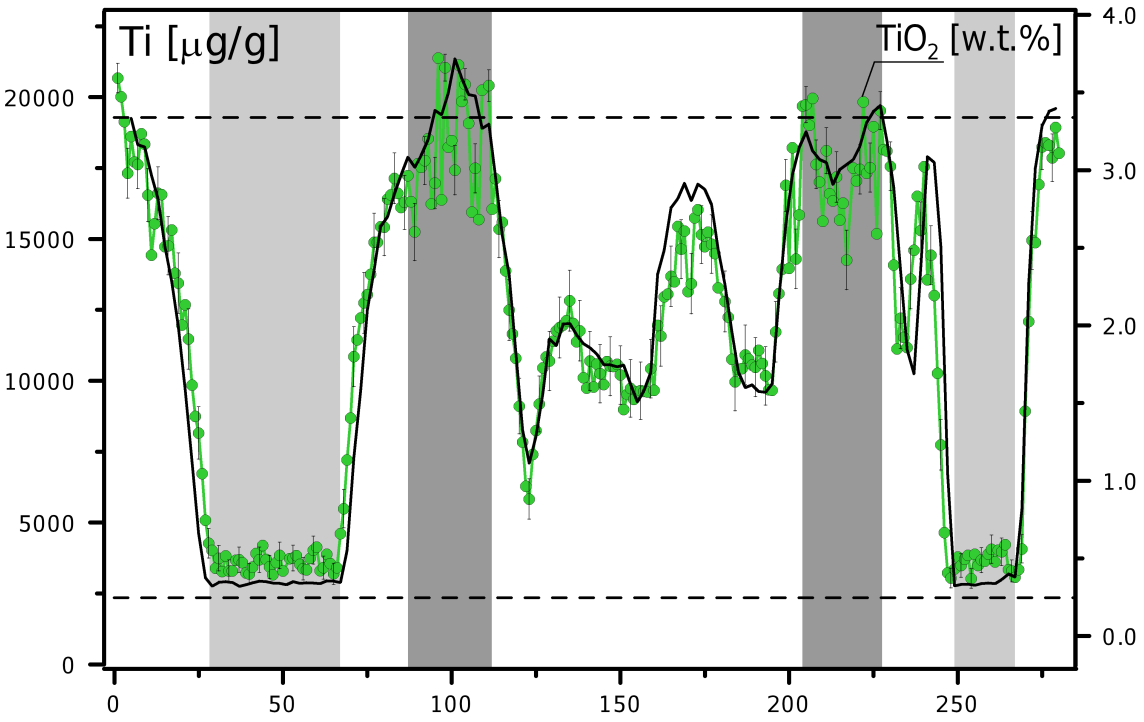

Figure 3.1: representative Ti transects from Exp2 comparing EPMA (green) and LA-ICP-MS (black) data. Legend: vertical bars indicate rhyolitic (light grey) and basaltic (dark grey) filaments; dashed lines indicate the starting composition; left scale represents LA-ICP-MS investigation (in μg/g); right scale represents EPMA investigation (in wt.%).

Table 3.1: starting compositions of end-members used in chaotic mixing experiments. Oxides were determined by EPMA (Vicentini et al., 2023) and are given in [wt.%]. Trace elements were obtained by LA-ICP-MS and are given in [µg/g] and the atomic mass *m* is included for each ion.

Elem/Sample	*m*	LMC-018	LMC-020	LMC-027	KS-700
SiO_2	-	72.96	70.64	76.55	50.31
TiO_2	-	0.26	0.44	0.14	3.6
Al_2O_3	-	14.77	14.9	12.48	12.88
Fe_2O_{3t}	-	1.79	2.75	1.87	14.8
MnO	-	0.05	0.05	0.02	0.21
MgO	-	0.27	0.84	0.12	5
CaO	-	1.32	2.14	0.65	9.33
Na_2O	-	3.11	2.96	2.7	2.48
K_2O	-	5.43	5.08	5.43	0.92
P_2O_5	-	0.03	0.19	0.03	0.46
Mg	24	1504	4745	680	28267
Al	27	81703	82403	69800	71470
Ca	42	8634	13657	4441	63310
Sc	45	16.56	17.02	17.56	37
Ti	47	1311	2346	814	19280
V	51	8.09	33.94	1.64	455.47
Cr	52	4.04	5.16	1.3	50
Mn	55	281	400	115	1646
Ni	60	9.18	1.47	7.55	55.07
Ga	71	19.54	19.02	22.14	22.36
Rb	85	330.1	196.7	305.1	15.8
Sr	88	128.9	355.3	33.9	459.9
Y	89	49.93	13.66	95.23	28.88
Zr	90	1322.7	178.4	2127.7	212.2
Nb	93	23.86	12.33	25.44	18.22
Cs	133	8.98	4.49	5.36	0.19
Ba	137	399.3	812.7	156.2	393.4
La	139	71.07	50.3	157.83	29.97
Ce	140	123.5	95.9	244.5	63.5
Pr	141	11.71	9.8	30.68	7.81
Nd	146	39.82	36.6	116.03	35.56
Sm	147	6.87	6.36	20.7	7.82
Eu	153	0.72	1.25	1.11	2.58
Gd	157	5.57	4.64	19.59	7.38
Tb	159	0.81	0.55	2.85	1.05
Dy	163	4.83	2.8	16.41	6.07
Ho	165	0.99	0.49	3.31	1.15
Er	166	2.92	1.28	8.81	2.99
Tm	169	0.48	0.18	1.25	0.39
Yb	173	3.46	1.17	8.32	2.62
Lu	175	0.56	0.17	1.27	0.37
Hf	178	33.65	5.06	52.98	5.69
Ta	181	3.59	1.04	1.96	1.21
Pb	208	53.3	22.84	34.19	4.13
Th	232	45.16	16.2	35.42	2.76
U	238	10.3	2.66	6.85	0.57

The elemental transects in Figures 3.2 – 3.4 depict single point analyses normalized by the basaltic starting composition. Areas that represent rhyolitic filaments are characterized by a plateau that reaches up to dozens of times the basaltic starting composition (e.g., Cs and Rb). Filaments with basaltic compositions are represented by smooth arcs that might achieve the unit in some cases (e.g., Ba in Exp1 and Exp3, Y in Exp2 and Exp3). Nevertheless, these arcs are clearly smoother and larger compared to those from major oxides (e.g., Ti curve in black), indicating different chemical exchange rates (i.e., diffusivities). An additional evidence of diffusion is the presence of data points with intermediate compositions between the two end-members forming asymmetric sigmoidal (S-shape) curves. They develop between adjacent filaments over all transects presenting slopes that vary according to the element. These features are more pronounced than those observed for major oxides in the same experimental glasses (Vicentini et al., 2023).

The vast majority of elemental transects reveal a peculiar emerging feature at the interfaces between the end-members: centred at the boundary we observe a marked deep minimum (rhyolitic side) followed by a comparatively wider and weaker maximum peak (basaltic side). With the exception of the trace elements (group referred as G1) V, Sc, Sr, Cs, Rb, U and Th, besides Ti, Mg, Ca and Mn (major/minor elements), the following elements show this behaviour (referred as G2): Ga, Nb, Zr, Y, Ba, REE, Ta, Hf and Pb, also Al (major element). Few experimental studies (e.g., Sato 1975; Watson, 1982; Richter, 1993; Lesher, 1994; González-Garcia et al., 2018) registered and modelled the same phenomenon, named uphill diffusion. It is defined as diffusion against the concentration gradient. However, such studies were developed in less complex scenarios than we simulated here.

Regarding the ICP investigations, elements Ni and Cr present similarities with G1. However, their low initial concentrations on felsic phases (see Table 3.1) resulted in a higher dispersion along transects and in a lack of determinations at several points along rhyolitic filaments. Therefore, they are not considered in the discussions.

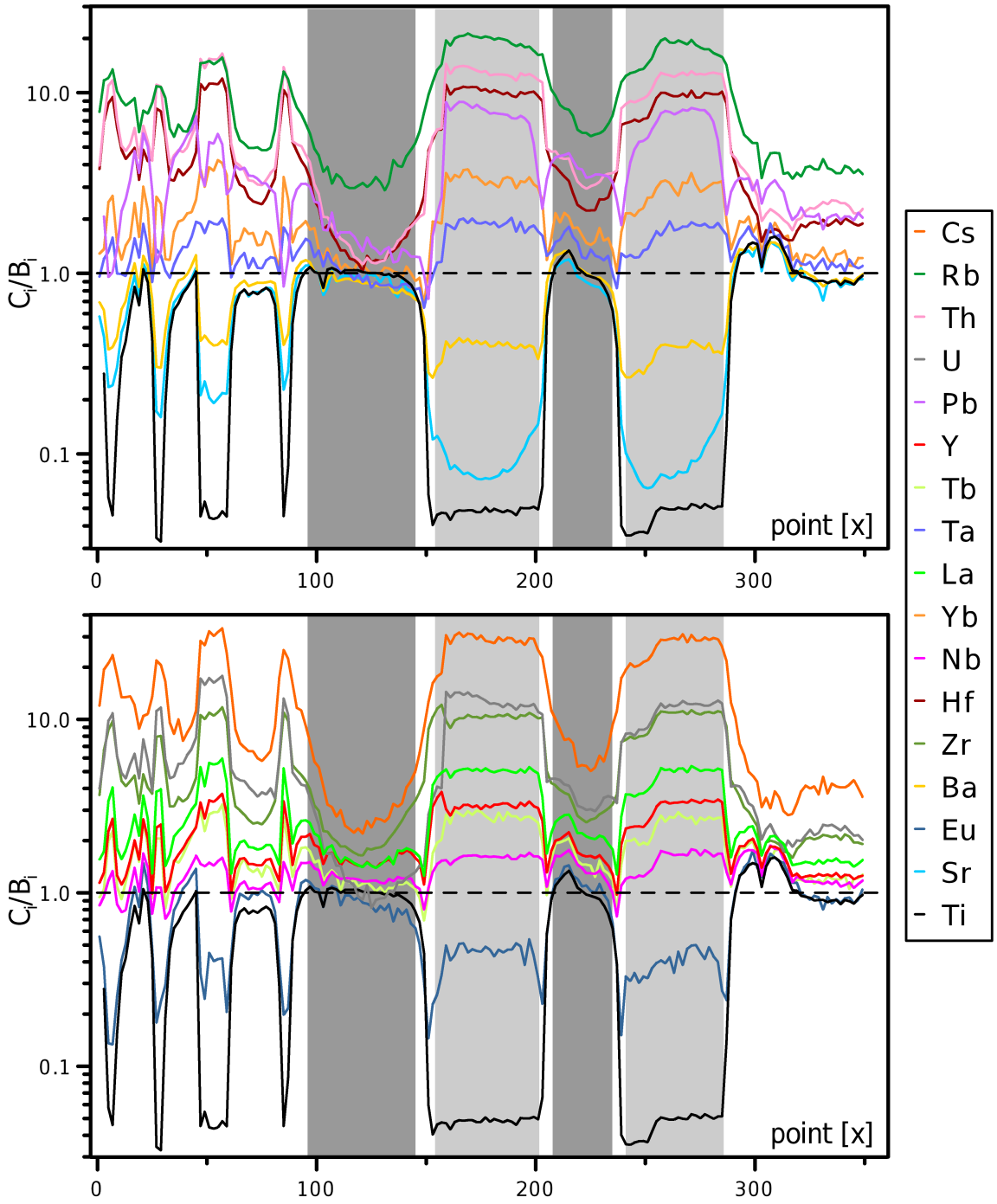

Figure 3.2: transects of 16 representative trace elements in Exp1. The concentrations C_i are normalized to the starting concentration B_i of KS-700 basaltic glass. Black line corresponds to Ti that is used as reference. Vertical bars indicate rhyolitic (light grey) and basaltic (dark grey) filaments crossed over LA-ICP-MS profiles.

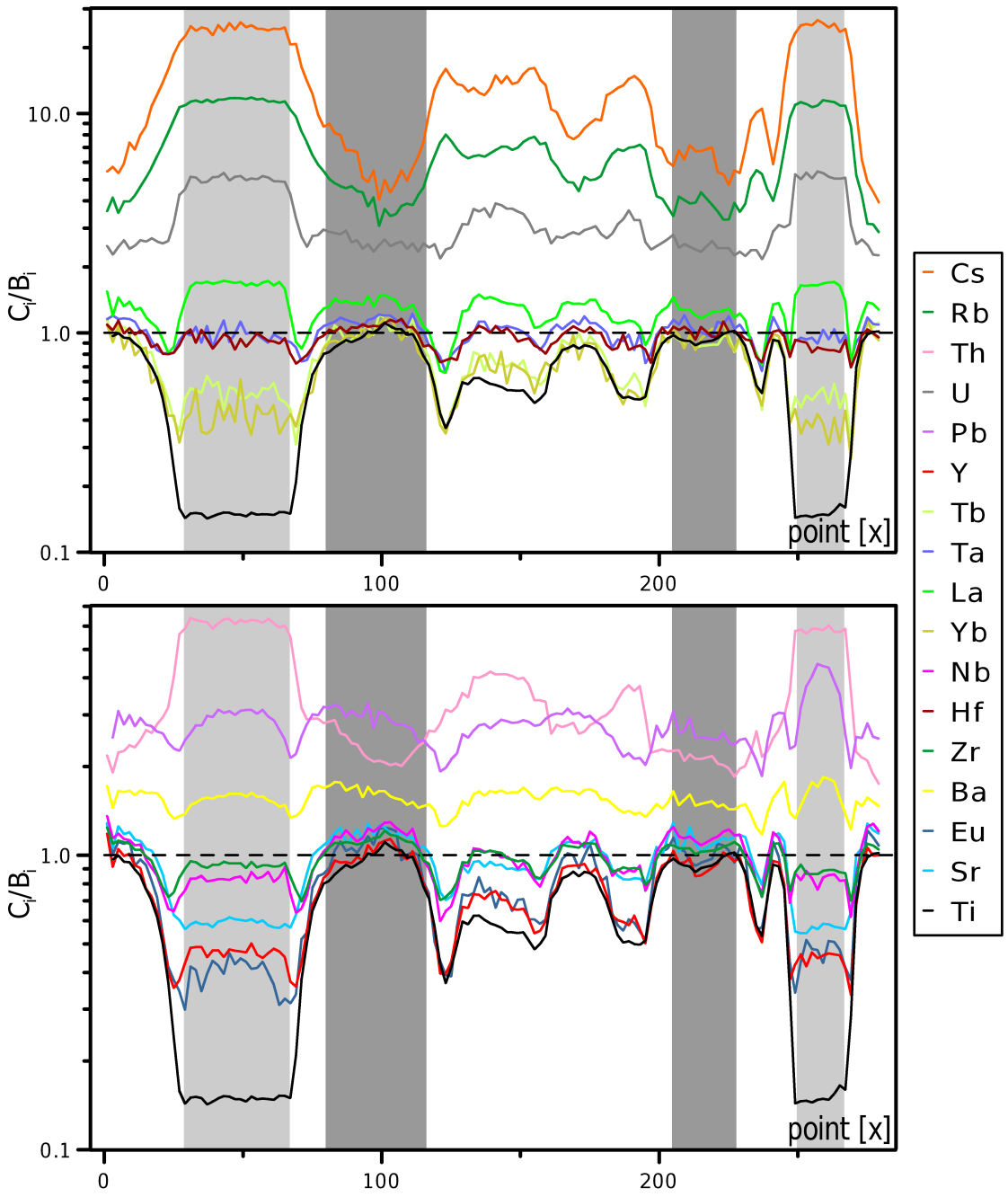

Figure 3.3: transects of 16 representative trace elements in Exp2. The concentrations C_i are normalized to the starting concentration B_i of KS-700 basaltic glass. Black line corresponds to Ti that is used as reference. Vertical bars indicate rhyolitic (light grey) and basaltic (dark grey) filaments crossed over LA-ICP-MS profiles.

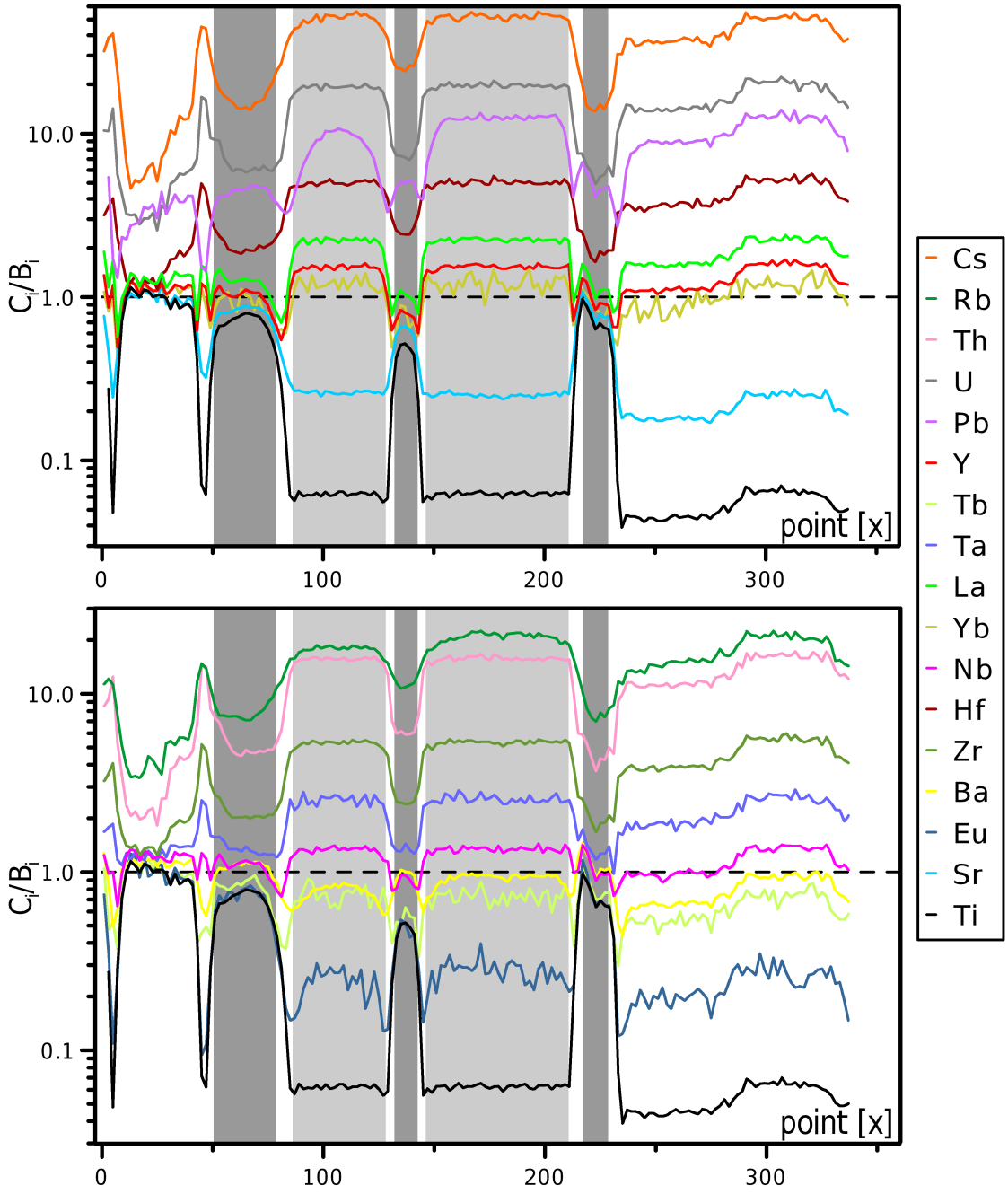

Figure 3.4: transects of 16 representative trace elements in Exp3. The concentrations C_i are normalized to the starting concentration B_i of KS-700 basaltic glass. Black line corresponds to Ti that is used as reference. Vertical bars indicate rhyolitic (light grey) and basaltic (dark grey) filaments crossed over LA-ICP-MS profiles.

Variation diagrams in Figure 3.5 illustrate how data are correlated. The colour curves (yellow for Exp1 and blue for Exp3) link the analyzed points in sequence (i.e., point #1, point #2, etc.) for a representative experiment, which emphasizes a generic alignment in plots. In addition, it highlights parallel curves representing basaltic

filaments that lost its original composition (e.g., “Th vs Rb” in Exp1), in agreement with the arcs described in Figures 3.2 – 3.4. Using elements from the same group, plots are straight lines that might show some deviation of the linear trend depending on the diffusivity contrast. This result stands independently of G1 (e.g., “Th vs Rb”, “U vs Cs”) or G2 pairs (e.g., “Ta vs REE”). The effect of uphill diffusion is visible on diagrams of “G1 vs G2” type, as exemplified by “Sr vs Sm”, “U vs Lu”, “Sc vs Nb” and “Rb vs Pb”. The trend changes along the curve, varying part-to-part from non-linear trends (first half of “Rb vs Pb”) to positive/negative correlation (“Sr vs Sm”).

Taking into account the relation between trace and major elements, similar patterns are observed. Figure 3.6 shows a positive correlation on “Ti vs Sc” diagram (G1), whilst “Ti vs Y” and “Mg vs Ce” (G2 vs G1) portray different slopes along the curve. It includes parallel trends on basaltic-intermediate regions (higher Mg contents). “Mg vs U” presents more dispersion in basaltic-intermediate side and a clear alignment in the rhyolitic portion. Notice that diagrams of Fig 3.6 use data from ICP analyses, which present major elements as ions. In this case, the concentrations are given in μg/g as well.

Figures 3.7 – 3.9 display the correlation matrix (maps) for all analyzed elements from each experiment and the respective colour-coded bar associated to correlation coefficients r^2 values. As closer to unit a given r^2 value is, more correlated is that pair. Histograms of r^2 are also included. Correlation matrices present data on major and minor oxides from EPMA analyses, discussed separately though.

The maps demonstrate systematic differences between following groups: i) pairs of oxides determined by EPMA; ii) couple of trace elements with mass $m < 70$ determined by ICP (i.e., Mg to Mn); and iii) elements with mass $m > 70$ determined by ICP (i.e., Ga to U). The oxides present a general good correlation between each other independently of the experiment, with the exception of Al_2O_5 and Na_2O. Group ii) shows the same result and reinforces Al behaviour (i.e., strongly uncorrelated to other elements). Group iii) indicates higher r^2 values inside the intervals: Ga to Ba, REE (excepted for Eu, which correlates better with Ga to Ba), and Hf to U. In general, r^2 are lower when elements from different groups are compared (i.e., “i) vs. ii)”, “iii) vs. i)”, etc.).

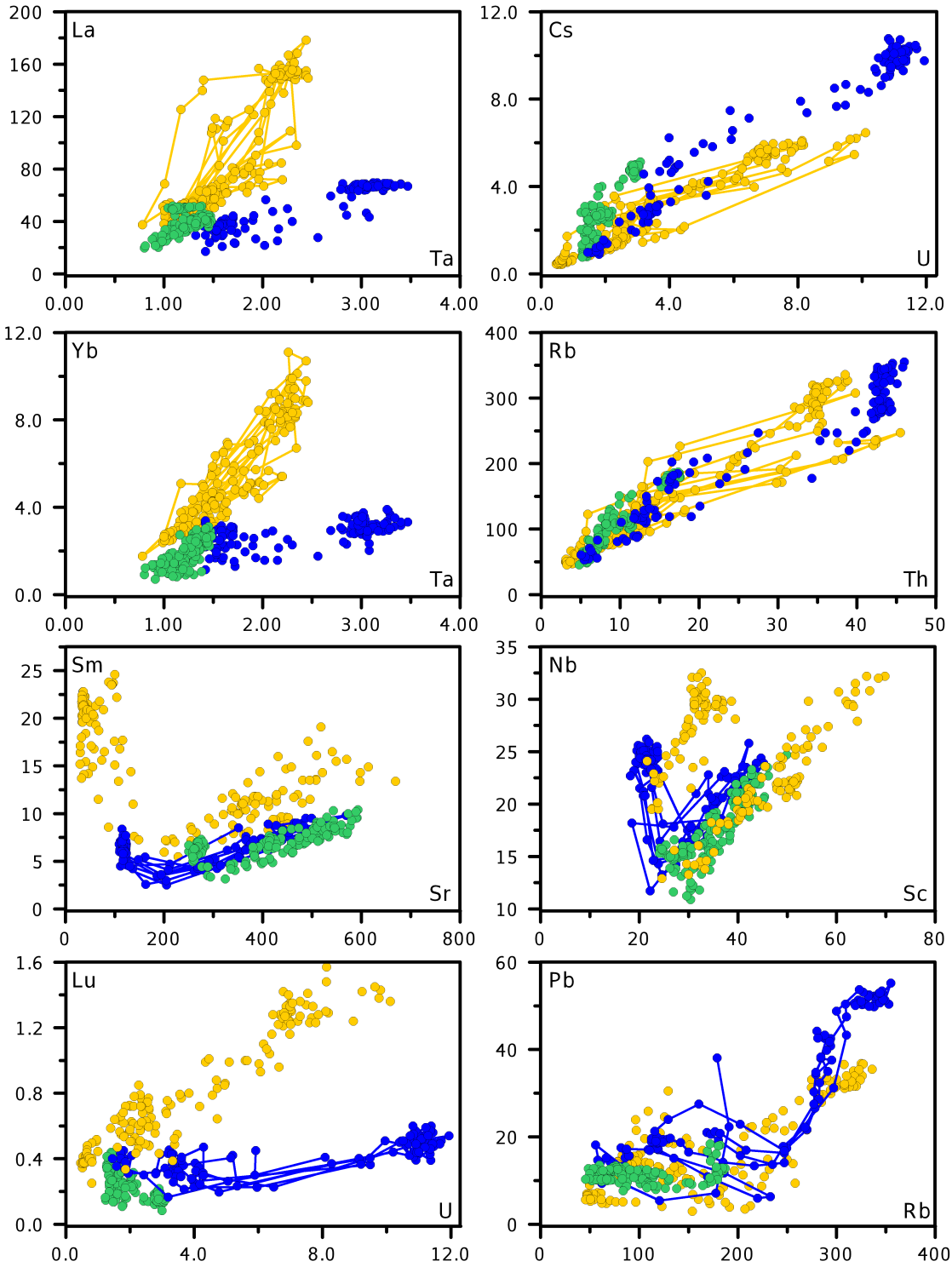

Figure 3.5: representative variation diagrams of trace elements obtained by ICP analyses. Concentrations are given in µg/g. Legend: yellow = Exp1; green = Exp2; blue = Exp3; lines = analytical points linked in sequence (point#1, point#2, etc.).

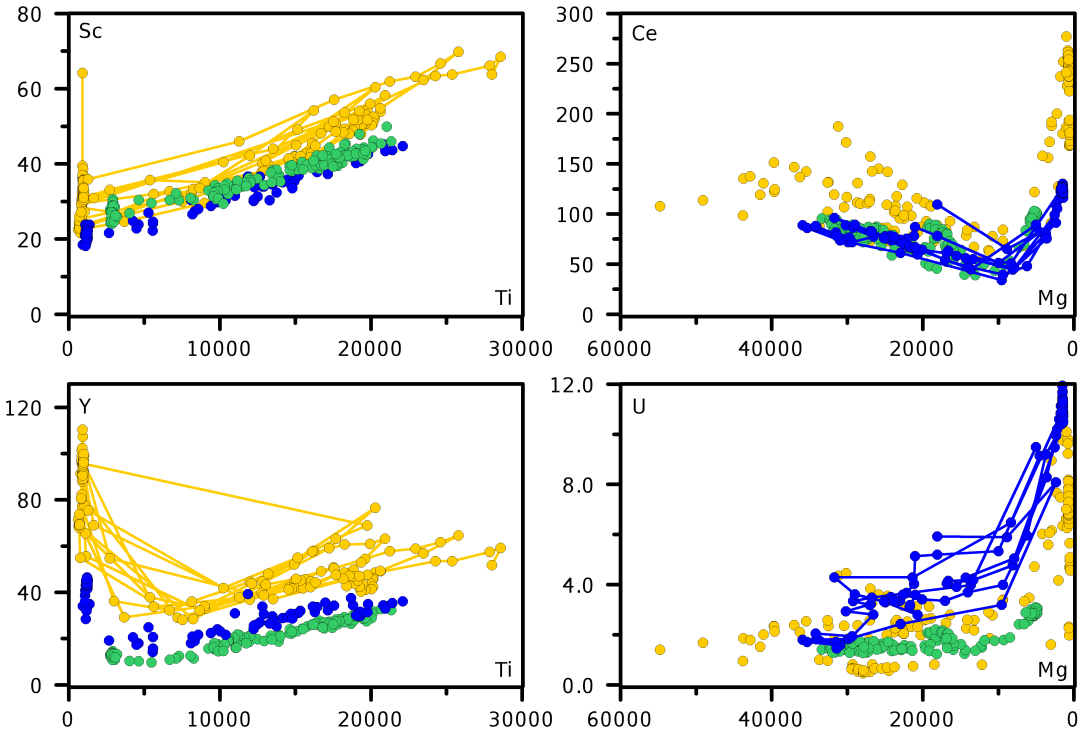

Figure 3.6: representative variation diagrams of "trace vs major" elements obtained by ICP analyses. Concentrations are given in µg/g including for major elements. Legend: yellow = Exp1; green = Exp2; blue = Exp3; lines = analytical points linked in sequence (point#1, point#2, etc.).

Figure 3.7: correlation matrix CM of experiment 1. Colour-coded bar indicates r^2 values for a given couple. Histogram indicates the relative distribution of r^2, with calculated average at $r^2 = 0.52 \pm 0.30$.

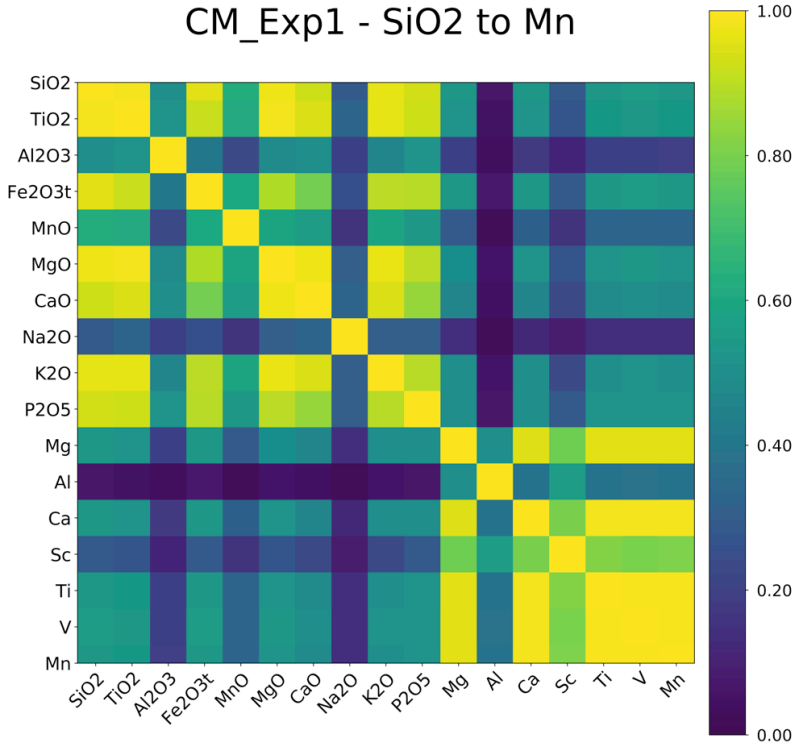

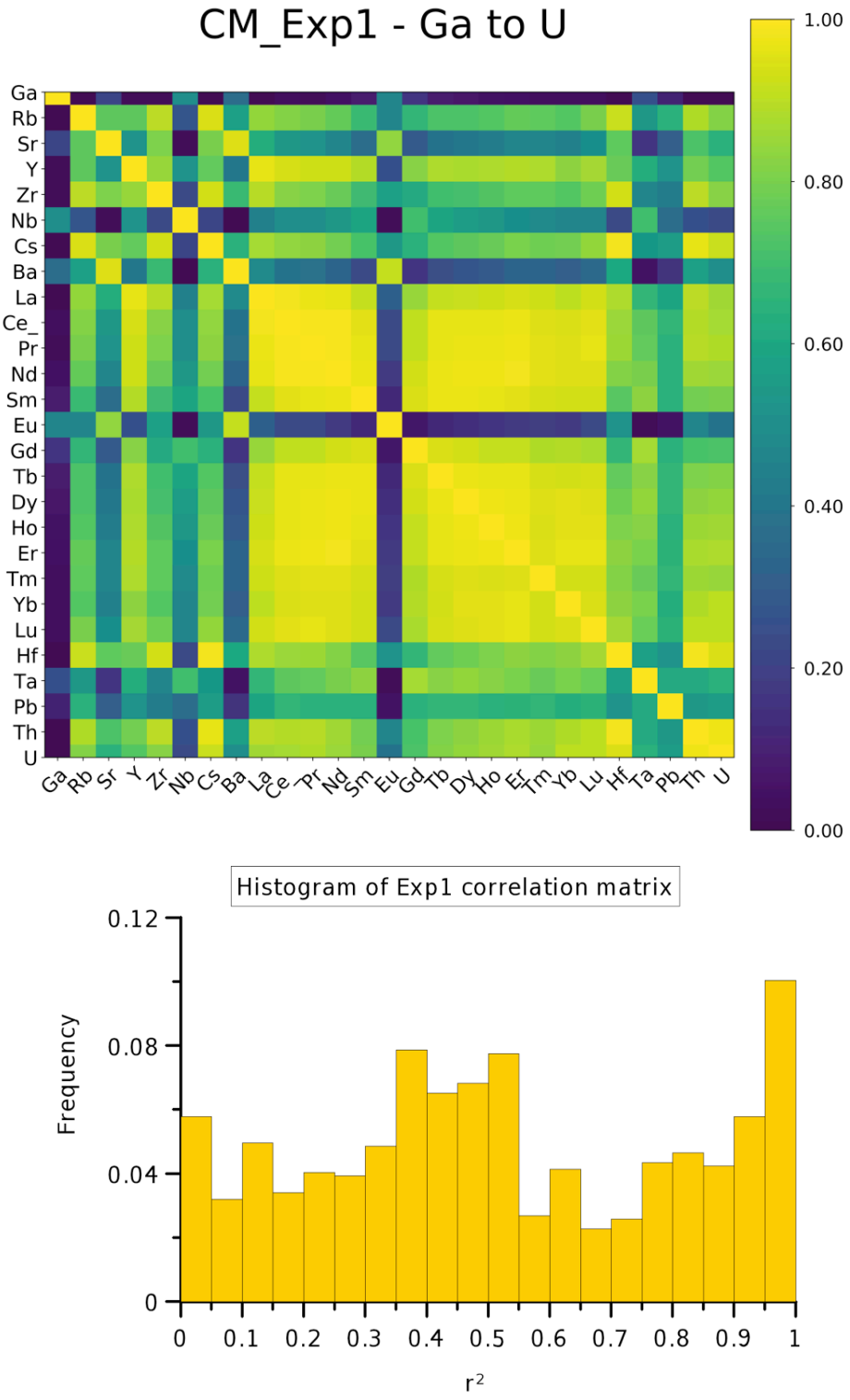

Figure 3.8: correlation matrix CM of experiment 2. Colour-coded bar indicates r^2 values for a given couple. Histogram indicates the relative distribution of r^2, with calculated average at $r^2 = 0.51 \pm 0.32$.

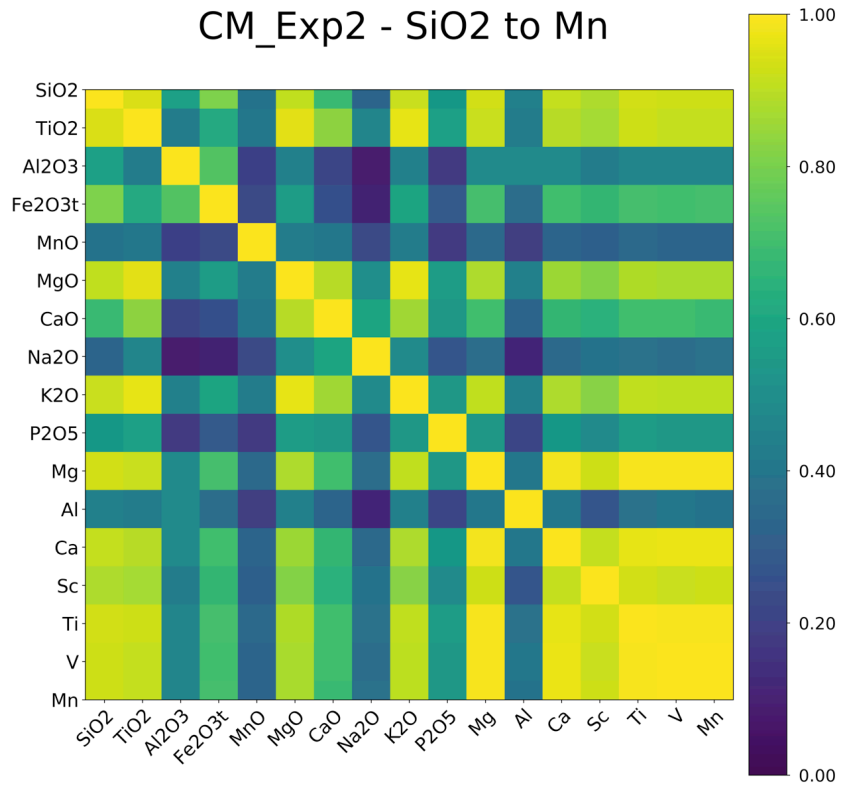
CM_Exp2 - SiO2 to Mn
SiO2
TiO2
Al2O3
Fe2O3t
MnO
MgO
CaO
Na2O
K2O
P2O5
Mg
Al
Ca
Sc
Ti
V
Mn
1.00
0.80
0.60
0.40
0.20
0.00

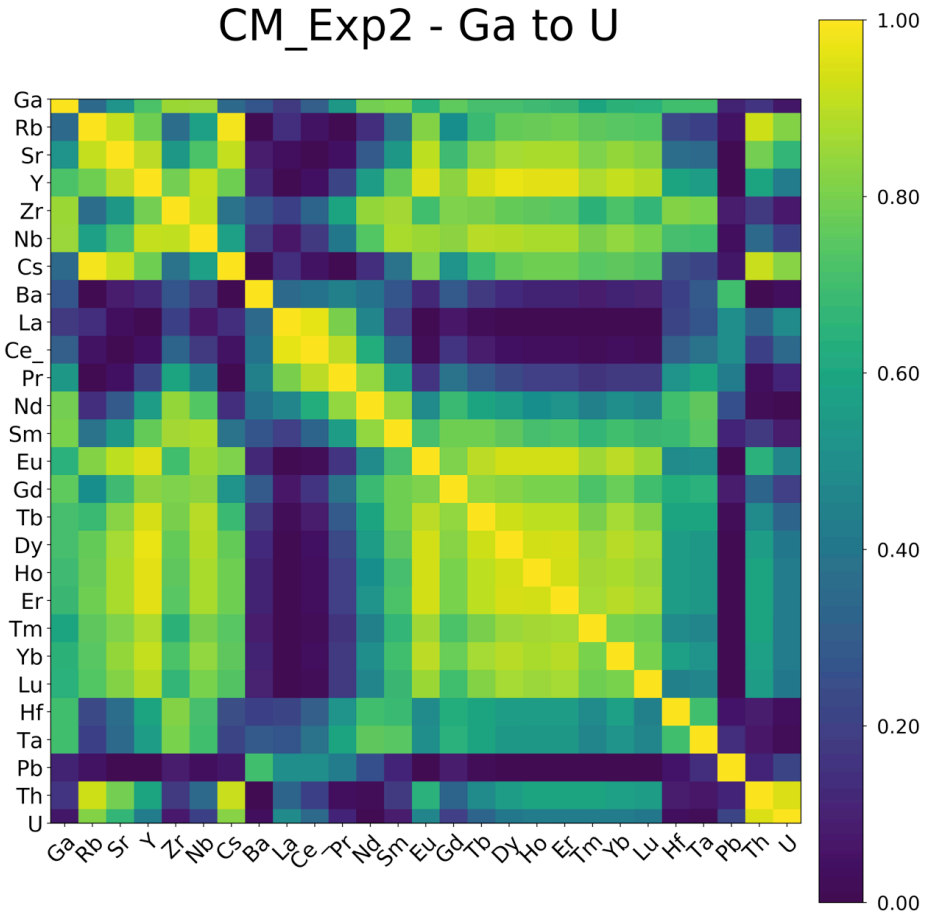
CM_Exp2 - Ga to U
Ga
Rb
Sr
Y
Zr
Nb
Cs
Ba
La
Ce_
Pr
Nd
Sm
Eu
Gd
Tb
Dy
Ho
Er
Tm
Yb
Lu
Hf
Ta
Pb
Th
U
1.00
0.80
0.60
0.40
0.20
0.00

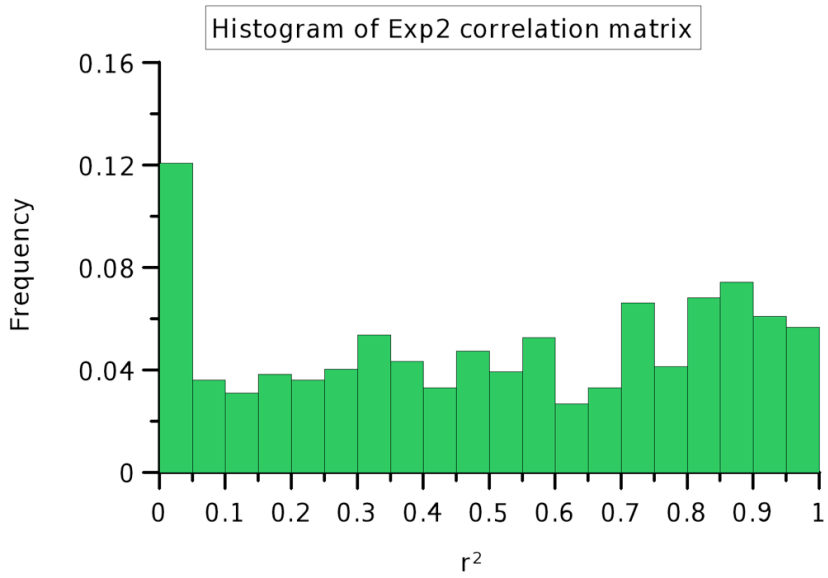

Figure 3.9: correlation matrix CM of experiment 3. Colour-coded bar indicates r^2 values for a given couple. Histogram indicates the relative distribution of r^2, with calculated average at $r^2 = 0.43 \pm 0.32$.

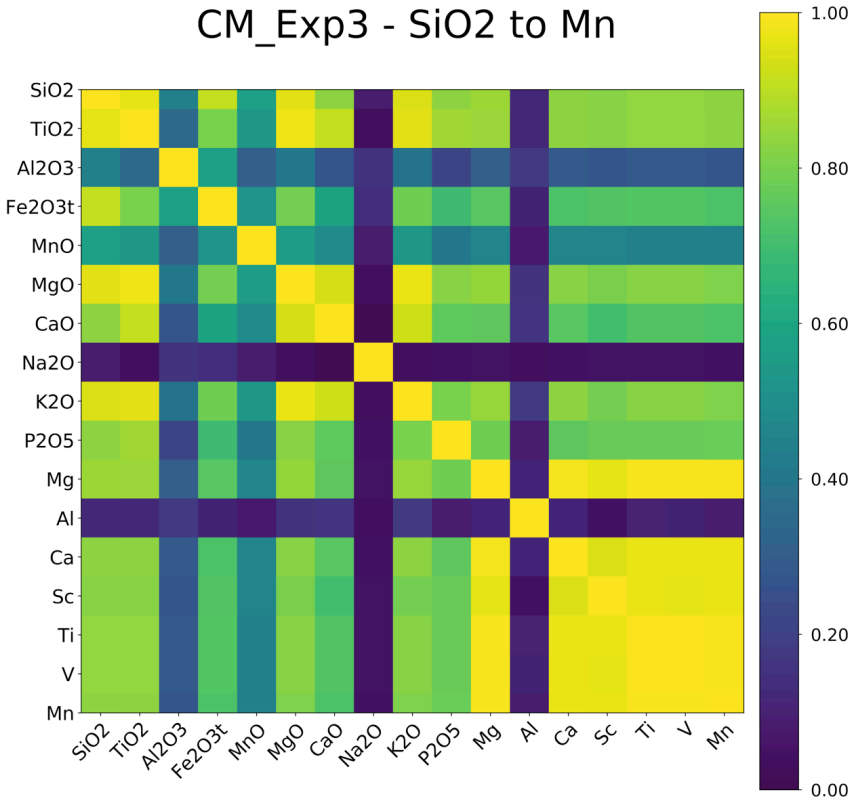

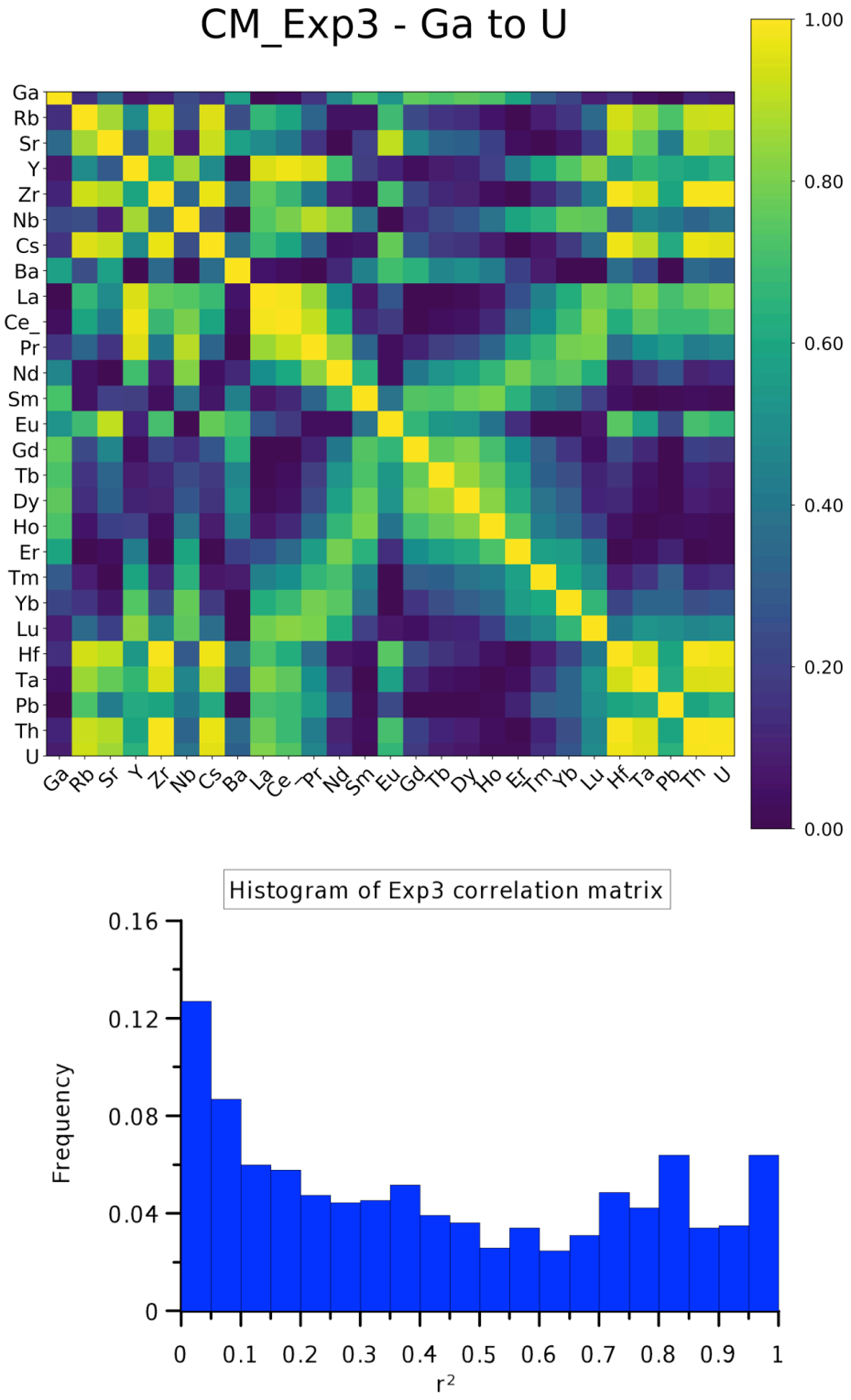

Comparing the three experiments, observations are coherent for i) and ii). However, results vary substantially regarding group iii) in particular for Exp3. Experiments 1 and 2 are in good agreement for Ga to Ba and Eu, whilst Exp1 is in better agreement with Exp3 considering Hf to U. Exp2 and Exp3 show a convergence

from light REE (La to Sm) behaviour, while heavy REE (Ga to Lu) correlate similarly in all experiments. Histograms show 10% to 25% of data inside the range 0.0 – 0.1 reinforcing the non-linear character of data, although it is more evident in Exp3. Regarding $r^2 > 0.1$, experiments 1 and 3 depict a bimodal distribution with higher r^2 frequencies in ranges 0.0 – 0.1 (Exp3), 0.4 – 0.5 (Exp1) and 0.8 – 0.9 (Exp1 and Exp3). It produced an average of $r^2 = 0.52 \pm 0.30$ for Exp1 and $r^2 = 0.43 \pm 0.32$ for Exp3. In contrast, Exp2 distribution shows a slight increase from 0.1 to 0.8, where it reaches the maximum (average $r^2 = 0.51 \pm 0.32$). A substantial difference among the three histograms is the main peak: in Exp1 it centres at 0.5, in Exp2 it centres at 0.85 and in Exp3 it centres at 0.1.

3.3 DISCUSSION

3.3.1 ELEMENTAL MOBILITY EVALUATION

The concept of concentration variance (σ^2) has proven useful to evaluate the degree of homogenization in silicate melt mixing systems (*e.g.*, Morgavi et al., 2013a,b; Rossi *et al.*, 2017; Vicentini et al., 2023). Thus, we applied this concept to quantify individual trace mobilities during the chaotic mixing experiments. The variance of concentration for a given chemical element (C_i) can be calculated as:

$$\sigma_{C_i}^2 = {\sum_{k=1}^{N}(C_{i\,k} - \mu_i)^2}/{N} \qquad \text{(Eq. 3.I)}$$

where N is the number of samples, C_i is the concentration of element i and μ is the mean composition of element i. After $\sigma_{C_i}^2$ computation, the values must to be normalized by the initial variance $\left(\sigma_{C_i}^2\right)_{t=0}$ (*i.e.*, prior the mixing starts) to allow direct comparisons, since trace concentrations range from few to hundreds of mg/g. Therefore, Eq. (3.I) turns into:

$$\sigma_n^2 = {\left(\sigma_{C_i}^2\right)_t}\Big/{\left(\sigma_{C_i}^2\right)_{t=0}} \qquad \text{(Eq. 3.II)}$$

where $\left(\sigma_{C_i}^2\right)_t$ and $\left(\sigma_{C_i}^2\right)_{t=0}$ are the concentration variance of a given chemical element C_i

at time t (*i.e.*, 106 minutes in the experiments) and time $t = 0$ respectively. The initial variance $\left(\sigma_{C_i}^2\right)_{t=0}$ was calculated using the end-member compositions reported in Table 3.1.

Normalized concentration variance (σ^2_n) (also called normalized variance) quantifies how far from the homogeneity a dataset is at a given t. Ideally, homogeneity increases with time (i.e., (σ^2_n) decreases) varying between unity at $t = 0$ (i.e., the system is most heterogeneous) and zero at $t = \infty$ (i.e., the system is completely homogeneous). The three chaotic mixing experiments are performed during identical time (i.e., $t = 106$ min), leading to a time-independent analysis. Homogeneity is expected to correspond to the equilibrium point, whose concentration might lie on between the end-member compositions in case of a linear mixing process. Table 3.2 summarizes the normalized variances calculated for each element as well other relevant parameters.

Figures 3.10 and 3.11 show the variation of (σ^2_n) for each experiment according to the elemental field strength (FS), which is defined as the nominal charge Z of the element divided by its effective radius squared r^2 (after Shannon, 1976). Elements of G1 (normal diffusion) delineate two trends on diagram of Fig 3.10. Although present in major/minor levels, Calcium and Magnesium data obtained by ICP are included as divalent ions to compare their behavior with other alkaline-earth metal ions (i.e., Sr and Ba). We observe that (s^2_n) lies on the expected field (i.e., ≤ 1.0), including Mg within respective standard deviation. The exception is Sr of Exp2 though. Such anomalous (σ^2_n) is a consequence of the depletion on rhyolitic portion (i.e., plateau lower than the initial concentration) and the enrichment on basaltic side (e.g., the blue curve in Fig 3.3 are above the unit). However, the Sr profile shows a distinct curve compared to that described for uphill diffusion. Comparing (σ^2_n) of different experiments for a given element, it shows up: i) an increase from Exp2 to Exp3; and ii) an increase from Exp3 towards Exp1. This indicates that the viscosity contrast between end-members plays an important role during normal diffusion processes, which is in good agreement with major oxides results (Vicentini et al., 2023).

The normalized variance is positively correlated with the field strength FS for elements with FS < 4.0 (Rb, Cs, Sr and Ca), whilst those presenting FS > 4.0 align in a curve with negative slope. G1 shows no FS data ranging between 2.5 and 3.5, where the inflexion change occurs at some point close to Mg (FS approx. 4.0). In both curves we observe lower values of (σ^2_n) for elements with FS < 1.0 (low field strength, LFS) and

FS > 5.0 (high field strength, HFS). It lies on the fact that such elements do not fit well inside the melt structure due to their higher radii (LFS) or charges (HFS), which leads to higher mobilities. Elements plotting inside the interval 1.0 < FS < 5.0 are relatively less mobile than LFS and HFS elements (e.g., Mg). The SiO_2 field strength falls inside this interval (= 1.5) considering the metal-oxygen distance to calculate r^2 (Brown Jr. et al., 1995). Comparing diffusion rates of Si and Mg, experimental data shows that they diverge from one order of magnitude at the same P-T conditions (Shimizu & Kushiro, 1991). In addition, the average diffusivity of SiO_2 along a mafic-felsic profile is D_{SiO2} = 10^{-10} [cm^2/s] (Watson, 1982), while Rb presents diffusivities ranging from 10^{-7} [cm^2/s] on jadeite melt to 10^{-5} [cm^2/s] on diopside melt (Nakamura & Kushiro, 1998). Thus, SiO_2 might influence some trace elements to homogenize slower.

Table 3.2: normalized variance (σ^2_n) calculated for each element from G1 according to the experiment.

Exp.	Elem.	Ion R	Valence	Z/r^2	R_i/B_i	(σ^2_n)
1	Mg	0.72	2	3.86	0.02	1.12
1	Rb	1.52	1	0.43	19	0.41
1	Sr	1.18	2	1.44	0.07	0.80
1	Zr	0.72	4	7.72	10	0.64
1	Cs	1.67	1	0.36	27	0.60
1	Hf	0.71	4	7.93	9.3	0.70
1	Th	0.94	4	4.53	13	0.60
1	U	0.89	4	5.05	12	0.71
1	Ca	1.00	2	2.00	0.07	0.96
1	Ti	0.61	4	10.9	0.04	0.96
2	Mg	0.72	2	3.86	0.17	0.63
2	Rb	1.52	1	0.43	12	0.24
2	Sr	1.18	2	1.44	0.77	-
2	Zr	0.72	4	7.72	0.84	-
2	Cs	1.67	1	0.36	23	0.40
2	Hf	0.71	4	7.93	0.89	-
2	Th	0.94	4	4.53	5.9	0.37
2	U	0.89	4	5.05	4.7	0.30
2	Ca	1.00	2	2.00	0.22	0.47
2	Ti	0.61	4	10.9	0.12	0.51
3	Mg	0.72	2	3.86	0.05	0.62
3	Rb	1.52	1	0.43	21	0.32
3	Sr	1.18	2	1.44	0.28	0.63
3	Zr	0.72	4	7.72	6.2	0.31
3	Cs	1.67	1	0.36	47	0.46
3	Hf	0.71	4	7.93	5.9	0.30
3	Th	0.94	4	4.53	16	0.40
3	U	0.89	4	5.05	18	0.50
3	Ca	1.00	2	2.00	0.14	0.51
3	Ti	0.61	4	10.9	0.07	0.51

Table 3.2 (cont.): normalized variance (σ^2_n) calculated for each element from G2 according to the experiment.

Exp.	Elem.	Ion R	Valence	Z/r^2	R_i/B_i	(σ^2_n)
1	Ba	1.35	2	1.10	0.40	1.2
1	Pb	1.19	2	1.41	8.3	0.41
1	Sr	1.18	2	1.44	0.07	-
1	La	1.03	3	2.82	5.3	0.48
1	Ce	1.01	3	2.94	3.9	0.53
1	Pr	0.99	3	3.06	3.9	0.52
1	Nd	0.98	3	3.10	3.3	0.54
1	Sm	0.96	3	3.27	2.7	0.61
1	Eu	0.95	3	3.35	0.43	1.7
1	Gd	0.94	3	3.41	2.7	0.61
1	Tb	0.92	3	3.52	2.7	0.61
1	Dy	0.91	3	3.62	2.7	0.61
1	Ho	0.90	3	3.70	2.9	0.60
1	Y	0.90	3	3.70	3.3	0.49
1	Er	0.89	3	3.79	2.9	0.62
1	Tm	0.88	3	3.87	3.2	0.63
1	Yb	0.87	3	3.96	3.2	0.66
1	Lu	0.86	3	4.05	3.4	0.62
1	Zr	0.72	4	7.72	10	-
1	Ga	0.62	3	7.80	0.99	-
1	Hf	0.71	4	7.93	9.3	-
1	Al	0.54	3	10.5	0.98	-
1	Nb	0.64	5	12.2	1.4	1.9
1	Ta	0.64	5	12.2	1.6	1.4
2	Ba	1.35	2	1.10	2.1	0.06
2	Pb	1.19	2	1.41	5.54	0.04
2	Sr	1.18	2	1.44	0.77	4.2
2	La	1.03	3	2.82	1.68	0.58
2	Ce	1.01	3	2.94	1.51	0.86
2	Pr	0.99	3	3.06	1.25	2.5
2	Nd	0.98	3	3.10	1.03	-
2	Sm	0.96	3	3.27	0.81	4.2
2	Eu	0.95	3	3.35	0.48	1.1
2	Gd	0.94	3	3.41	0.63	1.2
2	Tb	0.92	3	3.52	0.53	0.83
2	Dy	0.91	3	3.62	0.46	0.72
2	Ho	0.90	3	3.70	0.43	0.71
2	Y	0.90	3	3.70	0.47	0.75
2	Er	0.89	3	3.79	0.43	0.67
2	Tm	0.88	3	3.87	0.45	0.75
2	Yb	0.87	3	3.96	0.44	0.76
2	Lu	0.86	3	4.05	0.46	0.78
2	Zr	0.72	4	7.72	0.84	2.2
2	Ga	0.62	3	7.80	0.85	1.9
2	Hf	0.71	4	7.93	0.89	3.5
2	Al	0.54	3	10.5	1.2	0.65
2	Nb	0.64	5	12.2	0.68	1.2
2	Ta	0.64	5	12.2	0.86	3.1
3	Ba	1.35	2	1.10	1.0	-
3	Pb	1.19	2	1.41	13	0.38
3	Sr	1.18	2	1.44	0.28	-

Exp.	Elem.	Ion R	Valence	Z/r^2	R_i/B_i	(σ^2_n)
3	La	1.03	3	2.82	2.4	0.54
3	Ce	1.01	3	2.94	1.9	0.77
3	Pr	0.99	3	3.06	1.5	1.2
3	Nd	0.98	3	3.10	1.1	11
3	Sm	0.96	3	3.27	0.88	9.3
3	Eu	0.95	3	3.35	0.28	0.59
3	Gd	0.94	3	3.41	0.76	2.5
3	Tb	0.92	3	3.52	0.77	2.4
3	Dy	0.91	3	3.62	0.80	2.6
3	Ho	0.90	3	3.70	0.86	6.3
3	Y	0.90	3	3.70	1.7	0.65
3	Er	0.89	3	3.79	0.98	-
3	Tm	0.88	3	3.87	1.2	4.1
3	Yb	0.87	3	3.96	1.3	2.0
3	Lu	0.86	3	4.05	1.5	1.1
3	Zr	0.72	4	7.72	6.2	-
3	Ga	0.62	3	7.80	0.9	5.8
3	Hf	0.71	4	7.93	5.9	-
3	Al	0.54	3	10.5	1.1	3.5
3	Nb	0.64	5	12.2	1.3	1.5
3	Ta	0.64	5	12.2	2.9	0.31

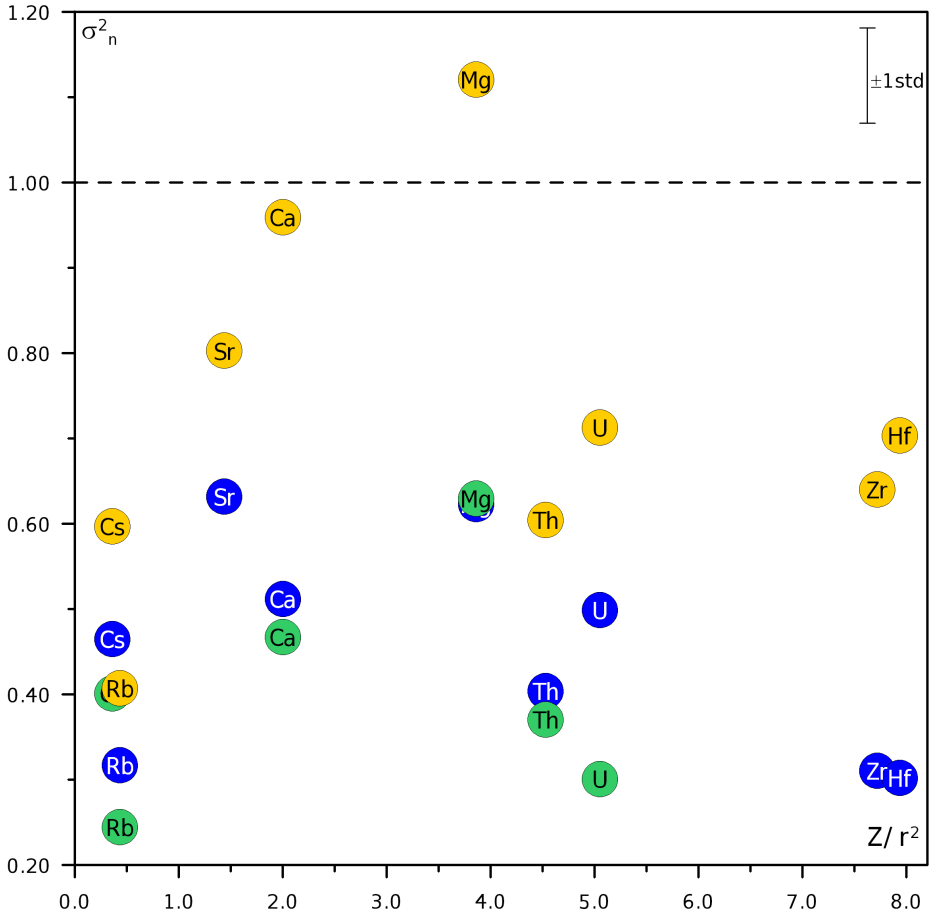

Figure 3.10: Variation of the normalized variance (σ^2_n) calculated for trace elements from group G1 as a function of the field strength (nominal charge Z of the element divided by the ionic radius squared r^2 – after Shannon, 1976) for experiments 1, 2 and 3. Legend: yellow = Exp1; green = Exp2; blue = Exp3.

Elements of G2 are shown in Figure 3.11 in which no trends are well delineated. Generically, an increase in FS affects positively (σ^2_n) of Exp1, however Exp2 and Exp3 are considerably scattered. Additionally, for a given element, (σ^2_n) is not only dependent on the viscosity contrast as registered for G1. In cases of FS < 2.0, Exp2 produced the lowest (σ^2_n) values, followed by Exp3 and Exp1 (considering Pb). In the next segment (inset "b)"), Lanthanides and Yttrium show a positive correlation between (σ^2_n) and FS for Exp1 and Exp2. Furthermore, Exp1 shows higher homogeneity compared to Exp2, while Exp3 data is more scattered and with higher (σ^2_n) except by Eu and Y. In the HFS zone, the diagram depicts $(\sigma^2_n)_{Ta}$ pointing towards an increase from Exp3 to Exp1, and from Exp1 to Exp2, contrasting with $(\sigma^2_n)_{Nb}$ ascending from Exp2 to Exp3, and from Exp3 to Exp1 in spite of their proximity. These observations reflect the non-linear behavior of G2 that is believed to occur due to uphill diffusion. Specifically, the uphill diffusion moves the system towards heterogeneity.

Uphill diffusion can also be visualized taking into account melt structure information. The presence of SiO_2 gradient on silicate melts (e.g., end-members of a mixing system) implies different polymerization degrees and transient structures that tend to disappear with the homogenization. The SiO_2 tetrahedra dynamics is related to breaking and re-connection of Si-O bonds, playing a fundamental role in this scenario. Prior the system achieves the stability, a given element will constantly move towards the region where it is better accommodated (i.e., smaller activity) (Watson, 1976, 1982). Since each chemical potential (or activities) varies according to the composition, until the system reaches stability, some elements may move against its own gradient (e.g., Sato, 1975; Emmanuel et al., 2004).

The behavior of Sr in Exp2, represented by (σ^2_n) > 1.0 in Fig 3.11, might be analogous to alkaline elements accumulating into felsic phases, when melts with contrasting compositions (i.e., SiO_2) come into contact. This may be explained due to the fact that, at a given concentration, alkalis activities are higher in mafic phases (Watson, 1982). Experimental data from two-liquid partitioning have demonstrated that Sr is enriched in silica-poor melts in comparison to silica-rich melts (Hess & Rutherford, 1974; Watson, 1976; Vicenzi et al., 1994). Therefore, data indicate that when the initial gradient is sufficiently small, structural factors will produce uphill diffusion.

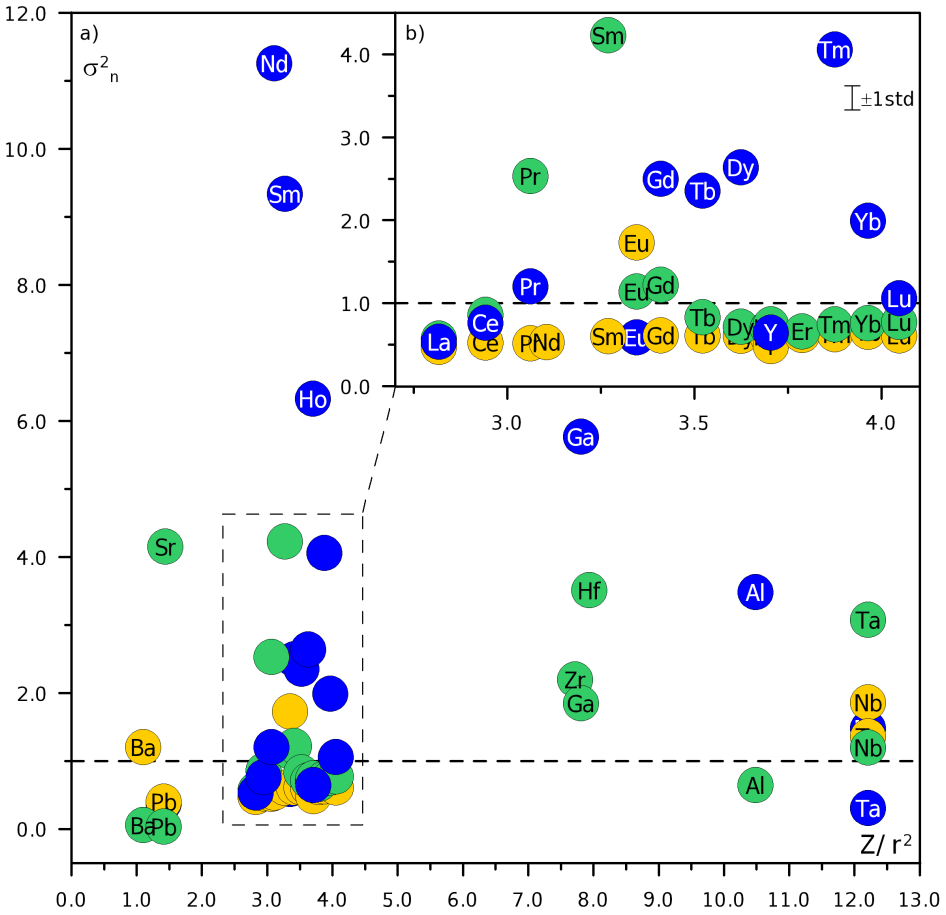

Figure 3.11: Variation of the normalized variance (σ^2_n) calculated for trace elements from group G2 as a function of the field strength (nominal charge *Z* of the element divided by the ionic radius squared r^2 – after Shannon, 1976) for experiments 1, 2 and 3. Legend: yellow = Exp1; green = Exp2; blue = Exp3.

3.3.2 HAFNIUM AND ZIRCONIUM

During the preparation of rhyolites LMC-027 (Exp1) and LMC-018 (Exp3) a ceramic balls mill was used to powder the material, which lead to a contamination of Zr and Hf in these samples. Previous analyses confirmed an enrichment of 4.5 – 6.0 times for Hf, and 6.5 – 8.5 times for Zr on produced glasses. As a consequence, we observe that the Hf and Zr curves in Fig 3.2 (Exp1) and Fig 3.4 (Exp3) are closer to G1, whilst in Fig 3.3 (Exp2) the similarity is with G2. Therefore, the use of this data is strictly restricted to the discussion of the initial gradient effect on uphill diffusion.

In Fig 3.11, the elements Hf and Zr from Exp2 portray (σ^2_n) > 1.0 in contrast with results displayed in Fig 3.10 for Exp1 and Exp3. It was shown that (σ^2_n) is strongly affected by uphill diffusion. This phenomenon has been detected in Hf and Zr profiles (Fig 3.3). These elements are pointed out as substitutes of Si (e.g., Brown-Jr et al.,

1995; Ferry & Watson, 2007; Jollands et al., 2014). If the Zr and Hf gradients are sufficiently small (the case in Exp2), it is reasonable to imagine that the driven force of SiO_2 gradient is able to move Zr and Hf in the same direction (i.e., opposite to their gradients in Exp2).

3.3.3 THE ROLE OF THE INITIAL GRADIENT ON UPHILL DIFFUSION

Figure 3.12 shed some light on the effect of elemental gradients on homogenization process. Ordinate-axis plots the initial ratio between rhyolitic and basaltic concentrations R_i/B_i for a given element and abscissa-axis displays the normalized variance (σ^2_n). All available data from the three chaotic mixing experiments are included as a single dataset and M13 data are included as well. Light grey circles represent elements from G1 (normal diffusion), whilst dark grey circles represent elements from G2 (uphill diffusion). The smallest white circles represent M13 (normal diffusion). This diagram highlights that as much R_i/B_i tends to unit, meaning smaller initial gradients, higher is the probability of such element being influenced by uphill diffusion. From this diagram one realizes that R_i/B_i inside the interval 0.3 – 7.0 is critical to the occurrence of this phenomenon. In addition, we observe a large number of points plotting bellow the dashed line (i.e., (σ^2_n) < 1.0) for G1 elements with the exception of Sr from Exp2. The zone where G1 and G2 coexist, as exemplified by Pb in Fig. 3.12, indicates that other factors account to uphill diffusion occurrence, although the elemental gradient plays an important role on this process.

Points from M13 plot preferentially inside the coexisting zone (i.e., 3.0 to 7.0). In general, M13 data are less dispersed than data presented here, which is believed to occur, at least in part, due to M13 sample ages (ca. 15 Ma; Cathey & Nash, 2009), thus, fresher than PEMP end-members used here. Nevertheless, it is in agreement with the idea of Fig 3.12. Additionally, the behaviour of Zr and Hf presented in Exp1 and Exp3 (strongly enriched) agree with this argumentation as well, since their initial gradients are sufficiently high (R_i/B_i > 5.0) to behave as G1, whilst in Exp2 theses elements present uphill diffusion (R_i/B_i < 1.0).

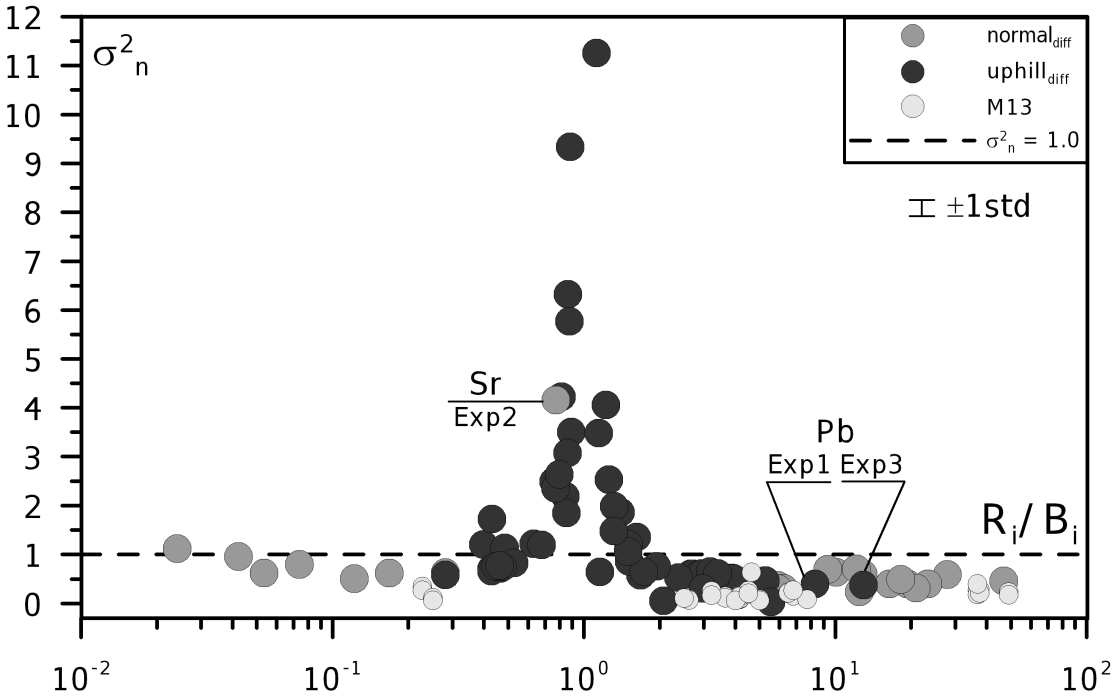

Figure 3.12: normalized variance (σ^2_n) as a function of initial ratio R_i/B_i between rhyolitic and basaltic concentration for each element. Data from the three chaotic mixing experiments are included as well as data from Morgavi et al. (2013a,b) referred as M13. The legend is displayed in the diagram.

Previous experiments describing uphill diffusion were mainly conducted in static conditions (e.g., diffusion couple method), whilst here we used a dynamical approach (i.e., chaotic mixing). The exception might be the use of a stirring method to maintain the homogeneity of the melt while one phase is dissolved inside the other (e.g., Watson, 1982). Such experiments pointed towards this phenomenon in a few number of elements, mostly in alkalis, Al_2O_3 and Sr and Nd isotopic systems. It is worthy to mention the novelty of reporting it in dynamical conditions (i.e., chaotic mixing experiments) and in experiments that systematically vary the rhyolitic end-member, leading to a more comprehensive overview on this matter. Results for all three experiments are robust, demonstrating that the elements develop similar patterns in distinct natural systems. Based on these evidences, it is proposed that differences up to 30% in gradients (i.e., $0.7 < R_i/B_i < 3.0$) substantially increase the probability of the uphill diffusion development. Elements with gradients diverging more than 30% are suggested as the most predictable and, thus, the most reliable to focus the further analysis (e.g., Rb and Th).

3.3.4 POTENTIAL APPLICATION OF RESULTS ON PEMP CHAPECÓ PETROGENESIS

The main challenge faced by Chapecó dacites petrogenetic models is the integration of major/minor oxides, trace and isotopic data. This information was obtained using distinct analytical methods, which might cause problems in this integration. The existing models commonly indicate different degrees of evolution depending on the dataset. The aim of this section is to compare the experimental results with the chemical analyses reported in the literature and the linear mixing model LM, which was calculated using the classical mixing equation (Langmuir et al., 1978):

$$C_H = C_R^i * f + C_B^i * (1 - f) \qquad \text{(Eq. 3.III)}$$

where C_B^i and C_R^i are respectively the initial concentrations of an element i in the basaltic and rhyolitic glasses, f is the proportion of the rhyolite (or contamination degree) and C_H is the hybrid glass final concentration.

Regarding published data, determinations in Chapecó dacites via ICP analysis are scarce (Janasi et al., 2007; Nardy et al., 2008; Freitas, 2008). This thesis produced new data on six CGD samples and five COD samples (see Appendix). In contrast, analyses in bulk rock for major oxides and some trace elements via X-ray fluorescence XRF, and for trace elements via neutron activation are abundant (Piccirillo & Melfi, 1988; Garland et al., 1995; Janasi et al., 2007; Nardy et al., 2008; Freitas, 2009). Therefore, in order to minimize bias, only works presenting ICP data were taken into consideration for trace analysis. The use of XRF data is restricted to the diagrams of major oxides (i.e., Figure 3.13) and to convert TiO_2 in Ti contents for the largest number of Chapecó samples as possible. Previous tests on the produced glasses indicate that EPMA and XRF analyses diverge up to 15%, which is acceptable.

The following analysis is carried out considering the IUGS nomenclature convention (Le Bas et al., 1986) to divide experimental datasets 1, 2 and 3 (Vicentini et al., 2023). Titanium data from ICP was used as reference instead SiO_2 since: i) the oxides TiO_2 and SiO_2 are strongly correlated (i.e., Figs. 3.7 – 9) being possible to correspond Ti from ICP to TAS diagram; ii) TiO_2 behaves as network former in melts, such as SiO_2; iii) TiO_2 is used as a proxy to discriminate PEMP rocks, including

Chapecó dacites subgroups Guarapuava (CGD; TiO_2 > 1.3%) and Ourinhos (COD; TiO_2 < 1.3%).

3.3.4.1 MAJOR VS. TRACE DIAGRAMS

The "TiO_2 vs. SiO_2" diagram in Figure 3.13 displays the EPMA data on experimental glasses of Exp1 (yellow), Exp2 (green) and Exp3 (blue) from Vicentini et al. (2023). Dark and light grey points are the most representative data on Chapecó dacites, CGD (N = 77) and COD (N = 27) respectively. This diagram demonstrates that Chapecó lies on the TiO_2 range between 1.0% and 1.7%, which corresponds to the interval of 63% < SiO_2 < 70%, i.e., dacitic field on TAS diagram (considering 10% of standard deviation in FRX analyses). Black straight lines correspond to linear mixing curves (f is indicated) for experiments 1 (LM1 upper curve) and 2 (LM2 lower curve) that were calculated based on the starting glass analyses from the respective experiment. Exp3 model LM3 lies on between the two curves (not drawn) and presents f's close to those of LM1 model. Inside the interval of intermediate compositions, linear mixing models fit the respective experimental dataset that slightly vary between each other.

In comparison with Chapecó TiO_2 contents, models of Exp1 and Exp3 indicate 60% of mixture to generate CGD and 70% to generate COD, whilst the Exp2 model points to 70% and 80% of mixture to produce CGD and COD compositions respectively. The variation in SiO_2 points out that f would reach 0.5 for CGD (Exp1 model) and 0.9 for COD (Exp2 model) in the most extreme cases.

3.3.4.2 TRACE VS. TRACE DIAGRAMS

In Figure 3.13, the behaviour of Rb, Pb, Th and U is indistinguishable comparing Exp1 and Exp2 concentrations with the Chapecó data. The exception is Pb contents in CODs (more enriched in crustal material) that lie on closer to the Exp3. However, a clear distinction comes up in Sr diagrams (closer to the Exp2 results) and REEs (more proximity to the Exp1), represented by La and Yb diagrams. The fact of experimental and natural chemical analyses converge supports the chaotic mixing as a feasible process. Regarding LM models, the best fits appear in: i) Exp2 for Rb and heavy REEs (represented by Yb), and ii) Exp3 for Sr. In general, the curves are similar

(i.e., shapes) independently of the experiment since it depends on the diffusivity contrast of each couple. Nevertheless, the diffusivity depends on the viscosity, which is higher in Exp1 rhyolitic glass. Thus, changes in viscosity contrast affects Rb and HREEs differently than it does to Ti.

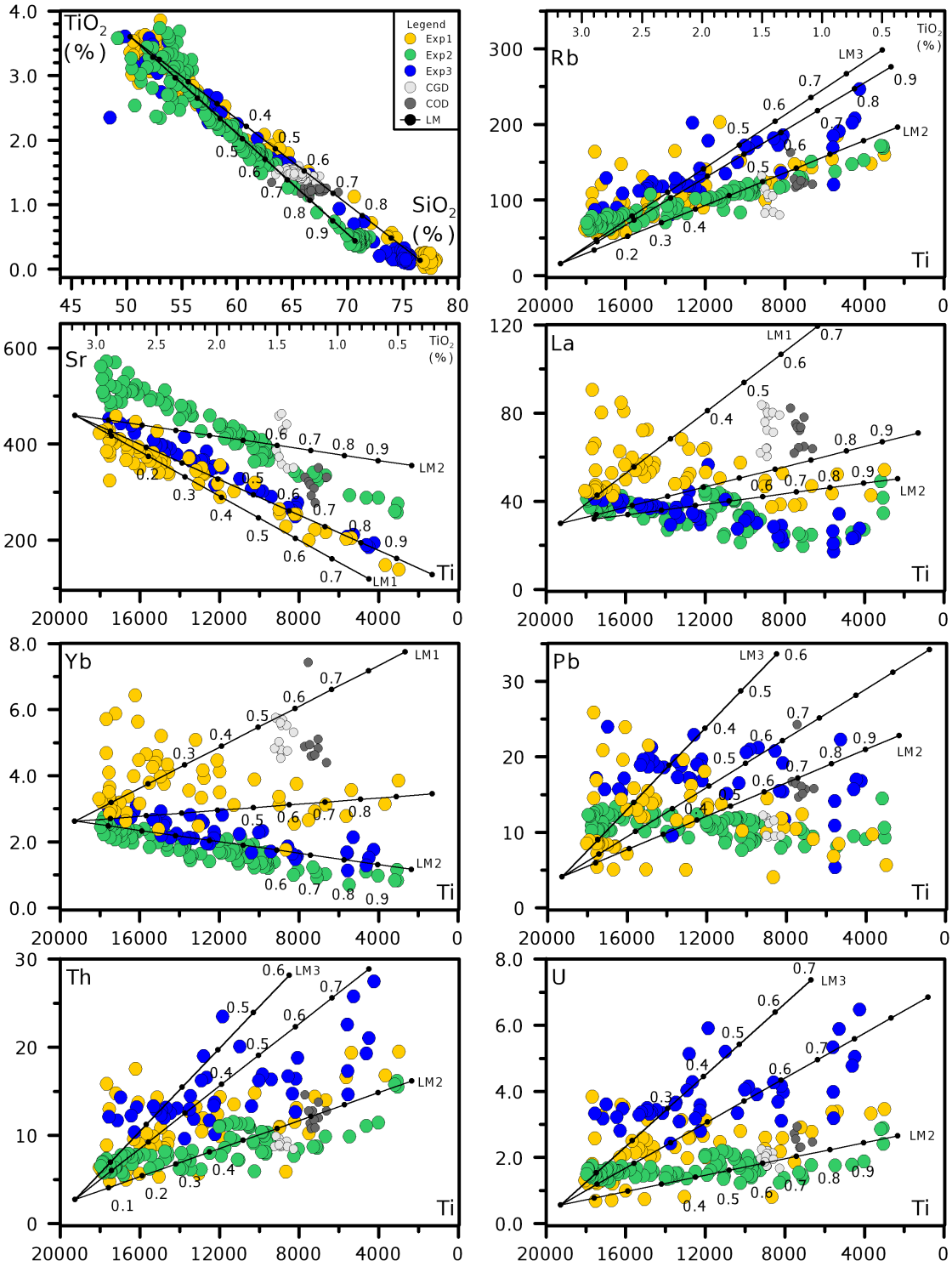

Figure 3.13: “Trace vs. Ti” diagrams consider only samples in which ICP data are available (Janasi et al., 2007; Nardy et al., 2008; Freitas, 2009; this work). Concentrations are given in μg/g, with the exception of major oxides (wt.%). Legend: yellow = Exp1; green = Exp2; blue = Exp3; light grey = CGD; dark grey = COD; LM = linear mixing model with *f* in representative points.

LM models show that the contamination degree varies significantly. In the case of Rb, the best fit is between Chapecó and Exp2 data giving $f_{CGD} = 0.5$ and $f_{COD} = 0.6$. This result diverges in 0.2 from models of “SiO_2 vs. TiO_2” diagram (maintaining the range of Ti contents). In addition, LM1 and LM3 (i.e., models using Exp1 and Exp3 end-members respectively) indicate that expected Rb data should plot around 150 μg/g for CGD and 200 μg/g for COD, which is in evident disagreement with both experimental and natural data. Extending the analysis to the other trace elements, it is realized that LM2 is closer to CGD for Sr, Th and U resulting in $f = 0.6$ in all cases. For COD, Pb is also included and results $f = 0.7$ in all cases, even though U curve is slightly below. Chapecó REEs plot between LM1 and LM3 models and a more depleted group, especially La, fits Exp1 data. It would indicate that more than one contaminant are involved in the process.

Figure 3.14 shows variation diagrams of representative pairs of trace elements. Rubidium and Thorium were used as references due to their most expressive initial gradients (R_i/B_i ranges from 6 to 21). The plots are restricted to points with Ti contents inside the interval $0.9\% < TiO_2 < 2.1\%$ that is relative to the Chapecó dacites (considering 15% of standard deviation). Diagrams highlight a remarkable enrichment in Ba, Nb and Ta for natural Chapecó (this is the case for Zr and Hf as well). COD data consistently appear associated with Exp1 (Sr, Y, LREE represented by La, and Pb), whilst CGD partially plot next to Exp2 (Sr and Pb), and partially at the limits of Exp1 (Y and HREE symbolized by Yb). Variations in *f* are observed for different couples. In respect to CGD, the model LM2 points towards $f_{Sr} = 0.5$ and $f_{Pb} = 0.4$. However, Pb of CGD and Exp2 plot together in a wider-ranging area that reaches LM1 ($f_{CGD} = 0.2$) and LM3 ($f_{CGD} = 0.15$) as well. For Y, CGD are above all LM models remaining closer to Exp1 though. Regarding COD, LM1 systematically reproduces this group exhibiting $f = 0.3$ to Sr, Y and La, and $f = 0.4$ to Yb and Pb. Additionally, LM3 indicates $f_{Pb} = 0.25$ to produce COD, whose data are spread and reach LM2 ($f = 0.6$) as well as they lie on Exp1 and Exp3 fields.

3.3.4.3 GENERAL COMMENTS

Figure 3.15 summarizes the comparison between the averages of natural and experimental data from Exp1 and Exp2, which show the best results. The number of points *N* used to calculate the averages of trace element concentrations follows: Exp1 – N_{CGD} = 8 and N_{COD} = 6; Exp2 - N_{CGD} = 32 and N_{COD} = 9; natural samples – N_{CGD} = 19 and N_{COD} = 17 (Janasi et al., 2007; Nardy et al., 2008; this work). It is important to notice that the number of determinations via ICP is scarce compared to the total chemical analyses in literature (N_{COD} = 27 and N_{CGD} = 77). Averages for major oxides in Exp1 and Exp2 were included as well, calculated using data from Vicentini et al. (2023). Figure 3.15 points out that the chaotic mixing is able to reproduce the Chapecó trace signatures for the majority of elements especially for CGD in Exp1. This conclusion relies on a standard deviation of 15% represented by the shadow rectangle in Fig. 3.15. Notice that the main difference between CGD and COD is the REEs contents (slightly better for CGD). It is worthy to mention that the averages represent dispersed points in Figs. 3.13 and 3.14, in where CODs are better associated to experimental results than CGD. In all scenarios, COD and CGD diverge approx. 10% in terms of interaction degree of basaltic and rhyolitic phases.

The discrepancies, as well illustrated in the variation diagrams, might be partially attributed to uphill diffusion processes that were observed in the experiments. The higher divergences occur to the elements Ba, Y, Nb, Zr, Ta and Hf. The involvement of different contaminants is valid though, corroborated by the diagrams of Figs. 3.13 and 3.14. The Paraná Basin developed on a basement with a complex tectonic history that involves several cratonic blocks (*e.g.*, São Francisco and Angola), large orogenic belts surrounding them (*e.g.*, Araçuaí-Ribeira and West Congo), smaller continental blocks and magmatic arcs prior to the opening of Atlantic Ocean (Almeida et al., 2013). This work does not consider that the three contaminants selected to the chaotic mixing experiments represent the full range of basement compositions that are strongly heterogeneous (Prazeres Filho et al., 2003; Rodrigues et al., 2011). Such reports present rocks with higher Ba, Y, Zr and Hf contents (e.g., granites from Apiaí-Mirim Nuclei) that might generate the observed patterns.

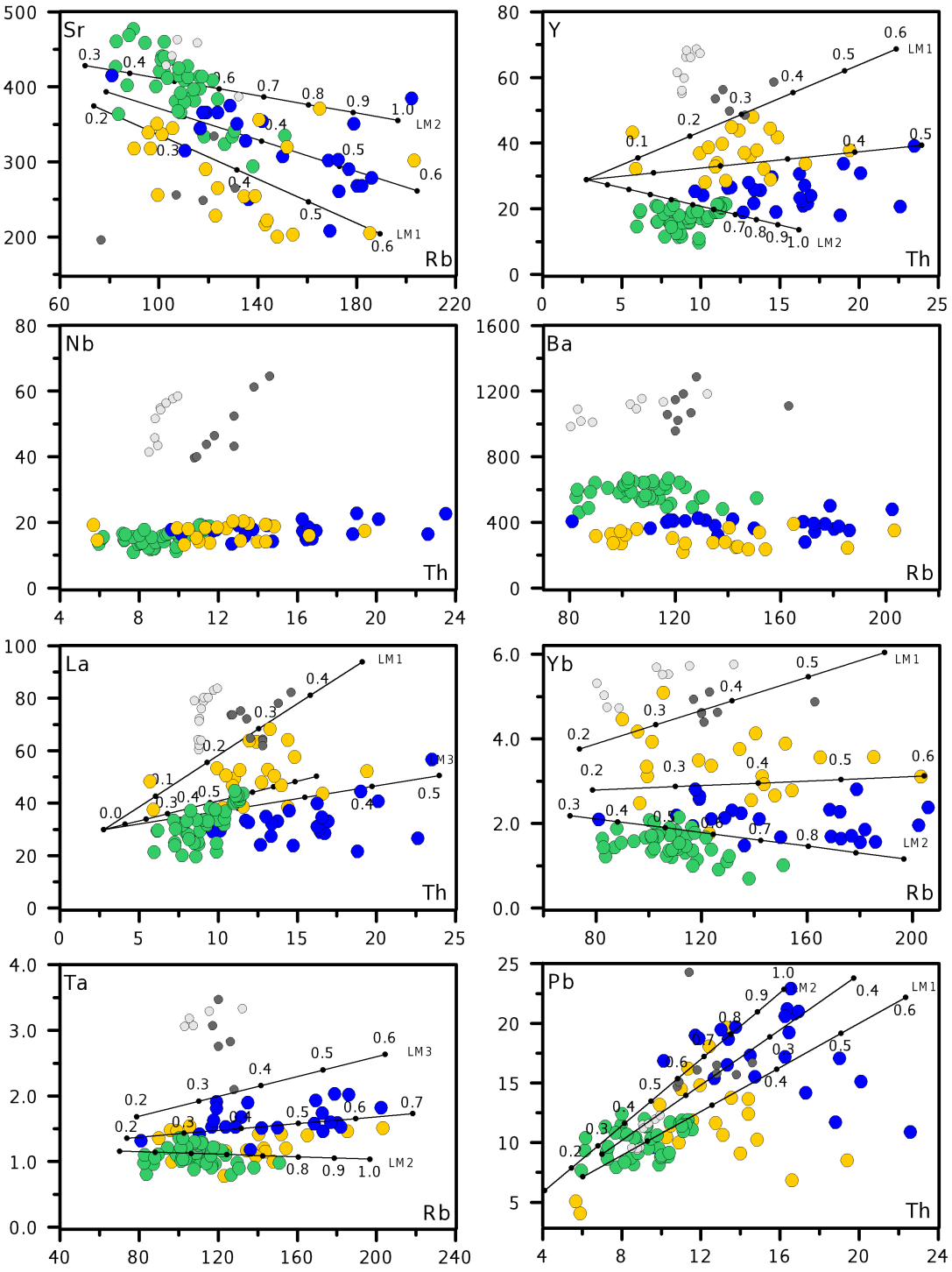

Figure 3.14: "Trace vs. Trace" diagrams consider only samples in which ICP data are available (Janasi et al., 2007; Nardy et al., 2008; Freitas, 2009; this work). Concentrations are given in µg/g. Legend: yellow = Exp1; green = Exp2; blue = Exp3; light grey = CGD; dark grey = COD; LM = linear mixing model with *f* in representative points.

Recent geophysical investigations on lithosphere beneath the Paraná Basin agree with the complexity of the tectonic settings. Mechanical and electromagnetic properties

suggest a typical juvenile lithosphere (Bologna et al., 2011, 2013; Padilha et al., 2015; Chaves et al., 2016), opposite to the expected for cratonic regions (i.e., stability and refractory lithology). High P-wave anomaly values of, density contrast, and electrical conductivity indicate that some condition lead to the occurrence of this significant magmatism in Paraná Basin. Geochemical and isotopic data suggest that metassomatic processes on the lithosphere, associated to an older asthenospheric mantle, are responsible for the isotopic Os signatures and for rejuvenating (or weakening) the subcontinental lithospheric mantle (Rocha-Júnior et al., 2013, 2020; Marques et al., 2018).

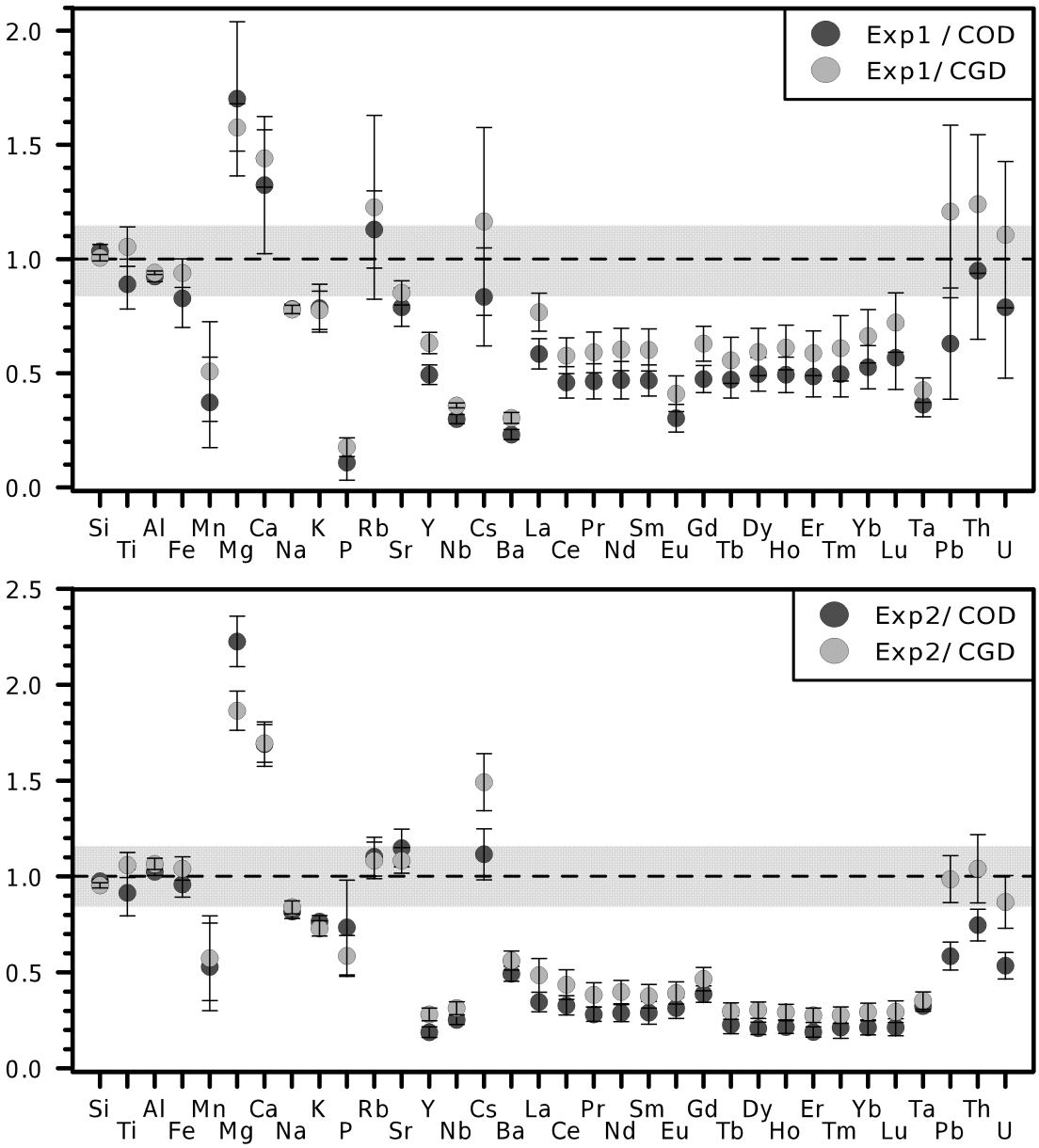

Figure 3.15: the comparison between experimental and natural data is summarized for the elements investigated (major/minor are included from Vicentini et al., 2023). The shadow rectangle represents the interval 0.85 – 1.15; error bars indicate ±1σ.

Alternatively, the discrepancies can be related to processes that might occur after mixing. The presence of xenocrystals or anticrystals in Chapecó dacites pointed by CSD analyses (Luchetti et al., 2018) is an indicative that magmas at distinct evolution stages got into contact at some point. This context depicts a scenario of interconnected magma chambers leading to heterogeneities and possibly to the development of different contamination rates. Considering it, an option would be the contact (maybe replenishment) with more evolved HTi magmas that underwent fractional crystallization of plagioclase, pyroxene and Ti-magnetite (main phases in Chapecó), also accessories as ilmenite and apatite, from the same sources (i.e., HTi Pitanga-type from PEMP). Models of fractional crystallization along with crustal assimilation (AFC) support some contribution of it (e.g., Garland et al., 1995). Elements such as Nb and Ta are assimilated during the crystallization of Ti-bearing minerals such as ilmenite (Green & Pearson, 1986), which would explain their anomalous enrichment in Chapecó dacites (up to 3 times higher than in rocks from the basement) through this contact. It is important to notice that Ba enters into the plagioclase structure during crystallization. In dacitic melts this will be in smaller amounts (Blundy & Wood, 1991; Iveson et al., 2018), however a similar effect might cause its enrichment especially due to accumulation of plagioclase as large phenocrysts in such rocks.

In addition, HTi dacites from PEMP are sufficiently old (i.e., 134 Ma – Janasi et al., 2011) to lose their pristine characteristics at some level. A recent investigation on mafic dykes from the Cabo Frio Tectonic Domain (southeastern Brazil) reveals a complex combination of intrusive ages that strongly points towards water-rock interaction caused by fluid circulation (Carvas et al., 2021). It is reasonable to infer that results for Chapecó dacites will present some deviations caused by secondary processes. The comparison with M13 data (e.g., Fig. 3.12) supports this idea as well, since it generically shows that PEMP data is more scattered than data from younger Snake River samples (i.e., approx. 15 Ma - Cathey & Nash, 2009).

The parameter *f* fails to explain the mixing between very contrasting melts since it implies: i) the diffusion rates are equal for all elements; and ii) the diffusion efficiency

is global in the experimental charges (analogously to a magma chamber). The variations observed according to the pair reflect non-linear dynamics, appointed here as chaotic. Variation diagrams indicated *f* descending from "major vs. major" to "major vs. trace" and finally to "trace vs. trace". It mirrors the relative mobility that different specimens present in melts, which depends on the diffusivity and is enhanced by the stretching and folding mechanism. Further, magma mixing is a highly complex three-dimensional process as illustrated in the advection-diffusion equation:

$$\frac{\partial n_C}{\partial t} + V_{\hat{x}}.\nabla n_C = D\nabla^2 n_C \qquad \text{(Eq. 3.IV)}$$

where $\partial n_C/\partial t$ is the variation of the particle density n_c in time t (*i.e.*, particle flux); $V_{\hat{x}}$ is the vectorial velocity field (*i.e.*, $\hat{\imath}$ direction) that such a particle is submitted; D is the diffusivity; and ∇ is the divergence operator.

Eq. (3.IV) expresses that initially the physical mingling starts from shearing caused by the spindle and crucible rotations (i.e., terms of the left side). The created filaments are continuously stretched and folded. This process increases the contact surfaces while the filaments are getting systematically thinner. Finally, this thinning reaches a sufficiently small length scale that exponentially enhances the diffusion efficiency (i.e., the term of right side) and brings the original two melts to their local intermediate equilibrium composition. Therefore, this is a highly non-linear and locally inhomogeneous process (over sample size) resulting in distinct *f*'s and mixing efficiencies.

Finally, the elemental behaviour reported here implicates in the generation of peculiar non-linear patterns. The ratios used in the study of magma sources, including isotopic systems, are affected in different ways by chaotic dynamics. The experiments indicate that points corresponding to the COD interval are twice more enriched in Rb/Sr than CGD, which does not occur to Sm/Nd that present equivalent values. The Th/U and U/Pb ratios for CGD and COD intervals diverge less when compared to Rb/Sr, however presenting anomalous higher values in comparison to the rhyolitic initial ratios. In addition, REEs fractionation are also affected presenting $(La/Sm)_N$ (N = normalized to chondrites) more homogeneous than $(Sm/Yb)_N$, and with Eu/Eu* negative anomalies popping up along the transects.

3.4 FINAL REMARKS

The results of chaotic mixing experiments demonstrate that the two phases mixed into each other at different levels after the experimental runs. Transects of trace elements depict points of intermediate compositions and sigmoidal asymmetric curves that are related to the elemental diffusion. The number of points presenting such compositions is less expressive than that inside the range of original glasses. Comparing the remnant filaments of basalt (arcs) and rhyolite (plateaux), the basaltic phase is strongly contaminated and loses its original signature completely for the vast majority of elements. It occurs especially for the most enriched elements such as Cs and Rb. The frequency of intermediate compositions and the contamination patterns are systematically reproduced in all experiments revealing the relevance of these phenomena during the chaotic mixing.

Two different diffusive patterns were identified, named normal and uphill diffusion. It divides the elements into two groups as follows: G1 (normal) – V, Sc, Sr, Cs, Rb, U, Th, Ti, Mg, Ca and Mn; and G2 (uphill) – Ga, Nb, Zr, Y, Ba, REE, Ta, Hf, Pb and Al. For the first time in chaotic mixing experiments uphill diffusion was identified and described for a large number of trace elements showing the same patterns, which systematically stands independently of the experiment. A direct consequence is a higher deviation from the linearity observed in variation diagrams of G1 vs. G2 elements. The correlation matrices reinforce the stark non-linear character of data, which is a feature of chaotic dynamics. Therefore, uphill diffusion is relevant in the simulated scenario.

The normalized variance (σ^2_n), which is an efficient parameter to express the homogeneity in silicate melt mixing (e.g. Rossi et al., 2017), consistently indicates the connection between viscosity and mobility for G1 elements. This result is in total agreement with those for major data (Vicentini et al., 2023). Exp1 exhibits the highest contrast in viscosity (η_{rhy}/η_{bas}) in comparison to Exp3 and Exp2 respectively, expressing the higher values of (σ^2_n). For a large number of G2 elements, (σ^2_n) reaches values that are not expected (i.e., > 1.0), which has been associated to their starting chemical gradients. Therefore, it is proposed that differences up to 30% in gradients substantially increase the probability of uphill diffusion develops and produces heterogeneities in the

mixing system. Elements with gradients diverging more than 30% are the most predictable and, thus, the most reliable to focus the argumentation.

In respect to the generation of Chapecó dacites, the comparison between experimental and natural data points towards the chaotic mixing as a feasible process to reproduce their signatures. Particularly, for COD it stands for the majority of the analyzed elements. Comparing the averages from experimental and natural data, we conclude that CGDs are well represented as well. Both CGDs and CODs compositions would be generated during mixing processes involving the end-members of Exp1. However, CGD and COD diverge 10% in terms of interaction degree of basaltic and rhyolitic phases. In addition, results from Exp2 indicate that the involvement of multiple sources in the origin of Chapecó dacites is very likely.

The linear mixing models fails in to explain the mixing between very contrasting melts, which becomes evident from the parameter *f*. The variations in *f* depend on the pair and reflect non-linear dynamics, which is the assumption of this study. Therefore the experimental data presented here shows that the generation of Chapecó dacites through partial or total melting and assimilation of pre-existent crustal material (contaminants) might be simulated, followed, reproduced, attestable and well possible. Further studies on isotopic systems in the hybrid experimental glasses are still necessary and will help to understand more deeply the overview on generation of such expressive magmatic rocks.

CHAPTER 4 – CHAOTIC MIXING EXPERIMENTS: UNRAVELLING CONTAMINATION PROCESSES ON DACITIC MELTS (SUBMITTED TO GEOSCIENCE FRONTIERS)

Caio M. Vicentini[1, 2], Cristina P. De Campos[1], Werner Ertel-Ingrisch[1], Donald B. Dingwell[1], Leila S. Marques[2]

[1] Department of Earth and Environmental Sciences, Ludwig Maximilians University, Munich 80333, Germany
[2] Institute of Astronomy, Geophysics and Atmospheric Sciences, University of São Paulo, São Paulo 05508-090, Brazil

ABSTRACT

Mixing dynamics is thought to decisively influence volcanism on Earth. Using a chaotic mixing approach we experimentally studied the contamination of a Chapecó-Guarapuava high-Ti dacite (CGD) by a rhyolitic/granitic rock from the basement of the Paraná-Etendeka Magmatic Province (PEMP). The experimental apparatus, based on the Journal Bearing System, is operated at atmospheric pressure and a temperature of 1,500 °C. It simulates a dacitic magma chamber under the assimilation of crustal material. The experimental products (dry/bubble free glasses) show concentric folded and stretched filaments of contrasting compositions with a chaotic morphology. The fractal dimension calculated for the representative section is D_{box} = 1.60(3) and confirms that chaotic dynamics have been achieved. Further electron probe micro analysis (EPMA) clearly showed SiO_2 contamination, while Al_2O_3 data indicated lower levels of contamination. As a consequence, different elements depict dissimilar curves in chemical transects. We used the parameter σ_n^2 (normalized variance) to quantify the mixing efficiency and differential mobilities. In addition, our data reproduced the chemical behaviour of some elements in Chapecó-Ourinhos dacites (COD), especially those that usually act as network formers in melts such as Fe, Al, Ti and Si. EPMA analyses revealed clear deviations from the linear mixing model suggesting a selective contamination process. Finally, the calculated elemental mobilities expected for the

CGD-COD end-members support the generation of COD from the interaction of CGD pre-existing melts with crustal rocks from the PEMP basement via chaotic dynamics.

Keywords: chaotic dynamics; dacitic contamination; journal bearing system at high-temperature; magma mixing; Paraná-Etendeka Magmatic Province.

4.1 INTRODUCTION

Mixing of silicate melts is a widely observed phenomenon in igneous petrogenesis (Morgavi *et al.*, 2022). Evidence for magma mixing can be found on many scales. It is responsible for a large compositional variability in rock suites as well as for triggering volcanic eruptions (e.g., Anderson, 1982; Bateman, 1995; Leonard *et al.*, 2002; Perugini *et al.*, 2010; Tomiya *et al.*, 2013). On their way to the surface or during residence in magma chambers, andesitic and dacitic melts may easily be in contact with granitic crustal materials (e.g., Eichelberger, 1974; Bidias *et al.*, 2018; Chen *et al.*, 2020). The extent of the chemical interaction between these materials remains a topic of debate, particularly among petrologists and volcanologists. Field observations point to chaotic dynamics controlling mixing processes (Flinders and Clemens, 1996; Perugini and Poli, 2000; De Rosa *et al.*, 2002; Perugini *et al.*, 2003a,b). Volcanic suites present structures that have been discussed in terms of their fractal geometry (Perugini and Poli, 2000; De Rosa *et al.*, 2002; Perugini *et al.*, 2003b), which clearly points towards a chaotic dynamic process.

An experimental apparatus based on the Journal Bearing System *JBS* (Swanson and Ottino, 1990) has proven capable of reproducing chaotic dynamics under controlled conditions (i.e., high temperature and mixing protocol able to produce chaotic conditions). However, mixing experiments involving natural basalt–rhyolite systems were not able to reproduce the theoretically patterns predicted by chaotic dynamics (e.g., Poincaré sections) (Morgavi et al., 2013a,b; Vicentini et al., 2023). This work reproduced, for the first time, such patterns on representative sections of a dacite-rhyolite natural system. The generated patterns are comparable to field observations by means of fractal dimensional analysis. Associated to the chemical patterns, the results enable new insights on rock generation.

4.1.1 GEOLOGICAL SETTINGS

The Paraná-Etendeka Magmatic Province (PEMP; Figure 4.1) is the second largest igneous province (LIP) on Earth. It was formed ca. 133 Ma ago (Piccirillio and Melfi, 1988; Marzoli *et al.*, 1999; Janasi *et al.*, 2011; Gomes and Vasconcelos, 2021) covering an area of ca. 10^6 km² (Frank *et al.*, 2009). Basalts are the most common rocks ($SiO_2 \approx 50$ wt.% in their composition), which can be divided into two groups: one with lower TiO_2 contents ($TiO_2 < 2$ wt.%; low-Ti), and one consisting of higher TiO_2 contents ($TiO_2 \geq 2$ wt.%; high-Ti). Subsidiary dacites and rhyolites (i.e., $SiO_2 \geq 63$ wt.%) occur associated with each basaltic group (only 2.5% by area). The most accepted hypothesis for the origin of these evolved rocks is the differentiation from basalts with similar TiO_2 contents and the interaction with other crustal rocks (Piccirillo *et al.*, 1987; Piccirillio and Melfi, 1988; Garland *et al.*, 1995; Paete, 1997).

The high-Ti dacites from PEMP are termed the Chapecó dacites. They are porphyritic, and enriched in K_2O, P_2O_5, Ba, Nb, Zr, Y, and REE (La, Ce, Nd, Yb, Lu), and depleted in Rb, Th, and U, relatively to the low-Ti rhyolites from PEMP, the so-called Palmas rhyolites. Chapecó dacites can be subdivided into two main groups named Chapecó-Guarapuava (CGD) and Chapecó-Ourinhos dacites (COD). The CGDs exhibit lower contents of SiO_2, total alkalis ($Na_2O + K_2O$), incompatible trace elements Rb, Ba, Th, U, and Pb, and initial $(^{87}Sr/^{86}Sr)_i$ ratios (approx. 0.7060) relative to COD. It also presents higher amounts of TiO_2, Fe_2O_{3t}, MgO, P_2O_5, as well as Sr, Zr and Y. Due to its higher Sr_i isotopic ratios, the CODs are considered to be contaminated with crustal material (approx. 0.7085) relative to CGD (Piccirillo *et al.*, 1987; Garland *et al.*, 1995; Nardy et al., 2008; Freitas, 2009).

4.1.2 MOTIVATION AND GOALS

The present study aims to experimentally verify the role of chaotic dynamics on the formation of Chapecó-Ourinhos dacites (COD). As these rocks are compositionally similar to CGDs, the hypothesis whether CODs could be formed from CGDs during ascent and/or replenishment events has been evaluated. This hypothesis is supported by: i) the reported existence of distinct crystal populations in Chapecó dacites (e.g., anticrystals and/or xenocrystals suggested by Luchetti *et al.*, (2018)); and ii) the higher

Sr_i isotopic ratios. These are a clear signs of assimilation of crustal material during CODs evolution. In this respect, it is worth noting that our experimental set is able to mimic the ascent of magmatic phases towards a magma chamber and/or the replenishment within it. Thus, we present here the first experimental attempt to reproduce the interaction between and mutual contamination by dacitic and rhyolitic melts under controlled conditions via chaotic dynamics, and using as end-members natural materials from the same province.

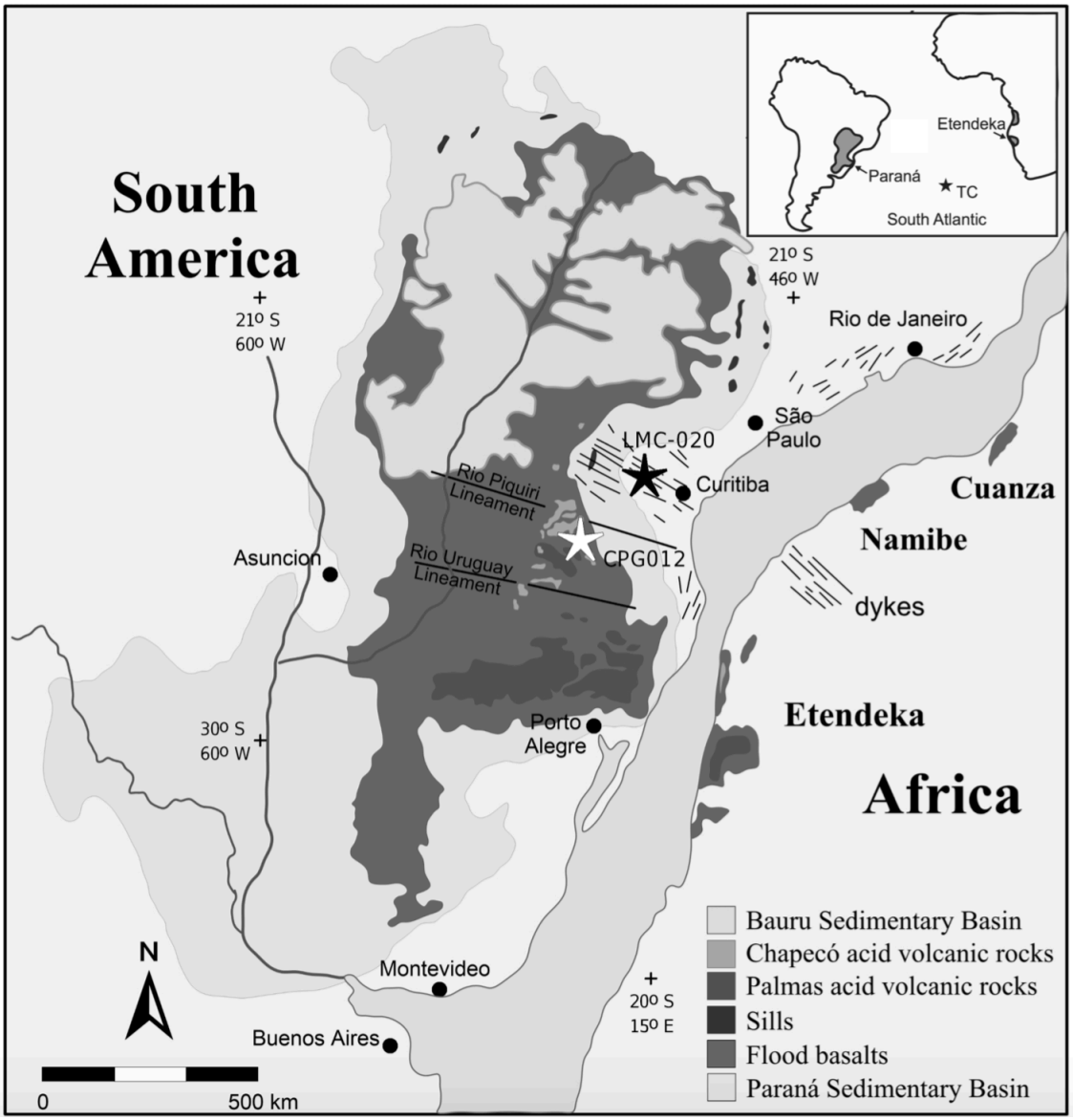

Figure 4.1: Map of Paraná-Etendeka Magmatic Province (PEMP) with sample location. Stars represent the end-members: black – contaminant (granite) and white – high-Ti Chapecó-Guarapuava dacite (CGD). Based on Nardy *et al.* (2008), Machado *et al.* (2018) and references therein.

4.2 METHODS

4.2.1 SAMPLE PREPARATION AND ANALYSIS

The performed chaotic mixing experiment was conducted using two end-members (reported in Vicentini *et al.*, 2023) from the PEMP: i) a Chapecó-Guarapuava dacite CPG-012; and ii) a monzogranite from Cunhaporanga batholith LMC-020 (which crops out at the eastern border of the PEMP basement). A total of 200 g of each end-member was crush to a powder and then melted at 1,600 °C in a Pt_{80}-Rh_{20} crucible in a $MoSi_2$ box resistance furnace, equipped with a viscometer, which was used to homogenize the formed melt by stirring, and subsequently cooled down to room temperature resulting in a glass free of volatiles, bubbles and crystals. Details on the homogenization process are given by Dingwell (1986) and Morgavi *et al.* (2013b). Table 1 shows the initial chemical composition with some relevant physical properties of the starting components.

The major oxide concentrations of the glassy samples obtained were measured using a Cameca SX100 electron microprobe at the Department for Earth and Environmental Sciences of the Ludwig Maximilian University Munich (DEES/LMU). Analytical conditions were accelerating voltage of 15 kV at a probe current of 5 nA with a beam size of 5 μm. To minimize potential loss of alkali elements (especially Na and K) during analysis, these elements were measured first. Precision was calculated using the standard deviation *std* of *N* individual analyses performed over starting materials (Table 4.1). Calculated uncertainties *std* (i.e., 1σ) are lower than 5.3% for all analyzed elements, except for P (= 10%) and Mn (= 20%) due to their by far lower concentrations approaching the detection limits of the EPMA. Accuracy is reported to be within 3% relative for all elements (MPI-DING glasses – Jochum *et al.*, 2000). The standards used were: synthetic wollastonite (Ca), periclase (Mg), Fe_2O_3 synthetic (Fe), natural orthoclase (Al, K), albite (Si, Na), apatite (P), ilmenite (Ti) and bustamite (Mn). Matrix correction was performed using the PAP procedure (Pouchou and Pichoir, 1984).

4.2.2 CHAOTIC MIXING EXPERIMENTS

4.2.2.1 CONCEPT

The chaotic mixing experiment was performed using a custom-built chaotic mixing (CM) apparatus developed by De Campos *et al.* (2011) based on the Journal Bearing System (*JBS*; see Swanson and Ottino, 1990). A graphic sketch is shown in Figure 4.2. This CM apparatus is capable to generate chaotic flow patterns based on its well-defined geometry and a specific mixing protocol for a crucible in relation to a spindle placed off-centre. Crucible and spindle can be rotated independently of each other. By applying a special mixing protocol (see below), the starting components are mingled by stretching and folding processes, resulting in flow lines and mixing patterns within the melt which are analyzed on quenched samples after the experiment is terminated.

The concept of the experiment (and further analysis) is based on the one-dimensional advection-diffusion equation:

$$\frac{\partial n_C}{\partial t} + V_{\hat{x}}.\nabla n_C = D\nabla^2 n_C \qquad \text{Eq. (4.I)}$$

where $\partial n_C/\partial t$ is the variation of the particle density n_c in time t (i.e., particle flux); $V_{\hat{x}}$ is the vectorial velocity field (i.e., î direction) to which such particle is subjected; D is the diffusivity; and ∇ is the divergence operator. It is worthy to mention that D is viscosity dependent (e.g., Zhang et al., 2010).

Eq. (4.I) expresses that the physical mingling starts from the spindle and crucible rotations (i.e., terms on the left side). The emerging filaments are continuously stretched and folded. This process increases the contact surfaces while the filaments are getting systematically thinner. Finally, this thinning reaches a sufficiently small length scale that exponentially enhances the diffusion efficiency (i.e., the term on the right side).

Prior to the experiment starts, the pre-machined samples are mechanically juxtaposed inside a Pt_{80}-Rh_{20} crucible that is then positioned in the hot spot region of a well-calibrated high-temperature oven (Figure 4.2). During the experiment the contact surface between the samples will deform mainly due to the motion protocol, forming

new contact areas and enhancing the diffusion. Melt parameters such as viscosity, density, wetting/surface tensions, influence the mixing between silicate melts, however Eq. (4.I) well represents this process as it considers advection (i.e., stretching and folding) and chemical diffusion (i.e., compositional gradients) (Perugini *et al.*, 2003b; De Campos *et al.*, 2011).

4.2.2.2 APPARATUS AND PARAMETERS

Figure 4.2 illustrates the geometry of experimental apparatus. Two motors execute the motion protocol: (i) the upper (inner) motor fixes and rotates an off-centered spindle that is extending throughout the entire vertical sample height; and (ii) the lower (outer) motor fixes and rotates the Pt_{80}-Rh_{20} crucible containing the starting materials. The system was designed to enable independent rotations of inner and outer cylinders at variable speeds, directions and stirring protocols. The protocol used to generate the chaotic streamlines is: (i) two clockwise rotations of outer motor (within 35 min); (ii) six anticlockwise rotations of inner motor (within 18 min); (iii) two clockwise rotations of outer motor (within 35 min); (iv) six anticlockwise rotations of inner motor (within 18 min). The total run duration of the experiment is 106 min of non-simultaneous and independent movements, resulting in chaotic flow lines. For details on experimental apparatus see De Campos *et al.* (2011).

Prior to the experiment, two vertical cylindrical holes were drilled into the dacitic glass within the Pt_{80}-Rh_{20} crucible. The dimensions of the holes are selected such that the relative proportions of the end-members (i.e., dacite to rhyolite) results in a ratio of 80-20, simulating a scenario where a dacitic magma body comes into contact with a rhyolitic magma body during its emplacement. In Figure 4.2, the location of the rhyolitic glass is shown. A glass cylinder made of the homogenized material is inserted into one of the holes and the spindle (Al_2O_3 sheathed in Pt foil) is inserted into the second hole. The entire setting is then transferred into the hot spot region of a well-calibrated high-temperature tube furnace, connected to the external mechanical drives and then heated to run conditions (T_{exp} = 1,500 °C at atmospheric pressure). The temperature chosen enables significant mingling and mixing of the two melts. Although it is higher than the actual temperatures expected to be encountered in the natural process, the absence of volatiles in the experiment counteracts the effect of temperature

on lowering the viscosity. As a consequence, the final viscosity conditions are approximately those expected for the natural system (e.g., Giordano *et al.*, 2021). At 1,500 °C, measured viscosities and calculated densities (Lange and Carmichael, 1987) for dacitic and rhyolitic initial glasses are given in Table 4.1. The viscosity ratio between starting materials at 1,500 °C is η_{rhy}/η_{dac} = 10.3.

Table 4.1: Starting composition of dacitic and rhyolitic end-members reported in Vicentini *et al.* (2023), respectively, CPG-012 and LMC-020, and respective relevant physical properties at experimental temperature T_{exp} = 1,500.0 ± 0.5 °C. Uncertainty *std* refers to one standard deviation (i.e., 1σ) of *N* chemical analyses on starting glasses. Units: oxide composition = weight percent [wt.%]; viscosity η = [Pa.s]; density ρ = [g/cm³] calculated according to Lange and Carmichael (1987).

	CPG-012	***std* (*N*=18)**	**LMC-020**	***std* (*N*=20)**
SiO_2	64.74	0.55	70.64	0.24
TiO_2	1.58	0.11	0.44	0.07
Al_2O_3	13.46	0.16	14.90	0.14
Fe_2O_{3t}	7.74	0.27	2.75	0.14
MnO	0.15	0.06	0.05	0.04
MgO	1.39	0.07	0.84	0.04
CaO	3.17	0.16	2.14	0.09
Na_2O	3.06	0.10	2.96	0.11
K_2O	4.26	0.13	5.08	0.12
P_2O_5	0.44	0.06	0.19	0.04
Physical Properties at T_{exp} = 1,500 °C				
	CPG-012	***std***	**LMC-020**	***std***
η_{1500}	200	3	2052	31
ρ_{1500}	2.31	0.02	2.30	0.02

Upon reaching the run temperature, the experimental deformation is initiated by turning on the computer control and activating the pre-set mixing protocol. During the experiment, the end-members mingle, creating new net contact surface between them, as deformation occurs determined by the motion protocol. Contact areas undergo stretching and folding, whereas forming filaments that become systematically thinner. This enhances the efficiency of chemical diffusion and leads the system towards homogenization.

At the end of the experiment, the furnace power is switched off resulting in a cooling off the mingled and partially mixed melt assembly to a heterogeneous glassy sample at an initial cooling rate of 85 °C/min. At room temperature, the crucible is recovered, the spindle is severed just about the sample surface, and the glass sample containing the spindle tip is cored out from the crucible using a diamond saw. The recovered glass cylinder (approx. 23 mm diameter and approx. 4.5 cm height) is sectioned perpendicular to the rotation axis into sections of 2.5 mm thickness. The nomenclature of sections is according to their original position in the cylinder, ranging from 0 (located at crucible bottom) to 15 (crucible top), followed by "top". Section 9top was used for microscopic and subsequent EPMA.

4.3 RESULTS

4.3.1 MORPHOLOGICAL FEATURES

The experimental sections exhibit complex patterns of non-centered lamellar and vortex structures. In general, the morphology is in agreement with previous studies performed using a synthetic basalt-rhyolite system (e.g., De Campos *et al.*, 2011; Perugini *et al.*, 2012), containing remarkable stretched and folded arms of initial end-members. Figure 4.3 displays the results of optical and scanning electron microscopic (SEM) investigations of section 9top (respectively 4.3a and 4.3b). Both images illustrate that the structures consist of rhyolitic lens-like filaments (dark) alternating with dacitic filaments (light) in the mixed system. Figure 4.3a (SEM image) illustrates that the contrast between the phases is less clear, with the rhyolitic end-member apparently occupying a smaller area compared to the optical image. Figure 4.3b was taken using a Carl Zeiss Discovery V.8 microscope under reflected light and reveals distinct morphological aspects around the spindle hole in comparison with the region above it. Filaments tend to be more concentric, stretched and diffuse proximal to the spindle, while the thickest arms, strongly folded and more preserved are observed at the top part of section 9top.

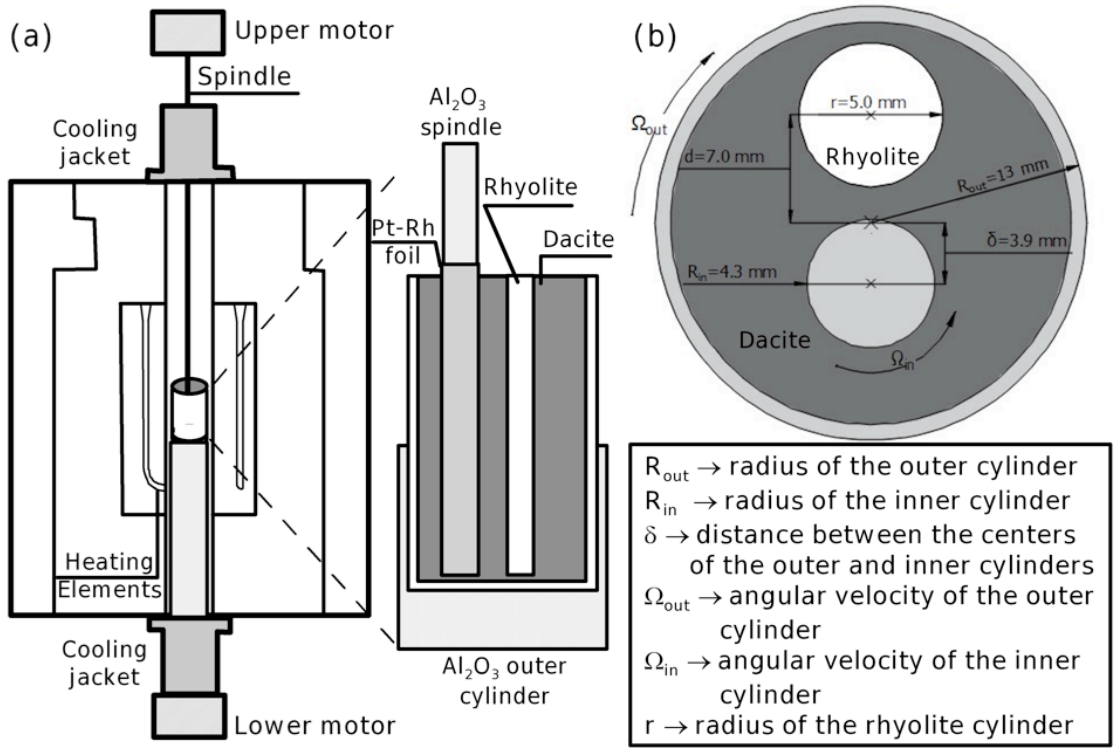

Figure 4.2: Schematic cross section of the chaotic mixing (CM) device and the experimental setup: a) CM apparatus composed by the vertical tube furnace in where the sample is placed, and the upper and lower motors adapted to independently rotate, respectively, the spindle and the Al_2O_3 outer cylinder; b) 2D-sketch detailing the particular geometry of this experiment (the crucible upper view). Details about the experimental setup can be found in De Campos *et al.* (2011).

At the right side of the spindle hole (comp. dashed square) one circular rhyolitic body is visible. Regions with similar shape have been recognized and classified as coherent regions (CR: Ottino, 1989; Perugini *et al.*, 2003b), in where mixing is less efficient. A thin filament comes out from this body circling the spindle hole until it intersects two other thin and, more or less, concentric filaments, one at the left and other at the right side of the circular body, forming an eye-like structure. Strongly stretched and folded filaments are characteristic of active regions, where mixing is well established (AR: Ottino, 1989; Perugini *et al.*, 2003b). The eye-like feature is well delineated and observed under reflected light, yet poorly visible in the SEM image. Since SEM is a technique that measures density contrasts, Figure 4.3a suggests that diffusion occurred more effectively and the composition is expected to be more homogenous in this part of the section, although optical observations may lead to

different interpretation. Subsequent EPMA was performed along the white line in Figure 4.3, starting at point T1 and extending over the entire length to the section rim.

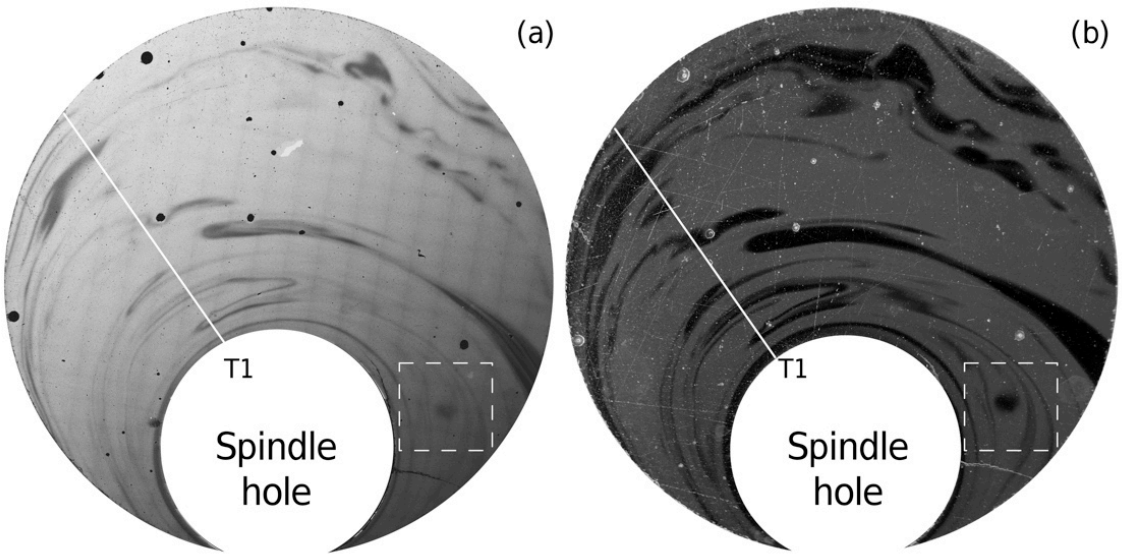

Figure 4.3: a) Section 9top analyzed by scanning electron microscopy (SEM); b) Section 9top analyzed by optical binocular under reflected light. White line: the chemical transect T1 analyzed by electron microprobe (EPMA); dashed square: eye-like structure (see text for details).

4.3.2 FRACTAL DIMENSION OF EXPERIMENTAL PRODUCTS

Self-similarity has been appointed as a fundamental characteristic in geological settings, meaning that the geometrical patterns arise in nature independently of their scale (Ottino *et al.*, 1993; Perugini and Poli, 2000; De Rosa *et al.*, 2002; De Campos *et al.*, 2011). One simple manner of studying these patterns is to apply the "box-counting" method (Mandelbrot, 1982) on an image to calculate its fractal dimension. This approach has been used in both geological (Perugini and Poli, 2000; Guimarães *et al.*, 2018) and experimental environments (De Campos *et al.*, 2011; Morgavi *et al.*, 2013b). The "box-counting" method consists of the division of the total area of an image in N square boxes of side length r, and counting the number of boxes N_r containing pixels referring to the interface between contrasting bodies. The fractal dimension D_{box} behaves according to the equation:

$$N_r = r^{-D_{box}} \quad \text{Eq. (4.II)}$$

Applying a logarithmic form result in a linear expression of both sides:

$$\log\ (N_r) = -D_{box} * \log\,(r) \quad \text{Eq. (4.III)}$$

As consequence, varying the side *r* of the box and plotting over N_r on a log-log diagram, the data lies on a straight-line and the slope of this line is an estimative of the fractal dimension D_{box}.

Applying the "box-counting" method, Figure 4.3b was treated using "ImageJ" software (Abramoff *et al.*, 2004) to generate the binary image (i.e., black and white) shown in Figure 4.4, which highlights the interface dacite-rhyolite. The resultant fractal dimension was D_{box} = 1.60(3). Comparing with available experimental data, the value is consistently higher than D_{box} = 0.91 obtained for synthetic sample experiments (De Campos *et al.*, 2011), and is within the interval 1.15 < D_{box} < 1.68 found analyzing experiments with natural samples (Morgavi *et al.*, 2013b). It is important to note that these experiments were performed using end-members with higher viscosity contrasts (i.e., basalt and rhyolite) than the end-members of the present study (i.e., dacite and rhyolite). As a consequence, the result for dacite-rhyolite system after a 106 min experiment is comparable to those presented for basalt-rhyolite systems after longer run durations (i.e., 212 min – Morgavi *et al.*, 2013b).

With respect to natural occurrences, a wider range can be observed: 1.01 < D_{box} < 1.84 (De Rosa *et al.*, 2002); 1.67 < D_{box} < 1.92 (Perugini *et al.*, 2003b); 1.39 < D_{box} < 1.62 (Guimarães *et al.*, 2018); 1.32 < D_{box} < 1.42 (De Campos, 2015). The present result of D_{box} = 1.60(3) lies well within this range, and is practical identical to D_{box} = 1.62 obtained for PEMP outcrops (Guimarães *et al.*, 2018). It generically points to a better agreement with more complex scenarios (i.e., longer linear interfaces), thus representing higher degrees of mixing (i.e., higher D_{box} according to De Rosa *et al.*, 2002).

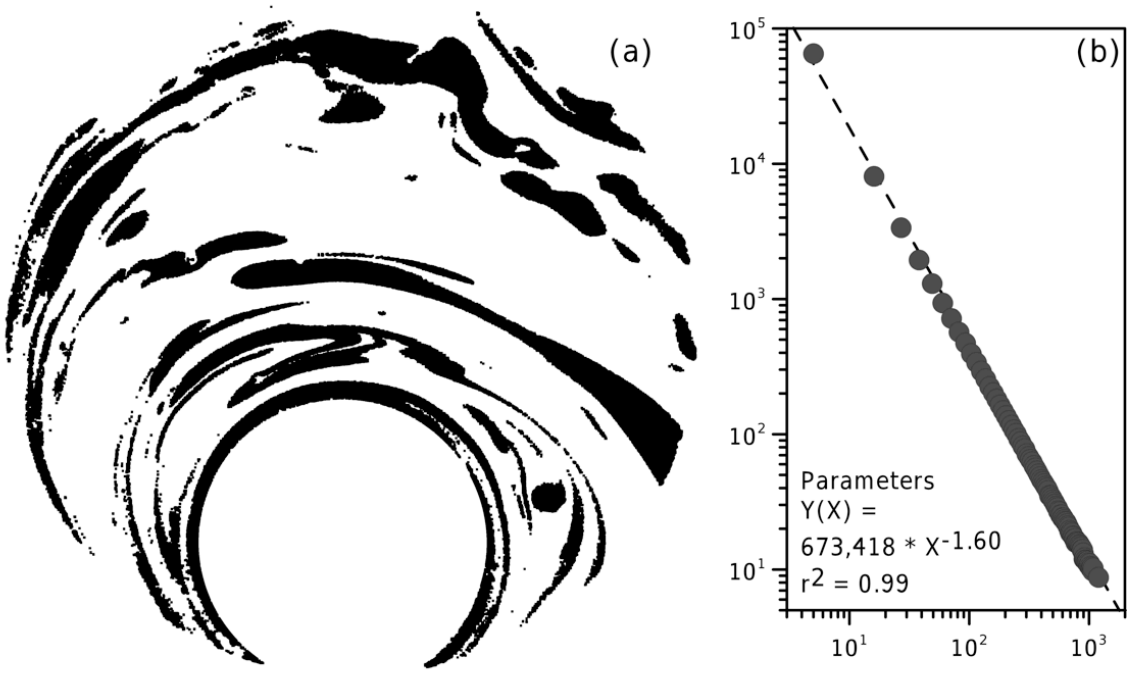

Figure 4.4: a) Binary image generated on ImageJ software and used to evaluate the fractal dimension of section 9top; b) Log (N_r) versus log (r) diagram showing the result of the linear interpolation D_{box} = 1.60(3).

4.3.3 GEOCHEMICAL ANALYSIS

The major oxide compositions along the transect T1 are displayed in Figure 4.5. Dark and light grey bars represent, respectively, the intervals of rhyolitic and dacitic initial compositions (EPMA determinations on starting materials). The error bars shown for selected points in Figure 4.5 correspond to 1σ. Figure 4.5 does not include data for MnO due to its low concentration level (i.e., the highest uncertainties), and for Na_2O since the initial small gradient (Table 4.1) represents a pre-experimental artefact.

Figure 4.5: Chemical analyses performed by EPMA on the representative transect T1 (white line in Figure 4.3). Concentrations are given in [wt.%]; dx = 40 μm; N = 141 points. Legend: dark and light horizontal grey bars represent, respectively, the interval of rhyolitic and dacitic starting compositions including their uncertainties (= ±1σ); the vertical grey area between points 150 and 200 indicates data plotted in Figure 4.7; error bars = ±1σ.

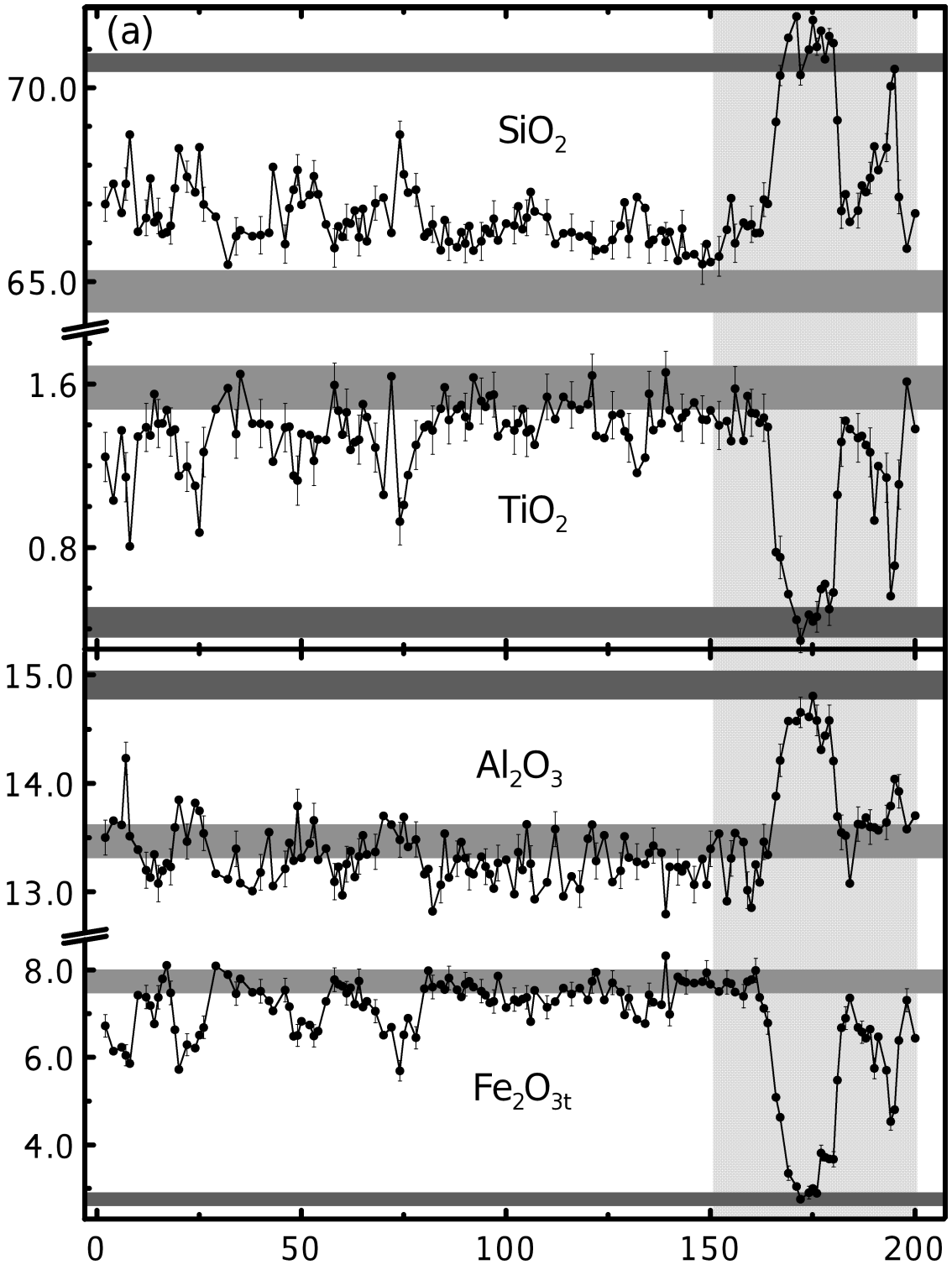
(a)
70.0
65.0
SiO2
1.6
0.8
TiO2
15.0
14.0
13.0
Al2O3
8.0
6.0
4.0
Fe2O3t
0
50
100
150
200

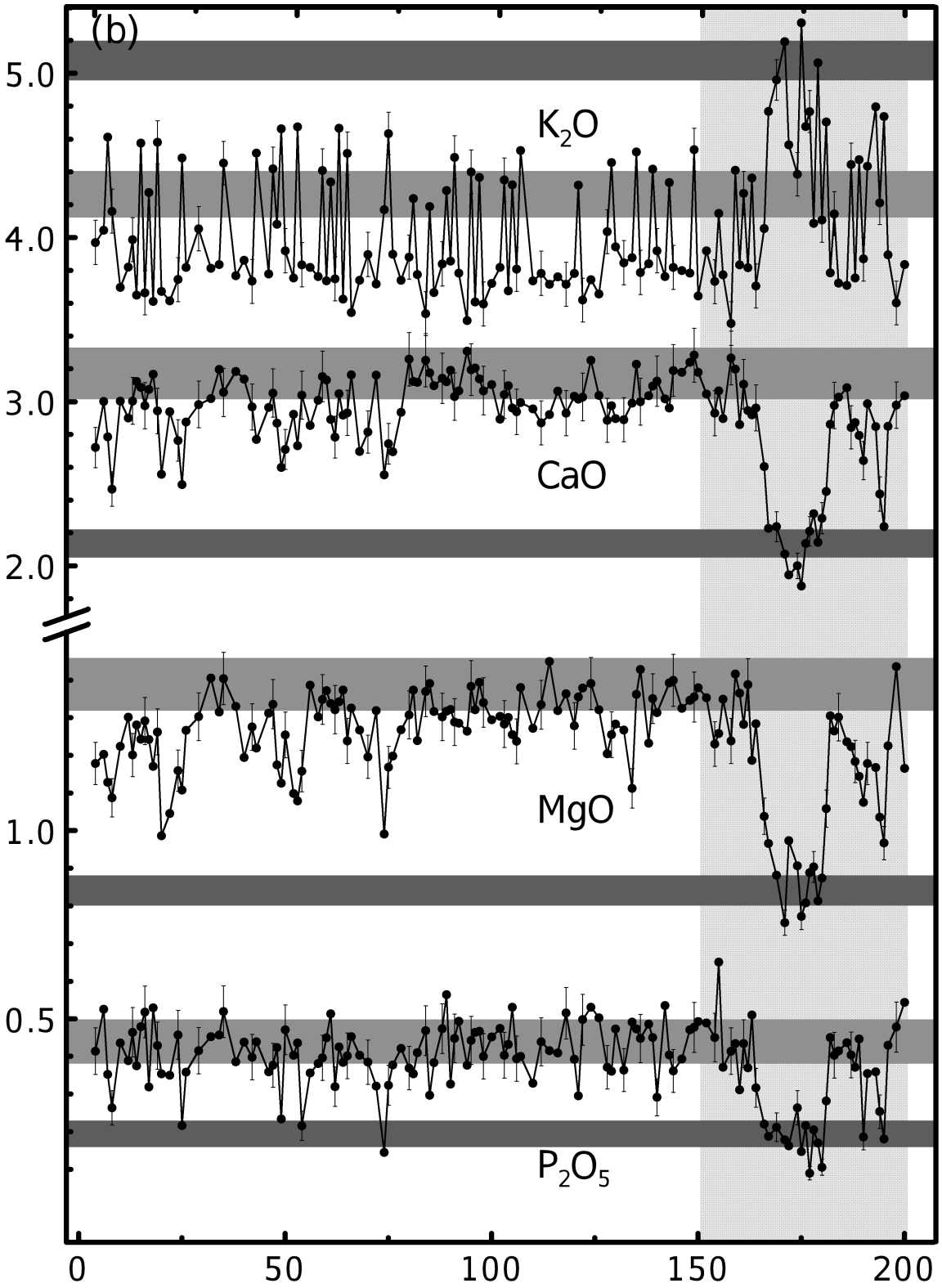

The general elemental behaviour in T1 as shown in Figure 4.5 is an oscillatory pattern with peaks corresponding to determinations on dacitic and rhyolitic portions. Regions in where mixing did not occur effectively should yield points lying within the

grey bars (i.e., starting material compositions), in contrast with portions where mixing is more effective exhibiting points lying in between. The mixing degree is proportional to the amplitude, meaning that a flat curve corresponds to local complete homogenization and, hence, maximum mixing efficiency. Along the measurement points 1 and 150 (x axis), a large number of points lie on dacitic composition for all compounds, except from SiO_2. The chemical transect indicates the dacitic glass was contaminated with SiO_2 resulting in concentrations higher than starting interval. Two segments in T1 can be identified: i) points 1 to 80; and ii) points 81 to 150. Comparing both segments, one realizes that i) shows more scattered data than ii), reaching the local maximum (SiO_2 > 68%) and minimum (TiO_2 < 1.0%, Fe_2O_{3t} < 6.0%, CaO < 2.6%, MgO < 1.1 and P_2O_5 < 0.2%) three times (i.e., close to points 10, 25 and 75). Supporting this observation, Table 4.2 shows the calculated average content and its respective standard deviation for segments i) and ii). Standard deviations indicate the dispersion in portion i) is up to 2 times higher for SiO_2, TiO_2, and Fe_2O_{3t} and approx. 1.5 times higher for MgO and CaO in comparison with portion ii). At the end of T1 ($151 < x \leq 200$), all chemical compounds display a well-delineated curve, whose principal peak is at approx. 175 revealing a well-preserved rhyolitic filament. The EPMA data also point an anomalous enrichment of SiO_2, TiO_2, CaO, MgO and P_2O_5 compared with the original rhyolitic concentration, which was unexpected.

Table 4.2: Average and respective standard deviation of T1 chemical analyses. Segment i) corresponds to points 1 to 80, and ii) refers to points 81 to 150.

	SiO_2	**TiO_2**	**Al_2O_3**	**Fe_2O_{3t}**	**MgO**	**CaO**	**K_2O**	**P_2O_5**
i)	66.93	1.31	13.40	7.02	1.24	2.92	4.02	0.39
std	0.77	0.18	0.25	0.62	0.10	0.19	0.35	0.08
ii)	66.24	1.44	13.24	7.49	1.33	3.07	3.95	0.43
std	0.42	0.10	0.19	0.32	0.07	0.12	0.31	0.07

4.3.4 ELEMENTAL MOBILITY

The concentration variance (σ^2) is a quantity commonly used to evaluate the mixing degree in fluid dynamics (Liu and Haller, 2004; Perugini *et al.*, 2015; Rossi *et al.*, 2017). It is defined as:

$$\sigma_{C_i}^2 = {\sum_{k=1}^{N}\left(C_k^i - \mu_i\right)^2}\Big/{N} \qquad \text{Eq. (4.IV)}$$

where N is the number of samples, C^i is the concentration of element I and μ is the mean composition of element i. For purposes of comparison, variance ($\sigma_{C_i}^2$) defined by Eq. (4.IV) must be normalized due to its dependency on the absolute values of elemental concentration that range from a few to tens of percent in silicate melts (e.g., TiO_2 in comparison with SiO_2). Thus, the initial variance (σ_0^2) of each element (i.e., before the mixing experiment) can be used as the normalizing parameter. The normalized variance of concentration σ_n^2, or here named normalized variance, is then defined as:

$$\sigma_n^2 = {\left(\sigma_{C^i}^2\right)_t}\Big/{\left(\sigma_{C^i}^2\right)_{t=0}} \qquad \text{Eq. (4.V)}$$

where $\left(\sigma_{C^i}^2\right)_t$ and $\left(\sigma_{C^i}^2\right)_{t=0}$ are the concentration variance of a given chemical element C^i at time t (i.e., t_{exp} = 106 minutes) and time t = 0 respectively. The initial variance $\left(\sigma_{C^i}^2\right)_{t=0}$ was calculated using the end-member compositions reported in Table 4.1 and Eq. (4.V) was applied to the dataset shown in the transect T1. This approach has already been applied systematically and successfully in previous experiments (De Campos *et al.*, 2011; Perugini *et al.*, 2012; Morgavi *et al.*, 2013a,b).

Figure 4.6 compares σ_n^2 and the field strength of corresponding element. The field strength is defined as the nominal charge Z of the element divided by the distance between metal cation and oxygen at room temperature R^2 = d(M-O) at 298 K (after Brown Jr *et al.*, 1995). The equation of the line corresponding to the linear fitting of data (with the exceptions of K and P) indicates no trend of σ_n^2 with increasing field strength within the uncertainties. Analyzing elements according to their typical functionality within the melt structure, such as network modifiers (Na – data not applicable in this study, K, Ca and Mg: KCM group), σ_n^2 shows a strong drop from K to Ca, followed by an only minor decrease between Ca and Mg. In contrast, network forming elements (Fe, Al, Ti, and Si: FATS group) display only σ_n^2 minor changes between them considering their uncertainties. It indicates a very similar behaviour of

FATS during approach to equilibrium. Finally, σ_n^2 increases again from Si to P by nearly a factor of 2.

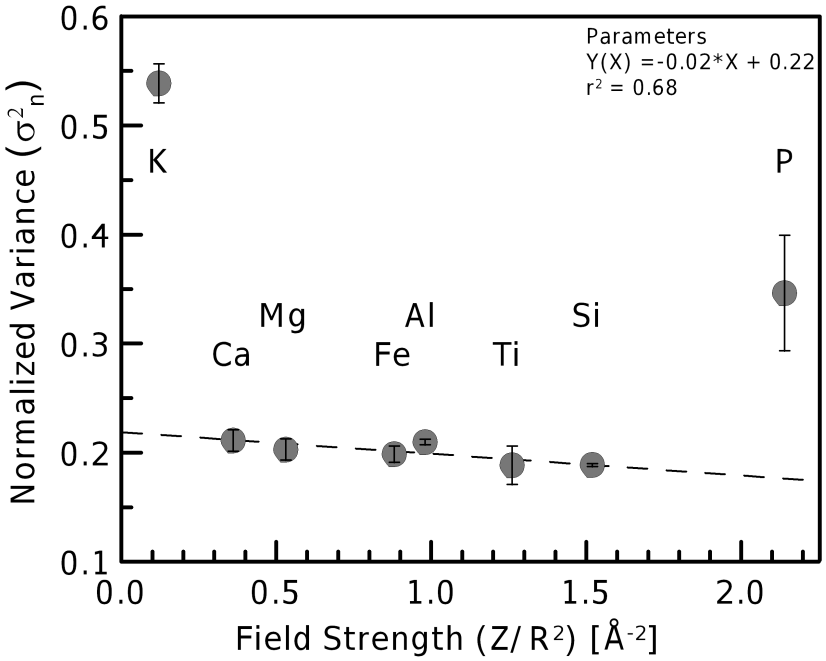

Figure 4.6: Variation of the major oxide normalized variances σ_n^2 as a function of the field strength (elemental nominal charge Z divided by the ionic radius squared R^2 – after Brown Jr *et al.*, 1995). The equation of the curve corresponding to the linear fit (with the exception of K and P) and the relative correlation coefficient are also reported. Error bars = ± 1σ.

4.4 DISCUSSION

The results are analyzed with experimental and natural studies with respect to their morphological aspects, and their chemical behaviour and elemental mobility as well.

4.4.1 COMPARING CHAOTIC MIXING PATTERNS

According to Figure 4.3, T1 crosses a large number of filaments with different thicknesses that would result in an amplification of the oscillatory pattern. For the case where filaments are only mingling (i.e., without chemical diffusion), the chemical analysis would show two compositional alternating plateaus abruptly interrupted in their interface (i.e., a maximum amplitude). However, chemical exchanges are evident and

occur over all transects. Figure 4.3 clearly indicates that segment i) starts near to the spindle hole and continues in direction towards the section edge, while crossing several filaments. These filaments are visible both in optical and SEM images in Figure 4.3, although blurred (= less visible) in Figure 4.3a. Instead of the predicted abrupt step after $x = 25$ and $x = 75$, a relatively smooth increase of TiO_2, Fe_2O_{3t} and MgO is observed. This "S"-shaped curve is characteristic for a diffusion related exchange process (e.g., Crank, 1975). Additionally, the segment ii) intersects one well-preserved filament which is more predominant in Figure 4.3b, although not evident in the transect. The best match between observed filament structures from Figures 4.3 and data shown in Figure 4.5 is found at the end of T1. At this point the transect crosses two rhyolitic filaments, visible both in SEM and optical microscope images. Although optical observations clearly indicate the presence of unaltered and better-preserved filaments that are visible over a larger area (see Figure 4.3b), chemical analyses reveal a more effective diffusion process already in progress. This process progressively hinders the optical identification of clearly preserved filaments of initial composition (see Figure 4.3a), leading to smaller preserved areas. This outcome can be considered a consequence of chaotic dynamics.

Previous experiments performed using our CM device are directly comparable in respect to starting geometry, composition of end-members, experimental temperatures and run duration (= number of protocols). Therefore, all experimental products can be directly compared in respect to their general morphological aspects. Notice that minor deviations are considered meaningless since chaotic mixing systems are very sensitive to the initial conditions (Ottino, 1989). Table 4.3 summarizes general aspects of previous experimental studies conducted by Perugini *et al.* (2012) and Morgavi *et al.* (2013a,b) (P12, M13A and M13B respectively) using the identical CM apparatus as used here, and comparing qualitatively their results with our data (V23). The presence of mafic thin filaments is frequent inside a rhyolitic glass for all experiments, as the presence of felsic thick filaments or blobs (deformed or not) inside the mafic glass matrix as well. The main characteristic in P12 is filaments of alternating phases, whilst the presence of blocks and blobs is more remarkable in M13A and M13B. In this study, these three types of structure arise relatively proportionally.

Table 4.3: Comparison between main morphological features produced by chaotic mixing experiments. Complexity refers to the chemistry of end-members (low or high number of compounds). References: P12 = Perugini *et al.* (2012); M13A = Morgavi *et al.* (2013a); M13B = Morgavi *et al.* (2013b); V23 = this study. Symbols: n = number of cylinders; r = radius of cylinders in mm; F = felsic end-member; M = mafic end-member; T = temperature in Celsius degrees; t = experimental time in minutes; η_F/η_M = viscosity ratio between felsic and mafic phases.

Reference	P12	M13A	M13B	V23
Figure on refer.	6a	2b	2c	3
Material	synthetic	natural	natural	natural
Complexity	low	high	high	high
System (*F*-*M*)	rhyolite-basalt	rhyolite-basalt	rhyolite-basalt	rhyolite-dacite
Ratio (*F*/*M*)	65/35	80/20	80/20	20/80
Geometry (*n* x *r*)	3 x 3	1 x 5	1 x 5	1 x 5
T (°C)	1,400	1,400	1,350	1,500
t (min)	108	106	212	106
η_F/η_M	1,100	5,900	7,700	10
Dominant Morphological Features	continuous and strongly deformed bodies; lots of thin filaments	continuous and few deformed bodies; few and thick filaments	broken, multiple and deformed bodies; lots of thick filaments	continuous and strongly deformed bodies; lots of thin filaments

Nonetheless, the main parameter believed to control the degree of interaction between melts is the viscosity contrast, which is the ratio between viscosities of felsic η_F and mafic η_M phases – η_F/η_M. This parameter is dependent on composition and temperature. Degree of interaction means the ability of a melt to deform, penetrate and spread inside another by means of stretching and folding processes. Based on η_F/η_M parameter, the closest result should be P12 even with a difference of 2 orders of magnitude. The distribution of the thin filaments diverges, being more homogeneously distributed in P12, whilst they are more concentrated around the spindle hole in Figure 4.3. However, the visual equivalency is in better agreement with P12 than other experiments, evidence of the η_F/η_M influencing the final geometry of a certain section. It is worth to mention that by the first time a chaotic mixing experiment performed with contrasting natural end-members (i.e., more complexity), confirmed by further chemical analyses, resulted in morphologies similar to Poincaré sections (see Ottino, 1989), which is a way to numerically simulate the final configuration after the mixing protocol computing it from the starting parameters (as P12 achieved using synthetic materials).

Considering temperature, time and geometry, our results resemble those of M13A in some visual aspects. Microscopic images however diverge with respect to the degree of deformation of initial small cylinder (i.e., rhyolitic in V23 vs. basaltic in M13A), and the number and thickness of filaments (Table 4.3). This indicates that stretching and folding acted more effectively in V23 probably due to its comparatively lower η_F/η_M. The lack of information on a quantitative parameter (such as D_{box}) prevents further comparisons.

Visually comparing V23 with M13B, the similarities are restricted to the presence of multiple filaments. Nevertheless, fractal dimension of M13B is statistically equivalent to D_{box} calculated for Figure 4.4 (1.60 versus 1.68, respectively – see section 4.3.2 for details), which would argue for similar morphologies. However, M13B reported filaments of rhyolitic glass more fragmented and less deformed than in the present study. This implies that the interaction degree between melts (e.g., measured by D_{box}) can be equivalent for different scenarios in which the dominant morphological feature dramatically diverges (such as stretched and folded arms in V23 vs. blobs and blocks in M13B). It means the chaotic mixing protocol at high temperatures results in an increase of contact areas between the phases, and a consequent increase in mixing efficiency, independent of the final geometry.

4.4.2 COMPARING CHEMICAL ANALYSES AND ELEMENTAL MOBILITY

Figure 4.5 gives analytical results measured by EPMA. The comparison with previous studies points to more consistency with those performed over longer run durations (e.g., M13B). The most remarkable feature is the tendency of data plotting next to the bar representing the initial composition of the phase with more volume in the Pt_{80}-Rh_{20} crucible (i.e., dacitic in V23 and rhyolitic in P12 and M13B). Preserved (unaltered/pristine) starting materials appear as peaks or plateaus both in Figure 4.5 and previous studies. The evolution of the chemical composition between unaltered end-member phases appears in form of “S”-shaped curves, which is a typical feature of diffusion. However, the majority of the elemental composition in T1 shows a distribution that does not attain the original composition (i.e., before the experiment starts). It is a clear evidence that mixing was efficient and resulted in elemental signatures that are generally in between the end-member compositions to various

degrees. In contrast, TiO_2, Fe_2O_{3t}, CaO, MgO and P_2O_5 data demonstrate that dacitic melts are less susceptible to rhyolitic contamination than basaltic melts. T1 reveals a larger amount of data points that corresponds to the dacitic starting composition, whilst in basalt-rhyolite systems the basaltic starting composition is barely recognized in chemical transects. Nevertheless, observe that all data for SiO_2 plot above the grey bar in Figure 4.5 that represents the original dacitic signature. This feature is a clear indication of contamination, which means a selective contamination process is occurring in the dacite-rhyolite system.

Figure 4.5 also shows a strong scattering of K_2O, where a large number of points plots below the light grey bar, compared with that reported for basalt-rhyolite systems in P12, M13A and M13B. Aluminium shows a significant number of points lying bellow the light grey bar as well. Additionally, averages of K_2O contents for segments i) and ii) (Table 2) are about 5% lower than the dacitic initial content (Table 4.1). A potential explanation for these observations is that values of K are closer to the intermediate equilibrium in the present study before the experiment starts (Table 4.1), situation in where uphill diffusion can play a significant role (e.g., Watson and Jurewicz, 1984; Emmanuel *et al.*, 2004; González-Garcia *et al.*, 2018). In the case of Al, M13A suggested that this element is sensitive to uphill diffusion processes in chaotic mixing experiments. An alternative explanation for K results is that the alkaline elements are highly volatile and might have experienced substantial loss due to the higher experimental temperature (e.g., 1,500 °C versus 1,400 °C in M13A). Nonetheless, the general behavior of K measured along T1 is compatible with other elements, as duplicated by the appearance of one peak at x = 175 reaching even higher values than for the initial rhyolitic glass. It is worth to mention that points plotting out of the starting compositional range arise in P12 (e.g., K_2O) and M13A (e.g., FeO_t) as well.

Phosphorus was not analyzed in previous experiments. The absolute P concentrations in starting materials and the initial gradient are low. Based on the fact that determined P concentrations are close to detection limit of EPMA (approx. 0.06 wt.%), precise P determinations are harder to obtain and error bars are by far larger. Further, an increased viscosity of the corresponding melts might affect P. The originally dacitic phase is enriched in P and would loose this element during the interaction with the more viscous rhyolitic melt. However, an increase in viscosity would counteract the

attainment of equilibrium, leading to the preservation of P in the dacitic glass (Figure 4.5) and increasing σ_n^2 consequently (Figure 4.6).

To compare σ_n^2 in the systems, only the qualitative general behaviour should be considered. Basalt-rhyolite systems in P12 and M13B indicated an increase of σ_n^2 with the elemental field strength (positive slope), meaning the most mobile (i.e., to achieve first the equilibrium composition) elements are those with the smallest ratio Z/R^2. The influence of field strength in the present study slightly diverges from this pattern though. Figure 4.6 depicts the elements aligning in a slightly negative/constant slope (considering uncertainties) with the exception of K and P. The alkaline element K is a large (ionic radius IR = 1.51 Å – Shannon, 1976) and single-charged cation (small field strength), highly mobile and easily replaced inside the melt structure, and, therefore, exhibits a strong network modifying behaviour. For this reason, K should plot near to the lower values of σ_n^2 in Figure 4.6 instead presenting the highest σ_n^2 of 0.54. However, taking the assumption that alkalis were lost during the experiment, it is completely viable that this effect is responsible for the increase observed in the normalized variance of K. In this case, the denominator in Eq. (4.V) represents a smaller interval than that plotted in the Figure 4.5, which increases the ratio.

The alkaline earth elements, Ca and Mg, are smaller (IR_{Ca} = 1.00 Å and IR_{Mg} = 0.57 Å – Shannon, 1976) and double-positive charged cations (higher field strength compared with K). They present lower mobilities (e.g., M13A) and stronger bonding within the silicate network. As a consequence, they might exhibit similar values of σ_n^2 when compared with network forming cations (FATS). In basalt-rhyolite systems (e.g., M13A), σ_n^2 reported for Mg is similar to that for Ti and Si, whilst σ_n^2 for Ca is slightly smaller, and closer to Al. Using it as a reference, σ_n^2 for Ca and Al are comparatively higher than expected in the present study.

The differences observed in the elemental behaviour might also be related to the initial chemical gradients that play an important role for the melt interaction towards the equilibrium state. Particularly, SiO_2 dominates melt structure formation and strongly influences the melt viscosity. In basalt-rhyolite systems, the SiO_2 gradient is significantly greater (approx. 3 times higher), yielding higher chemical potential gradients as driving forces for homogenization.

4.4.3 PETROGENETIC IMPLICATIONS FROM CHAOTIC MIXING EXPERIMENTS

4.4.3.1 EFFECTS ON VARIATION DIAGRAMS

Figure 4.7 present variation diagrams that illustrate the effect of the differential mobility on chemical plots. Elements on the left column are plotted against SiO_2 (4.7.a, 4.7.c, 4.7.e, and 4.7.g), whilst elements on the right side are plotted against MgO (4.7.b, 4.7.d, 4.7.f, and 4.7.h). Stars and dashed lines represent, respectively, the composition of starting materials and their corresponding mixing line. Error bars (= ± 1σ) are drawn for representative points. We observe the scattering more pronounced in figures 4.7.e and 4.7.h in comparison with figures 4.7.a, 4.7.b and 4.7.f. This difference in the scattering degree also occurs comparing figures 4.7.c and 4.7.d, where Al_2O_3 is plotted against SiO_2 and MgO respectively. The points plot more dispersed around the dacitic starting composition (indicated by the light grey star) than closer to the rhyolitic end-member. It suggests that dacite is the first to be contaminated in contrast to the rhyolite.

The distribution of data along the mixing lines is also evident in Figure 4.7. Data systematically fall above these lines in figures 4.7.a, 4.7.f and 4.7.g, whilst consistently plotting below the curve in 4.7.e. In addition, figures 4.7.b-d and 4.7.h depict an "S" shaped curve. Points tend to increase from dacitic end-member towards the intermediate portion, where the curve changes its inflexion and turns to beneath the mixing line. In the final part, data increase towards the rhyolitic end-member composition.

The effects described here were reported in previous studies using more contrasting end-members (i.e., basalt-rhyolite mixing systems) and were attributed to a particular product of chaotic dynamics (De Campos *et al.*, 2011; Perugini *et al.*, 2012; Morgavi *et al.*, 2013a; Vicentini *et al.*, 2023). If two elements with similar mobilities are plotted against each other, the result is a straight line. However, during chaotic mixing experiments we observe elements with higher mobilities moving further then those less mobile elements. Particularly, the experimental time (e.g., 106 min) enhances this effect since the homogenization is incomplete. It results in non-linear paths on diagrams that display elements with distinct mobilities. Points systematically falling below (or above) the theoretical mixing curve indicate that the compounds reach the equilibrium concentration at different moments. This can be interpreted as a

contamination process where efficiency is element dependent. Elements with similar mobilities will plot near to the theoretical mixing line meaning similar contamination degrees. However, the diagram might show a deviation from the theoretical curve for pairs that contaminate at different degrees.

4.4.3.2 EXPERIMENTAL VERSUS NATURAL DATA

Next, we present the comparison of experimental results with COD compositions. For this goal, it is assumed that transect T1 is a valid representation of the global composition of our sample (total of 141 points analyzed). Table 4.4 provides averages of *N* samples of CGD and COD (Piccirillo *et al.*, 1987; Piccirillio and Melfi, 1988; Garland *et al.*, 1995; Nardy *et al.*, 2008; Freitas, 2009; this work). Comparing the concentrations, the average compositions of T1 (AC; N = 141) and COD are identical within the respective standard deviation (Na and Mn included). According to Nardy *et al.* (2008), COD and CGD can be discriminated in respect to their TiO_2 (COD < 1.4%) and P_2O_5 (COD < 0.4%) contents. Thirteen points of T1 (roughly 10% of the data) follow this criteria and their average (A13) are statistically identical to COD average as well. Referring to data on Table 4.2, the segments i) and ii) are indistinguishable from the COD mean.

Figure 4.8 shows the relative deviations (RD) when averages are normalized to a given parameter (e.g., COD average). The good correlation between segment i) and COD is evident. Segment i) crosses a region with multiple filaments, leading to increased chemical exchanges (i.e., contamination) between CGD and the rhyolite. The final composition is comparable to COD, with the FATS group showing differences of up to 7%. Segment ii) exhibits greater levels of scattering compared to segment i), with increased dispersion even for FATS (up to 18% to TiO_2). Figure 4.5 depicts that the majority of points in segment ii) lies on the grey bar that represents CGD. Thus, we expect that the contamination levels in this region should be significantly reduced. With respect to the elements K, Ca, and Mg (KCM group), the relevant differences that occur, mainly in segment ii) (e.g., 30% for MgO), might be explained by the fact that Chapecó dacites exhibit evidence of alteration (e.g., Nardy et al., 2008, Freitas, 2009; Luchetti et al., 2018). It may affect KCM more than FATS and could enhance the discrepancies. In

summary, the current data agree well with natural observations when contamination (i.e., chemical exchanges) is considered a viable process to produce COD compositions.

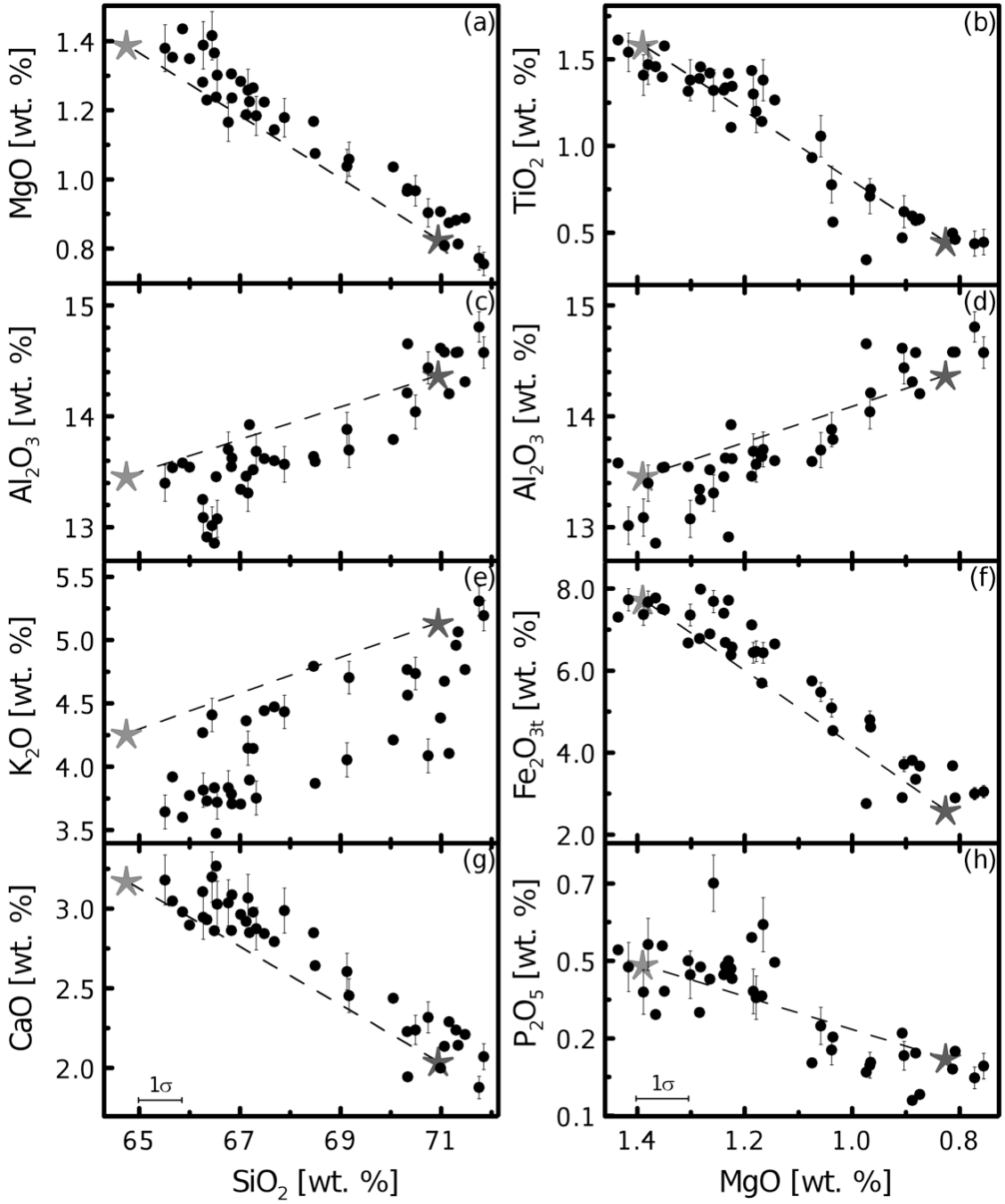

Figure 4.7: Variation diagrams showing the effect of the differential mobility. Data correspond to the vertical grey area in Figure 4.5 at the end of transect T1. Concentrations are given in [wt.%]; N = 40 points. Legend: dark and light grey stars represent, respectively, rhyolitic and dacitic starting compositions; dashed lines correspond to the linear mixing curves; error bars = ±1σ.

Table 4.4: Representative samples KS-1335 and PU-1005 from Chapecó-Guarapuava dacites (CGD) and KNO-436 from Chapecó-Ourinhos dacites (COD) (Nardy *et al.*, 2008) used in the calculation of σ_n^2; and average of CGD and COD for *N* samples (Piccirillo *et al.*, 1987; Piccirillio and Melfi, 1988; Garland *et al.*, 1995; Nardy *et al.*, 2008; Freitas, 2009; this work).

	KS-1335	**PU-1005**	**KNO-436**	**CGD (*N*=90)**	***std* CGD**	**COD (*N*=42)**	***std* COD**
SiO_2	63.46	64.40	69.12	65.33	0.73	67.05	1.07
TiO_2	1.47	1.49	1.19	1.48	0.07	1.22	0.08
Al_2O_3	12.99	13.36	12.78	13.06	0.34	13.11	0.44
Fe_2O_{3t}	8.51	7.83	6.05	7.48	0.41	6.72	0.43
MgO	1.73	1.30	0.41	1.33	0.16	1.00	0.27
CaO	3.56	3.02	1.71	2.99	0.22	2.48	0.47
K_2O	4.19	3.69	3.26	4.35	0.27	4.64	0.26
P_2O_5	0.45	0.46	0.34	0.46	0.03	0.34	0.03
Na_2O	3.47	4.29	5.09	3.41	0.35	3.41	0.14
MnO	0.17	0.16	0.05	0.15	0.02	0.13	0.08

The second approach for evaluation of the obtained results with natural findings is modelling the chemical data from natural occurrences by a linear combination of the selected end-member compositions. Hybrid compositions calculated vary according to an assumed fraction of mixing *f* between these end-members. It is based on the classic linear mixing equation (Langmuir *et al.*, 1978):

$$C_H = C_R^i * f + C_D^i * (1 - f) \qquad \text{Eq. (4.VI)}$$

where C_D^i and C_R^i are respectively the initial concentrations of an element *i* in the dacitic and rhyolitic glass, and C_h is the hybrid glass final composition. E.g., the selected fraction of $f = 0.2$ means that 20% of the contaminant (rhyolitic end-member) is mixed into the dacite, which represents the initial ratio between the end-members. Assuming that linear mixing does occur, we normalized the calculated averages AC and A13 for C_h (diagrams AC/LM and A13/LM in Figure 4.8) checking on the relative deviation. For FATS, the normalization of AC and A13 reveals relative deviations of approx. 4%. The relative deviation increases to 9% for KCM (Na included). In the case of P_2O_5, the best result stands for AC/LM. When AC and A13 are normalized to COD, FATS exhibit deviations of roughly 2%, whereas KCM(N) differ by up to 18%. In this instance, P demonstrates a stronger correlation with A13.

The ratio A13/LM represents better the relation between experimental/expected products. Considering it, linear mixing predictions diverge from the group that better represent COD compositions, since only SiO_2, Al_2O_3 and Fe_2O_{3t} lie on the grey bar (RD = ± 5%). The ratio AC/LM presents the smallest dispersion in Figure 4.8, which indicates that the mixing process tends to the linear behaviour only when it is analyzed globally (even under chaotic dynamics). However, it is a general feature that FATS components are not reproduced in the same proportions as the KCM components. Decoupled behaviour has been described in natural systems (Lesher, 1990; Blichert-Toft et al., 1992) and is thought to be a consequence of chaotic dynamics (e.g., Perugini et al., 2012; Morgavi et al., 2013a; Vicentini et al., 2023).

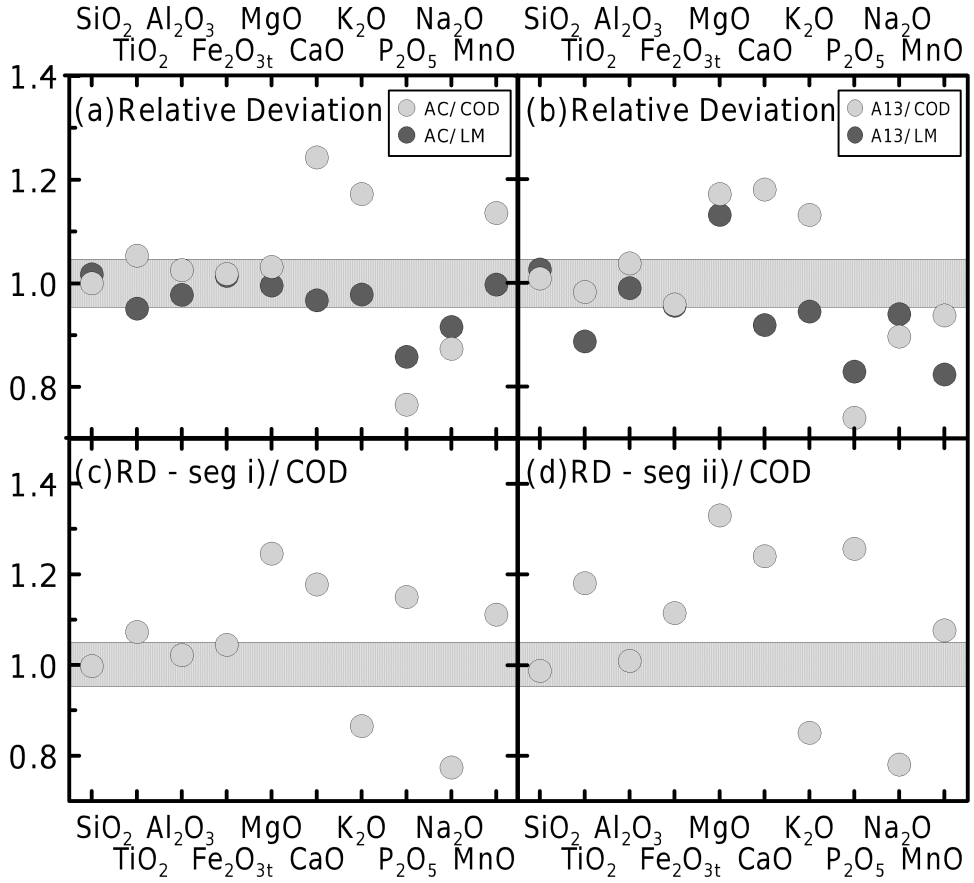

Figure 4.8: Relative deviations (RD) of the global average of T1 (AC), the average of 13 points with TiO_2 < 1.4% and P_2O_5 < 0.4% (A13), the average of segment i) and the average of segment ii) (Table 4.2) normalized by the given parameter COD average (Table 4.4) or linear mixing LM – the hybrid composition C_h calculated according to Eq. (4.VI) (see text for details). Grey rectangle represents an interval of RD = ± 5%.

In order to contrast the elemental mobility in the experiment with natural findings, we applied the procedure of De Campos (2015). It consists in to calculate the variance (Eq. (4.IV)) of a representative group of samples, and to normalize it to the maximum variance observed inside this group (assuming that the most primitive and the most evolved samples in this dataset are compositionally close to the true end-members). Table 4.4 provides the samples employed in this procedure. Two potential pairs of end-members were selected based on their distinct petrogenetic evolution, determined according to (Nardy et al., 2008): the SiO_2 content (*S* – samples PU-1005 and KNO-436); and the MgO content (*M* – samples KS-1335 and KNO-436). Figure 4.9 illustrates a comparison of σ_n^2 values for S and M, as well as experimental data, within a 2σ interval (grey field) in respect to the elemental field strength. The strong agreement between experimental and natural results is evident from the comparable patterns. Firstly, values of σ_n^2 for Ca, Mg, Fe, Si and P using *S* resemble the experimental results. For Na, σ_n^2 coincides with that is observed in the experiment (i.e., value anomalously high). Regarding *M*, only P is in perfect agreement, although the general behaviour is qualitatively identical to *S* and comparable to the experiment. Secondly, as the field strength increases, σ_n^2 remains fairly constant. The exception is σ_n^2 of P, which exhibits an increase in all scenarios. For KCM elements, the normalized variance decreases more significantly from K towards Ca than it occurs from Ca to Mg. In comparison, FATS show a greater dispersion. The diagram displays a significant increase from Fe to Al (which exhibits the highest σ_n^2), followed by an abrupt decrease from Al towards Ti, and from Ti to Si.

Larger differences in σ_n^2 appear for K, Al and Ti using *S* or *M*. The high concentration of these elements in mineral phases present in Chapecó dacites, such as plagioclase (Al), pyroxene (Ca, Mg), and Fe-Ti-bearing minerals, may explain these observations. Indeed, alkaline elements are susceptible to remobilisation, and Chapecó dacites show clear signs of alteration. (e.g., Piccirillo and Melfi, 1988; Nardy *et al.*, 2008).

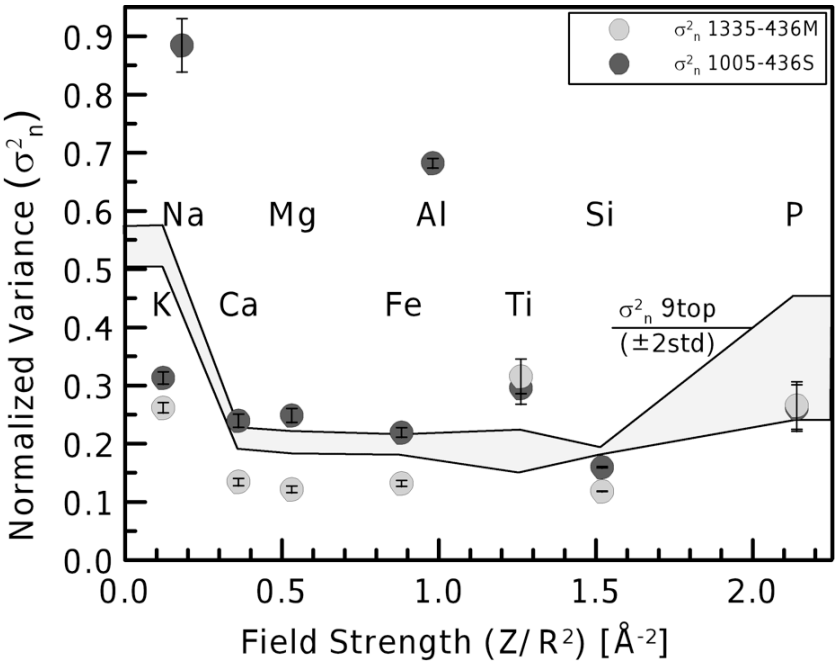

Figure 4.9: Variation of the major oxide normalized variances σ_n^2 for Chapecó dacites from PEMP as a function of the field strength (elemental nominal charge Z divided by the ionic radius squared R^2 – after Brown Jr *et al.*, 1995). The pair 1335-436*M* was selected according to MgO contents; the pair 1005-436*S* was selected according to SiO_2 contents (see text for details).

4.5. SUMMARY

1. This study shows that chaotic mixing experiments can be as well successfully applied to natural processes involving dacitic material. Morphological features such as stretched and folded filaments of alternating phases confirm that chaotic dynamics were effective at the high temperature conditions within the experimental charges. Such characteristics might be predicted by Eq. (4.I) that expresses the physical mingling starting from shearing caused by the spindle and crucible rotations in CM device. The created filaments are continuously stretched and folded, which increases the contact surfaces. Finally, while the filaments are getting systematically thinner, they reach a sufficiently small length scale that exponentially enhances the diffusion efficiency.

2. The comparison between microscopically features and chemical analyses performed over these structures sheds some light on the homogenization processes taking place due to chaotic dynamics. The presence of active regions AR, areas where mixing is more efficiently taking place and leads to a faster homogenization, is predicted by chaotic dynamics. This is observed along the representative transect T1.

Similarly, the presence of coherent regions CR, where mixing is not or by far less efficient, can be observed in the experimental charges. CR are capable to maintain its original composition and, in some cases, causing anomalous local enrichments. An important result of the present study is that optical features (filaments) might be unrelated to the chemical composition determined by EPMA, and can result in misleading interpretations.

3. Fractal dimensions were calculated for the representative section 9top. The value of D_{box} = 1.60(3) is in agreement with previous studies (e.g., Guimarães *et al.*, 2018). The similarity with the experiment suggests greater interaction levels between dacitic and rhyolitic magmas within the PEMP. This may have increased both the complexity and the efficiency of mixing.

4. EPMA analyses along the transect T1 demonstrated that dacitic material was mainly contaminated with SiO_2. In addition, original dacitic compositions loose other elements in variable degrees (i.e., contaminating the rhyolite). It indicates that different elements are attaining different amounts of equilibration, resulting in the particular patterns observed in variation diagrams (Figure 4.7). However, the main characteristic of diffusive curves is preserved in most regions of T1 (Figure 4.5). Chemical data agree with optical observations where clear end-member compositions were pertained. The comparison between the average compositions of T1 and natural outcrops revealed that the elements typically acting as network formers (FATS) are prone to generate a melt with COD signature.

5. The normalized variance σ_n^2 parameter is an important tool to evaluate the mixing evolution of a system (e.g., Perugini *et al.*, 2012, 2015; Morgavi *et al.*, 2013a,b, Vicentini et a., 2023). The comparison of σ_n^2 with previous results set some limitations, however the benefits of this approach are evident. Chaotic mixing experiments are very reproducible if experimental parameters (mainly temperature and mixing protocol) are kept constant amongst varying end-member compositions. Thus, it makes results directly comparable and can be accurately used to investigate the elemental mobility during mixing processes between natural materials, even when their rheology significantly differs.

6. A comparison of σ_n^2 calculated from experimental and natural data, as demonstrated by De Campos (2015), has shed light onto the role of mixing in the CGD-COD system. Similar patterns of σ_n^2 emerged for the major oxides, specifically for five

compounds using the pair *S*. Secondary processes like remobilization of some elements (i.e., K) or accumulation during recrystallization (i.e., Al) are plausible explanations for some of the discrepancies observed.

7. We reinforce that results presented in this study are based on a representative section analyses (i.e., 9top) of the chaotic mixing experiment. More specifically, the elemental mobility is calculated along one dimension in the elemental transects. This methodological approach has being systematically and successfully applied to better understand magma mixing processes (Perugini *et al.*, 2012; Morgavi *et al.*, 2013a,b; Vicentini *et al.*, 2023; this study). However, mixing dynamics take place three-dimensionally both in nature and inside the Pt_{80}-Rh_{20} crucible in experiments. Further investigations should consist of a multi-elementary analysis, including more analytical methods, across multiple sections, allowing comparison to clarify the evolution of chaotic mixing patterns at different depths within the crucible. This process will require a significant amount of analytical data and processing time, which is not yet available.

8. Finally, experimental results point towards short interaction times between melts and low convective forces as experimentally shown. Chaotic mixing are a feasible process to produce the melt compositions observed in COD, and are most likely correlated to the genesis of these rocks under circumstances where CGD interacted with crustal rocks from the PEMP basement via chaotic dynamics.

ACNKOWLEDGEMENTS

Authors are grateful by the staff support in IAG/USP and DEES/LMU. Vicentini thanks to A. Nardy, C. Luchetti, J. Silva, R. Zanon and D. Conego for helping with fieldtrips and sampling, and to V. Janasi for academic support. Authors thanks D. Müller for assistance with EPMA measurements, C. Cimarelli for SEM imaging, and H. Lohringer for sample preparation.

This work was financially supported by *Coordenação de Aperfeiçoamento de Pessoal de Nível Superior* (PROBAL CAPES/DAAD Grant No. 88887.363370/2019-00, responsible: V. Janasi), and European Research Council (2018 ADV Grant No. 834225, EAVESDROP).

REFERENCES

Abramoff, M. D., Magalhaes P.J., Ram S.J., 2004. Image Processing with Image. *Journal of Biophotonics International* 11, 36–42.

Anderson, D. L., 1982. Isotopic evolution of the mantle: the role of magma mixing. *Earth and Planetary Science Letters* 57(1), 1–12.

Bateman, R., 1995. The interplay between crystallization, replenishment and hybridization in large felsic magma chambers. *Earth-Science Reviews* 39, 91–106.

Bidias, L. A. Z., Chazot, G., Moundi, A., Nonnotte, P., 2018. Extreme source heterogeneity and complex contamination patterns along the Cameroon Volcanic Line: New geochemical data from the Bamoun plateau. *Comptes Rendus Geoscience*; 350, 100–109. https://doi.org/10.1016/j.crte.2017.11.004

Blichert-Toft, J., Lesher, C. E., Rosing, M. T., 1992. Selectively contaminated magmas of the Tertiary East Greenland macrodike complex. *Contributions to Mineralogy and Petrology* 110, 154–172.

Brown Jr., G. E., Farges F., Calas G., 1995. *X-ray scattering and x-ray spectroscopy studies of silicate melts*. In: Stebbins J.F., McMillan P.F. and Dingwell, D. B. (ed.). *Structure, Dynamics, and Properties of Silicate Melts*, Vol. 32, i-xvi + 616 pg., 317-410 p. ISBN: 0-939950-39-1; ISBN: 13 978-0-939950-39-3.

Chen, Z., Zeng, Z., Wang, X., Peng, X., Zhang, Y., Yin, X., Chen, S., Zhang, L., Qi, H., 2020. Element and Sr isotope zoning in plagioclase in the dacites from the southwestern Okinawa Trough: Insights into magma mixing processes and time scales. *Lithos*, 376–377. https://doi.org/10.1016/j.lithos.2020.105776

Crank, J., 1975. *The Mathematics of Diffusion*. Oxford: Clarendon, 414 pp.

De Campos, C. P., Perugini, D., Ertel-Ingrisch, W., Dingwell, D. B., Poli, G., 2011. Enhancement of magma mixing efficiency by chaotic dynamics: an experimental study. *Contributions to Mineralogy and Petrology* 161, 863–881.

De Campos, C. P., 2015. Chaotic Flow Patterns from a Deep Plutonic Environment: a Case Study on Natural Magma Mixing. *Pure and Applied Geophysics* 172(7), 1815–1833. DOI: 10.1007/s00024-014-0940-6

De Rosa, R., Donato, P., Ventura, G., 2002. Fractal analysis of mingled/mixed magmas: an example from the Upper Pollara eruption (Salina Island, southern TyrrhenianSea, Italy). *Lithos* 65, 299–311.

Dingwell, D., 1986. Viscosity–temperature relationships in the system $Na_2Si_2O_5$–$Na_4Al_2O_5$. *Geochimica et Cosmochimica Acta* 50, 1261–1265.

Eichelberger, J. C., 1975. Origin of andesite and dacite: Evidence of mixing at Glass Mountain in California and at other circum-Pacific volcanoes. *Geological Society of America Bulletin* 86, 1381-1391.

Emmanuel, S., Cortis, A., Berkowitz, B., 2004. Diffusion in multicomponent systems: a free energy approach. *Chemical Physics* 302, 21–30.

Flinders, J., Clemens, J. , 1996. Non-linear dynamics, chaos, complexity and enclaves in granitoid magmas. *Earth and Environmental Science Transactions of the Royal Society of Edinburgh* 87(1-2), 217–223. DOI: 10.1017/S0263593300006623

Frank, H. T., Gomes, M. E. B., Formoso, M. L. L., 2009. Review of the areal extent and the volume of the Serra Geral Formation-Paraná Basin, South. *Pesquisas em Geociências* 36(1), 49–57.

Freitas, V. A., 2009. *A geração de magmas ácidos na Província Magmática Paraná, região de Piraju-Ourinhos (SP): uma contribuição da geoquímica isotópica e de elementos traço em rochas e minerais* (Acid magma generation in the Paraná Magmatic Province, Piraju-Ourinhos (SP) region: a contribution of isotopic geochemistry and trace elements in rocks and minerals). São Paulo, University of São Paulo (master dissertation).

Garland, F., Hawkesworth, C. J., Mantovani, M. S. M., 1995. Description and petrogenesis of the Paraná rhyolites, Southern Brazil. *Journal of Petrology* 36(5), 1193–1227. https://doi.org/10.1093/petrology/36.5.1193

Giordano, D., Vona, A., Gonzalez-Garcia, D., Allabar, A., Kolzenburg, S., Polo, L. A., de Assis Janasi, V., Behrens, H., De Campos, C. P., De Cristofaro, S., Freitas Guimarães, L., Nowak, M., Müller, D., Günther, A., Masotta, M., Roverato, M., Romano, C., Dingwell, D. B., 2021. Viscosity of Palmas-type magmas of the Paraná Magmatic Province (Rio Grande do Sul State, Brazil): Implications for high-temperature silicic volcanism. *Chemical Geology* 560. https://doi.org/10.1016/j.chemgeo.2020.119981

Gomes, A. S., Vasconcelos, P. M., 2021. Geochronology of the Paraná-Etendeka large igneous province. *Earth-Science Reviews* 220. https://doi.org/10.1016/j.earscirev.2021.103716

González-Garcia, D., Petrelli, M., Behrens, H., Vetere, F., Fischer, L. A., Morgavi, D., Perugini, D., 2018. Diffusive exchange of trace elements between alkaline melts: Implications for element fractionation and timescale estimations during magma mixing. *Geochimica et Cosmochimica Acta* 233, 95–114.

Guimarães, L. F., De Campos, C. P., Janasi, V. A., Lima, E. F., Dingwell, D. B., 2018. Flow and fragmentation patterns in the silicic feeder system and related deposits in the Paraná-Etendeka Magmatic Province, São Marcos, South Brazil. *Journal of Volcanology and Geothermal Research* 358, 149–164. https://doi.org/10.1016/j.jvolgeores.2018.03.021

Janasi, V. A., Freitas, V. A., Heaman, L. H., 2011. The onset of flood basalt volcanism, Northern Paraná Basin, Brazil: A precise U–Pb baddeleyite/zircon age for a Chapecó-type dacite. *Earth and Planetary Science Letters* 302, 147–153.

Jochum, K. P., Dingwell, D. B., Rocholl, A., Stoll, B., Hofmann, A. W., *et al.*, 2000. The preparation and preliminary characterisation of eight geological MPI-DING reference glasses for in situ microanalysis. *Geostandard Newsletter* 24, 87–133.

Lange, R. A. and Carmichael, I. S. E., 1987. Densities of Na_2O-K_2O-CaO-MgO-FeO-Fe_2O_3-Al_2O_3-TiO_2-SiO_2 liquids: new measurements and derived partial molar properties. *Geochimica et Cosmochimica Acta* 51, 2931–2946.

Langmuir, C. H., Vocke, R. D., Hanson, G. N., 1978. A general mixing equation with applications to Icelandic basalts. *Earth and Planetary Science Letters* 37(3), 380–392.

Leonard, G., Cole, J., Nairn, I., Self, S., 2002. Basalt triggering of the c. AD 1305 Kaharoa rhyolite eruption, Tarawera Volcanic Complex, New Zealand. *Journal of Volcanology and Geothermal Research* 115, 461–486.

Lesher, C. E., 1990. Decoupling of chemical and isotopic exchange during magma mixing. *Nature* 344, 235–237.

Liu, W., Haller, G., 2004. Strange eigenmodes and decay of variance in the mixing of diffusive tracers. *Physica D* 188, 1–39.

Luchetti, A. C. F., Gravley, D. M., Gualda, G. A. R., Nardy, A. J. R., 2018. Textural evidence for high-grade ignimbrites formed by low-explosivity eruptions, Paraná Magmatic Province, southern Brazil. *Journal of Volcanology and Geothermal Research* 355, 87–97.

Machado, F. B., Rocha-Júnior, E. R. V., Marques, L. S., Nardy, A. J. R., Zezzo, L. V., Marteleto, N. S., 2018. Geochemistry of the Northern Paraná Continental Flood Basalt (PCFB) Province: implications for regional chemostratigraphy. *Brazilian Journal of Geology* 48(2), 177–199. DOI: 10.1590/2317-4889201820180098

Mandelbrot, B. B., 982. *The Fractal Geometry of Nature.* Freeman, W. H. (ed.), New York, 468 p.

Marzoli, A., Melluso, L., Morra, V., Renne, P. R., Sgrosso, I., D'Antonio, M., Duarte Morais, L., Morais, E. A. A., Ricci, G., 1999. Geochronology and petrology of Cretaceous basaltic magmatism in the Kwanza basin (western Angola), and relationships with the Paraná-Etendeka continental flood basalt province. *Journal of Geodynamics* 28, 341–356.

Morgavi, D., Laumonier, M., Petrelli, M., Dingwell, D. B., 2022. Magma Mixing in Igneous Systems. *EGU General Assembly 2022*. 23–27 May 2022, Vienna, Austria, EGU22-6510. https://doi.org/10.5194/egusphere-egu22-6510.

Morgavi, D., Perugini, D., De Campos, C., Ertel-Ingrisch, W., Lavallée, Y., Morgan, L., Dingwell, D., 2013a. Interactions between rhyolitic and basaltic melts unraveled by chaotic mixing experiments. *Chemical Geology* 346, 199–212.

Morgavi, D., Perugini, D., De Campos, C. P., Ertel-Ingrisch, W., Dingwell, D. B., 2013b. Morphochemistry of patterns produced by mixing of rhyolitic and basaltic melts. *Journal of Volcanology and Geothermal Research* 253, 87–96. http://dx.doi.org/10.1016/j.jvolgeores.2012.12.007

Nardy, A. J. R., Machado, F. B., Oliveira, M. A. F., 2008. As rochas vulcânicas mesozoicas ácidas da Bacia do Paraná: litoestratigrafia e considerações geoquímico-estratigráficas. *Revista Brasileira de Geociências* 38(1), 178–195.

Ottino, J. M., Muzzio, F. J., Tjahjadi, M., Franjione, J. G., Jana, S. C., Kusch, H. A., 1993. Chaos, symmetry, and self-similarity: exploiting order and disorder in mixing processes. *Science* 257, 754–760.

Ottino, J. M., 1989. *The Kinematics of Mixing: Stretching, Chaos and Transport.* Cambridge University Press, 364 p.

Peate, D. W., 1997. *The Paraná-Etendeka Province*. In: Mahoney, J., Coffin, M., (ed.) *Large Igneous Provinces: Continental, Oceanic, and Planetary Flood Volcanism.* AGU Geophysical Monograph 100, 217–245.

Perugini, D., Poli, G., 2000. Chaotic dynamics and fractals in magmatic interaction processes: a different approach to the interpretation of mafic microgranular enclaves. *Earth and Planetary Science Letters* 175, 93–103.

Perugini, D., Busa, T., Poli, G., Nazzareni, S., 2003a. The role of chaotic dynamics and flow fields in the development of disequilibrium textures in volcanic rocks. *Journal of Petrology* 44, 733–756.

Perugini, D., Poli, G., Mazzuoli, R., 2003b. Chaotic advection, fractals and diffusion during mixing of magmas: evidence from lava flows. J*ournal of Volcanology and Geothermal Research* 124, 255–279.

Perugini, D., Petrelli, M., Poli, G., De Campos, C., Dingwell, D. B., 2010. Time-scales of recent phlegrean fields eruptions inferred from the application of a 'diffusive fractionation' model of trace elements. *Bulletin of Volcanology* 72, 431–447.

Perugini, D., De Campos, C. P., Ertel-Ingrisch, W., Dingwell, D. B., 2012. The space and time complexity of chaotic mixing of silicate melts: implications for igneous petrology. *Lithos* 155, 326–340.

Perugini, D., De Campos, C. P., Petrelli, M., Dingwell, D., 2015. Concentration variance decay during magma mixing: a volcanic chronometer. *Scientific Reports* 5, 14225. DOI: 10.1038/srep14225

Piccirillo, E. M., Melfi, A. J., 1988. *The Mesozoic flood volcanism of the Paraná Basin: petrogenetic and geophysical aspects.* University of São Paulo, IAG, 600p.

Piccirillo, E. M., Raposo, M. I. B., Melfi, A. J., Comin-Chiaramonti, P., Bellieni, B., Cordani, U. G., Kawashita, K., 1987. Bimodal fissural volcanic suites from the Paraná Basin (Brazil): K-Ar age, Sr-isotopes and geochemistry. *Geochimica Brasiliensis* 1, 53–69.

Pouchou, L., Pichoir, F, 1984. A new model for quantitative X-ray microanalysis: part i: applications to the analysis of homogeneous samples. *Recherche Aerospatiale* 3, 13–38.

Rossi, S., Petrelli, M., Morgavi, D., González-García, D., Fischer, L. A., Vetere, F., Perugini, D., 2017. Exponential decay of concentration variance during magma mixing: Robustness of a volcanic chronometer and implications for the homogenization of chemical heterogeneities in magmatic systems. *Lithos* 286–287, 396–407.

Shannon, R. D., 1976. Revised effective ionic radii and systematic studies of interatomic distances in halides and chalcogenides. *Acta Crystallographica* A32, 751–767.

Swanson, P. D., Ottino, J. M., 1990. A comparative computational and experimental study of chaotic mixing of viscous fluids. *Journal of Fluid Mechanics* 213, 227–249.

Tomiya A, Miyagi I, Saito G, Gesh N., 2013. Short time scales of magma-mixing processes prior to the 2011 eruption of Shinmoedake volcano, Kirishima volcanic group, Japan. Bulletin of Volcanology, 75, 750, DOI:10.1007/s00445-013-0750-1.

Vicentini, C. M., De Campos, C. P., Ertel-Ingrisch, W., Perugini, D., Marques, L. S., Dingwell, D. B., 2023. Contamination of basalt through silicic melts: The first chaotic dynamics experiments with Paraná-Etendeka starting materials. *Chemical Geology* 615, 121200. https://doi.org/10.1016/j.chemgeo.2022.121200

Watson, B. E., Jurewicz, S. R., 1984. Behavior of alkalies during diffusive interaction of granitic xenoliths with basaltic magma. *The Journal of Geology* 92, 121–131. https://doi.org/10.1086/628843

Zhang Y., Ni, H., Chen, Y, 2010. Diffusion Data in Silicate Melts. Reviews in Mineralogy & Geochemistry, 72, 311–408. DOI: 10.2138/rmg.2010.72.8

CHAPTER 5 – FINAL CONSIDERATIONS

This PhD thesis provides original insights on the role of chaotic dynamics on the formation of Chapecó dacites from Paraná-Etendeka Magmatic Province. The approach was to experimentally test the hypothesis that contamination processes are involved in the generation of such rocks. Using the chaotic mixing device (De Campos et al., 2011), the experiments were designed: i) to mimic a process in which a hotter basaltic magma encounters pre-existing continental crust during ascent; and ii) to test whether Chapecó-Ourinhos dacites (COD), the most evolved unit of Chapecó dacites, could be formed from Chapecó-Guarapuava dacites (CGD) during ascent and/or replenishment events. In both scenarios the ingestion of felsic blocks by hotter mafic magmas and the establishment of chaotic mixing is assumed. The efforts were concentrated in to produce high quality experimental data and in the interpretation of it. The main contributions are summarized below.

This thesis is relevant at least in three general aspects:

1) Performing an experimental study, which is relatively rare;

2) Producing new chemical analyses on Chapecó dacites that are less studied in comparison to the other units from PEMP;

3) Applying non-linear dynamics to solve a geological problem, while the most common approach is to use linear models.

5.1 THE EXPERIMENTS INVOLVING BASALTIC AND RHYOLITIC END-MEMBERS

Major oxide profiles performed by electron probe microanalysis EPMA in experiments 1, 2 and 3, which comprises the Chapter 2, are published in the Chemical Geology periodic and entitled *"Contamination of basalt through silicic melts: The first chaotic dynamics experiments with Paraná-Etendeka starting materials"*. This paper presents the first attempt to simulate experimentally the impact of underplating high-Ti basaltic melt from Paraná-Etendeka Magmatic Province (PEMP) on a pre-existing continental crust. In addition, the same samples were analyzed for trace elements using laser ablation inductively coupled plasma mass spectrometry LA-ICP-

MS. These data comprise the Chapter 3 and were discussed taking into consideration the morphological and chemical aspects reported in Chapter 2.

The results confirmed that the mixing between melts with vastly different viscosities is physically possible. Concerning the morphological aspects, emerging features such as stretched and folded filaments, and vortex structures are direct products of chaotic dynamics. The interaction between end-members can directly been observed in all experiments. Three distinguishable regions were identified and associated to basaltic, rhyolitic and intermediate portions. Orbicular structures containing dendritic crystals and remnant portions of glass were observed and described in the basaltic areas for the first time. These areas indicate an early crystallization process during the initial quench phase of the experiment, and that the crystallization process does not happen homogeneously.

Chemical analyses show transects where the initial rhyolite is preserved more widely than the initial basalt (*i.e.*, plateaus of original concentrations). The observed asymmetric diffusion profile argues that a basaltic phase becomes faster contaminated than rhyolitic phase during chaotic mixing processes. The trace element profiles depict similar characteristics presented by major oxides indicating different levels of contamination according to the element.

Moreover, two distinct diffusive patterns were identified in trace analysis, named normal and uphill diffusion. It divides the elements into two groups as follows: G1 (normal) – V, Sc, Sr, Cs, Rb, U, Th, Ti, Mg, Ca and Mn; and G2 (uphill) – Ga, Nb, Zr, Y, Ba, REE, Ta, Hf, Pb and Al. For the first time in chaotic mixing experiments uphill diffusion was identified and described for a large number of trace elements. The same patterns systematically stand independently of the experiment. A direct consequence is a higher deviation from the linearity observed in variation diagrams of G1 vs. G2 elements.

Mixing was evaluated in terms of the efficiency to move a given element towards its equilibrium, which is well represented by the normalized variance (σ^2_n). The positive correlation between field strength and mobility of network formers (FATS) differs significantly from network modifiers (KNCM), indicating a decoupled behaviour between these groups. For G1 elements the result consistently indicates the connection between viscosity and mobility, which is in total agreement with major element data. Exp1 exhibits the highest contrast in viscosity (η_{rhy}/η_{bas}) compared to Exp3 and Exp2

respectively, expressing the higher values of (σ^2_n). A large number of G2 elements, (σ^2_n) reaches values that are not expected (i.e., > 1.0), which has been associated to their starting chemical gradients. It is proposed that differences up to 30% in gradients substantially increase the probability of uphill diffusion develops and produces heterogeneities in the mixing system. Elements with gradients diverging more than 30% are the most predictable and, thus, the most reliable to focus the argumentation.

In respect to the formation of Chapecó dacites, the results point to that basalts commonly melt crustal rocks, partially or totally, on their way to the surface. The interaction between these contrasting melts is a highly complex process, which will result in some peculiar geochemical signatures. The linear mixing models fails in to explain such signatures, which becomes evident from the variations in parameter *f*. Therefore, the study concluded that chaotic mixing experiments were able to reproduce the signatures, particularly for CODs, for the majority of elements. Similarly, CGDs are well represented comparing the averages from experimental and natural data. The study concludes as well that CGDs and CODs compositions would be generated during mixing processes involving the end-members of Exp1. However, CGD and COD diverge 10% in terms of interaction degree of basaltic and rhyolitic phases. Particular features of Exp2 results indicate the involvement of multiple sources in the origin of Chapecó dacites. The complexity of geological setups certainly contributed to this peculiarity, and even may have facilitated the involvement of multiple contaminants and stages of contamination. This thesis points out that chaotic mixing experiments have proven to be suitable to study complex scenarios since the experiments are very reproducible and, thus, comparable.

Finally, the reproduction of the basaltic compositional variability and chemical similarities with HTi dacitic rare outcrops from PEMP point towards short interaction times, low convective forces, and a predominance of density driven separation of contrasting melts (*i.e.*, simulated conditions) as possible mechanisms involved in the genesis of Chapecó dacites. Further studies on isotopic systems in the hybrid experimental glasses are still necessary and will help to understand more deeply the overview on generation of such expressive magmatic rocks.

5.2 THE EXPERIMENTS INVOLVING DACITIC AND RHYOLITIC END-MEMBERS

Data from micro probe microanalysis EPMA transects performed in experiment 4 comprises the Chapter 4, which was submitted to Geoscience Frontiers journal in a paper entitled *"Chaotic Mixing Experiments: Unravelling Contamination Processes on Dacitic Melts"*. This paper presents results for chemical and morphological analysis of a representative sample.

In respect to the morphology, two important results follows. The first is that optical features, such as filaments, can be unrelated to the chemical composition determined by EPMA, and can result in misleading interpretations. The second is the fractal dimension D_{box} calculated for a representative section. The value of D_{box} = 1.60(3) is in agreement with previous studies (e.g., Guimarães *et al.*, 2018). The similarity with natural outcrops (including PEMP) indicates a higher degree of interaction (i.e., enhanced complexity) between dacitic and rhyolitic magmas.

The comparison between the average composition of the representative transect and compositions of natural outcrops showed that those elements usually acting as network formers (FATS) are prone to generate a melt with COD chemical characteristics. Experimental results point towards short interaction times between melts and low convective forces as experimentally shown. Chaotic mixing processes are undoubtedly a feasible scenario to produce the melt compositions observed in COD, and are most likely correlated to the genesis of these rocks under circumstances where CGD interacted with crustal rocks from the PEMP basement via chaotic dynamics. Further thorough investigations may include multi-elementary analysis including LA-ICP-MS analysis of multiple sections (i.e., comparing each other) to clarify the evolution of chaotic mixing patterns through different depths in the crucible.

REFERENCES

Alberti, A., Piccirillo, E.M., Bellieni, G., Civetta, L., Comin-Chiaramonti, P., Morais, E.A.A., 1992. Mesozoic acid volcanics from southern Angola: petrology, Sr-Nd isotope characteristics and correlation with the acid stratoid volcanic suites of the Paraná basin (south-eastern Brazil). European Journal of Mineralogy 4, 597–604.

Almeida, J., Dios, F., Mohriak, W.U., Valeriano, C.D.M., Heilbron, M., Eirado, L.G., Tomazzoli, E., 2013. Pre-rift tectonic scenario of the Eo-Cretaceous Gondwana break-up along SE Brazil–SW Africa: insights from tholeiitic mafic dyke swarms. Geological Society, London, Special Publications, 369, 1, 11-40.

Anderson, D.L., 1982. Isotopic evolution of the mantle: the role of magma mixing. Earth and Planetary Science Letters, 57, 1, 1–12.

Angelini, P.G., 2018. Petrological and volcanological insights into acid lavas from the Paraná-Etendeka Magmatic Province on the surroundings of Guarapuava city, Paraná, Southern Brazil: A contribution of detailed textural characterization combined with in situ Sr isotopes in plagioclase phenocrysts. IGc, São Paulo, University of Sao Paulo (mester dissertation). DOI: 10.11606/D.44.2018.tde-17072018-145409

Bateman R., 1995. The interplay between crystallization, replenishment and hybridization in large felsic magma chambers. Earth-Science Reviews, 39, 91–106.

Bellieni, B., Comin-Chiaramonti, P., Marques, L.S., Melfi, A.J., Nardy, A.J.R., Piccirillo, E.M., Roisenberg, A., 1984. High- and Low-TiO_2 flood basalts from the Paraná plateau (Brazil): petrology and geochemical aspects bearing on their mantle origin. Neues Jahrbuch für Mineralogie Abhandlungen, 150, 273-306.

Bellieni, G., Comin-Chiaramonti, P., Marques, L.S., Melfi, A.J, Nardy, A.J.R., Papatrechas, C., Piccirillo, E.M., Roisenberg, A., Stolfa, D., 1986. Petrogenetic aspects of acid and basaltic lavas from the Paraná plateau (Brazil): mineralogical and petrochemical relationships. Journal of Petrololy, 27, 915-944.

Bellieni, G., Montes-Lauar, C.R., De Min, A., Piccirillo, E.M., Cavazzini, G., Melfi A.J., Pacca, I.G., 1990. Early and late Cretaceous magmatism from São Sebastião Island (SE - Brazil): Geochemistry and Petrology, Geochimica Brasiliensis, 4, 1, 59-83.

Blundy, J.D., Wood, B.J, 1991. Crystal-chemical controls on the partitioning of Sr and Ba between plagioclase feldspar, silicate melts, and hydrothermal solutions. Geochimica et Cosmochimica Acta, 55, 1, 193-209.

Bologna, M.S., Padilha, A.L., Vitorello, Í., Pádua, M.B., 2011. Signatures of continental collisions and magmatic activity in central Brazil as indicated by a magnetotelluric profile across distinct tectonic provinces. Precambrian Research, 185, 55–64.

Bologna, M.S., Nunes, H.O., Padilha, A.L., Vitorello, Í., Pádua, M.B., 2013. Anomalous electrical structure in the northwestern Paraná Basin, Brazil, observed with broadband magnetotellurics. Journal of South American Earth Sciences, 42, 74-82.

Brown Jr., G.E, Farges, F., Calas, G., 1995. X-ray scattering and x-ray spectroscopy studies of silicate melts. In: "Structure, Dynamics, and Properties of Silicate Melts", Jonathan F. Stebbins, Paul F. McMillan and Donald B. Dingwell, editors, 1995, Vol. 32:i-xvi + 616 pg. ISBN: 0-939950-39-1; ISBN: 13 978-0-939950-39-3.

Carvas, K.Z., Vasconcelos, P.M.P., Marques, L.S., Ubide, T., Carmo, I.O., Babinski, M., 2021. Geochronology of mafic magmatism and hydrothermal alteration during early stages of South Atlantic opening. Geochimica et Cosmochimica Acta, 314, 358–380.

Cathey H.E., Nash, B.P., 2009. Pyroxene thermometry of rhyolite lavas of the Bruneau–Jarbidge eruptive center, Central Snake River Plain. Journal of Volcanology and Geothermal Research, 188, 173–185.

Chaves, C., Ussami, N., Ritsema, J., 2016. Density and P-wave velocity structure beneath the Paraná Magmatic Province: refertilization of an ancient lithospheric mantle. Geochemistry, Geophysics, Geosystems, 17, 3054-3074. DOI:10.1002/2016GC006369.

Cordani, U. G., Sartori P.L.P., Kawashita, K., 1980. Geoquímica dos isótopos de estrôncio e a evolução da atividade vulcânica na Bacia do Paraná (sul do Brasil) durante o Cretáceo. Anais da Academia brasileira de Ciências, 52, 811-818.

De Campos, C. P., Perugini, D., Ertel-Ingrisch, W., Dingwell, D. B., Poli, G., 2011. Enhancement of magma mixing e ciency by chaotic dynamics: an experimental study. Contributions to Mineralogy and Petrology, 161, 863–881.

De Rosa, R., Donato, P., Ventura, G., 2002. Fractal analysis of mingled/mixed magmas: an example from the Upper Pollara eruption (Salina Island, southern Tyrrhenian Sea, Italy). Lithos, 65, 299–311.

Emmanuel, S., Cortis, A., Berkowitz, B., 2004. Diffusion in multicomponent systems: a free energy approach. Chemical Physics, 302, 21–30.

Ferry, J. M., Watson E. B., 2007. New thermodynamic models and revised calibrations for the Ti-in-zircon and Zr-in-rutile thermometers. Contribution to Mineralogy and Petrology,154, 429–437. DOI 10.1007/s00410-007-0201-0

Frank, H. T., Gomes, M.E.B., Formoso, M. L. L., 2009. Review of the areal extent and the volume of the Serra Geral Formation - Paraná Basin, South. Pesquisas em Geociências, 36, 1, 49-57.

Freitas, V.A., 2009. *A geração de magmas ácidos na Província Magmática Paraná, região de Piraju-Ourinhos (SP): uma contribuição da geoquímica isotópica e de elementos traço em rochas e minerais* (Acid magma generation in the Paraná Magmatic Province, Piraju-Ourinhos (SP) region: a contribution of isotopic geochemistry and trace elements in rocks and minerals). São Paulo, University of São Paulo (master dissertation). DOI: 10.11606/D.44.2009.tde-08062009-153408

Garda, G.M., 1995. Os diques básicos e ultrabásicos da região costeira entre as cidades de São Sebastião e Ubatuba, estado de São Paulo. IGc, São Paulo, São Paulo University (PhD thesis).

Garda, G.M., Schorscher, J.H.D., 1996. Os diques costeiros básicos e ultrabásicos adjacentes ao canal de São Sebastião (litoral norte do Estado de São Paulo). Revista Instituto Geológico de São Paulo, 17, 1/2, 7-31.

Garland F., Hawkesworth C.J., Mantovani M.S.M., 1995. Description and petrogenesis of the Paraná rhyolites, Southern Brazil. Journal of Petrology, 36, 5, 1193-1227. https://doi.org/10.1093/petrology/36.5.1193

González-Garcia, D., Petrelli, M., Behrens, H., Vetere, F., A. Fischer, L.A., Morgavi D., Perugini, D., 2018. Diffusive exchange of trace elements between alkaline melts: Implications for element fractionation and timescale estimations during magma mixing. Geochimica et Cosmochimica Acta, 233, 95–114. https://doi.org/10.1016/j.gca.2018.05.003

Green, T.H., Pearson, N.J., 1987. An experimental study of Nb and Ta partitioning between Ti-rich minerals and silicate liquids at high pressure and temperature. Geochimica et Cosmochimica Acta, 51, 55–62.

Hess, P.C., Rutherford, M.J., 1974. Element Fractionation Between Immiscible Melts. Abstracts of the Lunar and Planetary Science Conference, volume 5, page 328.

Iveson, A.A., Rowe, M.C., Webster, J.D., Neill, O.K., 2018. Amphibole-, Clinopyroxene- and Plagioclase- Melt Partitioning of Trace and Economic Metals in Halogen-Bearing Rhyodacitic Melts. Journal of Petrology, 59, 8, 1579–1604. Doi: 10.1093/petrology/egy072

Janasi, V.A., Montanheiro, T.J., Freitas, V.A., Reis, P.M., Negri, F.A., Dantas, F.A., 2007. Geology, petrography and geochemistry of the acid volcanism of the Paraná Magmatic Province in the Piraju-Ourinhos region, SE Brazil. Revista Brasileira de Geociências, 37, 4, 745-759.

Janasi, V.A., Freitas, V.A., Heaman, L.H., 2011. The onset of flood basalt volcanism, Northern Paraná Basin, Brazil: A precise U–Pb baddeleyite/zircon age for a Chapecó-type dacite. Earth and Planetary Science Letters, 302:147–153.

Jollands, M.C., O'Neill, H.St.C., Hermann, J., 2014. The importance of defining chemical potentials, substitution mechanisms and solubility in trace element diffusion studies: the case of Zr and Hf in olivine. Contributions to Mineralogy Petrology, 168, 1055. DOI 10.1007/s00410-014-1055-x

Langmuir, C.H., Vocke, R.D., Hanson, G.N., 1978. A general mixing equation with applications to Icelandic basalts. Earth and Planetary Science Letters, 37, 3, 380–392.

Le Bas, M.J., Le Maitre, R.W., Streckeisen, A., Zannetin, B., 1986. A chemical classification of volcanic rocks based on total alkali-silica diagram. Journal of Petrology, 27, 745-750.

Leonard, G., Cole, J., Nairn, I., Self, S., 2002. Basalt triggering of the c. AD 1305 Kaharoa rhyolite eruption, Tarawera Volcanic Complex, New Zealand. Journal of Volcanology and Geothermal Research, 115, 461–486.

Lesher, C.E., 1990. Decoupling of chemical and isotopic exchange during magma mixing. Nature, 344, 235-237.

Lesher, C.E, Walker, D., 1896. Solution properties of silicate liquids from thermal diffusion experiment. Geochimica et Cosmochimica Acta, 50, 1397-1411.

Liu, W., Haller, G., 2004. Strange eigenmodes and decay of variance in the mixing of diffusive tracers. Physica D, 188, 1–39.

Luchetti, A.C.F., Nardy, A.J.R., Machado, F.B., Madeira, J.E.O., Arnosio, J.M., 2014. New insights on the occurrence of peperites and sedimentary deposits within the silicic volcanic sequences of the Paraná Magmatic Province, Brazil. Solid Earth, 5, 1, 121-130.

Luchetti, A.C.F., Gravley, D.M., Gualda, G.A.R., Nardy, A.J.R., 2018. Textural evidence for high-grade ignimbrites formed by low-explosivity eruptions, Paraná Magmatic Province, southern Brazil. Journal of Volcanology and Geothermal Research, 355, 87–97.

Machado, F.B., Rocha-Júnior, E.R.V., Marques, L.S., Nardy, A.R., 2015. Volcanological aspects of the northwest region of Paraná continental flood basalts (Brazil). Solid Earth, 6, 227–241.

Mantovani, M.S.M., Marques, L.S., Sousa, M.A. de, Atalla, L.T., Civetta, L., Inoccenti I, F., 1985a. Trace element and strontium isotope constraints on the origin and evolution of the Paraná Continental flood basalts of Santa Catarina State (Southern Brazil). Journal of Petrology, 26, 187-209.

Mantovani, M.S.M., Cordani, U.G., Roisenberg, A., 1985b. Geoquímica Isotópica em vulcânicas ácidas da Bacia do Paraná e implicações genéticas associadas. Revista Brasileira de Geociências, 15, 61-65.

Marques, L.S., 1988. Caracterização geoquímica das rochas vulcânicas da Bacia do Paraná: implicações petrogenéticas. IAG, São Paulo, University of São Paulo (PhD thesis).

Marques, L.S., Piccirilo, E.M., Melfi, A.J., Comin-Chiaramonti, P., and Bellieni, G., 1989. Distribuição de terras raras e outros elementos traços em basaltos da Bacia do Paraná, Geochimica Brasiliensis, 3:33–50.

Marques, L.S., De Min, A., Rocha-Júnior, E.R.V., Babinski, M., Bellieni, G., Figueiredo, A.M.G., 2018. Elemental and Sr-Nd-Pb isotope geochemistry of the Florianópolis Dyke Swarm (Paraná Magmatic Province): crustal contamination and mantle source constraints. Journal of Volcanology and Geothermal Research, 355, 149–164.

Marsh, J.S., Ewart, A., Milner, S.C., Duncan, A.R., Miller, R. McG., 2001. The Etendeka Igneous Province: magma types and their stratigraphic distribution with implications for the evolution of the Paraná-Etendeka flood basalt province. Bulletin of Volcanology 62, 464–486.

Marsh, J.S., Swart, R., 2018. The Bero Volcanic Complex: Extension of the Paraná-Etendeka Igneous Province into SW Angola. Journal of Volcanology and Geothermal Research 355, 21-31.

Milner, S.C., Duncan, A.R., Ewart, A., 1992. Quartz latite rheoignimbrite flows of the Etendeka Formation, north-western Namibia. Bulletim of Volcanology, 54, 200-219.

Morgavi, D., Perugini, D., De Campos, C., Ertel-Ingrisch, W., Lavallée, Y., Morgan, L., Dingwell, D. (2013a). Interactions between rhyolitic and basaltic melts unraveled by chaotic mixing experiments. Chemical Geology, 346, 199–212.

Morgavi, D., Perugini, D., De Campos, C., Ertel-Ingrisch, W., Dingwell, D., 2013b. Time evolution of chemical exchanges during mixing of rhyolitic and basaltic melts. Contributions to Mineralogy and Petrology, 166, 615–638.

Morgavi, D., Laumonier, M., Petrelli, M., Dingwell, D.B., 2022. Magma Mixing in Igneous Systems, EGU General Assembly 2022, Vienna, Austria, 23–27 May 2022, EGU22-6510. https://doi.org/10.5194/egusphere-egu22-6510, 2022.

Nakamura E, Kushiro I., 1998. Trace element diffusion in jadeite and diopside melts at high pressures and its geochemical implication. Geochimica et Cosmochimica Acta, 62, 3151–3160.

Nardy, A.J.R., 1996. Geologia e petrologia do vulcanismo mesozoico da região central da Bacia do Paraná. IGCE, São Paulo State University (PhD thesis).

Nardy, A. J. R., Oliveira, M. A. F., Machado, F. B., 2002. Geologia e estratigrafia da Formação Serra Geral. Geociências, 21:13–30.

Nardy, A.J.R., Machado, F.B., Oliveira, M.A.F., 2008. As rochas vulcânicas mesozoicas ácidas da Bacia do Paraná: litoestratigrafia e considerações geoquímico-estratigráficas. Revista Brasileira de Geociências 38, 1, 178–195.

Padilha, A.L., Vitorello, Í., Antunes, C.E., Pádua, M.B., 2015. Imaging three-dimensional crustal conductivity structures reflecting continental flood basalt effects hidden beneath thick intracratonic sedimentary basin. Journal of Geophysical Research Solid Earth, 120, 4702–4719.

Peate, D.W., Hawkesworth, C.J., Mantovani, M.S.M., 1992. Chemical stratigraphy of the Paraná lavas, South America: classification of magma types and their spatial distribution. Bulletin of Volcanology, 55, 119-139.

Peate, D.W., 1997. The Paraná-Etendeka Province. In: J Mahoney & M Coffin (eds), Large Igneous Provinces: Continental, Oceanic, and Planetary Flood Volcanism. AGU Geophysical Monograph, 100, 217-245.

Perugini, D., Poli, G., 2000. Chaotic dynamics and fractals in magmatic interaction processes: a different approach to the interpretation of mafic microgranular enclaves. Earth and Planetary Science Letters 175, 93–103.

Perugini, D., Poli, G., 2004. Analysis and numerical simulation of chaotic advection and chemical diffusion during magma mixing: petrological implications. Lithos 78:43–66.

Perugini D., Poli G., Mazzuoli R., 2003a. Chaotic advection, fractals and diffusion during mixing of magmas: evidence from lava flows. Journal of Volcanology and Geothermal Research, 124, 255–279.

Perugini, D., Busà, T., Poli, G., Nazzareni, S., 2003b. The role of chaotic dynamics and flow fields in the development of disequilibrium textures in volcanic rocks. Journal of Petrology, 44, 733–756.

Perugini, D., Petrelli, M., Poli, G., 2006. Diffusive fractionation of trace elements by chaotic mixing of magmas. Earth Planetary Science Letters, 243, 669–680.

Perugini, D., De Campos, C.P., Dingwell, D.B., Petrelli, M., Poli, G., 2008. Trace element mobility during magma mixing: Preliminary experimental results. Chemical Geology, 256, 146–157.

Perugini, D., Petrelli, M., Poli, G., De Campos, C., Dingwell, D.B., 2010. Time-scales of recent phlegrean fields eruptions inferred from the application of a ‘diffusive fractionation’ model of trace elements. Bulletin of Volcanology, 72, 431–447.

Perugini, D., De Campos, C.P., Ertel-Ingrisch, W., Dingwell, D.B., 2012. The space and time complexity of chaotic mixing of silicate melts: implications for igneous petrology. Lithos, 155, 326–340.

Perugini, D., De Campos, C.P., Petrelli, M., Dingwell, D., 2015. Concentration variance decay during magma mixing: a volcanic chronometer. Scientific Reports, 5, 14225.

Petrelli M., Morgavi D., Vetere F., Perugini D., 2016a. Elemental imaging and petro-volcanological applications of an improved Laser Ablation Inductively Coupled Quadrupole Plasma Mass Spectrometry. Period. Mineral. 85, 25–39.

Petrelli M., Laeger K., Perugini D., 2016b. High resolution trace element determination of geological samples by laser ablation quadrupole plasma mass spectrometry: implications for glass analysis in volcanic products. Geosci. J. 20(6), 851–863.

Piccirillo, E.M., Raposo, M.I.B., Melfi, A.J., Comin-Chiaramonti, P., Bellieni, B., Cordani, U.G., Kawashita, K., 1987. Bimodal fissural volcanlc suites from the Paraná Basin (Brazil): K-Ar age, Sr-tsotopes and geochemtstry. Geochimica Brasiliensis, 1, 53-69.

Piccirillo, E.M., Melfi, A.J., 1988. The Mesozoic flood volcanism of the Paraná Basin: petrogenetic and geophysical aspects. São Paulo, Brazil. IAG, University of São Paulo (ed.). 600p.

Piccirillo, E.M., Comin-Chiaramonti, P., Bellieni, B., Civetta, L., Marques, L.S., Melfi, P., Petrini, R., Raposo, M.I.B., Stolfa, D., 1988. Petrogenetic aspects of continental flood basalt-rhyolite suites from the Paraná Basin. In: "The Mesozoic flood volcanism of the Paraná Basin: petrogenetic and geophysical aspects". Piccirillo E. M. & Melfi A. J. (eds.), IAG, University of São Paulo, Brazil, 179-205p.

Polo, L.A., Janasi, V.A., Giordano, D., Lima, E.F., Cañón-Tapia, E., Roverato, M., 2018. Effusive silicic volcanism in the Paraná Magmatic Province, South Brazil: evidence for locally-fed lava flows and domes from detailed field work. Journal of Volcanology and Geothermal Research, 355:204-218. http://dx.doi.org/10.1016/j.jvolgeores.2017.08.007.

Prazeres Filho, H.J., 2005. Caracterização geológica e petrogenética do batólito granítico Três Córregos (PR-SP): geoquímica isotópica (Nd-Sr-Pb), idades (ID-TIMS/SHRIMP) e $\delta^{18}O$ em zircão. São Paulo, University of São Paulo (PhD thesis). DOI: 10.11606/T.44.2005.tde-29102015-131336

Prazeres-Filho, H.J., Harara, O.M., Basei, M.A.S., Passarelli, C.R., Siga Jr., O., 2003. Litoquímica, Geocronologia U-Pb e Geologia Isotópica (Sr-Nd-Pb) das Rochas Graníticas dos Batólitos Cunhaporanga e Três Córregos na Porção Sul do Cinturão Ribeira, Estado do Paraná. São Paulo, Geologia USP Série Científica, 3, 51-70.

Richter, F.M., 1993. A method for determining activity-composition relations using chemical diffusion in silicate melts. Geochimica et Cosmochimica Acta, 57, 2019–2032.

Rocha-Júnior, E.R.V., Marques L.S., Babinski, M., Nardy, A.J.R., Figueiredo, A.M.G., Machado, F.B., 2013. Sr-Nd-Pb isotopic constraints on the nature of the mantle sources involved in the genesis of the high-Ti tholeiites from northern Paraná Continental Flood Basalts (Brazil). Journal of South American Earth Sciences, 46, 9-25.

Rocha-Júnior, E.R.V., Marques, L.S., Babinski, M., Machado, F.B, Petronilho, L.A., Nardy, A.J.R., 2020. A telltale signature of Archean lithospheric mantle in the Paraná continental flood basalts genesis. Lithos, 364–365, 105519. https://doi.org/10.1016/j.lithos.2020.105519

Rodrigues, S.W.O., Caltabeloti, F.P., Almeida, V.V., Brumati, M., Archanjo, C.J., Hollanda, M.H.B.M., Salazar, C.A., Liu, D., 2011. Petrography, Geochemistry and Geochronology of the Patrimônio Santo Antônio and São Domingos Granites (Cunhaporanga Granitic Suite, Paraná, Southeast Brazil). São Paulo, Geologia USP Série Científica, 11, 3, 03-21.

Rossi, S., Petrelli, M., Morgavi, D., González-García, D., Fischer, L.A., Vetere, F., Perugini, D., 2017. Exponential decay of concentration variance during magma mixing: Robustness of a volcanic

chronometer and implications for the homogenization of chemical heterogeneities in magmatic systems. Lithos, 286–287, 396–407.

Sato, H., 1974. Diffusion coronas around quartz xenocrysts in andesite and basalt from Tertiary volcanic region in northeastern Shikoku, Japan. Contributions to Mineralogy and Petrology, 50, 49-64.

Shannon, R.D. (1976). Revised effective ionic radii and systematic studies of interatomic distances in halides and chalcogenides. Acta Crystallographica Section A 32, 751–767.

Shimizu N., Kushiro I., 1991. The mobility of magnesium, calcium, and silicon in diopside-jadeite liquids at high pressures. In Physical Chemistry of Magmas (ed. L.L. Perchuk and I. Kushiro), pp. 192–212. Springer-Verlag.

Vicentini, C.M. (2015). Caracterização geoquímica e isotópica (Sr-Nd-Pb) dos litotipos subalcalinos diferenciados do Enxame da Serra do Mar. IAG, São Paulo, University of São Paulo (master dissertation). DOI: 10.11606/D.14.2019.tde-05062018-110939

Vicentini, C.M., De Campos, C.P., Ingrisch, W.E., Marques, L.S., Dingwell, D.B., Perugini, D., 2023. Contamination of basalt through silicic melts: The first chaotic dynamics experiments with Paraná-Etendeka starting materials. Chemical Geology, 615, 121200. https://doi.org/10.1016/j.chemgeo.2022.121200

Vicenzi, E., Green, T., Sie, S., 1994. Effect of oxygen fugacity on trace-element partitioning between immiscible silicate melts at atmospheric pressure: A proton and electron microprobe study. Chemical Geology, 117, 355-360.

Waight, T.E., Lesher, C.E., 2010. Pb isotopes during crustal melting and magma mingling — A cautionary tale from the Miki Fjord macrodike, central east Greenland. Lithos, 118, 191–201.

Watson, E.B., 1976. Two-liquid partition coefficients: experimental data and geochemical implications. Contributions to Mineralogy and Petrology, 56, 119-134 .

Watson E.B., 1982. Basalt contamination by continental crust: some experiments and models. Contributions to Mineralogy and Petrology, 80, 73– 87.

Watson, E.B., Harrison, T.M., Ryerson, F.J., 1985. Diffusion of Sr, Sm and Pb in fluorapatite. Geochimica et Cosmochimica Acta, 49, 1813-1823.

Zhang, Y., Walker, D., Lesher, C.E, 1989. Diffusive crystal dissolution. Contributions to Mineralogy and Petrology, 102, 492-513.

Zhang, Y., Ni, H., Chen, Y., 2010. Diffusion data on silicate melts. Reviews in Mineralogy & Geochemistry, 72, 311-408.

APPENDIX

A. BULK ROCK ANALYSIS

The collected samples present X-ray fluorescence, laser ablation inductively coupled plasma mass spectrometry, and thermal ionization mass spectrometry (Sr-Nd-Pb) analytical data available on:
https://figshare.com/articles/dataset/Bulk_rock_analysis_xlsx/23499171

DOI: 10.6084/m9.figshare.23499171

B. EPMA ANALYSIS

The analysed experimental glasses present the EPMA transect data available on:
https://figshare.com/articles/dataset/EPMA_xlsx/23499174

DOI: 10.6084/m9.figshare.23499174

C. LA-ICP-MS ANALYSIS

The analysed experimental glasses present the EPMA transect data available on:
https://figshare.com/articles/dataset/LA-ICP-MS_xlsx/23499177

DOI: 10.6084/m9.figshare.23499177